UNIVERSITÀ
DEGLI STUDI
FIRENZE

DOTTORATO DI RICERCA IN ENERGETICA E
TECNOLOGIE INDUSTRIALI E AMBIENTALI INNOVATIVE

CICLE XXXIII

COORDINATOR Prof. Eng. Giampaolo Manfrida

# Wave-to-wire modelling of oscillating water column wave energy converters and design optimisation for the Mediterranean Sea

Settore scientifico disciplinare ING-IND/08


**Ph.D. Candidate**
Lorenzo Ciappi

**Supervisors**
Prof. Eng. Giampaolo Manfrida
Prof. Eng. Lorenzo Cappietti
Prof. Eng. Jacek Smołka


**Coordinator**
Prof. Eng. Giampaolo Manfrida

*Firenze, 2017/2020*

UNIVERSITÀ
DEGLI STUDI
FIRENZE

DOTTORATO DI RICERCA IN ENERGETICA E
TECNOLOGIE INDUSTRIALI E AMBIENTALI INNOVATIVE

CICLE XXXIII

COORDINATOR Prof. Eng. Giampaolo Manfrida

# Wave-to-wire numerical modelling of oscillating water column wave energy converters and design optimisation for the Mediterranean Sea

Settore scientifico disciplinare ING-IND/08


**Ph.D. Candidate**
Lorenzo Ciappi
*Department of Industrial Engineering, University of Florence, Italy*

**Supervisor**
Prof. Eng. Giampaolo Manfrida
*Department of Industrial Engineering, University of Florence, Italy*

**Co-Supervisors**

Prof. Eng. Lorenzo Cappietti
*Department of Civil and Environmental Engineering, University of Florence, Italy*

Prof. Eng. Jacek Smołka
*Institute of Thermal Technology, Silesian Univeristy of Technology Gliwice, Poland*


---

*Firenze, 2017/2020*

*"Io sto ancora imparando".*
Michelangelo Buonarroti

*A mio padre e mia madre,*
*che mi hanno sempre sostenuto e motivato*
*dimostrandomi piena fiducia ed ammirazione;*
*anche grazie a voi sono giunto*
*a questo importante traguardo.*

*A mia sorella e mio fratello,*
*con cui sono cresciuto e maturato;*
*insieme abbiamo vissuto tante esperienze*
*e molte ancora ci aspettano.*

*Alle mie nipotine,*
*che mi riempiono sempre di gioia*
*in tutti i momenti trascorsi insieme.*

# Acknowledgements

*Coming towards the end of the challenging and satisfying journey done during the last three years, I feel that there are many people I wish to thank.*

*First of all, I would like to express my gratitude to Prof. Giampaolo Manfrida and Prof. Lorenzo Cappietti for the opportunity of joining their research groups. The studies performed with their supervision have further raised my great interest in scientific activities. I became increasingly passionate about renewable energy and especially energy conversion from the sea. Thinking to the very beginning of this path, I realise how it made me grow, from either a professional and a human point of view. Thank you also for the trust that you constantly showed to me and the advice you gave me.*

*I wish to demonstrate my sincere gratefulness to Prof. Jacek Smołka, who allowed me to live unforgettable and valuable experiences at the Institute of Thermal Technology of the Silesian University of Technology. I will always have a special thought for the time spent with him. The admirable competence and passion for research and the ability to transmit knowledge have always been of fundamental importance. I really wish to thank everyone in his group, as they contributed to my professional growth with fundamental advices that I have treasured. A very special thanks is for Eng. MichałStebel for his collaboration on my research project. I also wish to especially thank Dr. Karolina Petela, Dr. Bartłomiej Melka, Eng. Agata Waida, Eng. Magdalena Bogacka, Eng. Jakub Bodys, and Eng. Mieszko Tokarski.*

*I wish to thank Prof. Daniele Fiaschi and Dr. Lorenzo Talluri for having involved me in the research activities on Tesla*

*turbine. I am very pleased of contributing to this interesting activity.*

*I am also particularly grateful to Dr. Alessandro Bianchini for the accuracy and clarity of his advices. I wish to thank Dr. Irene Simonetti and Eng. Lapo Cheli for their collaboration to the development of my research.*

*I wish to express my gratitude to Prof. Luís Gato and Dr. Devaiah Nalianda for having reviewed my thesis and for the very interesting and useful comments provided, that allowed to improve the quality of the work.*

*I am grateful to all my past and present colleagues, with a very special thanks to Eng. Leonardo Pacini for the fruitful and pleasant cooperation that we always had. I am also very thankful to Eng. Piotr Wisniewski and Eng. Krystof Rusin for the very good time spent together in Firenze and Gliwice and our exchange of knowledge.*

*I acknowledge the European Union and the Republic of Poland for having supported my research in the framework of the NAWA Project with the grant agreements 10/P/2019 and 01/P/2020.*

*My thoughts also go to the people, outside the academic world, who influenced my life. A huge acknowledgement goes to my friends with whom I have spent unforgettable moments during which thoughts have always given way to fun.*

*The biggest thanks goes to my family, who have always supported me with love and admiration and allowed me to reach this coveted objective.*

# Abstract

One of the global challenges of the millennium is bringing renewable energy conversion systems to industrial maturity. The aim is to increase their contribution to the satisfaction of the continuously increasing energy demand that is still mainly supplied by fossil fuels, subject to depletion and strongly related to the negative impact on the environment.

The sea is an important renewable energy resource for its extension and the power conveyed by waves, currents, tides, and thermal gradients. Amongst these physical phenomena, sea waves are the resource that combines the highest energy density and availability. Despite the potential of sea waves, their harnessing is still a technological challenge.

Oscillating water column (OWC) systems are among the most credited solutions for effective conversion of this potential. Despite a renewed interest, however, they are often at a demonstration phase, and additional research is required to foster their installation worldwide.

Within this framework, the thesis aims to the development of an analytical wave-to-wire model of OWC wave energy converters for the investigation of the entire process of energy transformation from sea waves to electric wire. This approach is particularly suitable during the early design stages to evaluate the energy extractable from sea waves and properly select the location and the main geometric and operating parameters of the system.

The model performs a comprehensive simulation of the entire system to estimate the electric energy production for a specific sea state, based on the joint solution of the analytical models of

the three main converters, represented by the chamber, turbine, and generator.

An analytical rigid piston model of the primary converter was realised by applying the linear wave theory. The hydrodynamics, thermodynamics, and aerodynamics of the chamber, fixed and detached regarding the seabed, were solved together with the aerodynamics of the air turbine.

Regarding the secondary converter, two typologies of turbines were considered. An analytical model relying on the actuator disc theory and the blade element momentum theory was applied to solve the aerodynamics of Wells turbines. A novel analytical model of an axial impulse turbine was developed based on the blade element momentum theory and proposing the application of experimental correlations widely used in turbomachinery to design axial turbines.

An analytical model for controlling the coupling of the secondary and tertiary converters was realised. The algorithm regulates the angular velocity of the rotor and the mechanical transmission of the torque from the turbine to the electric generator.

In addition to the analytical approach, computational fluid dynamics models of the secondary converter were developed for both the turbine typologies. They allow for an accurate evaluation of the flow characteristics and the detailed analysis of the power transmission stage from pneumatic to mechanical power.

The analytical and numerical models of the Wells and impulse turbines were validated through the comparison with analytical and experimental literature data in operating conditions typical of the Mediterranean Sea, showing a good agreement.

The developed wave-to-wire model was applied to evaluate the operation of OWC systems in two favourable locations in Italy. The sites were determined as highly energetic spots for the Italian wave climate with characteristics proper of a moderate Mediterranean sea state. One location is positioned in the central area of Tuscany and the other in front of the north-west coast of Sardinia.

An optimisation procedure was performed to determine the geometric and operating parameters of the Wells and impulse turbines that maximise the annual energy harvesting from waves to wire. The performance parameters, the operating curves and maps, and the energy conversion of the entire system were achieved. Finally, the functioning of the two optimal configurations of the system was analysed considering the seasonal wave conditions of the application sites to further enhance the global energy harnessing.

# Contents

# List of Figures

# List of Tables

# Nomenclature

**Roman Letters**

| | | |
|---|---|---|
| $A$ | Area | $m^2$ |
| $AE$ | Annual specific wave energy | $^{kWh}/_{m}$ |
| $AR$ | Aspect ratio | – |
| $\mathfrak{a}$ | Distance | $m$ |
| $\mathcal{B}$ | Radiation damping coefficient | $^{Ns}/_{m}$ |
| $\mathfrak{B}$ | Clearance coefficient | – |
| $B_c$ | Chamber breadth | $m$ |
| $b$ | Blade height | $m$ |
| $C$ | Coefficient | – |
| $\mathcal{C}$ | Hydrostatic restoring coefficient | $^{N}/_{m}$ |
| $C_A$ | Input coefficient | – |
| $C_D$ | Drag coefficient | – |
| $C_{\mathfrak{g}}$ | Geometric coefficient | – |
| $C_T$ | Torque coefficient | – |
| $C_x$ | Axial force coefficient | – |
| $C_\theta$ | Tangential force coefficient | – |
| $cf$ | Correction factor | – |

| | | |
|---|---|---|
| $D$ | Front wall draught length | $m$ |
| $\mathcal{D}$ | Discharge coefficient | $-$ |
| $d$ | Diameter | $m$ |
| $d_o$ | Chamber opening diameter | $m$ |
| $E$ | Energy | $kWh$ |
| $\mathfrak{E}$ | Total specific energy | $^{J}/_{kg}$ |
| $\mathcal{F}$ | Flux | $^{J}/_{m^2}$ |
| $F_c$ | Front wall freeboard length | $m$ |
| $f$ | Force | $N$ |
| $G$ | Chamber height | $m$ |
| $g$ | Gravitational acceleration | $^{m}/_{s^2}$ |
| $H$ | Sea wave height | $m$ |
| $H_{m0}$ | Significant sea wave height | $m$ |
| $h$ | Seawater depth | $m$ |
| $\hbar$ | Air volume height | $m$ |
| $\mathfrak{h}$ | Specific energy | $^{J}/_{kg}$ |
| $i$ | Generic blade element | $-$ |
| $\mathfrak{i}$ | Flow incidence angle | $Degrees$ |
| $J$ | Rotational inertia | $m^2kg$ |
| $K$ | Damping coefficient | $-$ |
| $k$ | Wavenumber | $^{1}/_{m}$ |
| $\mathcal{k}$ | Permeability | $-$ |
| $\mathfrak{k}$ | Effective thermal conductivity | $^{W}/_{Km}$ |
| $L$ | Specific work | $^{J}/_{kg}$ |
| $\mathfrak{L}$ | Characteristic length | $m$ |
| $l$ | Chord length | $m$ |
| $\mathfrak{l}$ | Turbulent length scale | $m$ |

| | | |
|---|---|---|
| $\ell$ | Length | $m$ |
| $M_{CH}$ | Nominal flow deviation coefficient | $-$ |
| $M_{HW}$ | Flow deviation coefficient | $-$ |
| $Ma$ | Mach number | $-$ |
| $m$ | Mass | $kg$ |
| $\mathfrak{m}$ | Machine typology coefficient | $-$ |
| $\dot{m}$ | Mass flow rate | $kg/s$ |
| $n$ | Peak number | $-$ |
| $\mathcal{O}$ | Flow rotation | $1/s$ |
| $P$ | Power | $W$ |
| $p$ | Pressure | $Pa$ |
| $\dot{q}$ | Volume flow rate | $m^3/s$ |
| $\mathcal{R}$ | Air specific gas constant | $J/kgK$ |
| $Re$ | Reynolds number | $-$ |
| $r$ | Radius | $m$ |
| $rf$ | Relative frequency | $\%$ |
| $\mathcal{S}$ | Arbitrary quantity source or sink | |
| $s$ | Sound speed | $m/s$ |
| $T$ | Period | $s$ |
| $\mathcal{T}$ | Temperature | $K$ |
| $T_{m-1,0}$ | Sea wave energy period | $s$ |
| $t$ | Time | $s$ |
| $\mathfrak{t}$ | Rotor pitch | $m$ |
| $t$ | Tip clearance gap | $m$ |
| $\bar{t}_{h,max}$ | Maximum blade thickness | $m$ |
| $\bar{t}_o$ | Porous medium thickness | $m$ |
| $\bar{t}_w$ | Wall thickness | $m$ |

| | | |
|---|---|---|
| $ti$ | Turbulence intensity | $\%$ |
| $tr$ | Time ratio | $-$ |
| $U$ | Blade velocity | $^{m}/_{s}$ |
| $\mathbf{u}$ | Velocity vector | $^{m}/_{s}$ |
| $V$ | Volume | $m^3$ |
| $v$ | Air absolute velocity | $^{m}/_{s}$ |
| $W$ | Chamber length | $m$ |
| $w$ | Air relative velocity | $^{m}/_{s}$ |
| $x$ | Axial coordinate | $m$ |
| $Z$ | Blade number | $-$ |
| $z$ | Vertical coordinate | $m$ |

**Greek Letters**

| | | |
|---|---|---|
| $\alpha$ | Absolute flow angle | *Degrees* |
| $\beta$ | Relative flow angle | *Degrees* |
| $\Gamma$ | Blade loading | $N$ |
| $\Gamma$ | Flow circulation | $^{m^2}/_{s}$ |
| $\gamma$ | Heat capacity ratio | $-$ |
| $\gamma$ | Rotor blade angle | *Degrees* |
| $\delta$ | Flow deviation | *Degrees* |
| $\delta_{i,j}$ | Kronecker delta | $-$ |
| $\epsilon$ | Flow deflection | *Degrees* |
| $\epsilon$ | Turbulence energy dissipation | $^{m^2}/_{s^3}$ |
| $\zeta$ | Damping ratio | $-$ |
| $\eta$ | Sea wave displacement | $m$ |
| $\Theta$ | Camber angle | *Degrees* |
| $\theta$ | Tangential direction | |
| $\theta$ | Stator blade angle | *Degrees* |

| | | |
|---|---|---|
| $\kappa$ | Turbulence kinetic energy | $m^2/s^2$ |
| $\lambda$ | Wavelength | *Degrees* |
| $\lambda$ | Flow acceleration parameter | – |
| $\mu$ | Air kinematic viscosity | *Degrees* |
| $\mu_t$ | Turbulent viscosity coefficient | $m^2/s$ |
| $\Xi$ | Annual efficiency ratio | – |
| $\xi$ | Efficiency | % |
| $\rho$ | Density | $kg/m^3$ |
| $\Sigma$ | Annual energy harvesting ratio | – |
| $\sigma$ | Rotor solidity | – |
| $\varsigma$ | Logarithmic decrement | – |
| $\tau$ | Torque | $Nm$ |
| $\boldsymbol{\tau}$ | Stress tensor | $kg/m^2s^2$ |
| $\boldsymbol{\tau}^{Re}$ | Reynolds stress tensor | $kg/m^2s^2$ |
| $\Upsilon$ | Loss coefficient | – |
| $\upsilon$ | Seawater particle velocity | $m/s$ |
| $\dot{\upsilon}$ | Seawater particle acceleration | $m/s^2$ |
| $\Phi$ | System flow coefficient | – |
| $\phi$ | Turbine flow coefficient | – |
| $\varphi$ | Phase | $s$ |
| $\boldsymbol{\varphi}$ | Arbitrary quantity | |
| $\chi$ | Seawater surface displacement | $m$ |
| $\Psi$ | System pressure coefficient | – |
| $\Omega$ | Turbine rotational speed | $rad/s$ |
| $\omega$ | Seawater angular frequency | $rad/s$ |
| $\boldsymbol{\omega}$ | Specific turbulence dissipation | $1/s$ |

**Subscripts**

| | |
|---|---|
| $\mathit{0}$ | Initial condition |
| 0 | IGV inlet section |
| 1 | Rotor inlet section |
| 2 | Rotor outlet section |
| 3 | OGV outlet section |
| $a$ | Air |
| $AM$ | Ainley and Mathieson |
| $add$ | Added |
| $ae$ | Aerodynamic |
| $amb$ | Ambient |
| $ann$ | Annulus |
| $av$ | Average |
| $b$ | Blade |
| $bp$ | Biplane |
| $c$ | Chamber |
| $\mathit{c}$ | Continuity |
| $D$ | Drag |
| $d$ | Device |
| $\mathit{d}$ | Actuator disc |
| $dn$ | Damped natural |
| $do$ | Downstream |
| $e$ | Electric |
| $eq$ | Equivalent |
| $exc$ | Excitation |
| $ext$ | External |
| $FK$ | Froude-Krylov |
| $fr$ | Free stream |

| | |
|---|---|
| $\mathfrak{g}$ | Generator |
| $HW$ | Howell |
| $hd$ | Hydraulic diameter |
| $hst$ | Hydrostatic |
| $I$ | Input |
| $i$ | Blade element index |
| $i$ | Row index |
| $\mathfrak{i}$ | Flow incidence angle |
| $id$ | Ideal |
| $in$ | Inlet |
| $ine$ | Inertial |
| $is$ | Isentropic |
| $j$ | Column index |
| $K$ | Kinetic |
| $L$ | Lift |
| $m$ | Blade midspan |
| $\mathfrak{m}$ | Momentum |
| $max$ | Maximum |
| $n$ | Peak number |
| $O$ | Output |
| $o$ | Organic |
| $o$ | Opening |
| $\mathfrak{o}$ | Origin |
| $out$ | Outlet |
| $par$ | Particle |
| $pr$ | Profile |
| $pto$ | Power take-off |

| | |
|---|---|
| $\mathcal{R}$ | Rotor |
| $r$ | Radial direction |
| $r$ | Relative |
| $rad$ | Radiating |
| $rdp$ | Radiating damping |
| $ref$ | Reference |
| $Rot$ | Rotor |
| $\mathcal{S}$ | Stator |
| $s$ | Season |
| $se$ | Secondary |
| $sf$ | Skin friction |
| $st$ | Stall |
| $T$ | Turbine |
| $t$ | Total condition |
| $\mathfrak{t}$ | Turbine |
| $tc$ | Tip clearance |
| $te$ | Trailing edge |
| $tr$ | Translational |
| $un$ | Undamped natural |
| $up$ | Upstream |
| $V$ | Viscous |
| $x$ | Axial direction |
| $w$ | Seawater |
| $y$ | Year |
| $z$ | Vertical direction |
| $\theta$ | Tangential direction |

**Superscripts**

| | |
|---|---|
| $*$ | Nominal value |
| $\prime$ | Quantity fluctuation |
| $\bar{x}$ | First row |
| $\bar{\bar{x}}$ | Second row |
| $\overline{x}$ | Average value |

**Acronyms**

| | |
|---|---|
| BBDB | Backward Bent Duct Buoy |
| BEM | Blade element momentum |
| CAD | Computer-aided design |
| CFD | Computational fluid dynamics |
| CIF | Cascade interference factor |
| DFIG | Doubly-fed induction generator |
| DM | Dynamic mesh |
| IGV | Inlet guide vane |
| JAMSTEC | Japan Agency for Marine-Earth Science and Technology |
| LABIMA | Maritime Engineering Laboratory |
| LCOE | Levelised cost of energy |
| LE | Leading edge |
| LIMPET | Land Installed Marine Powered Energy Transformer |
| MP | Mixing plane |
| MRF | Multiple reference frame |
| NAREC | National Renewable Energy Centre |
| OGV | Outlet guide vane |
| OM | Overset mesh |
| OSPREY | Ocean Swell Powered Renewable Energy |
| OWC | Oscillating water column |

PID Proportional-integral-derivative

PTO Power take-off

RANS Reynolds averaged Navier-Stokes

REWEC3 Resonant Wave Energy Converter

URANS Unsteady Reynolds averaged Navier-Stokes

SCIG Squirrel-cage induction generator

SERG Sustainable Energy Research Group

SIMPLE Semi-Implicit Method for Pressure-Linked Equations

SIMPLEC Semi-Implicit Method for Pressure-Linked Equations-Consistent

SM Sliding mesh

SRF Single reference frame

SST Shear-stress transport

STL Still water level

VFD Variable-frequency drive

WEC Wave energy converter

# Chapter 1

# Introduction

In recent years, energy demand has been continuously growing worldwide. Together with the possible exhaustion of fossil resources and the level of pollutant and greenhouse emissions, the increasing request has raised the global efforts towards enhancing the harvesting of renewable resources. In this framework, the sea is one of the renewable energies with the highest potential. The physical phenomena that can be exploited are waves, currents, tides, and thermal gradients. Since sea waves combine the highest energy density and availability of the resource amongst the cited ones, the wave energy conversion devices are attractive for contributing to satisfy energy demand [31].

Indeed, wave energy has remarkable potential, as the wave power incident on the world coastline is estimated among 0.5 and 2.2 TW [37, 38], which corresponds to more than 10% of the global power consumption [39]. Moreover, a key aspect of energy from waves is represented by the use of not impacting and not polluting technologies for power conversion. Besides,

wave energy converters (WECs) are prone to be coupled with photovoltaic plants and offshore wind turbines [40], leading to clustered production systems. There are three main categories of WECs [41], classified based on their working principle, namely oscillating water column devices (OWCs), overtopping devices (OTDs), and oscillating body devices (OBDs). Differently from other renewable energy fields, however, a predominant technology for wave energy conversion has not been identified yet [42].

Among other technologies, OWC devices are currently considered very promising. A wave energy converter based on the oscillating water column principle consists of three leading converters that determine energy transformation from sea waves to the electricity grid. They are the chamber structure (primary converter), the air turbomachine (secondary converter), and the electrical generator (tertiary converter).

The chamber of the system is conventionally a hollow partially submerged structure made of concrete or steel. It is provided with two openings for the interaction with the incident waves and the air crossing the turbine. One hole is underwater and faces the principal direction of wave propagation, while the other is above water and is connected with the duct embedding the air turbine and open to the atmosphere. The sea waves incident on the caisson cause an oscillating heave motion of the inner column of water that alternatively compresses and expands the volume of air trapped over the water level inside the structure. The air pressure gradients force the airflow to cross the turbine duct with an alternate sense, from the atmosphere to the chamber, and vice versa. Ideally, during the inflow phase, when sea wave reaches its maximum height, the water level inside the chamber decreases, causing a pressure reduction and the expansion of the air that flows inside the system from the atmosphere.

During the outflow phase, sea wave is at the minimum height, and the chamber water reaches its peak, promoting the release of air towards the outside. Therefore, the bidirectional airflow drives an air turbine embedded in the duct and coupled with an electrical generator. The two main categories of air turbines that have been used so far in this kind of system are conventional unidirectional flow turbines and bidirectional flow turbines. The former type requires a system of airflow rectification with non-return valves to make unidirectional the airflow generated by the action of sea waves impacting the chamber. However, this solution was proved to be feasible only for small devices, as navigation buoys [43]. The latter typology effectively operates without the need for the rectification system with valves, as they are self-rectifying turbomachines. Wells turbines and impulse turbines are the most widespread machines for wave energy converters based on the oscillating water column technology [44, 1].

The main advantages of OWC systems are the structural simplicity, reliability, and the motion of mechanical components only above water. Despite these interesting features these systems still need to undergo a real industrial development process prior to becoming a consolidated technology for energy conversion from the sea. This is mainly due to the still very high levelised cost of energy (LCOE), which in turn is connected to the high capital cost of the system. Indeed, the LCOE ranges from 90 to 101 €/MWh for onshore installations and between 180 and 490 €/MWh for offshore installations. Comparing these values with onshore (60 €/MWh) and offshore (102 €/MWh) wind energy, solar photovoltaic (68 €/MWh), and geothermal energy (50 €/MWh), it is apparent that wave energy is presently not competitive with other renewable energies in terms of cost-

effectiveness [45, 46].

The reduction of the LCOE is mainly achievable through the increase of the system efficiency and the decrease of the capital costs of structures and devices. Regarding the first aspect, the maximisation of the energy conversion of the overall transformation processes from incident sea waves to electric connection is pivotal at the present stage of the research to enhance their efficiency. This requires the joint optimisation of all the components for the specific wave conditions of the application site as the performance of an OWC system varies significantly with different climates [47, 48]. Concerning the second aspect, relevant infrastructures need to be built in locations suitable for a profitable and safe energy extraction. This issue can be tackled by promoting the diffusion of OWC systems in combination with the existing structures as breakwaters in harbours, developing new solutions like pre-assembled offshore floating platforms possibly dedicated to the energy production and storage, and by fostering the industrial standardisation of specific components as the secondary converters [33]. Moreover, the design of the system components has to be aimed at limiting their manufacturing and maintenance costs.

The power conversion chain of an OWC system is composed of several stages, starting with the periodic harvesting of the power transported by the sea waves and ending with the transfer of electrical power to the grid. The models that investigate the entire conversion chain are referred to as wave-to-wire models. In these models, four main stages are considered: absorption, transmission, generation, and conditioning. During the absorption stage, the wave motion is transformed into oscillating pneumatic power inside the chamber. Throughout the transmission

stage, this power is converted into mechanical power with an air turbine. In the generation stage, the electric generator, connected with mechanical transmission to the turbine and subject to a control strategy, converts the mechanical power into electrical power. Finally, during the conditioning stage, the electric power is adjusted to be delivered into the grid. These stages involve the analysis of the hydrodynamics, thermodynamics, and aerodynamics of the chamber, the aerodynamics of the turbine, and the rotor dynamics of the turbine and the electric generator [33].

State of the art on existing design solutions for the devices and modelling approaches for OWC systems indicates that the usual approach carried out so far relies on the separate design and optimisation of each of the three converters. Properly accounting for the fluid dynamic connection between the chamber and the turbine is critical to ensure an accurate prediction of the global energy conversion of the system. However, the presence of different physical phenomena and their complementarity in the correct functioning of the system makes this approach often not effective. Indeed, it leads to slow convergence towards the optimal configuration or even an incomplete exploration of the design space [33]. In addition, the separate analysis of the converters may determine the incorrect evaluation of their operating conditions as the components are mutually influenced.

Up to now, the individual study of the three converters was mainly carried out by different research groups. Although, several wave-to-wire models were realised considering the integrated modelling schemes of an OWC system, they typically focus on the analysis of the chamber or the electric generator [33]. Con-

versely, the level of detail regarding the turbine is limited to the use of a simplified approach. Indeed, the procedure applied is based on general correlations expressing the mass flow rate, pressure variation, power, and efficiency through the flow rate, pressure, and power coefficients, and the total-to-static efficiency of the turbine. This reduces the possibility of an inner coupling of the flow conditions delivered by the chamber with the operation of the air turbine and electric generator, regulated by the control strategy.

In this framework, the main objective of the thesis is to improve the analytical modelling of OWC systems with the development of a complete and reliable wave-to-wire model for engineering applications, able to account both for Wells or impulse turbines. The model allows the joint analysis of the chamber and air turbine for the peculiar wave conditions of a specific installation site. The hydrodynamics, thermodynamics, and aerodynamics of the caisson were determined with a rigid piston approach. Two original low-order aerodynamic models were created for the two turbines, providing an interesting compromise between accuracy and computational cost. Finally, a control strategy was implemented to monitor the instant rotor angular velocity and torque in both design and off-design conditions.

The key point of the novelty of the present study is the application of a refined analytical modelling of the air turbines within the wave-to-wire chain. In fact, the proposed approach allows the direct solution of the turbine aerodynamics, achieving a higher accuracy in the determination of the operation of this component and its interaction with the other components. Consequently, the accuracy of the estimation of the overall system energy conversion is enhanced.

A preliminary analysis was conducted on a wide set of locations to identify the most suitable ones for installing OWC systems in different regions of Italy. All the wave conditions and the related energy transport and frequency of occurrence were determined for each of them. Two sites positioned in the centre of Tuscany and in the north-west of Sardinia were selected as wave energy hotspots [49, 33, 24].

The model was applied to determine the optimal geometry and operating conditions of a monoplane isolated Wells turbine and an axial impulse turbine for a specific chamber under the wave conditions of the two selected hotspots. Four sets of parametric analyses were performed, maximising the objective function constituted by the global annual energy conversion of the system. The geometry and properties of the caisson were determined by scaling up the outcomes of experiments carried out at a laboratory scale to optimise the pneumatic efficiency of the system for wave conditions typical of a moderate Mediterranean climate.

The operating maps of the entire system were obtained considering a yearly energy extraction scenario. They were utilised to identify the most relevant parameters regulating the turbine functioning and select the optimal turbine configurations. Afterwards, the operating curves, performance parameters, and energy harnessing were determined for all the selected configurations of the system. The analyses were conducted considering average wave conditions determined either on annual and seasonal basis.

Furthermore, computational fluid dynamics (CFD) models were developed to analyse the aerodynamics of the airflow pass-

ing through monoplane isolated Wells turbines and axial impulse turbines for OWC systems. Three-dimensional multi-block techniques were implemented to create the computational domain with fully mapped grids composed of hexahedral elements. The employment of circumferential periodic boundary conditions allowed for the reduction of computational power and time. The models use steady and unsteady Reynolds-averaged Navier-Stokes (RANS and u-RANS, respectively) schemes with a multiple reference frame approach or the u-RANS formulation with a sliding mesh approach. Completely automated procedures were developed for the creation, solution, and post-processing of the entire models [31].

The results of the analytical and CFD models of the air turbines were compared between themselves and with literature analytical and experimental data, showing good agreement. The aim was to validate the single models for their application in the wave-to-wire model developed.

In this view, the development of the integrated wave-to-wire model proposed is of capital relevance for promoting the competitiveness of the OWC technology. It is particularly useful during the preliminary phase of the design process, as the reduced computational time and power required enable the investigation of a wide variety of system configurations for a broad set of application sites. After this preliminary phase, the turbine selection can be further investigated by applying numerical models like the ones developed.

The optimal selection of all the components of an OWC system for the distinctive wave conditions of its installation site results in the maximisation of the energy harvesting and the in-

crease of the efficiency of power conversion. This, in turn, fosters the reduction of the levelised cost of energy, and may favour the diffusion of the oscillating water column technology worldwide.

# Chapter 2

# Rationale

*A literature review on the approaches for modelling Wells and impulse turbines for oscillating water column systems is presented. Moreover, the state of the art of wave-to-wire models is considered to highlight the main novelties of the thesis. Afterwards, the development of the principal wave energy converters based on the oscillating water column technology is described. Finally, the research request determined by the gaps found in the literature is described, and the objectives and the methodology of the analysis are indicated.*

## 2.1 State of the art

State of the art considers the theoretical research on air turbines and wave-to-wire models for oscillating water column systems and the evolution of the wave energy converters from their first application to date.

The review of the literature is organised by subdividing the

main contributions to the development of the knowledge of this technology in chronological order. The attention is mainly focused on the secondary converter of these systems, represented by air turbines.

### 2.1.1 Wells turbine review

The research on air turbines for OWC systems showed particular interest in Wells and impulse turbines, which are currently the most widespread technologies [44, 1]. Many analyses of the aerodynamics were performed by applying analytical or CFD models and with laboratory and real field experiments. Generally, the duct comprising the turbine was considered for the optimisation of the secondary converter itself, and the airflow conditions at the turbine inlet were applied based on conventional literature results. In order to further investigate the airflow field, the motion of the air volume in the system chamber was in some cases modelled with a sinusoidal function.

Focusing now the attention on Wells turbines, several studies were conducted to analyse the steady and unsteady airflow and predict the turbine performance. Furthermore, various design solutions were proposed to improve the self-starting characteristics and the aerodynamic efficiency of the turbomachine.

In 1984, Gato and Falcão presented a theoretical investigation of the aerodynamics of a monoplane isolated Wells turbine functioning with a reciprocating airflow. The flow crossing the air turbine and the main performance parameters were analysed through the application of either the two-dimensional cascade theory and the actuator disc theory [50].

In 1985, Raghunathan et al. analytically and experimentally evaluated the effects of the principal geometric and aerodynamic

parameters on the operation of monoplane isolated Wells turbines. Two analytical models relying on the two-dimensional cascade theory and the isolated airfoil data were developed. The experiments were performed on a rig with unidirectional airflow and a rig with oscillating airflow [51].

In 1990, Gato and Falcão performed a theoretical and experimental investigation of the aerodynamics of a Wells turbine which had a stationary blade row added to each side of the rotor. The entire blade system was symmetrical with respect to a plane perpendicular to the turbine axis. A quasi-three-dimensional flow analysis was developed and applied to design and build a turbine model. The theoretical and experimental results presented indicate that the stationary blades can significantly increase the efficiency of the turbomachine [52].

In 1991, Raghunathan et al. further investigated the effects of the main design variables on the turbine functioning and proposed techniques for improving its performance [53]. In the same year, Kaneko et al. performed experiments to determine the influence of the setting angle, the gap-to-chord ratio, the solidity, and the biplane arrangement on Wells turbines [54].

In 1995, Raghunathan defined a methodology for designing Wells turbines for wave power plants based on an iterative calculation of the geometric and aerodynamic parameters [55]. The same author reviewed the analytical and experimental models for predicting the operation of monoplane and biplane Wells turbines [22].

In 1997, Curran and Gato experimentally evaluated the effects of various design solutions on the performance of Wells turbines [56].

In 1998, Govardhan and Dhanasekaran utilised guide vanes to direct the incoming flow in the direction of the turbine rotation for increasing the power and efficiency in preference to the operating range [57]. In 2001, Gato and Webster demonstrated the increase of the operating range provided by backward swept blades for either pitched or unpitched blades with symmetrical profiles, to the detriment of the peak efficiency [58].

In 2002, Brito-Melo et al. applied CFD to investigate the impact on the aerodynamics of the design solutions of Wells turbines, considering the presence or absence of guide vanes and a by-pass relief valve [59]. In that year, Kim et al. analysed the influence of the blade thickness and angle of attack on the hysteresis of the operating curves and the effects of variable pitch blades [60, 61]; the research was advanced by Setoguchi et al. the following year [62].

In 2003, Heikal applied a two-dimensional analysis relying on the radial equilibrium theory to determine the influence of the blade shape, rotor solidity, and Reynolds number on the functioning of turbomachines with and without guide vanes. The outcomes were compared with experimental data obtained with a unidirectional airflow rig [63].

In 2004, Kinoue et al. stated that reducing the rotor solidity and increasing the setting angle decrease the hysteresis loop extension [64]. Setoguchi showed how the influence of the blade thickness and the angle of attack on the hysteresis is greater than the setting angle and the gap-to-chord ratio [65]. During this year, Torresi et al. performed CFD analyses to evaluate the blade tip leakage and the hysteretic mechanism under oscillating flow conditions for a low-solidity Wells turbine [66].

In 2007, Thakker and Abdulhadi experimentally investigated the influence of the shape and the blade solidity under unidirec-

tional unsteady flow conditions [67]. In 2010, Taha et al. carried out steady-state CFD analyses to determine the effects of different values of uniform tip clearance gap [68]; the next year, the analyses were extended to non-uniform dimensions and were compared with experimental literature data [69].

Torresi et al. presented an actuator disc model of a high-solidity turbine and compared the predicted performance with the corresponding CFD model [70].

Starzmann and Carolus numerically analysed the impact of the hub-to-tip ratio and rotor solidity on the aerodynamics and aeroacoustics of a monoplane isolated Wells turbine. Numerical analyses were performed to predict the characteristic curves and determine the optimum operating coefficients and the stall margin. Afterwards, experiments were carried out on laboratory-scale models using a set of selected rotors. It was found that the optimal values of total-to-static efficiency and noise emissions are obtained with moderate values of hub-to-tip ratio and rotor solidity. Conversely, high values of these geometric parameters reduce the magnitude of the hysteresis loop and increase pressure head [71].

In 2012, Shaaban and Abdel Hafiz numerically determined the effects of the area ratio and angle of the duct of a Venturi tube embedding a Wells turbine at the throat section for optimising the operation [72].

In 2013, Paderi and Puddu experimentally investigated the causes of the hysteresis loop under unsteady flow conditions [73]. Mohamed and Shaaban applied a numerical optimisation to determine the optimal blade pitch angle for different aerofoil geometries and values of solidity [74].

Starzmann and Carolus analysed the effects of the blade skewness on the operating range and the aeroacoustics and pos-

sibilities for limiting the noise [75]. In 2014, Halder and Samad applied CFD to determine the implications of the guide vane angle on the turbine functioning [76].

In 2015, Ghisu et al. experimentally and numerically evaluated the fluid dynamics and the hysteresis of a high-solidity turbine under an unsteady bidirectional flow generated by a hydraulic piston [77].

In 2016, Shaaban numerically simulated the effects of the chord length increase from the hub to the tip on the power conversion and the cost of energy. In particular, the geometric optimisation of the rotor resulted in the reduction of the LCOE up to 15-20% for an OWC plant embedding a Wells turbine [78].

Halder et al. presented a multi-objective optimisation of the blade sweep to maximise the peak torque coefficient and the efficiency, considering the implications for the fluid dynamics and operating range width [79, 80].

In 2017, Ghisu et al. demonstrated that the hysteresis between the flow acceleration and deceleration phases is caused uniquely by the compressibility effects within the oscillating water column chamber, while the differences in the flow parameters and the secondary structures near the rotor are negligible [81, 82]. Shaaban presented a multi-objective optimisation algorithm to determine the aerofoil geometry from the coordinates of standard profiles [83].

In 2018, Halder et al. numerically compared conventional blades and optimised blades with modified profile thickness and sweep, with and without grooved-casing [84].

In 2019, Kumar applied CFD to analyse the curved blade tip, the static extended trailing edge, and the variable thickness blade to enhance the turbine performance [85].

In 2020, Ghisu et al. presented a lumped parameter model

for evaluating the hysteresis due to the delay between the flow conditions inside the chamber and the turbine duct [86]. Das et al. experimentally determined the hysteretic behaviour in the absence of resistive loading and with varying values of load [87]. In 2021, Licheri et al. theoretically and numerically compared the prediction of the power conversion based on both the first and second laws of thermodynamics [88].

Ciappi et al. developed fluid dynamics models to evaluate the functioning of monoplane isolated Wells turbines. A three-dimensional multi-block technique was implemented to create the computational domain with a fully mapped mesh composed of hexahedral elements. The employment of circumferential periodic boundary conditions allowed for the reduction of computational power and time. The models use RANS or u-RANS schemes with a multiple reference frame approach or the u-RANS formulation with a sliding mesh approach. The achieved results were compared with analytical and experimental literature data for validation. All the developed models showed good agreement [30]. The following year the CFD models were compared even with a blade element momentum code relying on the actuator disc theory with satisfactory results [31].

### 2.1.2 Axial impulse turbine review

Axial impulse turbines are one of the most widespread machines for secondary energy conversion. The first application dates back to 1974 with the Center Pipe Buoy designed by Masuda and installed in the Bay of Osaka in Japan as a floating navigation aid [89]. In 1988, Kim et al. suggested the application of an impulse turbine as a self-rectifying machine even for large OWC systems for wave energy conversion [90].

In 1999, Maeda et al. performed experiments to determine

the optimal geometry of the stators and rotor, with a particular focus on the angle of incidence of the flow impacting the rotor [91]. In 2001, Setoguchi et al. reviewed the state of the art of impulse air turbines for OWC systems and presented the optimal design parameters and their effects on the performance and the self-starting characteristics [92]. In 2004, the study was extended to the impact of the Reynold number and the hub-to-tip ratio [32]. In the same year, Thakker and Hourigan carried out a dimensional analysis of the results of experiments on impulse turbines at a laboratory scale and proposed a model to predict the performance of real-scale turbines [93].

In 2006, Setoguchi and Takao published a review of Wells and impulse turbines for OWC systems and analytically compared their performance under irregular waves [94].

In 2009, Thakker et al. proposed the use of charts obtained from experimental data as a support in the early design of impulse turbines [95]. In 2012, Gomes et al. developed a method for the optimisation of two-dimensional blade sections: an inverse design approach is used to impose an almost constant pressure load along the axial chord by varying the camber line slope, subsequently a thickness distribution optimisation levels the pressure distribution and reduces the suction peaks at the leading and trailing edges [96].

In 2014, Badhurshah et al. carried out CFD analyses to evaluate the fluid dynamics and detect the flow separation near the suction side at the trailing edge of the rotor blade [97].

Cui and Liu performed CFD analyses to determine the effects of the rotor solidity, considered in terms of the ratio between the number of stator and rotor blades, on the turbine performance [98].

In 2015, Badhurshah and Samad carried out CFD analy-

ses coupled with a multiple-surrogate-assisted genetic algorithm based on a multi-objective optimisation to improve the energy extraction of an axial impulse turbine [99, 100].

In 2016, Liu et al. performed numerical simulations for different setting angles under steady conditions and determined an optimal value of 5° for a modified design of an axial impulse turbine [101]. In 2017, George et al. numerically investigated the fluid dynamics of a bidirectional impulse turbine and compared it with a unidirectional impulse turbine in terms of operating curves [102].

In 2017, Ezhilsabareesh et al. proposed a shape optimisation procedure based on CFD and a multiple-surrogate algorithm with a multi-objective function [103]. In 2018, Badhurshah et al. performed an optimisation procedure to determine the number of rotor blades and guide vanes, guide vane angles and guide vane profile to that maximise the turbine efficiency [104].

### 2.1.3 Wave-to-wire modelling review

Several wave-to-wire models for OWC systems have been presented in the literature so far. Typically, these models focus on the analysis of the chamber or the electric generator, while the level of detail regarding the turbine is limited. A detailed modelling is typically implemented for solving the hydrodynamics, thermodynamics, and aerodynamics of the chamber. Moreover, different control strategies are considered to regulate the operation of the system. Although suitable models for directly solving the aerodynamics of the turbine are existing in the literature, as presented in Subsections 2.1.1 and 2.1.2, they are not applied in the existing wave-to-wire models. The approach of these models relies on the use of general correlations expressing the mass flow rate, the pressure variation, the power and the efficiency though

the flow rate, pressure, and power coefficients, and the total-to-static efficiency of the turbine. In particular, the coupling of the primary and secondary converters is achieved with ideal relations connecting the pressure coefficient to the flow coefficient of the system through the damping coefficient. This results in a very simplified modelling of the turbine impact on the airflow made available by the chamber. As a consequence, the proper integration of the converters is limited. Furthermore, these models often do not consider a specific design of the chamber and the turbomachine for the distinctive wave conditions of the application site. These aspects represent the main gaps of the literature that the present thesis aims to fill. For these reasons, an integrated analytical wave-to-wire model of a wave energy converter based on the OWC technology was developed. The model combines the solution of the hydrodynamics, thermodynamics, and hydrodynamics of the chamber with the aerodynamics and dynamics of the turbine, and the dynamics of the electric generator.

Literature reviews regarding wave-to-wire models for OWC systems were published by Nielsen et al. in 2014 [105], Faÿ et al. in 2015 [106], Falcão and Henriques [1], Penalba and Ringwood in 2016 [107], Wang et al. in 2018 [108], Maria-Arenas et al. in 2019 [109].

In particular, Nielsen et al. summarised the existing technologies for energy conversion from waves to wire for different typologies of wave energy converters.

Faÿ et al. presented key aspects of the control of OWC systems to improve energy extraction. The entire conversion chain was considered, focusing on the effects of the control strategies on the power transformation and quality.

Falcão and Henriques published a detailed review of the development of the technologies for OWC systems. Moreover, three

different control logics were considered: the reactive phase control, the phase control by latching and the turbine rotational speed control with airflow rate control. The first is based on the design of the chamber to achieve the optimal resonance frequency in a set of waves to maximise the efficiency of the primary energy conversion, especially under irregular wave conditions; the second relies on the full opening and closure of a valve positioned in series with the air turbine to increase the system energy extraction; the third is designed to ensure that the power transformed by the air turbine always matches the pneumatic power provided by the chamber and the breaking torque of the electric load, while valves disposed in parallel or series with the turbine limit the pressure head or the airflow rate, respectively.

Penalba and Ringwood presented a review of the components of wave-to-wire models, including the dynamics, the constraints and several examples of linear electric generators and pneumatic, hydraulic, mechanical or magnetic transmission systems driving rotary electrical generators. Wang et al. considered the control strategies for enhancing the hydrodynamics of the primary capture system, adjusting the speed or the efficiency of the power take-off and regulating the electric power fed into the grid or supplied to the load.

Maria-Arenas et al. focused on the damping, reactive, latching and model predictive control strategies applied to different typologies of wave energy converters. The damping control consists of tuning the damping of the power take-off to the power or the peak frequency of the wave spectrum. The damping control should be tuned to the instantaneous frequency of the wave excitation force as a function of the time for being effective on the power transformation. The model predictive control involves an optimisation procedure based on the definition of target func-

tions and constraints.

In 1999, Falcão and Justino developed an analytical model to simulate the power transformation from the sea waves to the turbine shaft of an OWC system consisting of a bottom-fixed floating chamber, a Wells turbine and a valve to control the air-flow [110]. The utilisation of a valve mounted in parallel with the turbine, named by-pass or relief valve, and of a valve installed in the turbine duct was considered and compared. This control approach allows to increase energy exploitation and it is expected to be very important for turbines whose performances are drastically affected by rotor stalling, such as Wells turbines.

In 2011, Amundarain et al. investigated two control strategies for an electric generator connected to a Wells turbine in an OWC system [111]. The purposes were to control the stalling behaviour of the mechanical converter and increase the average power output of the generator. A DFIG-based (doubly-fed induction generator) rotational speed control and a PID-based (proportional-integral-derivative) air valve control were analytically and experimentally simulated and compared. It was observed that both the strategies are able to raise and smooth the electric power in complementarity. In particular, the rotational speed control strategy can be used to increase the maximum pressure drop across the turbine rotor in conditions that avoid the stall and is suited to boost the maximum power delivered to the grid; the valve control strategy regulates the airflow and modulates the pressure difference through the turbine and is suited to regulate the delivered energy according to the grid demand. Alberdi et al. continued the analysis on the rotational speed control as a fast reaction to the abrupt and short changes in the

turbine speed and on a throttle valve to control the airflow for increasing the energy conversion, particularly for the most intense wave conditions [112].

In 2013, Henriques et al. presented an analytical model of the phase control by latching of an OWC spar-buoy equipped with a biradial turbine and operating in regular wave conditions. The chamber of a spar-buoy has an axisymmetric structure with a submerged vertical duct with opened at its bottom and top and fixed to a floating structure, mainly subject to the heave motion. The compressibility effects of the air inside the chamber on the fast opening and closing of the air valve in series with the turbine and on the energy conversion were assessed [113]. The following year, the analysis was extended to irregular waves and two alternative strategies for the latching and unlatching were comparatively considered [114]. Subsequently, Portillo et al. performed analytical and experimental studies of the latching control combined with the control of the turbine rotational speed. The impact of the control strategies on energy conversion under regular and irregular waves was determined [115].

In 2015, Kelly et al. presented an analytical wave-to-wire model of a backward bent duct buoy OWC system operating with an impulse turbine [116]. The hydrodynamics, thermodynamics and aerodynamics of the chamber were thoroughly analysed and calibrated with experiments. Global correlations were applied to solve the aerodynamics of the impulse turbine. The rotor torque was coupled with the frictional losses, the rotor inertia and the electrical torque to determine the variation of the turbine rotational speed. The estimated speed was utilised to adapt the electrical torque demand as requested by the controller on the

basis of an optimal relation between torque and speed to maximise the power conversion. In 2015 and 2016, Song and Park analysed the parameters that optimise the operation of an OWC system composed of a fixed chamber, an impulse turbine and an ideal direct current generator [117, 118]. The work focused on the control strategies, while global correlations were used for the chamber and the turbine. The turbine requires an optimal flow coefficient to maximise the efficiency of the power conversion, while the generator requests a constant angular speed to provide a constant voltage. Therefore, two control strategies in the time domain were proposed and analysed under an irregular wave environment: an instant tracking control of the maximum turbine efficiency and constant control of the angular velocity of the turbine rotor.

In 2016, Henriques et al. presented an analytical model of power take-off control for a spar-buoy OWC system operating with an impulse biradial turbine. Experimental analyses were carried out on a system composed by a grid-connected SCIG (squirrel-cage induction generator) driven by a motor, a hardware-in-the-loop simulator to test real sea operating conditions, and a data logging. Two control configurations were simulated. One configuration is based on a high-speed stop valve positioned in series with the turbine and the other on a relief valve mounted in parallel to the turbine. Both the configurations were beneficial to the control of the rotational speed, but only the latter was even able to prevent the negative and positive peaks in the air pressure [119]. On the same test rig, Portillo et al. investigated a real-time latching control strategy based on the prediction of the wave motion within the receding horizon time interval to increase the turbine power output [115].

Subsequently, the test rig was utilised to validate a constrained latching control algorithm relying on a sliding high-speed stop valve in series with the turbine. The control algorithm allowed to increase the generator load and to limit the power peaks [120].

Bailey et al. presented a numerical wave-to-wire model for a moored floating OWC system of backward bent duct buoy type, embedded with an impulse turbine [121]. The hydrodynamics and aerodynamics of the chamber were solved including the excitation, radiation, buoyancy forces and the forces exerted by the air pressure, the viscous drag and the moorings. The chamber thermodynamics was coupled with the turbine aerodynamics through global correlations expressing the airflow rate, the pressure variation, power and efficiency. A variable-frequency drive (VFD) was set between the turbine and the generator to control the system operation in a large variety of sea states representative of the West Coast of Canada. The optimal rated power for the VFD and the generator was determined from a gradient-based optimisation with the annual electrical energy generation as the objective function.

In 2018, Suchithra et al. investigated the energy conversion process of an OWC system by means of a wave-to-wire model [122]. An analytical model of the chamber was used to determine its hydrodynamics, thermodynamics and aerodynamics, while the interaction of a Wells turbine with the system was approximated with an equivalent pressure drop imposed by a calibrated opening and global correlations were applied to determine the operating parameters. A reduced-order model of the control is described, studying the generator dynamics using a doubly-fed induction generator modelled by means of third-order equations.

The power output of the system was determined for different sea climates under regular and irregular waves. In 2019, Henriques et al. presented wave-to-wire models to analyse the dynamics and the control of air turbines and electric generators for the OWC plant installed in the breakwater of the Bay of Biscay, located in Mutriku, in Spain [123]. The performance of a Wells and a biradial turbine were determined and compared. The impact of control strategies on the power and the efficiency of the turbine and the pneumatic and electrical power was assessed. Faÿ et al. developed six algorithms to control the biradial turbine designed for the OWC plant of Mutriku [124]. A wave-to-wire model was proposed for one chamber of the plant and the effects of the control strategies on the energy conversion and power output quality and reliability were evaluated in irregular sea states. A set of adaptive and predictive algorithms was considered and both turbine speed controllers and latching strategies were analysed and validated utilising an electrical test infrastructure.

Benreguig et al. developed wave-to-wire models of two OWC systems using the same floating spar buoy structure and embedded with a radial-inflow turbine with twin-rotor configuration or the Tupperwave turbine [125]. The Tupperwave operation is based on two large accumulator chambers of fixed volume with non-return valves to generate a unidirectional airflow that drives a unidirectional turbine in a closed circuit. The instantaneous efficiency of the turbine was maximised by adapting the braking torque of the electric generator to the mechanical turbine torque of the rotor expected at the maximum efficiency. A bypass valve, positioned in parallel to the turbine, was utilised to avoid the overload of the generator.

In 2020, Ciappi et al. developed an analytical wave-to-wire model of a wave energy converter operating with a fixed and detached chamber and an axial impulse turbine. A rigid piston model for the chamber, a blade element momentum model for the turbine, and a control strategy were jointly solved. An evaluation of the annual energy harvesting was performed to determine suitable configurations of the turbine for two hot-spots. Furthermore, this work provides a detailed description of the development of state of the art of wave-to-wire models [126, 33].

Scialò et al. investigated the design for a power take-off for a possible installation in a breakwater. An analytical wave-to-wire model was applied to determine the operation of a monoplane isolated Wells turbine and a biradial impulse turbine coupled with a U-type wave energy converter based on the OWC technology and equipped with a relief air valve. The turbine diameter and power output were optimised for both the machines and the effects of the interconnection of air chambers sharing a single turbine were assessed [127].

In 2021, Ciappi et al. applied the analytical wave-to-wire model developed to determine the optimal geometries and operating conditions of monoplane isolated Wells turbines and axial impulse turbines to maximise energy extraction in a selected location situated in Italy, in the north-west of Sardinia. The geometry and properties of the OWC chamber were determined by scaling up of factor 50 the data obtained from an experimental campaign previously performed under wave conditions typical of a moderate Mediterranean climate. The operating maps and curves, the performance parameters, and the energy harvested were determined considering the variation of wave conditions during the seasons of the year [24].

### 2.1.4 OWC system development

**Whistling Buoy**

In 1876, Courtney patented the Whistling Buoy (2.1). This was the first recorded device working with the oscillating water column principle, although this concept was not already conceived.

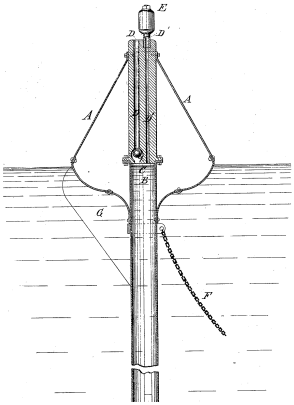

Figure 2.1: Scheme of the vertical central section of the Whistling Buoy.

The Whistling buoy consisted of a pear-shaped float made of iron with a central inner pipe, partially submerged, with a diameter of 0.3 m. The float had a maximum diameter of 3.6 m and an elevation of 3.6 m from the still water level [128]. It was anchored to the seabed with a chain fixed at its lower end. The chain was slack to allow the heave motion of the buoy under the action of waves. On the opposite side of the chain, there was a rudder plate extending from the still water level to a point on the central pipe, which avoided the rotating motion of the buoy. The buoy was constantly maintained vertical and the water level inside the lower section of the tube was always kept constant

corresponding with the still water level [128].

The pipe extended downwards from the top of the float and was divided into an upper and a lower section by a horizontal diaphragm or a partition plate. The lower section acted as an air chamber and was totally submerged, reaching a depth of 4 m from the still water level for not being affected by the motion of the surface waves even in storm conditions [129]. The diaphragm or plate was connected with the upper end of the buoy by two parallel ducts with different diameters. The duct with a larger diameter was provided at the lower end with a valve or a ball and allowed the air entrance inside the device. The duct with a smaller diameter was open at both ends to enable the discharge of the air. At the outlet of this duct, a whistle or another suitable sounding device was installed.

The air was alternatively compressed and expanded in the chamber by the action of sea waves. The waves lifted the buoy to a certain height, enlarging the disposable volume and forcing the air to enter the system through the bigger duct and the bottom valve. Then, the receding motion of waves, together with the weight of the device, determined its fast lowering and a rapid air compression, as the water level remained constant. The air compression closed the valve at the end of the larger duct forcing the compressed air to flow through the smaller duct for sounding the device. The duration of the sound produced by the whistle was directly proportional to the wave height [128].

The weight and the shape of the buoy had a significant effect on the ascendant and descendant motion of the buoy and, thus, on the pressure difference between the air inside the chamber and in the atmosphere [128]. In addition, the enlarged form of the buoy that was just above the floatation line allowed for a

faster ascension of the buoy with the upward wave and thus the entrance of a major quantity of air [128]. Larger dimensions of the buoy, and consequently greater weight, led to higher pressure gradients. However, the increase in the dimensions was limited, as the length of the duct needed to be proportional to the size of the device [128].

A total of 34 Whistling Buoys were installed in the USA. Other devices were also installed in Britain, France and Germany [129]. The main advantages of this kind of system were high reliability and the simple working mechanism [128, 129].

The Whistling Buoy was the direct successor of the Bell Buoy for navigational aid. However, the latter device was not based on the oscillating water column principle. Indeed, in this case, one or more clappers equipped on the buoy, inside or around the bell, moved with the wave motion hitting the bell to produce a sound [130].

**Center Pipe Buoy**

Masuda designed the Center Pipe Buoy and installed a prototype in Osaka Bay, in Japan. This device was a floating OWC, and it was conceived for navigational aid similar to the Whistling Buoy [130, 1]. The two systems had analogous working principles, but the main difference was represented by the device used to exploit the pressurised airflow made available by the chamber [131, 132]. In fact, the Center Pipe Buoy was the first example of the application of an air turbine and a generator to convert the pneumatic air energy into mechanical energy, and then into electrical energy to power a light for navigational aid (Figure 2.2).

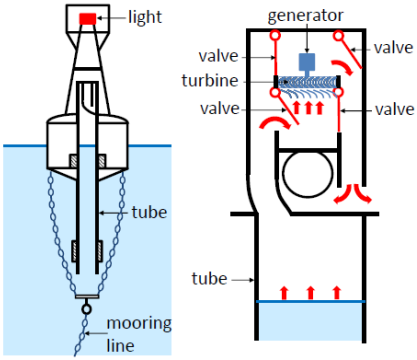


Figure 2.2: Scheme of the Center Pipe Buoy [1].

A unidirectional impulse turbine with a vertical axis equipped with a rectifying-valve system and guide vanes on the downward side was installed in the device [133].

The electric generator had maximum output of around 60 W at 5000 rpm and maximum efficiency of approximately 47% at 1100 rpm. Moreover, the average electric output was estimated in about 17 W under standard wave conditions with height 0.2 m and period 2.8 s [133, 5]. The device was equipped with a control unit and a storage battery system capable of supplying from 3 to 5 W of electric consumption [133]. Concerning the primary conversion efficiency from wave power to air power, the device had a pressure ratio of about 0.3 [131]. This parameter is defined as the amplitude of the pressure divided by wave height, and it is utilised to compare the performance of pneumatic wave power devices [134]. The overall secondary conversion efficiency was estimated to be around 21%, determined by the efficiencies equal to 95% for the valve, 55% for the turbine, and 40% for the electric generator [133].

The Center Pipe Buoy was a device embedded with a central vertical pipe extending downwards from the top of the buoy and operating as an air compression and expansion chamber. The buoy had a width of 2.60 m and the pipe had a diameter of 0.660 m and was partially submerged, reaching a depth of 4 m to avoid the interference of the wave motion at the surface of the sea, as in the Whistling Buoy.

The bottom weight and the bridle chain prevented the rotational movements of the buoy, allowing only the heave motion. In this way, the water column level inside the pipe was maintained constant, as the buoy followed the upward and downward movements of the waves. The weight proved to be effective in the absence of very high currents [133, 135].

The turbine had a diameter of 0.200 m and it was located at the top of the buoy, connected to the upper part of the pipe. An electric generator was coupled with the air turbine and powered a light for navigational aid positioned at the height of 4 m regarding the still water level. The rectifying valve system was constituted by four valves, arranged in pairs in the upper and lower parts of the chamber, above the still water level, as illustrated in Figure 2.3. The bottom valves forced the air to enter the turbine, while the upper valves to exit the turbine. The rectifying valve system allowed the operation of the unidirectional turbine under the action of alternate air compression and expansion. The sense of rotation of the air turbine was maintained constant regardless of the direction of the airflow during the inflow and outflow [132].

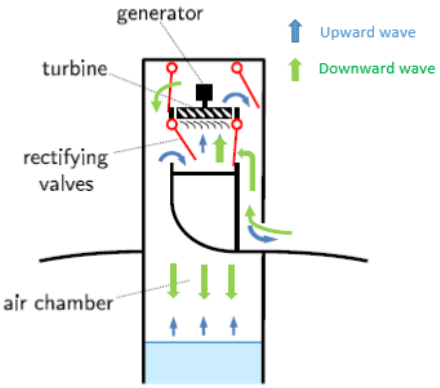


Figure 2.3: Scheme of the rectifying system with 4 valves of the Center Pipe Buoy [1].

The operation of the Center Pipe Buoy mainly depended upon the wave conditions and the system geometry.

The wave power absorption occurred between two close peaks. The peak corresponding with the lower wave period was related to the vertical oscillations of the buoy. The other peak was connected to the vertical oscillations of the water column and strictly depended on the pipe length [132]. To achieve a wide operational bandwidth, an optimal difference between the two periods had to be ensured. This implied the increase of the pipe length to enhance the energy conversion, in compliance with the deployment in relatively shallow water and the maintenance costs [132].

The good results of this OWC device showed the feasibility of the use of air turbines for wave energy conversion. This application enhanced the interest for a possible scaling up of wave power generators in order to supply electric power to the local grid [136, 135].

In 1965, The Japanese company Ryokuseisha Corporation produced the Center Pipe Buoy for its commercialisation [136]. The Japan Marine Safety Board used 700 buoys for navigation aid and 500 devices were sold to other countries, included 20 to the USA. This was the first OWC device to achieve a significant commercialisation [130, 133, 5].

After the rise of the power demand due to a new international regulation for navigational lighting on buoys, the enhancement of the power conversion of the Center Pipe Buoy was required. A significant increase of the dimensions of the device demonstrated to be not feasible, as aforementioned. Thus, the solution was the improvement of the efficiency of the processes of power conversion with particular focus on the air turbine [133].

The diameter of the impulse turbine was increased from 0.200 m to 0.250 m and the valve box was redesigned. The efficiency was raised from 55% to 65% [133].

Moreover, different typologies of air turbines were tested. A Wells turbine was installed as it was capable of operating without the need for a rectifying valve system and allowed the reduction of the weight and the increase of the design rotational speed. However, the average efficiency obtained with this turbine was lower regarding the case of the impulse turbine. Indeed, the use of a Wells turbine was not suitable for small buoys as opposed to the large power generators [133]. Even a Savonius turbine was tested, but the efficiency of energy conversion was lower than that of the Wells turbine [133].

Concerning the electric generator, two solutions were tested to improve efficiency. The Ryokuseisha Corporation improved the efficiency of the generator up to about 65% by replacing the previous one with a newer ordinary generator [133]. The com-

pany Tabaka-Kagaku-Kogyo Limited patented a special generator with a theoretical efficiency of around 80% by decreasing the iron and electric losses [133].

With these improvements, the new total efficiency of the Center Pipe Buoy reached approximately 49% [133].

**Kaimei**

The Japan Agency for Marine-Earth Science and Technology (JAMSTEC) designed and constructed a prototype of the Kaimei system in the March of 1976 [2]. This device can be considered the first application of a multi-chamber system based on the oscillating water column concept [13] and it was the first prototype of a large floating structure for this kind of technology. The system applied impulse turbines for the secondary energy conversion. The total output assumed to be generated by the Kaimei from theoretical calculations was equal to 4 MW with a wave height of 3 m and a wave period of 6 s [2].

The structure of the Kaimiei, represented in Figure 2.4, was 80 m long, 12 m wide, and 5 m high, with a weight of 500 t [2].


Figure 2.4: Image of the structure of the Kaimei [1].

The floating device had the form of a ship and consisted of several buoyancy rooms and air chambers floating on the water surface [130, 137, 134, 131]. The use of this particular shape was

selected after a study of two years on large wave power generators, during which it demonstrated to be the best solution for the lower mooring force required and the simplicity of construction [2]. Indeed, the structure with ship form of Figure 2.5 always adjusted to the direction of waves, reducing the forces on the moorings [137]. The Kaimei was moored with four chains at the bow and one slack chain at the stern to be capable of aligning with the wave direction [137, 134, 135, 131].

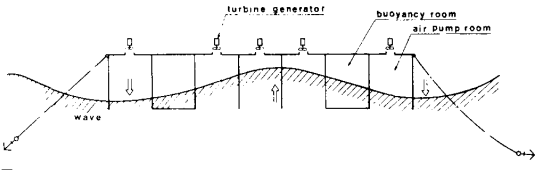


Figure 2.5: Scheme of the working principle of the Kaimei [2].

As a floating structure, the Kaimei was subject to pitch, heave, and roll motions due to the action of sea waves [2, 138]. These movements were limited by the massive structure of the system, but it was necessary to further reduce the oscillations of the barge to increase power conversion [137, 138]. Indeed, the floating structure was not able to follow all the upward and downward movements of waves with the same oscillation period, as the wave period was not constant. In particular, when the heave movement of the ship was in the opposite sense of the elevation of the wave, the relative wave height acting on the air inside the chamber increased. Conversely, when the structure moved in the same sense of the wave elevation, the relative wave height acting on the air chamber reduced [137]. For these reasons, studies were performed on the length and width of the structure to decrease the heave oscillation period to reduce the fluctuations in

relative height [137]. In addition, since the relative wave height ratio decreases as the significant wave height increases, the maximum height of the waves contributing to the energy harnessing was limited. This resulted in low conversion efficiency from wave power to air power, providing values between around 0.1 and 0.2 for the air pressure ratio [137, 2].

Two sea tests were performed: the first from the August of 1978 to the March of 1980 and the second from 1985 to 1986 [139, 5]. The Kaimei was provided with a measurement system and, during the entire operational period, all the data acquired were simultaneously transmitted through a wireless telemeter to a shore station where they were monitored and recorded [137]. The data mainly concerned the weather conditions, the sea state, the relative wave height, the barge movements, the mooring forces, the differential pressure at the turbines, their rotational speed, and the electrical power output.

In 1978, the first sea test was conducted by JAMSTEC to investigate the safety and durability of a floating moored large wave power generator [139]. The Kamiei was deployed in a location with a sea depth of about 40 m in the north-west of Yura, in the Yamagata Prefecture, on the west coast of Japan [131, 5]. In this site, the sea is quite calm in summer, while it is characterised by strong west or north-west winds during winter, significantly increasing the height of waves [136, 134, 135].

The system was equipped with three identical impulse turbines rated 160 kW each and operating with a design rotational speed of 950 rpm. The turbines were coupled to three electric generators with an average power of 125 kW and a maximum

output of 200 kW for each one. The turbo-generator units were located at the bow, midship, and stern [5, 2].

The impulse turbines were made of aluminium alloy and had a rotor diameter of 1.400 m and 60 rotor blades. A rectifying system with 2 valves was utilised and a row of 50 stator vanes was installed on the side facing the air chamber. Each turbo-generator unit was provided with an emergency valve, operating if the rotational speed 1200 rpm was exceeded [2].

During the first stage of this experimental campaign in real operating conditions, the measurement system acquired a significant set of data [2, 139]. The maximum tension registered on the mooring chains was 55 t with a maximum wave height of 8.8 m, which was largely under the breaking strength of the mooring chains [137].

The second part of the first sea test, from August 1979 until March 1980, was carried out in the same location near Yura [5, 2]. The test was conducted by JAMSTEC in a joint research project involving five countries of the International Energy Agency: Canada, Ireland, Norway, Sweden, United Kingdom, and United States of America [137, 5].

The second part of the test was focused on the investigation of the characteristics of the wave energy of the application site, the mooring forces, the barge motion, and the conversion efficiency of the equipment [139].

At this stage, a cable to transmit the electrical power generated to land was provided to one power take-off unit [137, 5]. A special armoured cable, effective again kinking, was produced for this purpose and it was installed with the combination of weights and buoys [137]. The electricity generated from wave power was supplied to the mainland grid for 4 months during winter [5].

The number of turbine and electric generator units equipped on the device was increased to nine [2, 137]. All of them were impulse turbines connected with various arrangements of rectifying valve systems to analyse their effects. Eight turbines were coupled with synchronous electric generators. One impulse turbine, with a rectifying system with 4 valves, was coupled with an induction generator. This turbo-generator unit was provided with a damper tank system [137]. The damper tank system consisted of small air chambers connected with large air damper tanks and the turbo-generator unit through a rectifying mechanism with four valves. The air pressure in each air chamber encountered pressure fluctuations. However, the differential pressure at the turbine was maintained relatively constant due to the system of damper tanks. This aspect was very important as a small fluctuation in differential pressure resulted in a large fluctuation of power output [137]. This was due to the type of induction generator adopted, which was not embedded with a control system. Therefore, it was forced to rotate at a fixed speed in the entire operating range, without the possibility of smoothing the electric power [137].

The induction generator provided the advantage of the absence of the exciter compared to the synchronous generator and, thus, allowed the simplification of the structure and its maintenance [137].

The number of items acquired by the measurement system increased to 82 and the maximum mooring tension registered raised to 84 t with a maximum wave height of 9 m. However, considering the breaking strength of the mooring chains, the operation was found to be sufficiently safe [137, 2].

It was observed that there was an output difference among the various power take-off units of the system depending on their installation point. This was found to be closely related to the wave period [137]. In particular, the measured outputs of the rectifying systems with 4 valves and 2 valves installed for the impulse turbines positioned at midship were compared [137]. The generators measured the same output corresponding to waves with a short period, while the latter valve system measured a double output with long-period waves. This proved that the system with 4 valves had a better performance concerning conversion efficiency and operating bandwidth [137].

The mooring chains were inspected at the end of the second stage of the first experimental campaign by taking samples for the pulling test. Since no abnormality was found, the same chains were also used for the second campaign [137].

The working principle and the functioning of the PTO system calculated with the theoretical modelling were confirmed by the experimental results of the first campaign [2]. However, it was decided to perform further tests to increase the conversion efficiency from wave to air power, reduce the dimensions of the air turbine, smooth the output of the electrical generator, and reduce the mooring costs.

The second campaign of sea tests was performed on the Kaimei by JAMSTEC near the coast of Yura where the sea has a depth of 40 m [139, 138]. It began in the summer of 1985 and ended in the spring of 1986. The objectives were analysing an optimal layout of the structure, testing different control methods to optimise the airflow, and studying a new mooring system [139, 5].

The device was equipped with five turbines. Three of them were impulse turbines, one was a contra-rotating McCormick

impulse turbine, and one a tandem Wells turbine [139, 5]. The Wells turbine was coupled with a synchronous generator rated 60 kW [136]. The McCormick turbine was rated 125 kW and had a rotor diameter of 1 m with 60 blades on each of the two rotors and 30 guide vanes on each side [5, 140].

As in the first sea test, many data were collected regarding the sea conditions, the motion of the barge, the mooring tension, the air chamber pressure, and the relative height [139].

It was observed that the energy absorption was heavily influenced by the position of the buoyancy rooms. During the first experimental campaign of 1976, semi-separate rooms were tested. A layout with separated buoyancy rooms increased the efficiency of even 2.5 times [136].

**Sanze plant**

The Research Development Corporation of Japan and the JAMSTEC cooperated to construct a shore-fixed OWC in Sanze, on the West coast of Japan, near the city of Tsuruoka [3, 131, 5]. The plant was equipped with two identical Wells turbines arranged in tandem and coupled to an electric generator rated 40 kW [3, 131]. It was the first worldwide shore-fixed OWC plant and the first to use Wells turbines in the tandem arrangement [131].

The structure depicted in Figure 2.6 was built on a shoreline gully, which is a small cove characterised by a naturally high level of wave energy [5]. The depth of the water was 3 m. As a fixed system, the water column oscillation movement inside the chamber was given by the motion of waves causing the water to enter and exit the bottom opening of the air chamber [130].

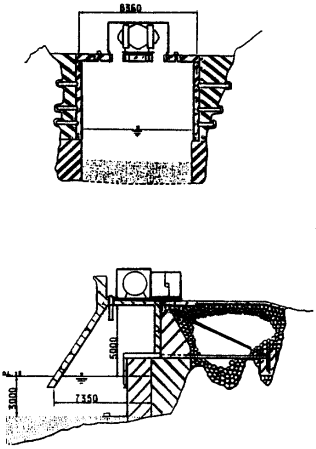


Figure 2.6: Central front and side sections of the Sanze plant [3].

The plant was composed of a caisson with a steel and concrete assembly with an inclined front wall, a power take-off unit, and a control and monitoring room [3]. Either the Wells turbines had a diameter of 1.400 m and rotated in the same direction. The turbines were installed with the tandem arrangement at the opposite sides of the generator to which they were coupled. This layout allowed to balance the axial thrust on the bearings as the airflow reached the turbines from two opposite directions during both the flow phases [3].

The electric generator had an average power of 10 kW and it was embedded with a control system to supply a constant voltage [3, 131].

The bottom opening of the air chamber had a length of 7 m and a width of 8 m, resulting in a total area of 56 $m^2$ [3].

The main data measured during the plant operational period

regarded the sea state, the air chamber parameters in terms of water column level and air pressure, and the power take-off parameters through the turbine rotational speed and the electric output of the generator [3].

The plant remained operational for six months, during which the theoretical estimated value of power output was confirmed [5, 3]. After this period, the plant was taken out of service [5].

**Toftestallen plant**

In 1985, the Kvaerner Company, with the collaboration of the Norwegian Hydrotechnical Laboratory, constructed a shore-fixed OWC on the west coast of Norway at Toftestallen, located at 40 km in the north-west direction from Bergen [5]. The plant was integrated into a cliff on the shoreline, where the water depth was 70 m and it was equipped with a vertical-axis Wells turbine coupled with a generator rated 500 kW [5, 1]. The structure of the plant shown in Figure (2.7) was composed of a concrete base caisson with a steel tower of 10 m of diameter [5]. At the top of the tower, the air chamber and the power take-off were installed [5].

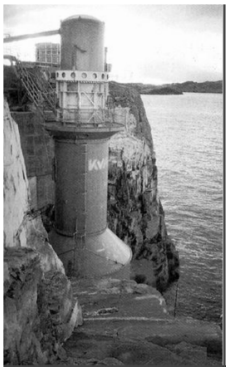

Figure 2.7: Image of the OWC plant installed at Toftestallen, in Norway [4].

The system was based on the harbour principle, which relies on extending the side walls of the air chamber towards the sea [4]. In the case of the Toftestallen plant, the cliff walls visible in Figure 2.8 were utilised to obtain this effect [5]. As a consequence, the waves were reflected into the walls of the structure and amplified, in particular corresponding with the higher values of period [4]. This allowed achieving an additional resonance frequency, enlarging the operational bandwidth of the device while keeping limited the dimensions of the structure concerning the wavelength [4]. A plant able to achieve resonance with two or more frequencies is called multi-resonant oscillating water column [4].

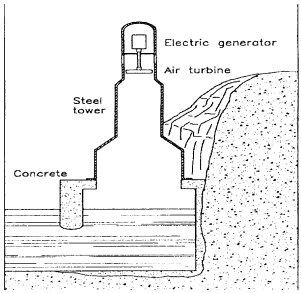


Figure 2.8: Scheme of the central side section of the Toftestallen wave energy converter [5].

A detailed description of the performance of the plant is not present in the literature. However, it is reported that the measured power output was lower than the theoretical values [1].

In 1988, the structure partially collapsed during a severe storm [5, 1]. Afterwards, the plant was dismissed [141].

**Backward Bent Duct Buoy**

Masuda and the JAMSTEC proposed the Backward Bent Duct Buoy (BBDB) concept as an improvement of the Center Pipe Buoy [6]. Subsequently, also Denmark, Ireland, and China cooperated in the development of this device. The objectives were the extension of the operating range of the system on a wider interval of wave periods, the functioning in a shallow sea maintaining high conversion efficiency, and a more stable and continuous power generation [132]. The advantages of the BBDB respect to the previous floating devices were the lower weight and simplicity and the reduced costs of maintenance [134].

The BBDB of Figure 2.9 was a floating OWC and it was conceived for navigational aid.

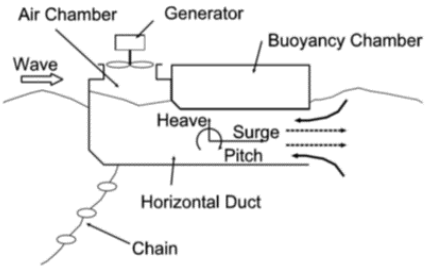


Figure 2.9: Scheme of the Backward Bent Duct Buoy [6].

The dimensions were between 2 and 6 m in length, between 2 and 3 m in width and of 2 m in height [134, 135, 142]. The device comprised a buoyancy chamber and an air chamber with a bent horizontal duct. The power take-off was installed at the top of the air chamber [1]. The system was able to provide a power output between 5 W and 40 W [135].

Regarding the previous floating devices, the BBDB wave energy absorption was achieved from both the heave and pitch oscillations [5]. Therefore, an underwater bucket was hanged to the stern to maintain a high efficiency in a wide operational bandwidth [131]. For a given air chamber area and wave height, the BBDB absorbed 3 times the wave power with respect to the Center Pipe Buoy and 10 times regarding the Kaimei [5]. Several layouts of the BBDB for navigational aid were tested to find an optimal shape in order to get the maximum efficiency [142, 143]. The first design layout had a box-shaped float and duct. Two versions of this BBDB were proposed, one with an additional float in front of the air chamber and one without it. Both the models were tested in a water tank test and the former configuration had a pressure ratio of 0.28, while the latter had a pressure ratio of 0.50 in peak. The reason was the greater pitch oscillation

of the buoy in the absence of the additional float. The oscillation movement allowed the air chamber to ensure a relative seawater motion inside the chamber and, consequently, a higher efficiency.

Subsequently, the shape of the duct was changed to a fuselage form to further increase the system performance [134]. Water tank tests were conducted mainly by the Japan Ship Research Institute and sea tests were carried out in the application site situated near the coast of Yura. In the water tank tests, two models made of steel were examined: a single fuselage BBDB with a length of 0.242 m, a width of 0.60 m, and a weight of 350 kg, and a twin-fuselage BBDB with length of 0.242 m, width of 0.199 m, and weight of 550 kg. The former device was equipped with an impulse turbine, while the latter with a Savonius turbine [134]. Either models reached the maximum air pressure ratio of around 0.6 corresponding with wave periods between 2 and 2.5 s with a ratio of $^1/_{100}$ for nozzle and throttle. For the same conditions, the pressure ratio was about 0.3 for the Center Pipe Buoy and between 0.1 and 0.2 for the Kaimei [134]. A difference in conversion efficiency between the single and twin-fuselage BBDB configurations was not found. Thus, the latter configuration provided the double value of power output [134]. The twin-fuselage system had better stability about roll oscillation [134]. Moreover, it was measured that the efficiency of energy conversion was enhanced by the presence of moorings as they allowed greater oscillation movements, promoting energy absorption [6].

The BBDB with a single fuselage was tested both with the submerged opening directed towards and backwards regarding the incident wave. For the aforementioned conditions maximising pressure ratio, this parameter was estimated to be about 0.6

for the backward-facing duct and nearly 0.25 for the frontward-facing duct.

Furthermore, this configuration required a considerably lower mooring force with respect to the other floating devices, as the water entered the duct opening in the opposite direction of the incident wave during the downward movement [134].

In the April of 1987, the first sea test on the BBDB system was performed on a device with a single fuselage (2.4 m long and 0.6 m wide) with an outrigger, and on a device with a twin-fuselage (2.4 m long and 2 m wide). The two models for navigational aid were deployed without underwater weight and moored at a water depth of 40 m with three anchors each [135].

On the 22nd of April, both models were overturned due to a high wave of 6.5 m, as their centre of gravity was over the float centre. Subsequently, the stability was increased by adding another outrigger to the single hull BBDB and increasing the width between the two floats of the twin-hull BBDB. In addition, the weight was raised for both the models in order to lower their centre of gravity [131, 135].

With these refinements, the test restarted on the 21st of May until the 17th of September, when a typhoon with a maximum wave height of 9 m passed through the test site. Both models did not encounter major problems, but the registered output of the twin-fuselage was low, so it was thought that the wave period at the test site could be longer than expected [135]. Thus, a further test was planned in order to investigate this aspect.

In 1988, the second sea test of the BBDB with twin-fuselage structure started on the 12th of March 1988 [135]. The device was moored in the sea of Mikawa Bay on the Pacific side of

Japan. This location is characterised by an average wave period between 2 and 3 s [135]. It was discovered that the cause of the low output reached during the first test was not the wave period but a wrong selection of the turbine. In fact, the model was equipped with a Savonius turbine, having a low efficiency. Hence, it was replaced with a mono-valve impulse turbine that increased the electric output about 3 times, finally reaching the expected level. Values of about 60% and 40% were measured for the turbine and generator efficiency, respectively [135].

Another problem encountered during the first sea test was the oyster growing inside the air chamber and the duct, which affected the conversion efficiency. To overcome this problem, the company Chugoku Paint Limited produced a special anti-fouling paint called Bioclean. It was not poisonous and rejected the water on the surface in order to prevent fouling [133]. The test ended in July [135].

The main advantages of the BBDB with respect to the previous floating devices were the lightweight and the simplicity of maintenance [134].

Moreover, a scaling up of the device was also considered to construct a large-scale BBDB for either telemetering and fish gathering, or for supplying the local electric grid of coastal cities and islands [134, 135, 131, 142].

In 1989, the operation of a self-propelled BBDB system was analysed by McCormick. The device had a length of 35.6 m, a width of 10 m, and a weight of 500 t [131]. The system was a variation of the free-floating BBDB [6]. Part of the energy converted was utilised to drive a propeller that supplied the required power for station keeping. The energy needed to propel

the system was derived from the energy conversion subsystem [6].

The performance analysis was conducted starting from considering the internal fluid motion: the power of the air through the turbine was the result of both the external water pressure acting on the chamber opening, derived from incident wave energy, and the buoy motions inducted by waves like heave and pitch oscillations [6]. The maximum energy conversion was achieved corresponding with a wave period of 8.5 s.

Further analysis of the design of the BBDB determined the development of a new half-cylinder system, characterised by a floating part with a rectangular shape in the front and a half-cylinder shape in the rear. Liang performed water tank tests in the July of 1993 on a model with a length of 2.86 m, a width of 2.2 m, and a height of 2.1 m. The model had an air chamber area of 1.36 $m^2$ and a weight of 2400 kg [142].

Comparing the box shape with the half-cylinder shape, Liang observed that the former one had a single efficiency peak, while the latter had three efficiency peaks in the heaving period, pitching period, and duct oscillation period [142]. Subsequently, a comparison on the efficiency values was carried out by varying the ratio between the wavelength and the buoy length for both structure typologies, considering a wave period of 8 s and a wave length of 100 m [142]. It was found that for the box shape, the maximum peak efficiency was 35% with the length of the buoy of 25 m [142]. For the cylinder shape, the maximum efficiency peak was 80% or 60% corresponding with a length of 25 m or 17 m [142].

The half-cylinder shape increased the efficiency and also allowed to reduce the material needed for the hull regarding the

Kaimei [142].

The real scale model of the half-cylinder BBDB was about 10 times larger than the model for the water tank test. Thus, the dimensions of the boat were 28.34 m in length, 15 m in height, and 22 m in width, and the air chamber area was 136 $m^2$ [142].

An experimental campaign was carried out on a BBDB with half-cylinder shape to assess the effects of increasing duct extension. The tests were conducted in a wave tank with a length of 200 m, a width of 6 m, and a depth of 3 m at the Zhangshan University of Guangzhou, in China. The model with the twin-fuselage, the half-cylinder, and the half-cylinder with the extended duct were exposed to the action of waves with the height of 0.15 m and a variable period. The electric output of the twin-fuselage BBDB corresponding to waves with a period of 2.5 s was 3 W, while 25 W were obtained with the half-cylinder system for waves of 2.8 s, and 40 W were reached with the half-cylinder device with an extended duct for wave of 2.41 s. Both the power output and the width of the operating range were significantly increased.

In 1996, a new power take-off arrangement was tested at the Trivandrum wave energy plant with the aim of optimising the system performance [5]. The Wells turbine was replaced with a self-rectifying impulse turbine with variable-pitch guide vanes designed by Setoguchi and the generator was substituted with an induction generator rated 55 kW [8]. The theoretical estimations indicated that the output produced was 2.5 times higher regarding a Wells turbine for the same incident wave [143].

The rotor of the turbomachine had a diameter 1 m and 30

blades with a shape similar to that proposed by McCormick [143]. The inlet and outlet guide vanes had 26 moveable vanes, able to automatically modify their pitching angle from 15° to 60° under the action of the air motion [143]. The moveable guide vanes were linked with bars to ensure their operation [143].

The induction generator was patented by the Heller-Dejulio Corporation [131]. It generated the same frequency to the grid in a wide rotational speed range of the turbine, maintaining a good efficiency due to the slip ring connecting the capacitor and the resistor to the rotor circuit [131, 5]. With the use of a resistor, a capacitor and a reactor coil, the Heller generator was able to reach an efficiency of 86% [143].

**Sakata plant**

In 1989, the Ministry of Transport, under the direction of Yoshimi Goda, integrated the fixed OWC device of Figure 2.10 into the breakwater for the protection of the Sakata Port in the west coast of Japan [5, 7].

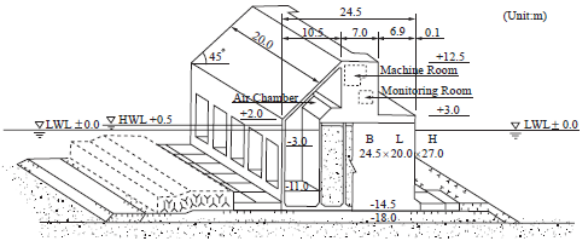


Figure 2.10: Scheme of the plant of Sakata [7].

The project was conducted with the collaboration of the First District Port Construction Bureau, Port and Harbor Research Institute and Coastal Development Institute of Technology. The construction was completed in summer and the plant became

operational in winter [7]. The system was equipped with two monoplane Wells turbines arranged in a tandem configuration and coupled with a generator rated 60 kW [144, 7]. Both turbines had 16 blades and a diameter of 1.337 m and were provided with 37 inlet and outlet guide vanes [144]. The maximum rotational speed of the generator was 3000 rpm [7]. The plant was conceived as a research and development project which lasted 5 years [7, 144].

This was the first successful plant with the structure integrated into a breakwater [145]. The advantages of this solution are paramount: simplified maintenance and operation, shared construction costs, and access for construction. The primary converter was constituted by a caisson containing five air chambers. The caisson was 20 m long, 24.5 m wide, and 12.5 m high, and the water depth was 11 m [144]. The total air chamber area was 155 $m^2$ [7]. The caisson was designed considering a significant wave height of 10.2 m and a significant wave period of 14.5 s to ensure the strength of the structure [7].

Besides the caisson, the plant was provided with a machine room and a monitoring room [144]. The machine room was located at the centre of the upper part of the rear wall of the caisson and contained the power take-off [7]. Moreover, the plant of Figure 2.11 was provided with a control system using three types of valves: a butterfly by-pass valve for the airflow regulation, a relief valve for the pressure release, and an emergency valve to cut-off the flow if the significant wave height exceeded 5 m [7].

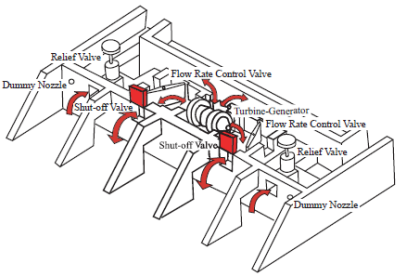


Figure 2.11: Scheme of the machine room arrangement of the Sakata plant [7].

The measurement system in the monitoring room acquired data regarding the wave state (height, period, and direction of the incident waves), the wave and air pressure to verify the resistance of the structure, the water column level inside the chamber, and the electric power of the generator and the rotational speed of the turbine. All the data were sent through a cable to a land monitoring station for being registered and analysed [7].

The wave monitoring indicated that the average wave direction was almost perpendicular to the breakwater [7]. The measured wave power was in a good agreement with the theoretical estimations. Only slightly higher average values were provided by the tests due to the refracting and reflecting effects on the incident waves determined by the breakwater caissons surrounding the plant [7].

A value of 37% was measured for turbine efficiency. A further theoretical estimation carried out on the tested system, showed that a turbine diameter of 2.4 m coupled with a generator rated 200 kW would have increased the energy extraction. The maximum output was expected for a significant height of 4 m [7].

An initial test on the Sakata plant was conducted until 1991 on the three central air chambers of the system [7]. The objec-

tives were confirming the design method of the breakwater caisson, verifying the resistance of the chambers, determining the power conversion efficiency of the chamber, turbine, and generator, analysing the method of construction of the breakwater, and demonstrating the feasibility of utilising the electric power generated for various purposes [7]. The test was conducted successfully and the design method was confirmed [7].

A second test was planned from the August of 1992 in order to analyse various systems for the use of the electric generated power with improvements on the caisson chamber and the turbine [7].

**Trivandrum plant**

The Ocean Engineering Center, together with the Indian Institute of Technology of Madras, supported by the Department of Ocean Development and the Government of India, constructed a bottom-fixed OWC pilot plant for wave energy conversion [8, 5].

The plant of Figure 2.12 was located on the south-west coast of India close to the Vizhinjam fishing harbour, near Trivandrum, facing the Arabian Sea. It was called Trivandrum wave energy plant. The site was chosen for the high wave power density and the water depth of 10.2 m [8, 146].

The caisson was composed of a bottom platform, 23 m long, 17 m wide, and 3 m high, anchored to the seabed, a rear wall, two side walls with height of 12 m, and a front lip [8]. The caisson was closed at the top by a dome that was, in turn, linked at its top with a duct connecting the air chamber with the power take-off system.

The dimensions of the caisson were selected to achieve an optimal power conversion depending on the predominant wave that had a significant period of 10 s, and to resist to the action

of waves with a maximum wave height of 7 m [8].

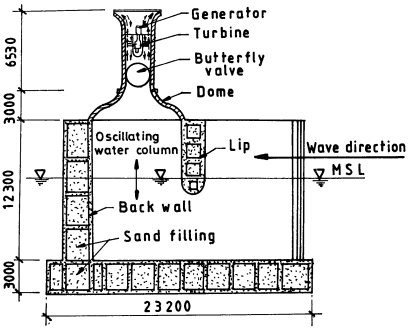


Figure 2.12: Side section of the Trivandrum plant [8].

The side walls were protruded from the air chamber, following the harbour principle previously tested in Norway [146].

The plant was initially equipped with a vertical-axis Wells turbine coupled with an induction generator. Afterwards, the system was equipped with two Wells turbines with a rotor diameter of 2 m, an electric generator, an emergency butterfly valve, and a control system [8].

An initial test was conducted until the end of the December of 1992 to monitor and evaluate the performance of the system. It provided encouraging results in agreement with the theoretical calculation [8].

**Islay plant**

In 1991, T. J. T. Whittaker of the Queen′s University of Belfast, with the support of the UK Department of Trade and Industry, constructed a prototype of a fixed OWC on a natural

shoreline gully on the Island of Islay, in front of the west coast of Scotland [12, 5].

The plant was equipped with a horizontal-axis Wells turbine coupled with a generator rated 75 kW [5, 147]. This facility was the first one with a structure with a caisson constructed on a shoreline gully in Europe. The aim was to demonstrate the technical feasibility of the operation of both the structure and the PTO system located in the marine environment [9].

The selected shoreline gully was sheltered and was not directly facing the incident waves, reducing the power conversion. However, the research and test facility provided significant data for increasing the knowledge on this technology in the real operation [9]. The data acquired provided useful information for the future design of the OWC plant in shoreline gullies [5].

The structure illustrated in Figure 2.13 was composed of a concrete caisson with a width of 5 m installed in a water depth of 3 m [5, 147]. The caisson had a front wall inclined of 30° submerged for 1 m. The length was 9 m and the height 4 m from the ground level [9]. The average area of the air chamber was 20 $m^2$ [9]. A horizontal duct connected the chamber with the PTO located behind the central upper part of the rear wall [5]. A butterfly valve was installed to control the airflow [9]. The secondary converter was a Wells turbine with a biplane rotor with a diameter of 1.2 m without guide vanes [5, 147].

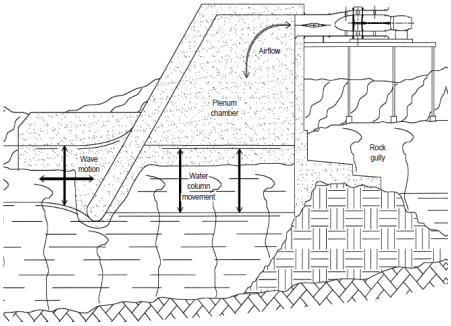


Figure 2.13: Scheme of the central side section of the Islay Plant [9].

From the measured data of the sea climate, a database of 53 different sea states characterising the location of the test site area was obtained, with wave height ranging from 1.5 m to 4.4 m [12].

Furthermore, the model tests showed that the installation of the plant in a more exposed area would have increased the power output of even three times [9].

Various arrangements of the PTO were tested during the last 2 year of the operational period and an increase in the output was observed. After 6 years of operation, the plant was dismissed [9, 5].

**OSPREY**

The Ocean Swell Powered Renewable Energy (OSPREY) was a bottom-fixed OWC device deployed near the coast of Dounreay in the north of Scotland [10, 5]. The project was conducted by the Applied Research and Technology Limited, which subsequently became the Wavegen, the Scottish Hydroelectric, and the Queen′s University of Belfast. It was supported by the European program JOULE II and other associations [10].

The device was designed to supply electricity for the grid, together with a hybrid system of wind power [5]. The total potential output was rated 2 MW for the wave power and 1.5 MW for the wind power [10, 5].

The structure of the OSPREY is illustrated in Figure 2.14. It was composed of a rectangular capture chamber made of steel, and it was installed on a water depth of 14.5 m. At the sides of the chamber, two prominent pyramid-shaped hollow structures filled with ballast material were positioned to guide the waves towards the chamber and stabilise the system [10, 5]. The structure had a width of 20 m and weighted 700 t without the ballast material [10].

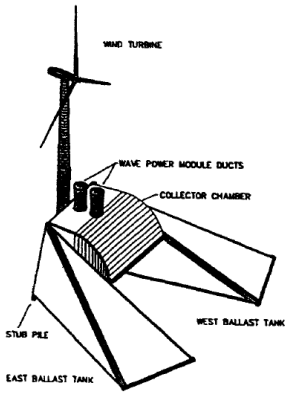


Figure 2.14: Scheme of the OSPREY system [10].

The capture chamber was connected to the PTO system with two vertical ducts positioned at its top [10]. Every duct was equipped with two contra-rotating Wells turbines, each coupled with an induction generator rated 500 kW and a control system [10].

A conning tower was designed for being positioned behind the air chamber. The installation of a wind turbine able to resist the marine environment was considered [10, 5].

An undersea cable was installed to transmit the electric power generated to the local grid [10].

Unfortunately, due to financial pressure and issues in the design, a structural failure occurred during the deployment of the OSPREY [10, 5].

After this event, Wavegen started working on a new design of the OSPREY in order to overcome the problems encountered with the first project [10, 5]. The new design relied on a structure mainly in concrete modules to reduce the costs [5]. The design of the chamber was the same as the first project, while the side stabilisers were substituted by rectangular concrete harbour walls [10]. The second version of the OSPREY was never built in the real scale [5].

**Haramachi system**

In 1996, the Tohoku Electric Power Company constructed a prototype of a fixed OWC into the breakwater of the city of Haramachi, in the Fukushima Prefecture, in Japan.

The prototype was equipped with two impulse turbines arranged in tandem and coupled to a generator rated 130 kW. The characteristic of this device was the presence of a water rectifying valve system.

**Mighty Whale**

In the May of 1996, the JAMSTEC completed the construction of a prototype of a large floating OWC device, the Mighty Whale [11]. The device was a scaled-up and improved version of the BBDB. However, its working principle was more similar

to that of a fixed OWC due to the massive structure, and power absorption was not achieved with heave and pitch oscillations [5]. In fact, the main difference with the BBDB was that the bottom openings of the air chambers faced the incident wave [5].

The device shown in Figure 2.15 was deployed 1.5 km off the Gokasho Bay entrance, in the Mie Prefecture, in Japan [11].

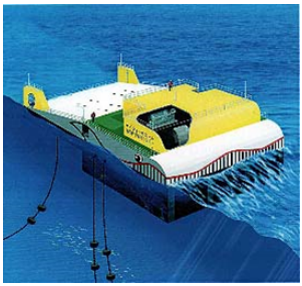

Figure 2.15: Rendering of the Mighty whale [11].

The water depth was 40 m and the predominant wave condition at the test site had values of significant height usually between 0.5 m and 4 m and a period of 6 s [148]. The maximum wave height registered was 11 m with a period of 15 s [149]. Between April and September, the region was crossed by typhoons and low-pressure weather conditions [148].

The structure was made of steel and it had a length of 50 m, a width of 30 m, and a height of 12 m [11]. The ending part of the structure consisted of a stabiliser made up by two vertical fins connected with a plate to reduce the pitching oscillations reducing the energy absorption for a large-scale floating structure [11, 148].

The prototype was moored with four chains at the front, and two chains at the rear [11]. Two intermediate weights were at-

tached on each chain to minimise the motion of the barge [11].

Three air chambers, each with an area of 80 $m^2$ were partially submerged and located on the front with the bottom openings facing the wave direction [11, 148].

The buoyancy rooms were located behind the air chambers, at both sides of the structure and in the rear section [11]. A room containing the on-board measurement and monitoring system, and the control system for the power take-off was located above the front buoyancy chambers [11]. The WEC shown in Figure 2.16 was provided with tandem Wells turbines with 8 blades and a rotor diameter of 1.7 m and inlet and outlet guide vanes. The total power output was rated 110 kW [11].

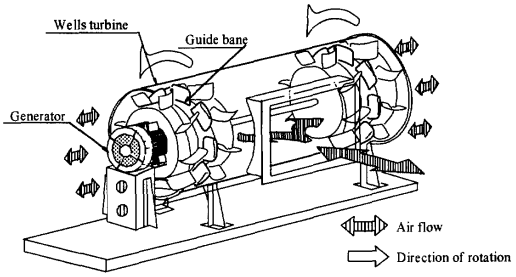


Figure 2.16: Scheme of the tandem arrangement of the Wells turbines installed in the Mighty Whale [11].

The control system for the generator consisted of variable-voltage and variable-frequency regulation for a regenerative breaking [11]. Thus, when the angular velocity of the generator was under the rated speed, the control system applied a fixed torque control [11]. Instead, when the angular velocity was over the rated speed, the control system used a weak field control [11]. Moreover, a safety-valve system was installed for each turbo-generator unit to cut-off the airflow when the wave height be-

came dangerous for the system [11].

All the generated electricity was utilised for the on-board loads and the measurement equipment [11]. The structure was linked by a telemetry system with an additional onshore measurement and control station, which monitored the parameters relative to the safety of the device and the status of the equipment [11].

The main parameters measured and analysed by the on-board station were the atmospheric and sea state, the structure motion due to waves, the mooring forces, the level of the water column inside the air chamber, the turbine rotational speed, and the electric power output of the generator.

In addition to the wave power absorption, the Mighty Whale had the characteristic of reducing underneath half the height of a wave with a length that doubled the length of the device [11]. This feature was considered to be useful for various purposes such as aquiculture [149, 11].

Another innovative aspect of the Mighty Whale was the possibility to equip the structure with a photovoltaic generation system, as there was enough space between the side buoyancy rooms [150]. This was the first time that a hybrid generation system with solar and wave power was tested [150]. The coupling of these two renewable resources was realised to increase the energy conversion during either periods with good and bad weather. The photovoltaic equipment consisted of 10 solar panel sets connected in parallel, each one in turn composed of 18 solar panels connected in series. The panels were inclined of 20° above the horizon [150].

The sea test on the Mighty Whale began on the 10th of September 1998 [11, 148]. A peak of the total efficiency of about 15% was measured corresponding with a wave period of 6.8 s [148]. The sea test ended in the March of 2002 when the prototype was retired [151].

**Pico plant**

An oscillating water column plant was installed in a shoreline gully on the Pico Island in the Azores Archipelago, in Portugal. The construction of the plant was coordinated by the Instituto Superior Técnico of Lisbon, with the collaboration of the United Kingdom and Ireland [152, 153]. The plant supplied about 9% of the energy demand of the island and was utilised as a research and development facility until 2018 [152, 154].

The system was equipped with a horizontal-axis Wells turbine coupled with an induction generator rated 400 kW [153]. The scheme of the facility is illustrated in Figure 2.17. The project of the plant was supported by the European program JOULE which promoted the building of a pilot plant for research studies and development purposes on wave energy [152]. Another aim of the project was to demonstrate the feasibility of supplying electricity to a small grid in a remote location [152, 153]. In particular, this was the first plant to perform this function permanently [153].

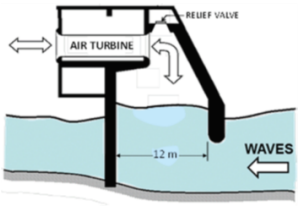


Figure 2.17: Scheme of the central side section of the Pico plant.

Pico Island was chosen as the construction site due the high wave energy levels, the suitable sea depth, the small tidal range, the easy access and the closeness to the grid station [152]. More precisely, the plant was constructed at Cachorro, on the northern side of Pico Island facing the Atlantic Ocean as the coast was characterised by several shoreline gullies with almost vertical side walls, where wave energy is naturally concentrated [152, 153]. The water depth at the test site was 8 m [153]. The data collected about the sea state showed a prevalence of waves with significant height in a range from 1 m to 3.5 m and significant periods that ranged from 8 s to 12 s even if in extreme conditions sea waves can exceed these values [152].

The upper part of the rear wall was provided with a circular opening connected with a horizontal duct to lead the airflow from the chamber to the turbine [153]. Two in-line valves for safety purposes were positioned inside the duct [153]. One had a slow mechanism driven by a hydraulic actuator, and it was utilised for the non-operational periods, and the other had a faster mechanism driven by a pneumatic actuator to be used during the operational period [152, 153].

The Wells turbine rotor had 59 fixed guide vanes on both sides and 8 rotor blades with an outer diameter of 2.3 m. It could rotate with a velocity range between 700 rpm and 1500 rpm. The generator was modified to allow the operation with a wide rotational speed range of the turbine in order to increase and smooth the power output [153]. The efficiency of the turbine was estimated to be about 80%.

The plant was equipped with a control and monitoring sys-

tem working with a programmable logic controller [152]. The main measured parameters concerning the safe operation of the equipment were the vibrations in the power take-off, and the turbine rotational speed [152]. For what concerns the evaluation of the performance, the measured data were the pressure in the air chamber, the water column oscillation, and the airflow through the duct [152].

The dimensions of the caisson were selected based on theoretical calculations and model tests in order to get resonance with the prevalent wave for optimising the power absorption [153]. For the first time in model testing, the air compressibility in the chamber was considered by linking the model with an air reservoir [153].

The conversion efficiency from wave power into air power was estimated with a model based on the linear water wave theory, employing data from tank tests with irregular waves [153]. With a boundary element method, the structure, the seabed, and the cliff walls were recreated [153]. The data about the site were collected during a bathymetric survey by a team of the Hydrographic Institute of the Portuguese Navy in 1978 [153]. From this model, the hydrodynamic coefficients were obtained [153].

A model simulating the energy conversion of the Wells turbine and the generator was applied to estimate the conversion efficiency from air power to electric power [153]. This model utilised the data of the aerodynamic performance of the turbine obtained from a previous laboratory test realised on a prototype [153]. The model simulated the control system and included the mechanical losses of the turbine and both the mechanical and electrical losses of the generator [153]. The simulations were

conducted using a series of 44 representative sea states previously measured for the application site [153]. In addition, in order to optimise the conversion, the results were obtained using different damping coefficients and rated values of turbine power [153]. Finally, a team of the Instituto Superior Técnico of Lisbon defined the turbine parameters for its realisation performed by Wavegen [152].

One of the major difficulties encountered in this project was the construction [153]. To limit the expenses, local contractors were hired and, due to the lack of experience with this sort of plant in a harsh marine environment, the construction took almost three years [153]. Issues with the realisation of the concrete underwater part of the structure heavily affected the plant strength during all its lifetime [153]. The remoteness of the plant and the marine conditions created difficulties in maintenance and increased the related costs [155].

Moreover, the excessive vibrations of the power take-off support and the stator vanes, which were not enough resistant, and the leakage of the lubricating system of the turbine bearings created operational problems [155].

The plant had to stop its operation shortly after the commissioning due to mechanical problems and water infiltrations, derived from not sufficient isolation of the PTO covering, that damaged the electrical equipment [152, 155]. The plant remained non-operational for 5 years due to a lack of funds for repair operations. For the same reason, no maintenance was done during this period. This contributed to accelerating the plant deterioration [152].

The Pico plant was re-activated in 2005 after a recovery

project, supported by the PRIME program of the Portuguese Innovation Agency, that was conducted by the Portuguese Wave Energy Center [152].

The main adjustments were the substitution of all the electrical equipment and the reparation of the damaged mechanical parts as the valve actuators, the lubrication system of the turbine bearings, and the supports for the structure and the turbine, which were even reinforced [152]. The upper opening of the turbo-generator group was adequately isolated [155].

Furthermore, a relief valve, provided in the original project but not equipped at the initial commissioning, was installed on a square opening on the chamber roof to release the air pressure in extreme weather conditions [152, 153].

A test was programmed from September 2005 to the end of October 2006 [152]. Since the vibration problems persisted despite the intervention, the turbine rotational speed was kept under 1200 rpm to avoid another interruption of the plant operation. This value was lower than the optimal design speed of 1500 rpm. Therefore, the aim of the test became to try different control methods for the generator and different valve positions to analyse their effectiveness [152]. This initial phase ended only after three months for maintenance as the stator vanes on the atmospheric side were damaged by the excessive pressure caused by the stall of the turbine [152].

In the May of 2006, the test on the Pico plant was planned to restart after removing the damaged row of guide vanes [152]. The test was conducted with only a row of guide vanes on the chamber side [152]. The target was testing different control strategies for various sea states in order to analyse the response of the system [152]. Actually, the test started in July due to problems

with the electrical equipment [152]. In addition, in that period, the sea was exceptionally calm and useful data were acquired only at the beginning of September [152]. However, by the end of that month, the plant operation was interrupted for maintenance due to the degradation of the bearings [152]. Therefore, the data acquired were not sufficient to conduct an appropriate analysis about the functioning of the plant with only one row of guide vanes [152]. In general, it was observed that with guide vanes positioned only on the chamber side the noise produced in stall conditions was consistently reduced [152]. This is due to the separated flow at the turbine blades resulting in a highly turbulent flow impacting the downstream guide vanes [152].

In the October of 2006, a new row of guide vanes was installed on the atmospheric side and all the bearings were replaced [152]. However, since the project ended at the end of October, not enough data were achieved [152]. During this last test, the rotational speed was kept under 1000 rpm and a consistent reduction of vibrations was observed [152]. Thus, it was necessary to redesign the turbine and the bearing support for solving the problem of vibrations to allow the optimal operation [152].

From the experimental campaigns carried out, it was observed that the airflow through the duct was uniform due to the configuration of the duct. This was an important feature for reaching a high efficiency with a wide operational range of the turbine [152].

The velocity field through the turbine was uniform for both the inflow and outflow phases, allowing an efficient turbine operation and delaying stall conditions. In addition, the inertia of the turbine contributed to smooth the electric power output

[152].

Since the design of the duct was correct, the equipment worked as predicted in theoretical calculation and model tests [152]. However, due to the non-linear behaviour of waves in shallow water, the crests were more concentrated and brief than the troughs and produced a faster outflow regarding the inflow. This aspect may cause the turbine stall and should be avoided [155]. The relief valve turned out to be reliable and efficient in reducing the onset of stall conditions and the consequent degradation of the mechanical equipment, but the fatigue remained an issue. For facing the stall issues of the Wells turbine, an innovative system for varying the pitch angle of the rotor blades that worked with eddy currents was patented and constructed. The turbine had a rotor with 15 blades and an outer diameter of 1.7 m. However, due to lack of funds, the new turbine could not be transported and installed in the plant [152].

The effective hydrodynamics of the chamber was estimated with good agreement by the theoretical modelling. Moreover, the control methods performed efficiently [152].

On the 17th of April of 2018, a strong sea storm caused a partial collapse of the structure. This led to the decision of definitely closing the plant [153].

**LIMPET**

In the September of 2000, the Land Installed Marine Powered Energy Transformer (LIMPET) plant based on the oscillating water column technology was constructed in a shoreline-gully on the west coast of the Island of Islay, in the United Kingdom. The project was supported by the European program JOULE III and it was carried on under the direction of the Queen′s University

of Belfast with the collaboration of Wavegen Limited, Charles Brand, and the Instituto Superior Técnico of Lisbon [12]. The plant illustrated in Figure 2.18 was rated 500 kW and was the improvement of the previous prototype with 75 kW of power [12]. The system had the double purpose of research and development facility and of supplying the electric output to the local grid [12]. The operational period of the LIMPET brought significant knowledge for the future applications [12].

The structure was built almost completely on-site and the gully was artificial made [12]. The aim of this design method was to manage to create a process that could be repeated for building modular units [156].

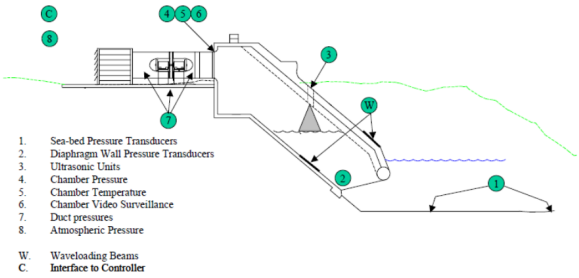


Figure 2.18: Scheme of the LIMPET plant [12].

The plant was composed of a rectangular concrete caisson of width equal to 21 m with an inclined front wall with a total area of 170 $m^2$ at the bottom opening. The front wall was conceived to resist an external pressure of 6 bar and an internal pressure of 1 bar.

Several improvements were made regarding the prototype of the system. The transversal area of the air chamber opening was subdivided into three square sections with a side of 6 m to

form three different oscillating water columns. The sections were divided from each other by two diaphragm walls going all along the caisson [12]. At the horizontal section level, each diaphragm was provided with a connection to uniform the pressure of the three chambers when opened. The possibility of closing the connection allowed to isolate the chambers to test different PTO systems at the same time [12]. The diaphragms also had two additional functions: contributing to the support of the structure, maintaining a restrained thickness of the upper wall and minimising the transverse wave excitation inside the chamber that could reduce wave power absorption [12].

On the top wall of two of the three air chambers, two openings, each one with area of 1 $m^2$, were positioned to insert two relief valves. Indeed, theoretical studies indicated that a relief valve within the main control system could improve the total conversion efficiency of the plant. However, during the earlier operational period, both the openings for the relief valves were kept closed [12].

The front and bottom walls of the air chamber were inclined of 40° to facilitate the water entry and minimise the power losses [12]. Moreover, a front lip at the bottom opening of the air chamber, together with the inclined walls, contributed to decreasing the turbulence at the entrance and the resulting internal sloshing, which decreased wave power absorption [12]. The front lip was downwards inclined of 60° above the horizon to reduce the entrance opening for creating a delay between the phases of the inside and the outside water levels. This ensures a continuous outflow of the water from the chamber [12].

A wave breaker located on the middle of the front wall limited the quantity of water that surmounted the caisson. Even if some

waves were able to override the wave breaker, their power was significantly reduced [12].

The bottom wall of the caisson ended at its top with a horizontal section to prevent the entrance of the seawater inside the duct embedding the PTO system [12]. Apposite blocks were positioned corresponding with this section to limit the water flow. In the unlikely event that the water column raised over the section level, there was still a height gap of 5 m for reaching the duct [12, 156].

On the upper part of the vertical rear wall, two circular openings connected the chamber with the PTO through a horizontal duct [12]. The duct was composed of an initial part with a length of 1.3 m and a bigger part with a length of 2.6 m. A butterfly valve was positioned after the first part and a radial vane valve after the second. The flow was guided to the valve through an annular ring embedded with an elliptical nose cone. The two valves had a different functioning mechanism and structure to avoid their failure at the same time and in the same manner. Their role was to reduce or even cut off the airflow in the event of harsh weather conditions or for maintenance [12, 156].

The power take-off units were disposed in line with the radial vane valve. The system was equipped with two identical horizontal-axis Wells turbines with 7 rotor blades and an external diameter of 2.6 m, mounted back-to-back to achieve a contra-rotating arrangement. Each turbine was coupled with an induction generator rated 250 kW, providing a total potential output of 500 kW. The PTO units were followed by a bell-mouth duct air discharge to reduce the sound produced by the airflow crossing the turbines [12, 157].

During the early operational period, only one opening was provided with a PTO system, while the other one was closed

[12].

The plant was equipped with the main control and monitoring system connected to a data logger and managed by an algorithm developed by Wavegen [12]. A significant innovation was the installation of 4 video cameras connected via LAN to a video server in order to monitor the water column oscillations and sea conditions [12]. Both the data logger and the video server were located in an facility positioned at a distance of 20 m from the main structure of the plant [12].

The control algorithm sent the torque request signal to the inverter driving each generator in order to regulate and smooth the power output [12]. The torque was set in a range between a maximum and a minimum value based on the turbine rotational speed. The algorithm provided a different signal to each generator independently. The algorithm even controlled the positioning of the valve as a function of the rotational speed [12].

Other functions managed by the Wavegen algorithm determined the safety of operation of the system, and controlled the operation of the machines [12].

The Queen's University of Belfast patented the pressure transducers located on the seabed near the bottom opening of the chamber and inside the lower end of the diaphragm walls of the chamber. The transducers were connected with the monitoring system and measured the fluctuations with respect to a pre-set static head of the water above the installation point [12].

The innovation of these transducers was the possibility of deployment on the seabed near the bottom caisson opening, allowing more precise measurement of the sea state for monitoring purposes.

During the initial monitoring of the plant, until 2002, the power output measured was significantly lower regarding the initial theoretical estimations for various aspects [12]. First of all, the expected output was determined using the data set of 53 representative sea states gained from the operation of the Islay plant and the data of a previous bathymetric survey regarding the water depth and seabed characteristics [12]. However, the exposition of the two sites was considerably different. Moreover, the seabed and the water level changed during the years regarding the first survey [12]. The water level decreased by 1 m and the 1:25 inclination of the seabed, which was considered starting at the cliff bottom, actually started at a distance of 60 m from it [12]. From a new wave tank test conducted by Wavegen in the light of the updated data, this resulted in a significant reduction of power output [12, 156]. Indeed, when the water depth decreases, the friction between the seabed and the wave increases, reducing wave power.

Another aspect that contributed to the low power output was the layout of the caisson [12]. Indeed, in the tank tests, the side walls of the model had a flare angle of 12.5°, while the real-scale prototype was constructed with straight side walls to simplify its realisation, causing the reduction of the wave power absorption [12].

These aspects determined the decrease of about 40% of the power output [12].

Even the model used to estimate the performance of the turbine was not sufficiently accurate for the design purposes [156]. In fact, the estimated values were obtained from a test conducted by the Instituto Superior Técnico of Lisbon on a turbine model

of 0.6 m of rotor diameter subject to a unidirectional steady flow [156]. However, the flow through the contra-rotating turbine was characterised by strong unsteadiness that was not modelled [156]. In addition, a study on the duct for the discharge of the air indicated that the inward flow through the duct was not correctly distributed. For these two reasons, the stall conditions were anticipated, and the operational bandwidth of the turbine was consequently reduced [156].

From this analysis, it was concluded that the monoplane and biplane configurations of the Wells turbine, for which the steady model was suitable, performed better than the contra-rotating configuration in terms of power output. Moreover, the former machines would require a simpler structure, a smaller space, and a single generator instead of two [157]. These considerations indicated the need for developing a model theory also considering the unsteady flow conditions within a contra-rotating Wells turbine to improve its design [157].

The plant structure proved to be safe and no significant problems occurred. All the measurement equipment operated reliably [12].

**Zelhang plant**

In the February of 2001, a shore-fixed oscillating water column system with rate power 100 kW was installed close to the town of Zelhang, in the Shanwei City of the Guangdong Province, in China [158]. The project was supported by the National Key Technologies Research and Development Program of China.

The PTO system equipped on the plant consisted of a self-rectifying turbine coupled with an asynchronous generator. The

maximum output was reached for a significant wave height of 1.5 m [158].

The Zelhang plant was the first large-scale OWC connected to the grid in China [158]. The plant supplied the generated electricity to the local grid for more than 2 years, demonstrating the capability of this renewable energy technology of contributing to energy demand [158].

**Port Kembla plant**

In 2005, the Australian Company Energetech, which after became the Oceanlinx, deployed a full-scale prototype of a bottom-standing OWC plant at a distance of 200 m from the breakwater of Port Kembla, in Australia [1].

The structure was made of steel and it was anchored to the seabed. It had a length of 36 m and a width of 35 m with a weight of 485 t. The distinctive characteristic of the structure of this system was the use of a parabolic-shaped collector in front of the chamber for amplifying the incident waves to enhance power conversion from waves with low energy [1].

The annual energy conversion of the plant was estimated of around 500 MWh and the system was planned to be connected to the grid with a 11 kV cable. It was equipped with a Denniss-Auld turbine with 21 blades, characterised by low rotational speed and high torque. Part of the electric power provided was utilised for water desalination on-board [159].

The plant remained operational until 2010, when the rough sea conditions broke the moorings and caused the collision of the

device on the breakwater.

**LEANCON**

In 2007, the LEANCON system was patented in Denmark by the homonym company LEANCON Wave Energy using a multi-chamber floating structure [160, 13]. The device illustrated in Figure 2.19 had an innovative V-shape provided by two floating beams set with an angle of 80° between them [161]. The full-scale prototype was planned to be 240 m wide with eight turbine-generator units equipped for a total installed capacity of 4 MW [161].

Figure 2.19: Prototype with scale 1:10 of the LEANCON [13].

Under each beam, two rows of cylindrical air chambers were installed with downward inclination to face the wave direction for decreasing the impact of the waves on the structure [161, 13]. Each chamber communicated through two rectifying valves with a high-pressure and a low-pressure duct crossing each beam [13].

One or more PTO systems could be installed between the two ducts. Since the airflow was made unidirectional by the rectifying system, the application of impulse turbines demonstrated to be a suitable solution [160, 13].

The distinctive structure of the system and the presence of

several chambers fostered the balancing of the vertical forces due to the heave oscillations [160]. This happens as the air is compressed in some chambers and expanded in the others when the wave passes under the structure [160]. Consequently, the weight of the structure can be reduced. This allowed the structure to follow the movements of the sea waves even in harsh conditions by changing the settings of some relief valves. Therefore, the structure was not exposed to high loads, reducing the costs of manufacturing and maintenance.

For its peculiar shape, the working principle of the LEANCON was a mixture between an attenuator and a terminator [13].

After that several tests were carried out by the LEANCON company in a wave flume tank to develop an optimal structure, a 6 m wide prototype with a 1:40 scale was constructed. From the water tank test emerged that the drift of the structure largely influences the conversion efficiency, requiring further tests [161]. Thus, a model with 15.7 m of length, 8.5 m of width, and 1.5 m of depth was tested even in the wave tank of the Hydraulics and Coastal Engineers Laboratory of the Aalborg University, confirming the validity of the working principle [161]. Subsequently, a sea test was conducted in the fall of 2007.

In 2015, with the support of the Danish electricity operator Energinet, a 1:10 scale model with a width of 24 m was built and deployed in the sea to determine the loads and verify energy production.

**OE Buoy**

The OE Buoy, a prototype of a floating OWC, was deployed and tested by Ocean Energy company in the Galway Bay, in

Ireland. The system illustrated in Figure 2.20 was a prototype with a 1:4 scale of the half-cylinder BBDB with the extended duct. The device had a width of 6 m and a length of 12 m, and operated in a water depth of 20 m [1].

Figure 2.20: Image of the OE Bouy operating in the Galway Bay, in Ireland [1].

The system was installed in 2007, and it was tested until 2011 [1]. During the test, the device was first equipped with a Wells turbine, with the support of the FP7 CORES project, and later with a self-rectifying impulse turbine [1].

Before the deployment, the OE buoy was tested in controlled conditions during three phases.

In the first phase, a 1:50 scale model was tested at the Hydraulics and Maritime Research Centre of the University College of Cork. The aim of this test was to optimise the hull configuration in order to maximise the power output. The model was tested under wave conditions that simulated the site selected for the installation.

In the second phase, experiments were performed on a 1:15 scale model in the wave basin of the Ecole Centrale de Nantes, in France. During this test, the theoretical estimations were

confirmed.

In the third phase, a 1:4 scale model was tested in the harbour of Cork. This test confirmed the stability, reliability, and safety of the device in real sea conditions [1].

**Seabreath**

In 2008, a multi-chamber floating OWC, named Seabreath, was patented by L. Rubino and it was developed at the University of Padova, in Italy, with the support of the Merighi Group [14].

Small-scale prototypes of the device were planned to be deployed and tested in the Mediterranean Sea close to Formia, Salerno, Riccione, and Civitavecchia [14]. Since the Mediterranean Sea is not characterised by high-energy waves, it is suitable for testing in the real sea small devices with a maximum rate of 10-20 kW to acquire data for building a larger prototype in a second development stage [14].

The expected power output of the Seabreath was 850 kW for a prototype with a length of 120 m, a width of 24 m, and a height of 20 m, to be installed in a more energetic sea [14].

The Seabreath was a wave attenuator device and had a structure with the form of a ship, with the elongated part aligned with the wave direction [14]. The device was moored with a system that allowed to maintain this position even when the direction of wave changed [162]. The structure illustrated in Figure 2.21 comprised several rectangular aligned chambers, opened at the action of the incident waves [14].

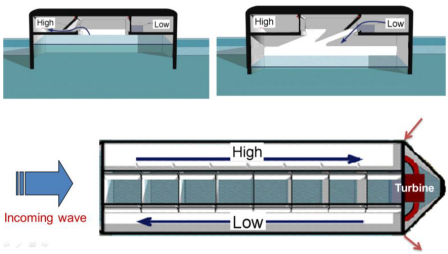


Figure 2.21: Scheme of the working principle of the Seabreath [14].

Each air chamber was connected at its top to a high-pressure duct and a low-pressure duct through a rectifying valve system [14]. The waves passed through each chamber with a little delay ensuring a uniform flow through the ducts [14]. The internal airflow communicated with the atmosphere through a relief valve [14]. This innovative feature enabled a better performance of the device, in particular with high waves [14].

When the air inside the chamber was compressed by the water motion, it entered the high-pressure duct. Conversely, when the air inside the chamber was expanded, an airflow crossed the low-pressure duct from the outside towards the chamber [14]. In this way, the sense of the airflow in the two ducts was constant [14].

The PTO was located between the two ducts in the rear of the structure [14].

Model tests were performed between 2009 and 2010 in the water tank of the University of Padova, which had a length of 36 m, a width of 1 m, and a height of 1.4 m. The water depth was 0.735 m and the maximum value of significant wave height tested was 0.25 [14].

The two models tested had a length of 1.5 m, a width of 0.3 m, and a height of 0.25 m, and comprised four equal air chambers [14]. The experiments were performed under regular

and irregular waves [14].

The air chambers of one model were opened at the top and the model was fixed in order to capture the water column vertical oscillations [14]. The other model had the air chambers closed at the top and was equipped with a butterfly valve mimicking the PTO system in order to analyse the efficiency of power conversion and measure the pressure inside the air chamber and the duct. The model was tested both with floating and fixed configurations [14].

It was found that the maximum efficiency of the system is achieved when the length of the wave and the device are equivalent [14]. When the wave is too long, the device was subject to large heave oscillations reducing efficiency. Conversely, if the length of the waves is too short, the troughs and peaks in a single air chamber are equal, hindering energy conversion [163].

Even if the tested waves were considerably different from the real sea conditions and both the duct and valve of the model were too small, resulting in a low conversion efficiency, a correlation between the incident wave height and the water column oscillation was found, allowing to simulate the airflow through the PTO system [14].

Subsequently, a design with a duct 2.5 times larger and valves opened along the whole chamber length was proposed [14]. The efficiency of this device was assessed and utilised to simulate the performance under the wave conditions off the coast of Riccione, in Italy. The estimated average power was 6.6 kW [14].

**U-GEN**

In 2010, S. Ribeiro e Silva patented the U-GEN concept, an innovative floating OWC system, after a preliminary study

conducted on a small-scale model in the wave tank of the French Research Institute for Sea Exploitation of Brest, in France [15].

This study, together with numerical simulations, proved the feasibility of the device to produce electricity [164]. The device was then developed at the Instituto Superior Técnico of Lisbon with the support of the WavEC Offshore Renewables company [164].

The U-GEN consisted of an asymmetric float embedding a U-shaped tank partially filled with water [15]. The dimensions of the float were 31 m in length, 19 m in width, and 5 m in height, as illustrated in Figure 2.22. The sides of the U-tank were connected at the top with two ducts converging in the PTO system and generating a circular airflow [15].

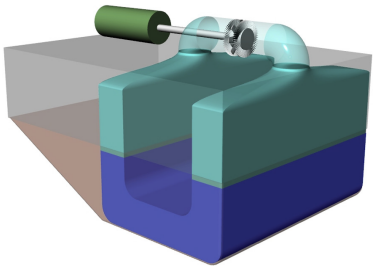

Figure 2.22: Structure of the U-GEN device [15].

The device was planned to be equipped with a Wells turbine rated 500 kW [15]. The aim was the development of a suitable design for its commercialisation through the deployment of 40 U-GEN devices arranged in a farm with a power potential of 20 MW [164].

The innovation of this device was the working principle. Indeed, there was no direct contact between the waves and the

oscillating water column in the U-tank since it was enclosed into the float. In this way, the oscillating movement of the water column was determined only by the roll and heave oscillations of the float caused by wave motion. The former oscillations provided the major contribution [15].

An analysis of the best-suited geometry and typology of PTO was performed to optimise the device by reducing the ratio between costs and energy conversion. A numerical model was developed for this purpose [15]. The model showed three peaks of efficiency related to the oscillation periods of the U-tank and to the heave and roll motions [164].

The quantity of water filled in the U-tank modified the total mass of the oscillating water. In this way, the natural oscillation period of the device can be regulated to maximise energy absorption [164]. However, the natural oscillation period of the U-tank needed to be smaller than the characteristic wave period of the site and the roll period to avoid the anti-roll stabilisation effect that would reset energy absorption [164].

In 2013, a floating structure with an enclosed oscillating water column, named UGEN, was theoretically analysed. The movement of the water column was obtained through the pitch oscillations. The device consisted of a cylindrical float free to pitch about an axis below its center. An enclosed annular tank with internal-shaped walls was partially filled with water for trapping the air below the water surface. With the pitching of the float, the water inside the tank achieved a sloshing movement forcing the air through an air turbine.

**Oceanlinx MK3**

In the February of 2010, the MK3 prototype of a multi-chamber floating OWC system shown in Figure 2.23 was constructed and deployed by the Oceanlinx about 100 m off the breakwater of the Port Kembla, in Australia [1].

Figure 2.23: Image of the Oceanlinx MK3 system [1].

The device was a 1:3 scale model with 8 air chambers, each one coupled with a power take-off. During the tests, only two different turbines were equipped on the prototype: a Dennis-Auld turbine and a Hydroair turbine [1].

The power output of the full-scale system was estimated to be 2.5 MW [1]. The MK3 was successfully connected to the grid from March to May. In this month, the system broke off from the anchoring pylons and sank due to harsh sea conditions [1].

**Mutriku plant**

In July of 2011, a multi-chamber OWC system was integrated into the breakwater of the port of Mutriku, in Spain, as visible in Figure 2.24.

Figure 2.24: Image of the breakwater of the port of Mutriku embedding the multi-chamber OWC system [16].

The project was conducted within the European project M-OWC of the Sixth Framework Programme NERIDA that involved Spain, United Kingdom through the Wavegen company, and Greece, and it was supported by the Basque Energy Board [130, 16]. The aims were building and testing a research system to achieve experimental data under real wave conditions for evaluating the possibilities of commercialisation of the technology.

The Mutriku plant was the first European multi-chamber system with multiple turbines, integrated into a breakwater and connected to the grid [16].

The representative sea conditions measured in the application site ranged from 0.88 m to 3.20 m in wave height and between 5.5 s and 12.5 s in wave period [165].

The whole structure is 440 m long and it is composed of 16 rectangular vertical caissons made of concrete layers, each one coupled with a PTO system. The caissons have a length of 3.1 m, a width of 4.3 m, and a height of 7.45 m regarding the still water level [16, 166].

Initially, the secondary converter was constituted by 16 bi-

plane Wells turbines with a vertical axis. Each turbine had a diameter of 0.5 m and it was composed of two rotors with five blades and provided with fixed inlet and outlet guide vanes. Every turbine was coupled with an induction generator rated 18.5 kW, leading to a total available power output of 296 kW for the entire system [16, 167]. The duct of a single PTO had a height of 2.83 m and a maximum width of 1.25 m [167].

The turbine, the generator, and a butterfly valve composed each PTO system. The valve controlled the airflow to cut it off in case of extreme wave conditions.

The Mutriku plant provided the opportunity of studying the interaction of multiple caisson units and the complexity of a multiple control [130]. Indeed, an efficient control method of the turbo-generator unit could avoid the need for safety valves reducing the cost of installation and improving the reliability and the time response of the plant [168].

Various new control methods were implemented and compared to the proportional integral derivative control method initially applied at the Mutriku plant [169]. The methods demonstrated to be both efficient and effective in avoiding the stall of the turbine, enhancing the absorption of wave energy and its conversion to the electric grid [169].

The Mutriku plant was able to provide the household electricity of about 100 domestic units of approximately 0.6 MWh each year.

During a strong storm in December 2011, four air chambers were severely damaged and until March 2012 the plant did not return operational citeHeras2013. In 2017, a disruptive storm occurred and produced significant damages to the plant. Af-

ter this event, 14 chambers were restored and one of them was utilised to test an impulse biradial turbine.

From the April to July of 2017, an impulse biradial turbine was planned to be tested under the European OPERA program [166]. Theoretical investigations were performed using a new numerical model developed for the Mutriku plant to compare the biradial turbine to the Wells turbine [166]. The results showed that the former turbine produced a slightly higher energy conversion regarding the latter, even if it was not optimised for the Mutriku plant but for the Marmok-A-5 device. In addition, the biradial turbine rotated at about half of the rotational speed of the Wells for the same sea state. This had positive effects on the coupled operation with the off-the-shelf generators [166]. The peak efficiency measured for the biradial turbine was about 70% [170].

**Spar Buoy**

In 2012, the Spar Buoy illustrated in Figure 2.25 was realised and tested by the National Renewable Energy Centre (NAREC) of Blyth, in the United Kingdom. The device was a 1:16 prototype of an OWC spar-buoy and it had a diameter of 1 m and a draft of 3 m.

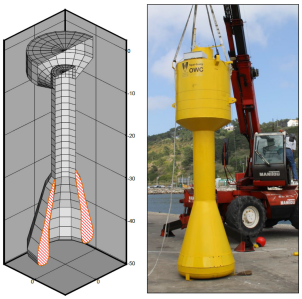

Figure 2.25: Image of the prototype of the Spar Buoy [17].

The device was equipped with a turbine simulator, and it was tested under regular and irregular waves in the NAREC large-scale wave flume with length 60 m, width 5.2 m, and height 7.1 m [17].

The Spar-buoy was an axisymmetric device insensitive to the wave direction [17]. As the previous Center Pipe Buoy, it consisted of a submerged centre pipe attached to a float that moved vertically with the heave oscillation determined by sea waves [17]. The innovation of the Spar-buoy was the non-uniform cross-section of the tube [17]. The volume of the oscillating water column should have the same order of magnitude of the water volume displaced by the float to ensure an efficient operation of the device [171]. Thus, the design of an enlarged inner diameter of the lower part of the tube reduced the optimal length needed [171].

The device was previously tested with a 1:150 scale in the wave flume of the Instituto Superior Técnico of Lisbon (20 m x 0.7 m x 0.5 m) and with a 1:35 scale in the wave tank of the Faculty of Engineering of the University of Porto (28 m x 12 m

x 1 m). The model was made of steel plates, apart from the enlarged lower part, which was made of concrete [17]. The lower part was also provided with a removable ballast module to adjust the weight during the tests [17].

**GreenWave**

On the 25th of the October of 2013, a new type of bottom-standing OWC, the GreenWave, was deployed at Port Adelaide, in Australia. The device was constructed by the wave energy company Oceanlinx. The plant project was supported by the Emerging Renewable Program of the Australian Renewable Energy Agency.

The total available power was 1 MW and the plant was designed to be connected to the grid, supplying about 1000 houses. A further scale-up of the system was considered for reaching the power output of 10 MW in case of success of the test conducted for one year.

The structure illustrated in Figure 2.26 was made of concrete and it was placed directly on the seabed at a water depth of 10 m. Since the WEC weighted 3000 t, an anchoring system was not necessary.

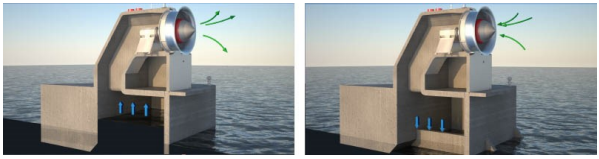

Figure 2.26: Scheme of the working principle of the GreenWave system.

The access for maintenance was promoted by a platform po-

sitioned over the sea level to access the powerhouse.

During the transport of the plant from Port Adelaide to Port MacDonnell on March 2 of 2014, the device sunk.

**V-shape system**

In 2013, a theoretical and wave tank test on a floating device with a V-shaped structure was presented. The system applied the working principle of the LEANCON device [18].

Experiments were conducted on a 1:50 scale model in the large oceanic basin of the Hydraulics and Maritime Research Centre of the Cork College University, in Ireland. The device was constituted by two long beams positioned at 90° from each other. Three rigid supports were provided between the beams to assure structural stability in harsh sea conditions. The device shown in Figure 2.27 embedded 32 OWC curved chambers with side openings located externally under the beams.

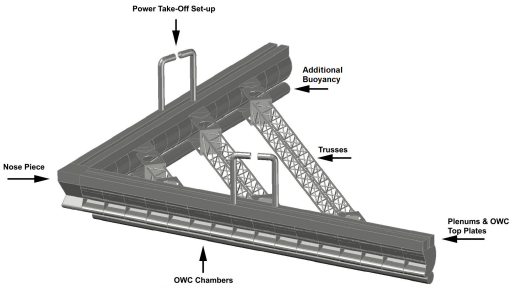


Figure 2.27: Scheme of the structure of the V-shape system [18].

**Compressible volume device**

In 2014, an axisymmetric device based on compressible volumes was presented [19]. The system was constituted by a large

box with an internal tube, both partially filled with air [19]. The two components were connected through the oscillating water column, as visible in Figure 2.28. The enclosed volume of air $V_2$ was connected with the atmosphere through the PTO system. The oscillating water column movement was given by two side-moving surfaces, which can be flexible membranes, interposed between the air volume $V_1$ and the seawater. The oscillation of the moving surfaces caused by waves, compressed and expanded the air volume $V_1$. This caused the motion of the water column, which compressed and expanded the air volume $V_2$, driving the air turbine.

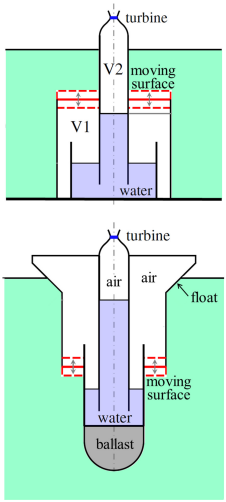


Figure 2.28: Scheme of the working principle of the OWC wave energy device with compressible volumes [19].

The system could be designed either with fixed or floating configurations. The air volume required was larger for the bottom-fixed version, which was able to operate in a wider frequency

range regarding the floating version.

**Resonant Wave Energy Converter**

In 2015, a new typology of multi-chamber OWC, named Resonant Wave Energy Converter (REWEC3), was integrated into the breakwater of the port of Civitavecchia, in Italy, as shown in Figure 2.29. The REWEC3 was the first multi-chamber plant integrated into a breakwater in the Mediterranean Sea and the biggest in the world [20].

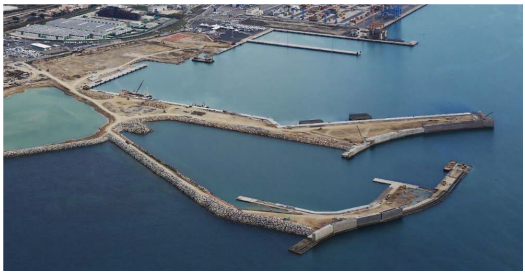

Figure 2.29: Image of the REWEC3 installation into the breakwater of the port of Civitavecchia [20].

The device was patented by P. Boccotti and it was also called U-OWC due to its innovative caisson layout [20, 172]. Indeed, the plant consisted of a caisson with an added front vertical wall that created a U-shaped duct for the air chamber [20]. In this way, the oscillating water column oscillation was given by the pressure fluctuations of the water at the top of the vertical duct [173].

Boccotti previously tested two small-scale models at the Natural Ocean Engineering Laboratory of Reggio Calabria off the east coast of the Strait of Messina to prove the feasibility of the device and to study its hydrodynamic behaviour [173]. The U-OWC markedly increased the primary conversion efficiency re-

garding a standard OWC for two main reasons [20]. The first reason is that the added vertical wall allowed the plant to reach the resonance in a wider range of values of natural oscillation period, enhancing the performance with high waves [20]. The second reason is that the entrance with vertical walls increased the pressure fluctuation with positive effects on performance even with small waves [20].

The external chambers had a 3.72 m width, while the internal chambers had a 3.87 m width along the caisson [172]. An individual unit of the REWEC3 was composed by a caisson with a base with a length of 22.7 m divided into 8 single chambers [172]. Since 17 caissons were installed, the total number of chambers was 136 for a total potential output of 2.7 MW [172]. However, only one chamber was equipped with a Wells turbine with a diameter of 0.738 m coupled to a generator rated 20 kW. The completed unit was tested in the summer of 2016.

**Jeju Island plant**

The bottom-standing OWC plant of Figure 2.30 was constructed and installed 1 km off the Yongsoo coast of Jeju Island, in South Korea [1].

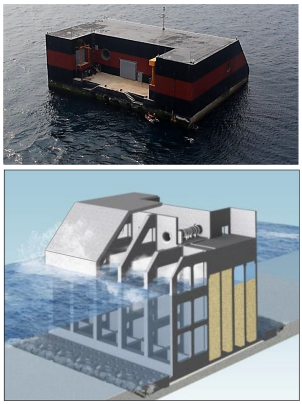

Figure 2.30: Image and scheme of the bottom-standing plant of the Jeju Island [1].

The caisson had a length of 37 m, a width of 31.2 m, and a height of 27.5 m, and weighted 14,650 t [1]. The PTO system was composed of two self-rectifying impulse turbines with horizontal-axis [174]. The rotor of each turbine had 26 blades and an outer diameter of 1.8 m [174]. One turbine was coupled to an induction generator rated 125 kW and the other to a synchronous generator rated 125 kW [174].

### MARMOK-A-5

In 2016, the MARMOK-A-5, a prototype of a 30 kW spar-buoy OWC, was deployed off the Bay of Biscay, near the port of Bilbao, in Spain. The structure of Figure 2.31 had a width of 5 m and a length of 42 m, extending for 6 m above the still water level and for 36 below it. The prototype was developed initially by Oceantec and then by IDOM. The installed capacity was 30 kW and the device was connected to the grid.


Figure 2.31: Image of the MARMOK-A-5 device.

The project aimed to demonstrate the resistance of the structure in the harsh marine environment with waves up to 14 m, and test at first two Wells turbines and afterwards a biradial impulse turbine.

The MARMOK-A-5 was deployed twice. The first time it was tested from October 2016 to June 2018, installing two Wells turbines developed by Oceantec. The structure was moored with polymer anchor lines.

The second time the system was tested from October 2018 to June 2019 in the framework of the European Horizon 2020 OPERA project to test an innovative equipment. The prototype was embedded with the biradial turbine previously tested at Mutriku. The turbine had a rotor with a diameter of 0.5 m and 7 blades and two rows of 64 concentric guide vanes on each side [175]. New control algorithms were applied and an elastomeric mooring system was utilised. All these innovations were estimated to reduce the cost of energy production by about 50%.

## 2.2 Research request

Upon examination of the current status of the technology, reported in Section 2.1, it is noticeable that OWC systems still need to undergo a real industrial development process prior to becoming a consolidated technology for energy conversion from the sea. This is mainly due to the still very high levelised cost of energy, which in turn is connected to the high capital cost of the system. Indeed, relevant infrastructures need to be built and the yearly production of energy is limited for most sea climates. On the economic side, these issues can be tackled by promoting the diffusion of OWC systems in combination with the existing structures as breakwaters in harbours, developing new solutions like pre-assembled offshore floating platforms (possibly dedicated to the production and storage of energy), and by fostering the industrial standardization of specific components as the secondary converters. On the other hand, improving the energy conversion efficiency is a key issue to make this technology competitive [33]. In this view, the development of fast and reliable integrated wave-to-wire tools for the analysis and design of OWC systems, like the approach presented in the study, is of capital relevance for the competitiveness of the OWC technology. The proposed model allows the joint selection of the primary and secondary converters for a specific location already from the very beginning of the design process. In particular, during the preliminary phase of the design, the reduced computational time and power required by the model enable the investigation of a wide variety of configurations. This approach is key for maximizing the overall performance of the system, as the two converters are intrinsically connected by the fluid dynamics of the flowing air, which in turn depends on the specific sea climate of the application site

[33]. Possible further development of the model can be in support of in situ OWC control strategies. In principle, considering that the incident wave conditions can be efficiently forecasted, days in advance, the availability of a tool, able to rapidly select the best OWC setting for maximizing the harvested energy, is of certain importance. In this respect, as proved in the present article, the regulation of the rotational speed of the turbine can be a strategy for increasing the energy conversion [33].

## 2.3 Objectives

The main objective of the thesis is the development of an analytical wave-to-wire model of oscillating water column wave energy converters. A complete, reliable, and fast tool for engineering applications, able to account both for Wells or impulse turbines, is required for the design of this kind of system. In particular, the model is paramount during the first stages of the design to select the optimal configuration of the system based on the distinctive wave conditions of the application site.

The model was applied to evaluate the energy harvested by two wide sets of system configurations operating with a Wells or an impulse turbine in two selected sites, characterised by wave conditions typical of the Mediterranean Sea.

With this aim, the analytical models of the primary, secondary, and tertiary converters were realised.

A rigid piston model applying the linear wave theory was created. The model solves the hydrodynamics, thermodynamics, and aerodynamics of a fixed and detached chamber regarding the sea bottom.

The actuator disc theory and the blade element momentum

theory were applied for the development of the analytical model of the Wells turbine.

A novel analytical model was proposed for an axial impulse turbine. It relies on the use of experimental correlations widely applied for the design of axial turbomachines.

Furthermore, a control strategy was defined to regulate the rotational speed of the rotor and the torque transferred from the turbine to the electric generator.

Overall, the three converters are solved in a coupled fashion to determine the power conversion from wave to wire.

The wave-to-wire model provides a suitable compromise between accuracy and computational cost. These characteristics are pivotal during the early design stages of an OWC system to evaluate the energy extractable from sea waves and to correctly select the siting and the main geometric and operating parameters of the device.

Moreover, computational fluid dynamics (CFD) models of both the Wells and impulse turbines were developed for achieving even more accurate prediction tools for further analysis of secondary converter.

Three-dimensional multi-block techniques were implemented to create the computational domain with a fully mapped mesh composed of hexahedral elements. The employment of circumferential periodic boundary conditions allowed for the reduction of computational power and time. The proposed models use RANS or u-RANS schemes with and multiple reference frame, mixing plane or sliding mesh approach for modelling rotation.

The analytical and CFD models of the Wells and impulse turbines developed were validated through the comparison with an-

alytical and experimental literature data in environmental conditions typical of the Mediterranean Sea, showing a good agreement.

## 2.4 Methodology

The structure of the developed wave-to-wire model is illustrated in the flow chart of Figure 2.32. At first, every wave condition representative of the wave spectrum of a specific application site is determined. Every wave condition has its specific annual and seasonal power transportation and frequency of occurrence. The analysis of the sea wave conditions is initially used independently for selecting the most suited application site and then included as input data of the wave-to-wire model. Afterwards, an iterative procedure for the coupled solution of the mathematical models of the primary, secondary, and tertiary converters is performed. This allows the joint solution of the thermo-fluid dynamics of the seawater and air inside the caisson and the fluid dynamics of air turbomachine, dynamically coupled with the electric generator. The machine functioning maps are utilised to iteratively match the characteristics of the airflow generated by the chamber and the damping imposed by the turbine, instantly coupled and regulated in terms of torque and rotational speed through the control strategy. The operating maps and curves of the entire system for every distinctive wave condition are obtained. Finally, the system performance parameters and annual and seasonal energy harvesting are achieved.

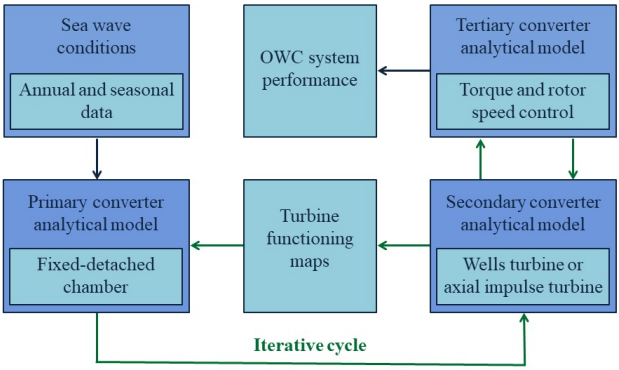


Figure 2.32: Flow chart of the main stages of the developed wave-to-wire model.

The integrated analysis of the entire OWC system allows to instantly determine the functioning of all the converters considering their mutual influence. This is a key aspect as the damping for the OWC caisson relies on its geometry and the local characteristics of the incident wave and, in turn, the performance of the air turbine, regulated by the control strategy, depends on the pressure difference made available by the chamber. Conversely, the separate analysis of the converters may determine the incorrect evaluation of their operating conditions. Thus, the optimisation of the design of a single component or all the components requires the investigation of the complete wave energy converter.

# Chapter 3

# Air turbines for OWC wave energy converters

*The chapter describes the main typologies of air turbines applied for the secondary energy conversion in oscillating water column systems. Firstly, the working principle of the Wells turbine is explained. Then, a wide variety of configurations are considered the design choices and their implications on the fluid dynamics. Subsequently, the functioning of impulse turbines is described, and the configurations with the axial and radial flow are presented.*

## 3.1 Air turbine typologies

Air turbines are the most widespread type of secondary converter installed in oscillating water column systems for wave energy conversion. The operation with air instead of directly with seawater provides the great advantage of reducing the corrosion

problems due to the harsh environmental conditions. The two main categories of air turbines that have been used so far in this kind of system are conventional unidirectional flow turbines and bidirectional flow turbines. The former typologies require a system of airflow rectification with non-return valves to make unidirectional the airflow generated by the action of sea waves impacting the chamber. The latter typologies effectively operate without the need for the rectification system with valves, as they are self-rectifying turbomachines. Indeed, the resulting tangential force acting on the rotor blades has a fixed sign regardless of the sign of the airflow crossing the turbine. The main advantage of conventional unidirectional turbines is the high efficiency of converting compressed air into mechanical energy compared to bidirectional turbines. However, the rectifying valve system is complex, mainly due to the dimensions of the vales required for medium and big plants, that usually have values of airflow rate of the order of $10^2$ $m^3/s$ and a response rate generally lower than 1 s. Moreover, it determines high-pressure losses, increases the production costs of the systems, and has significant maintenance requirements. For these reasons, it is feasible only for small devices as navigation buoys. To overcome this fundamental problem, the turbines currently installed in OWC systems are bidirectional air turbines. Amongst them, the most common are axial-flow turbines: the Wells and impulse turbines.

The conventional unidirectional flow turbines that have been applied in OWC wave energy converters are axial-flow turbines and Francis turbines. The use of a rectifying system with valves and a conventional unidirectional turbine was the standard solution implemented in the first OWC systems. As described in detail in Section 2.1.4, after these first applications, the bidirec-

tional turbines became the most widespread solution for OWC systems so far. Therefore, almost all of them have been provided with self-rectifying air turbines apart from the small navigation buoys and the Kaimei.

The Wells turbines are currently the most widespread technology as a secondary converter for wave energy conversion based on the principle of the oscillating water column due to their self-rectifying operation. The axial-flow impulse turbines found a renewed interest in the last decade and became the first alternative solution to Wells turbines. The common arrangement of an OWC system equipped with a self-rectifying air turbine with the axial flow is depicted in the scheme of Figure 3.1. Several studies are currently conducted to investigate the most suited design of this turbine for OWC applications.

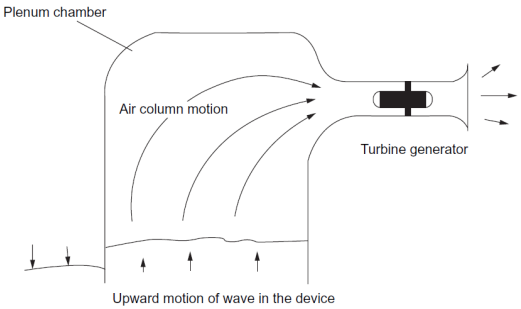


Figure 3.1: Typical arrangement of an OWC system equipped with a self-rectifying axial-flow turbine [21].

Recently, even the radial-flow impulse turbine has drawn new attention for this kind of application. Furthermore, other typologies of air turbines were proposed and tested: the Denniss-Auld, the *HydroAir*, the McCormick contra-rotating turbine, the Savonius, and the twin unidirectional impulse turbines.

## 3.2 Wells turbine

The Wells turbine is an axial-flow turbine invented by A. A. Wells in 1976 and it is the most widespread turbine for energy conversion from sea waves [176]. The original version of the Wells turbine is equipped with a single rotor composed of a set of uncambered blades with a symmetric profile to ensure a self-rectifying operation. This feature makes the Wells turbine particularly suited for operating in oscillating water column wave energy converters, as the resulting tangential force acting on the rotor blades has a fixed sign regardless of the sign of the airflow crossing the turbine, as explained in section 3.2.1. Therefore, the turbine operation is bidirectional as the sense of rotation of the rotor and consequently of the electric generator is constant even though the airflow oscillates like in OWC systems. A scheme of the Wells turbine is depicted in Figure 3.2.

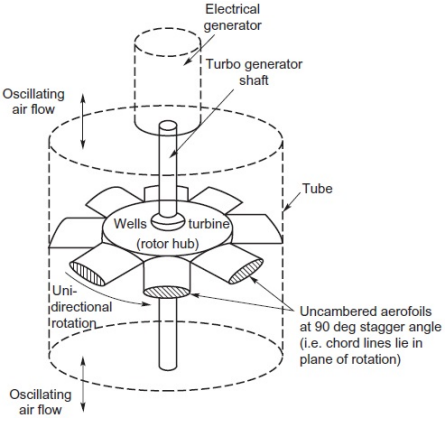


Figure 3.2: Scheme of a monoplane isolated Wells turbine for OWC systems [21].

The principal advantages of the Wells turbines are the bidi-

rectional operation, the geometrical and manufacturing simplicity, the reliability, the safety of operation, the low construction and maintenance costs, the high-efficiency peaks when compared to other turbines for OWC systems, the possible operation with low-cost electric generators, and the high energy storage due to its high rotational velocity compared to the speed of the airflow. Conversely, the main disadvantages are the large dimensions required, the high inertia, the narrow operating range, the high acoustic emissions and mechanical stresses at high rotational speed, the low or even negative torque for low airflow rates that reduces the power conversion and may impede the self-starting, and the relevant power losses due to the possible aerodynamic stall onset.

The key aspects of the success of Wells turbines are the bidirectional operation and the capability of extracting power even at low airflow rates, which are not achievable with conventional turbines. Indeed, the Wells turbine operation is self-rectifying, and the power exerted by the airflow on the rotor blades has a negative contribution on the energy conversion only for very low values of the flow rate during the inversion of the flow phases. Conversely, the main drawbacks are the low average efficiency regarding conventional unidirectional turbines and the narrower operating range. The Wells turbine is able to convert a significant time-averaged power with relatively high aerodynamic efficiency when the rotor reaches the design speed under the most suited flow conditions. The efficiency peaks that were measured with experimental analyses are approximately 65% under wave conditions maximising energy extraction [177], while analytical models predict average values of efficiency of about 75% in similar conditions [50]. However, the average efficiency of the turbine

reduces to nearly 40% considering the entire wave spectrum that characterises the real operation of a Wells turbine. For these reasons, the research on Wells turbines is focused on improving the average efficiency and the width of the operating interval under real sea wave conditions.

Several alternative configurations to the original version of the Wells turbine with a single rotor, named isolated monoplane, were developed to improve its operation. The most relevant alternatives are represented by the monoplane rotor with guide vanes, equipped with two stator cascades positioned symmetrically regarding the rotor cascade, the contra-rotating turbine with two rows of rotors rotating in opposite senses, and the biplane rotor without guide vanes comprised of two rotor rows rotating in the same sense. The biplane rotor configuration can even be equipped with a single row of intermediate guide vanes or with two rows of guide vanes. Other variants proposed and tested are the Wells turbines with a fixed stagger angle different from 90 degrees and an adjustable and controllable stagger angle.

### 3.2.1 Monoplane isolated Wells turbine

A monoplane isolated Wells turbine is composed of a single rotor cascade with symmetrical blades staggered around the central hub, symmetrically positioned regarding the plane normal to the rotation axis and thus at 90 degrees concerning the incoming flow, as visible in Figure 3.3. The blade airfoils are typically symmetrical NACA00XX four-digit profiles with constant stacking in the radial direction. The most suited profiles are the NACA0012, NACA0015, NACA0018, and NACA0021.

The evaluation of the performance of Wells turbines relies on

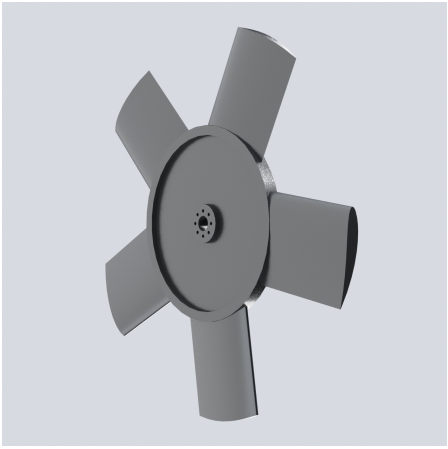

Figure 3.3: Rendering of the rotor of a monoplane isolated Wells turbine.

the classical airfoil theory. An isolated airfoil subject to the action of a flow with an angle of incidence $\beta$ generates a lift force $f_L$ normal to the direction of the incident flow. In a viscous fluid, the airfoil undergoes even a drag force $f_D$ in the direction of the incident flow. These forces are functions of the lift coefficient $C_L$ and of the drag coefficient $C_D$ that are in turn characteristics of the airfoil shape and functions of the angle of attack, the Reynolds number, and the Mach number. A wide variety of numerical and experimental data of the lift and the drag coefficients are available in the literature for the standard airfoils typically used in Wells turbines. The lift and drag forces can be combined through trigonometry to obtain the tangential and axial components of the force exerted by the fluid on each blade of the rotor cascade. The tangential force $f_\theta$ acts in the plane of rotation of the rotor and determines blade rotation. The axial force $f_x$ acts orthogonally to the plane of rotation, and it is responsible

for the mechanical load on the rotor bearings. The cyclically reciprocating airflow that characterises Wells turbines changes the sign of the incidence angle for each flow phase. However, for a symmetrical airfoil, the direction and sign of the tangential force are identical for both the directions of the airflow crossing the turbine and, thus, for the inflow and outflow phases. Due to this composition of the forces, the sense of rotation of the rotor is not affected by the sense of motion of the bidirectional flow crossing the turbine. This implies that a system of rectifying valves is not required. Once the tangential force acting on the blades is calculated, the torque applied on the rotor and the mechanical power output can be determined.

The possibility of utilising a monoplane configuration of a Wells turbine for wave energy conversion depends on the pressure difference across the rotor required for the turbine operation. Indeed, the pressure drop is proportional to the square of the tip speed, which has to be limited for avoiding the formation of shock waves. The transonic effects connected to shock waves would lead to relevant increases in the drag force and buffeting. The former results in a decrease in the aerodynamic performance, while the latter causes a reduction in the useful life of the rotor blades. A multi-plane turbine, with or without guide vanes, can be used instead of the monoplane configuration for wave energy devices designed for significantly large pressure amplitudes.

The performance of a monoplane isolated Wells turbine is influenced by the mutual interference amongst the blades composing the rotor. This interference is determined by the inviscid effects connected to the velocities induced by each blade on the others and the viscous effects caused by the wakes generating

downstream of the blades. The magnitude of the interference is a function of the airflow incidence on the blades and the rotor solidity. The effects of the interaction amongst blades with stagger angle orthogonal to the direction of the flow can be modelled by substituting the airfoils with a set of vortex singularities of strength $\Gamma$ positioned at a distance of $1/4$ of the blade chord from the leading edge. The effect of up-wash and down-wash on the flow surrounding the airfoil determines the reduction of the flow incidence angle in the region of the leading edge and its increase in the trailing edge region. This results in reducing the relative difference between the aerodynamic load at the leading edge and trailing edge. Moreover, the flow circulation and the lift force on the airfoil are enhanced by the rise of the velocities above the airfoil and their reduction below it caused by the adjacent airfoils [22].

Since the operation of a monoplane Wells turbine is significantly affected by the aerodynamic interference between the row blades, this aspect must be considered in the turbine modelling. Three possible approaches were proposed in the literature for taking into account the blade interference in the theoretical models of Wells turbines. Two methods rely on the potential flow theory, while the other one is a semi-empirical approach. The most widespread approach based on the analysis of the potential flow on the plate airfoils composing the cascade applies the cascade interference factor to correct the lift force [22]. The correction factor is a function of the blade chord length $l$ and the rotor pitch $\mathfrak{t}$ defined in Eq. (3.1) based on rotor geometry.

$$\mathfrak{t}_i = \frac{2\pi\overline{r}_i}{Z} \tag{3.1}$$

where $\overline{r}$ is the average radius of the blade element $i$ and $Z$ is the number of blades comprising the rotor row.

The cascade interference factor $C\tilde{I}F$ determined through the potential flow theory is given by Eq. (3.2).

$$C\tilde{I}F_i = \frac{2\mathrm{t_i}}{\pi l_i} \tan \frac{\pi l_i}{2\mathrm{t_i}} \tag{3.2}$$

Through this method, the modified lift coefficient, perturbed by the effects of the interaction amongst the rotor blades, is calculated with Eq. (3.3) by multiplying the lift coefficient of an isolated airfoil for the cascade interference factor of Eq. (3.2).

$$C_{LC\tilde{I}F,i} = C_{L,i} C\tilde{I}F_i \tag{3.3}$$

This method allows considering the interference effects only on the lift coefficient and not on the drag coefficient, as the drag is not predicted by the potential flow analysis [178, 179].

Another approach relying on the potential flow theory for assessing the row blade mutual interference is the Morteson method [178]. In this method, the surfaces of the airfoils in a cascade are replaced by flow vortex singularities. The strengths of the singularities are determined by imposing the condition of null mass flow normal to the blade surface at each location of a singularity. Even with this potential flow method, the effects of interference on the drag force are not determined. The drag can be computed through a boundary layer analysis based upon the pressure distribution achieved by the method of singularities [55].

The semi-empirical approach relies on the correlations between the mean values of axial and tangential force coefficients from experiments carried out on several configurations of Wells turbines with different solidity [180, 51, 181, 182, 183, 184, 185, 186], and the corresponding airfoil data from experiments inside wind tunnels [187, 188]. In this case, the cascade interference

factor $CIF$ is formulated with Eq. (3.4) as a function of the turbine solidity $\sigma$ that is directly applied to the axial force coefficient $C_x$ and the tangential force coefficient $C_\theta$ to calculate their modified values $C_{xCIF}$ and $C_{\theta CIF}$ with Eq. (3.5) and Eq. (3.6).

$$CIF_i = \frac{1}{1-\sigma_i^2} \tag{3.4}$$

$$C_{xCIF,i} = C_{x,i} CIF_i \tag{3.5}$$

$$C_{\theta CIF,i} = C_{\theta,i} CIF_i \tag{3.6}$$

The normalised values of the axial and tangential force coefficients calculated with the two methods based on the potential flow theory are compared with experimental data and are presented against the rotor solidity in Figure 3.4 for a NACA0021 profile to evaluate the effects of the different approaches. The force coefficients are normalised relative to the corresponding values of the coefficients obtained with an analogous method for isolated airfoils. The experiments refer to wind tunnel tests carried out with a unidirectional airflow.

In Figure 3.4 it is noticeable that the aerodynamic force coefficients rise significantly with the rotor solidity, leading to an increase in pressure difference upstream and downstream of the Wells turbine. The axial force coefficient is underestimated by the method of Weinig, while it is overestimated by the method of the singularities. By comparing Figures 3.4a and 3.4b, it is visible that the effect of rotor solidity on the non-dimensional values of the axial and tangential force coefficients is analogous in terms of magnitude and trend. Therefore, the aerodynamic forces on the blades rise significantly with solidity. The aero-

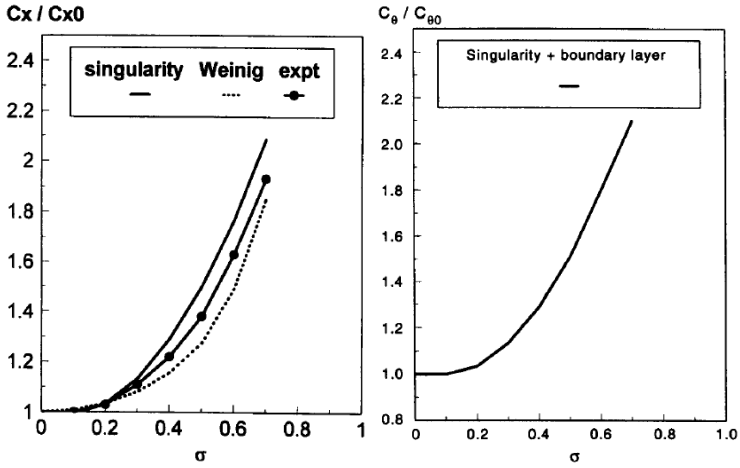


(a) Axial force coefficient (b) Tangential force coefficient

Figure 3.4: Comparison of the interference effects obtained with analytical and experimental models for the (**left**) axial and (**right**) tangential force coefficients of a NACA0021 profile [22].

dynamic efficiency of the turbine is not considerably affected by the interference amongst the blades of the rotor as the ratio between the peripheral and axial forces does not vary significantly. The correction factor of the semi-empirical method is based on the best fitting of a wide variety of wind tunnel experiments like the ones represented in Figure 3.4 to minimise the discrepancies between the predictions of analytical and experimental models [22].

### 3.2.2 Monoplane Wells turbines with guide vanes

The Wells turbine has an inherent critical aspect in terms of aerodynamic performance. Indeed, the power output of a monoplane isolated Wells turbine is usually limited due to the low ratio of the peripheral force to the axial force acting on the rotor determined by the slight angle of attack. This results in low values of the average efficiency of power conversion. Therefore, the turbine must be accurately designed to operate in a range close to the efficiency peak, and the relation between the solidity and the hub-to-tip ratio must be controlled. Another solution to this limitation is the use of stator rows upstream and downstream of the rotor. The upstream stator is named inlet guide vane (IGV), and the downstream stator is called outlet guide vane (OGV). The inlet guide vane controls the flow angle impacting the rotor blades to minimise the aerodynamic losses and avoid the onset of aerodynamic stall due to the separation of the boundary layer. Moreover, the IGV improves the angle of attack of the flow, determining a rise of the tangential force acting on the rotor. The outlet guide vane allows the partial recovery of the relevant amount of kinetic energy connected with the swirl component of the airflow exiting the rotor. For these reasons, the use of the guide vanes may lead to an increase in efficiency. On

the opposite side, installing these stator rows reduces the width of the operating range of the turbine, advancing the risk of stall onset on the blades. Furthermore, they increase the manufacturing, maintenance, and repair costs. Since the turbine operates in bidirectional flow conditions, the cascades need to have either a symmetric or an adjustable geometry. Therefore, the IGV is an accelerating row and the OGV is a diffusive row. The entire blade layout is symmetrical regarding a plane perpendicular to the machine axis and passing through the centre of the rotor. The guide vanes are usually sharp, and their shape is defined by a thin circular-arc profile and a thin straight line, as visible in Figure 3.5. They alternatively operate as leading and trailing edges.

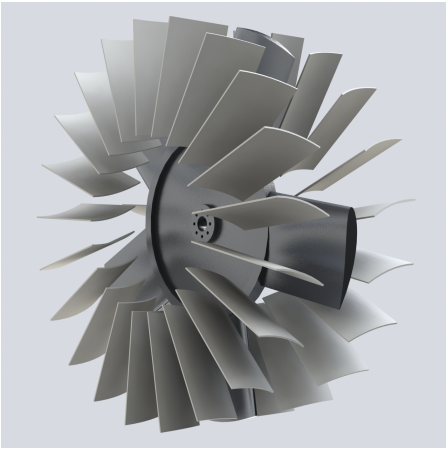

Figure 3.5: Rendering of the rotor of a monoplane Wells turbine with upstream and downstream guide vanes.

The guide vanes usually installed in Wells turbines for OWC systems are classified as two-dimensional guide vanes and three-dimensional guide vanes. In the former typology, the vanes have

a constant shape in the radial direction, defined by the constant radial staking of a single profile along the machine radius. The profile is defined by a circular arc to facilitate the manufacturing, or a circular arc and a straight line. The guide vanes defined by a two-dimensional geometry are generally designed based on the velocity triangles at blade midspan. In the latter typology, the vanes are twisted in the radial direction, and the shape is defined by the radial staking of different profiles along the radius. This configuration allows providing a constant angle of attack of the airflow with the radius. Therefore, the guide vane shape can be designed to optimise the performance of the turbine and to reduce the risk of stall. As a drawback, this solution complicates the manufacturing and increases the production costs.

### 3.2.3 Biplane Wells turbine

The typical configuration of the biplane Wells turbine consists of two identical rotor cascades mounted on a single shaft, as shown in Figure 3.6.

This solution allows the use of Wells turbines when the pressure drop made available by the chamber is excessive for avoiding the formation of shock waves in the operation of a single plane turbine. Indeed, the pressure difference between the inlet and outlet is proportional to the square of the tip speed for the single plane configuration. This parameter has to be limited to prevent the transonic effects connected to shock waves, which lead to relevant increases in the drag force and buffeting, as aforementioned.

The action of two co-rotating cascades determines the flow field of a biplane rotor. This implies an aerodynamic interference between the two planes of the blades of the two cascades. The interaction takes place between the lower blade surface of the

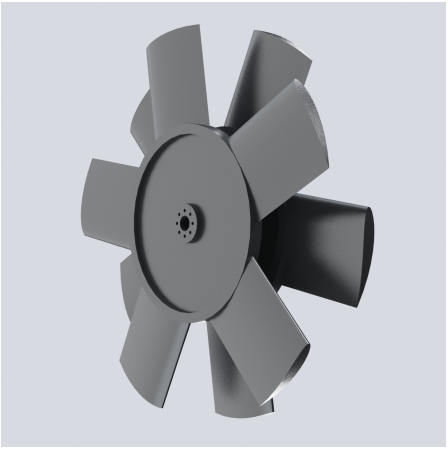

Figure 3.6: Rendering of the rotors of a co-rotating Wells turbine.

high-pressure region, and the upper blade surface of the low-pressure region and it is significant only if the non-dimensional distance of the two airfoils is low. This interference is added to the mutual interaction amongst the blades comprising each row, which characterises all the configurations of Wells turbines.

The causes of the interference between planes are three: the velocities induced by the airflow circulation in one plane on the blades of the other plane, the airflow deflection brought about by the upstream plane, and the wake generated by the blades of the upstream rotor. The induced velocities caused by the circulation on the upstream plane increase velocity of the airflow on the blade surfaces of the downstream row. This increase is higher on the pressure surface than on the suction surface. The velocity rise on the pressure side causes a reduction of the lift acting on the blades of the downstream rotor; the velocity enhancement and the related decrease in pressures on the suction side determine the advancement of the stall. The induced veloc-

ities caused by the circulation on the blades of the downstream row determine a velocity reduction on the blade surfaces of the upstream row. This effect is greater on the suction side than on the pressure side. This implies the reduction of the lift force acting on the upstream blades and the postponement of the stall for the upstream rotor [22].

The wakes generated by the blades of the upstream rotor influence the flow field of the downstream cascade due to viscous effects. As a result, the drag force acting on the downstream blades enhances, and the tangential force moving the rotor row reduces with a consequent decrease of the power output.

The mutual interaction between the planes affects the pressure distribution on the surfaces of the two blade rows. For the upstream blades, the induced velocities determine the decrease of the pressure distribution from the leading edge to the trailing edge of the pressure side and suction side. On the contrary, the induced velocities cause the pressure increase on the pressure and suction sides along the blade chord [22].

With the aim of assessing the magnitude of the mutual aerodynamic interference between the two rotors, experimental analyses were carried out [22, 189]. The parameters determining the interaction magnitude are the rotor solidity, the gap to chord ratio between the cascades, and the stagger angle between the counterpart blades on the two rows. A widespread approach for modelling the cascade interaction relies on a test rig with a unidirectional flow passing through two sets of flat plates, resembling a biplane configuration. Generally, the effects of the solidity, gap to chord ratio, and reciprocal stagger angle on non-

dimensional pressure drop, lift coefficient, torque coefficient, and turbine aerodynamic efficiency are evaluated to changes of the flow coefficient at a constant turbine rotational speed. Typical results show that the main parameter determining the cascade interference is the gap to chord ratio. For values of this parameter greater than the unit, the interference effects are small and become negligible when values higher than 2 are assumed by the gap to chord ratio. In particular, the total-to-static pressure drop across a biplane turbine is nearly doubled concerning a monoplane isolated turbine. For both the configurations, the relation between the volume flow rate and the total-to-static pressure drop is linear under aerodynamic conditions that avoid the stall onset. The differences in the values of pressure drop across each cascade of the two configurations are small, and they are mainly due to the different flow conditions upstream and downstream of the cascades rather than to the mutual aerodynamic interference [22, 189]. The lift coefficient reduces significantly for both the cascades when the magnitude of the gap between the two planes is lower than the blade chord length; the decrease is more intense when growing the rotor solidity. This effect is more marked for the downstream row than for the upstream row. Consequently, the torque coefficient decreases when the reduction of the lift coefficient is significant. With increasing the angle of attack up to about 15 degrees, the magnitude of the reduction of the torque coefficient for the aerodynamic interference between the two planes rises and reaches its maximum corresponding to the peaks of the torque coefficient; for greater angles of attack, the magnitude of the variation reduces [22]. The aerodynamic efficiency of the biplane turbine is approximately equivalent to that of a monoplane isolated turbine if the gap to chord ratio is greater than the unit. The differences are smaller with the

increase of the Reynold number [22, 189].

The flow incidence on the rotor blades could be decreased for the upstream row and increased for the downstream row by acting on their angle of installation regarding the plane of rotation. The result is an increase in the aerodynamic efficiency of the turbine [190]. However, the manufacturing complication compared to the limited increase of efficiency have not led to applications of this solution.

Another possibility for increasing the flow incidence on the downstream rotor is using a stator cascade between the two rotor cascades, as visible in Figure 3.7.

Figure 3.7: Rendering of the rotors and intermediate stator of a co-rotating Wells turbine with one row of guide vanes.

The guide vane deflects the airflow approaching the downstream rotor. The absolute velocity is deflected in the sense of the cascade rotation conversely to the case of a biplane turbine without guide vanes, determining the increase of the incidence

angle. Moreover, the kinetic energy losses are reduced by modifying the velocity triangle at the outlet of the downstream row. These aspects lead to the rise of the aerodynamic efficiency of the turbine. However, the operating range becomes narrower due to the advancement of stall on the rotor blades [44]. The decrease of the relative velocity determines a reduction of the pressure drop, which could be balanced out by increasing the rotational speed of the turbine velocity. Speeding up the turbine, it is possible to design a biplane Wells turbine with guide vanes operating in the same conditions of pressure drop and stall angle of a configuration without guide vanes.

Biplane Wells turbines can operate with a couple of symmetric guide vanes, one positioned upstream and one downstream of the rotor, as illustrated in Figure 3.8. The stators are installed to regulate the incidence angle of the flow impacting the rotor, as discussed in detail in Section 3.2.2.

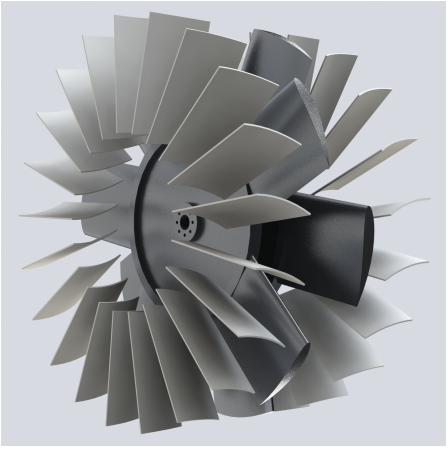

Figure 3.8: Rendering of the rotors and stator of a co-rotating Wells turbine with two single rows of guide vanes.

### 3.2.4 Contra-rotating Wells turbine

The contra-rotating turbine comprises two cascades of rotor blades moving in the opposite senses of rotation with the same velocity. The rotor blades have identical geometry, with the same profile and pitch, as visible in Figure 3.9.

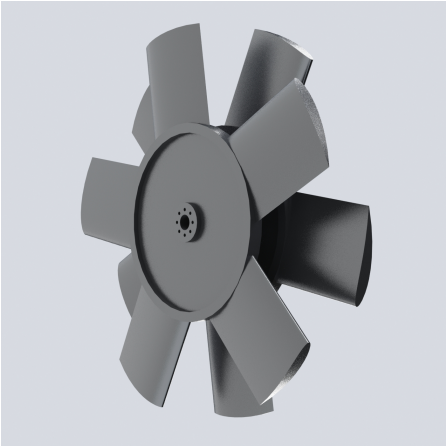

Figure 3.9: Rendering of the rotors of a contra-rotating Wells turbine.

Guide vanes are not present in this configuration to avoid the exit losses due to swirling flow. Indeed, the tangential velocity at the outlet of the upstream row is exploited by the downstream row.

As concerns the mutual interference amongst the blades of a rotor and between the two cascades, similar considerations to those discussed in detail in Section 3.2.3 can be applied.

## 3.3 Impulse turbine

The most frequently proposed alternative to the Wells turbine is the self-rectifying impulse turbine [44]. Two main configurations of this kind of turbine can be defined based on the airflow path inside the device: axial-flow turbines and radial-flow turbines.

### 3.3.1 Axial-flow impulse turbine

The typical configuration of an axial-flow impulse turbine for wave energy converters based on the oscillating water column technology is generally composed of one rotor row and two stator rows (Figure 3.10). The stators are symmetrically installed regarding the plane of symmetry of the three rows, and they are normal to the axis of rotation. The stator nozzles and the rotor blades are symmetrical and staggered around the central hub. The stators operate as inlet guide vane when impacted by the airflow upstream of the rotor or as outlet guide vane when the impact is after crossing the rotor; the operation changes based on the flow phases. The IGV is an accelerating row as its functions are to deflect and accelerate the incoming airflow before its interaction with the rotor blades. This cascade is essential to control the incidence angle of the flow impacting the rotor to minimise the aerodynamic losses and avoid the onset of aerodynamic stall due to the separation of the boundary layer. Since the airflow operating these turbomachines is bidirectional, the symmetry constraints determine the need for a second guide vane with the same geometry as the first. Moreover, the stator rows need to have a symmetric positioning or adjustable pitching. In the former case, an incompatibility situation arises as it is impossible to obtain the correct flow incidence at the rotor blades simultaneously and at the vanes of the downstream stator [44]. The OGV

is a decelerating and diffusive cascade, even if the efficiency of pressure recovery is limited by the requirements imposed to its metal angle.

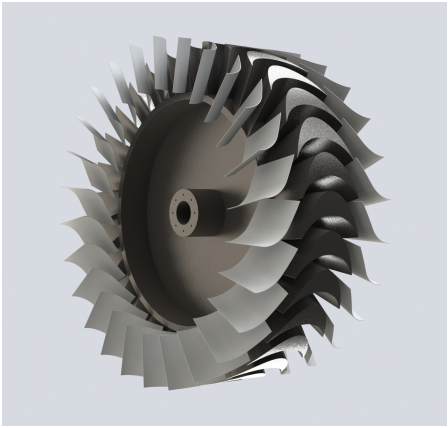

Figure 3.10: Rendering of the rotor and stators of an impulse turbine.

The geometry of the rotor blades is a modified version of the classical steam turbine of impulse type: for this application, the symmetry required by the bidirectional operation imposes two sharp edges and equal inlet and outlet blade angles.

These machines are action turbines, as the nozzles completely transform the potential energy into kinetic energy.

### 3.3.2 Radial-flow impulse turbine

In recent years, the study of radial-flow turbines with the self-rectifying operation was developed. The flow through the rotor blades and guide vanes is radially centrifugal or centripetal depending on the flow phase and thus on the wave cycle. This implies that the turbine is sensitive to the flow direction [44].

The turbine is connected to the OWC caisson by an axial duct, whereas the admission from the atmosphere and the exit to the atmosphere are radial.

The biradial turbine is a radial-flow impulse turbine with a symmetrical geometry relative to a plane orthogonal to the rotation axis. A pair of radial-flow guide vanes are positioned around the external diameter of the rotor. Each row of guide vanes is connected with the corresponding inlet and outlet of the rotor through a duct with walls composed of flat discs [1]. The flow across the rotor is radial during both the inflow and outflow phases.

Two configurations of the biradial turbine were developed. In the version with radially-offset fixed guide vanes, the stators are positioned with a radial distance from the rotor to reduce the losses caused by excessive incidence at the inlet of the second row of guide vanes. This allows the reduction of the circumferential and radial components of velocity of the flow exiting the rotor blades when passing through the connecting duct. The result is the decrease of the aerodynamic stall losses at the guide vanes [1].

In the configuration with axially-sliding guide vanes, their rows are movable in the direction of the rotation axis. Therefore, guide vanes can be positioned along the flow path or removed during the flow phases. In this way, removing the guide vanes downstream of the rotor during the outflow leaves the duct completely free for the passage of the flow. As a consequence, the rotor and the guide vanes can be set at a small radial distance [1].

The biradial turbine was investigated with both numerical

simulations and experiments, showing promising initial results. In particular, the measured peak efficiency of the configuration with axially-sliding guide vanes was approximately 79%. This is possibly the greatest value of efficiency of a self-rectifying air turbine measured up to now [1].

# Chapter 4

# Analytical models

*The analytical models of the individual converters comprising an oscillating water column system are described. Firstly, the equations applied in the rigid piston model for the solution of the dynamics of the fixed and detached chamber are presented. Afterwards, the modelling of the aerodynamics of the Wells turbine achieved by applying the two-dimensional cascade theory and the actuator disc theory is elaborated. Then, the model proposed for the analysis of the aerodynamics of the impulse turbine based on the application of experimental correlations widely used for the design of axial turbomachines is explained. Finally, the control strategy implemented for regulating the dynamics of the air turbine and electric generator is considered.*

## 4.1 OWC chamber analytical model

The analysis of the hydrodynamics, thermodynamics, and aerodynamics of a chamber of an oscillating water column wave energy converter is generally performed with analytical, numerical,

and experimental models. Amongst these approaches, the analytical models have the significant advantage of providing fast and sufficiently reliable solutions of the primary conversion of wave energy.

The analytical models are based on the potential flow theory and apply the hypotheses of incompressible and irrotational flow. The mutual interaction between the incident waves and the caisson is solved with two modelling schemes: the rigid piston model illustrated in Figure 4.1a and the uniform pressure distribution model depicted in Figure 4.1b.

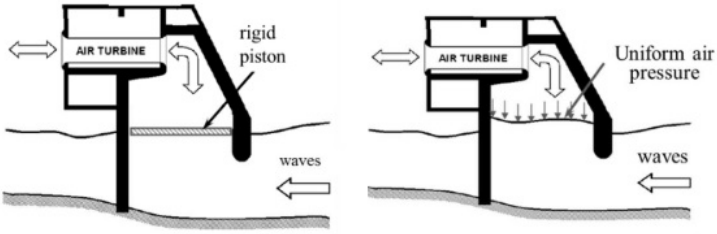


(a) Rigid piston model (b) Uniform pressure model

Figure 4.1: Schemes of the two main typologies of analytical models applied for the study of chambers for OWC wave energy converters [1]

The rigid piston approach models the free surface of the seawater inside the OWC chamber as a weightless piston moving as a rigid body, exclusively in the vertical direction. The hypothesis of uniform pressure distribution considers the possibility of the free surface deformation of the seawater internal to the caisson without assuming any peculiar shape.

The rigid piston model was developed as the earliest solution for the hydrodynamics of OWC chambers. The origins of this

modelling approach date back to 1971 when Wehausen investigated the mutual interference between sea waves and floating structures based on the forces acting on the inner water and its corresponding motion [191]. Relevant contributions to the development of the model were provided between 1970 and 1980 by Evans through the analysis of the velocity of the vertical motion of the inner water free surface, considered as a rigid piston [192, 193]. Subsequently, Robinson, Watts et al., Maeda et al., and Ma proved that this modelling approach ensures sufficiently predictive results if the incident sea wavelength is significantly larger than the size of the chamber [194, 195, 196, 197]. This requirement prevents the onset of significant sloshing phenomena inside the caisson. In 1996, Brendmo et al. introduced the analysis of the viscous losses in the rigid piston model by considering the contribution of the viscous friction forces [198].

More recently, in 2009, Lopes et al. further investigated the hydrodynamics of the chamber by comparing the results of experiments with those of a rigid piston model. Moreover, they introduced latching control techniques in the modelling, without requiring the prediction of waves or wave forces [199]. In 2010, Gouaud et al. evaluated the efficiency of power conversion from sea waves to compressed air inside the caisson for a fixed and bottom-standing oscillating water column chamber [200]. In 2011, Nunes et al. applied a rigid piston approach for the design and performance assessment of a floating off-shore chamber together with a control technique to improve energy extraction [201].

In 2011, Gervelas et al. applied a rigid piston model to solve the hydrodynamics and thermodynamics of an OWC caisson, with assigned damping imposed by a calibrated orifice, operating under regular and irregular wave conditions [202]. In the same

year, Sykes et al. [203], and in 2012, Falcão et al. [204] and Gomes et al. [205], applied the rigid plate modelling to perform an optimisation procedure to maximise the efficiency of floating OWC chambers in terms of the conversion of the incident wave power into the pneumatic power of the airflow. The analytical results obtained were compared with experiments to validate the rigid piston approach. The model was confirmed to be suitable for assessing the hydrodynamics of the primary converter for values of the wavelength of the incident waves markedly larger regarding the chamber dimensions. Conversely, it may determine approximated calculations of the pressure distributions acting on the inner free surface of the device when this condition is not fulfilled, with significant effects on the results of primary energy conversion.

In 2019, Suchithra included the rigid piston approach in a wave-to-wire model of an OWC system to determine the hydrodynamics, thermodynamics, and aerodynamics of the chamber, while the interaction with the air turbine, represented by a Wells turbine, was approximated with an equivalent pressure drop imposed by a calibrated opening [122].

The uniform pressure distribution approach was formulated more recently for extending the analysis of the chamber hydrodynamics to waves with low wavelengths and corresponding high frequencies. Indeed, in these wave conditions, the assumption of rigid motion of the inner free surface is no more valid, and its shape has to be determined by applying the condition of uniform pressure distribution.

The rigid piston model and the uniform pressure distribution model may be solved in the frequency domain or in the time

domain.

If the hypotheses of monochromatic incident waves and linearity of the power take-off are fulfilled, the solution of the hydrodynamic model may be achieved in the frequency domain. Instead, if the non-linear effects are relevant, the solution has to be achieved in the domain of time [206].

The main sources of non-linearity for OWC systems are resumed in the following list.

- ◇ Spectrum of sea wave characterised by irregular conditions.
- ◇ Sea waves with very large amplitude or close to breaking waves.
- ◇ Power losses caused by the unsteadiness of the seawater flow, mainly owed to the turbulence and vortices around the front wall of the chamber, and of the airflow [110].
- ◇ Thermodynamics of the air inside the caisson, primarily connected with compressibility effects that can be relevant in conditions of high-pressure gradients [207].
- ◇ Turbomachine with a non-linear operation, principally due to the non-linearity of the function relating the volume airflow rate through the system and the relative pressure provided by the chamber.
- ◇ Control system regulating the air pressure inside the chamber with air valves [110].

Regarding the resource, within the linear theory, sea waves may be characterised by a spectrum that can be exactly reproduced as the sum of a theoretically infinite number of harmonic wave components with a Fourier series. This condition can be approximated through the use of a sufficiently large number of

components. However, this approach in not valid for waves with very large amplitude or that are close to breaking waves. The wave conditions of the application sites considered in the developed model are far from these extreme circumstances.

Concerning the turbine, the condition is nearly satisfied if the OWC is equipped with a Wells turbine as the relation between the volume airflow rate and the pressure drop across the turbine is almost linear [50, 110]. For an impulse turbine, the relation between these quantities can be approximated to a quadratic function. Thus the non-linear effects depend on the discrepancy from the linear relation, and linearisation techniques may be applied to overcome this issue [208].

Time-domain models require higher computational power and time compared to frequency domain models. However, the analysis of the time series of the parameters regulating the operation of OWC wave energy converters allows for a more accurate evaluation of non-linear power take-off systems as impulse turbines. Moreover, this approach is required for the study of control strategies, as the methodologies applied for coupling the secondary and tertiary converters [122].

### 4.1.1 Rigid piston model

In this section, the non-linear and time-dependent analytical model of the chamber developed with *MATLAB* and *Simulink* is presented [209, 126, 33, 24]. In the framework of the current research activity, a preliminary and simplified version of the code was implemented at the *Maritime Engineering Laboratory* (*LABIMA*) of the *University of Florence*. This version of the code was decoupled from the model of the air turbine. Thus, a

separate analysis of the primary and secondary converters was necessary to impose the air conditions at the outlet of the domain of the chamber. Moreover, the model was able to consider only reduced sets of wave conditions and chamber geometries [210]. To overcome these limitations, the current version of the model integrates the solution of the dynamics of the chamber with the dynamics of the air turbine and electric generator. The model is fully automated and allows the analysis of comprehensive sets of wave conditions and geometric and operating parameters of the three converters, covering all the reasonable configurations of an OWC system.

The model is based on the well-established concept of the rigid piston model by applying the linear wave theory. The main assumptions of the modelling are resumed in the following list.

- ◇ Incompressible and irrotational flow.
- ◇ Heave motion of the water column inside the chamber.
- ◇ Free surface motion of the inner water as a rigid plate, without deformation effects.
- ◇ Incident wavelength significantly larger regarding the chamber dimensions.
- ◇ Symmetrical radiation of the incident waves impacting the chamber.
- ◇ Non-linearity of the system determined by the non-linear relation between airflow rate and pressured drop across the turbine.

The chamber is assumed to be detached and fixed regarding the sea bottom, and it is subject to the action of unidirectional waves moving in seawater of a constant depth (Figure 4.2).

Therefore, the only possible motion mode is the heave oscillation of the water column internal to the system. Since the dimensions of the caisson for the applications studied in the present thesis are small compared to the incident wavelength, the use of the rigid piston model can be considered appropriate.

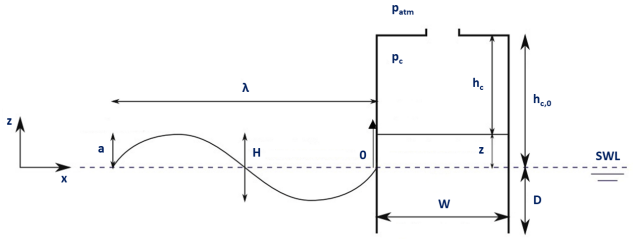


Figure 4.2: Scheme of the sea wave and the OWC chamber, detached and fixed regarding the sea bottom, analysed with the rigid piston model.

The geometric parameters establishing the geometry of the chamber and used as input data for the analytical model are provided in the following summary. Besides these parameters, the added mass $m_{add}$ has to be assigned to define the OWC chamber. The value used in the analytical model was determined based on the free decay experiments presented in Section 7.2.

- ◇ Height $G$.
- ◇ Length $W$.
- ◇ Breadth $B_c$.
- ◇ Front wall freeboard length $F_c$.
- ◇ Front wall draught length $D$.
- ◇ Wall thickness $\bar{t}_w$.
- ◇ Chamber opening diameter $d_o$.

In Figure 4.3, the computer-aided design (CAD) model of the chamber, indicating the main geometric parameters utilised in the analytical model, is shown.

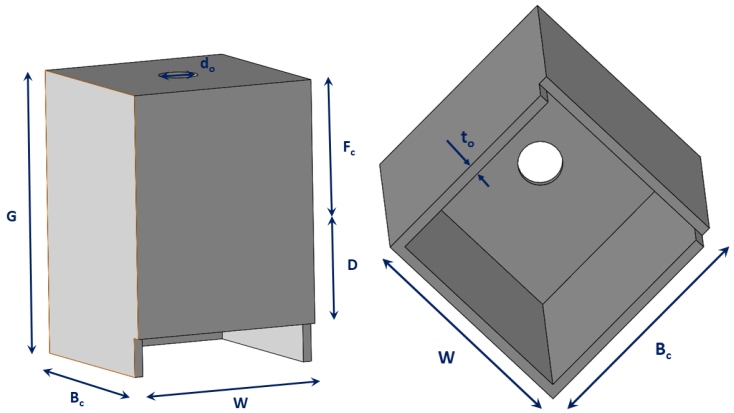


(a) Top view (b) Bottom view

Figure 4.3: Model of the OWC chamber, detached and fixed regarding the sea bottom, analysed with the rigid piston model.

The operating conditions of the caisson are determined by the wave conditions, the depth of the application site, and the atmospheric conditions of air, in accordance with the list below (Figure 4.3).

- ◇ Wavelength $\lambda$.
- ◇ Significant wave height $H_{m0}$.
- ◇ Wave energy period $\mathcal{T}_{m-1,0}$.
- ◇ Wave phase $\varphi_w$.
- ◇ Seawater depth $h$.
- ◇ Atmospheric pressure $p_{amb}$.

- ◇ Atmospheric temperature $\mathcal{T}_{amb}$.
- ◇ Air specific gas constant $\mathcal{R}$.
- ◇ Air kinematic viscosity $\mu$.

The present thesis achieves the sea wave states of the application sites investigated by considering regular wave conditions conveying the same energy of the related irregular wave motion. Therefore, the height $H$ of the regular wave is determined from the significant wave height $H_{m0}$ through Eq. (4.1), while the sea wave period $T$ coincides with the energy period $\mathcal{T}_{m-1,0}$ as expressed by Eq. (4.2). However, the analytical models are predisposed to operate even with irregular waves.

$$H = \frac{H_{m0}}{\sqrt{2}} \tag{4.1}$$

$$T = T_{m-1,0} \tag{4.2}$$

Subsequently, the angular frequency of the sea wave is determined by Eq. (4.3) based on the wave period.

$$\omega_w = \frac{2\pi}{T} \tag{4.3}$$

Within the linear wave theory, the water surface displacement of a sea wave $\eta_w$ can be written through Eq. (4.4) as a sinusoidal function.

$$\eta_w = \frac{H}{2}\cos(kx - \omega t) \tag{4.4}$$

where $H$ is the wave height, $k$ is the wavenumber, $x$ is the axial position, $\omega$ is the wave angular frequency, and $t$ is the time.

The wavenumber $\lambda$ is calculated by solving the dispersion relation of Eq. (4.5) for the specific seawater depth and wave period. The solution was achieved with the application of the Newton-Raphson scheme, and compared with the approach of Duane and Hunt [211] and the approach of Eckhart [212], providing average differences of 0.14% and 0.88%, respectively.

$$\omega^2 = kg \tanh(kh) \tag{4.5}$$

In this framework, the forces acting on the water column, considered as a rigid body, are listed below [126].

- ◇ The excitation force $f_{exc}$, due to the hydrodynamic pressure exerted by the incident wave on the bottom of the water column.
- ◇ The hydrostatic force $f_{hst}$, owed to the hydrostatic pressure.
- ◇ The radiating force $f_{rad}$, caused by the radiated wave produced by the pressure oscillation on the inner free surface, expressed in terms of the frequency-dependent added mass and the radiation damping coefficient.
- ◇ The force $f_{pto}$, due to the air pressure oscillation inside the air chamber, which is defined as a function of the free surface motion and the damping determined by the turbine.
- ◇ The inertial force $f_{ine}$, provoked by the heave motion of the water column.

The balance of the forces acting on the internal volume of water is obtained with Eq. (4.6) through the application in the vertical direction of Newton's second law (4.4).

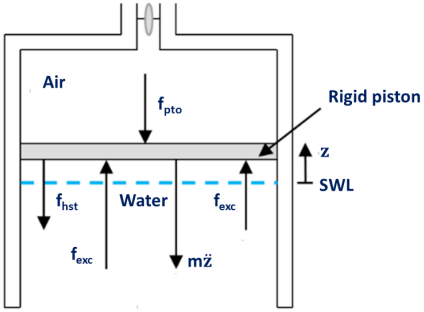


Figure 4.4: Scheme of the forces acting on the rigid piston modelling the hydrodynamics of the OWC chamber.

$$m_w \frac{d^2 z}{dt^2} = f_{exc} + f_{hst} + f_{rad} + f_{pto} \tag{4.6}$$

where $m_w$ is the mass of the water column and $z$ is the level of the free surface relative to the still water level (positive when above the SWL), which is a function of time.

The hydrostatic force $f_{hst}$ exerted by the hydrostatic pressure of the water column is provided by Eq. (4.7). This force varies between a minimum and a maximum of $\pm f_{hst}$ and it is equal to zero when the position of the rigid piston and the still water level are coincident.

$$f_{hst} = -\rho_w g A_c z \tag{4.7}$$

where $\rho_w$ is the seawater density, $g$ is the gravitational acceleration, and $A_c$ is the area of the horizontal cross-section of the chamber.

The force balance of Eq. (4.6) can be written as in Eq. (4.8) by substituting Eq. (4.7), expressing the hydrostatic force, into

it.

$$m_w \frac{d^2 z}{dt^2} + \rho_w g A_c z = f_{exc} + f_{rad} + f_{pto} \tag{4.8}$$

The radiating force $f_{rad}$ provoked by the radiated wave for the action of the pressure oscillation can be decomposed in two contributions: the added mass force $f_{add}$ and the radiating damping force $f_{rdp}$ given by the product of the radiating damping coefficient $\mathcal{B}$ and the velocity of the heave motion $\dot{z}$ of the water column. Therefore, the equation of motion of Eq. (4.6) may be written in the form of Eq. (4.9).

$$m_w \ddot{z} + \mathcal{B}\dot{z} + \mathcal{C}z = f_{exc} + f_{add} + f_{pto} \tag{4.9}$$

where $\mathcal{C}$ is the hydrostatic restoring coefficient.

The values of $m_w$, $\mathcal{B}$, and $\mathcal{C}$ can be calculated with the equations from Eq. (4.10) to Eq. (4.12), respectively, by considering the radiating damping coefficient as a function of the inertial properties of the system and the hydrostatic restoring coefficient [213, 202, 122].

$$m_w = \rho_w A_c (D + z) \tag{4.10}$$

$$\mathcal{C} = \rho_w g A_c \tag{4.11}$$

$$\mathcal{B} = 0.2\sqrt{\mathcal{C}(m_w + m_{add})} \tag{4.12}$$

The water column mass $m_w$ varies based on the water thermodynamic conditions, the free surface level of the inner seawater, and the geometry of the chamber in terms of area of the horizontal cross-section and draught $D$. The hydrostatic restor-

ing coefficient $\mathcal{C}$ depends upon the thermodynamic conditions of the seawater and the geometry of the caisson. The radiating damping coefficient $\mathcal{B}$ is a function of $\mathcal{C}$ and the inertia of the seawater, given by the sum of the water column mass and added mass $m_{add}$ in the vertical direction.

The excitation force $f_{exc}$ is exerted by the hydrodynamic pressure of the sea wave incident on the bottom of the water column. Under the assumption of the negligible contribution of its diffraction component, the excitation force is equal to the force of Froude-Krylov. The hypothesis is valid if the dimensions of the chamber are small compared to the wavelength, as the diffraction effects of the sea wave can be neglected [214]. The excitation force acting in the vertical direction is based on the simplification introduced by the linear wave theory, assuming that the displacement of the sea wave surface $\eta_w$ defines the position of the rigid plate modelling the motion of the water level inside the caisson [35]. Within this approach, the dynamic pressure of the seawater $p_w$ decreases with the depth along the vertical direction, as expressed through Eq. (4.13).

$$p_w = \eta_w \rho_w g \frac{\cosh(k(h+z))}{\cosh(kh)} \tag{4.13}$$

The Froude-Krylov force $f_{FK}$ and the wave excitation force $f_{exc}$ acting on a seawater level equivalent to the front wall draught $D$ of the chamber may be written as in Eq. (4.14) under the assumptions applied [215].

$$f_{FK} = f_{exc} = \eta_w A_c \rho_w g \frac{\cosh(k(h-D))}{\cosh(kh)} \tag{4.14}$$

The added mass force $f_{add}$ exerted on the water column by the added mass is determined through Eq. (4.15) as a function

of the acceleration $\dot{v}_{z,w} - \ddot{z}$ of the water particles relative to the water column in the vertical direction [126, 33, 24].

$$f_{add} = m_{add}(\dot{v}_{z,w} - \ddot{z}) \tag{4.15}$$

According to the wave linear theory, the velocity and the acceleration in the vertical direction of the water particles are expressed by Eq. (4.16) and (4.17), respectively, as functions of the water position inside the chamber [202, 122].

$$v_{z,w} = -\omega_w \frac{H}{2} \frac{\sinh(k(h+z))}{\sinh(kh)} \sin(\omega_w + \varphi_w) \tag{4.16}$$

$$\dot{v}_{z,w} = -\omega_w^2 \frac{H}{2} \frac{\sinh(k(h+z))}{\sinh(kh)} \cos(\omega_w + \varphi_w) \tag{4.17}$$

The force $f_{pto}$ determined by the compression and expansion of the air inside the OWC chamber can be calculated with Eq. (4.18). This force depends upon the velocity of the free surface level of the water column and the characteristics of the power take-off.

$$f_{pto} = -A_c p_{c,r} \tag{4.18}$$

where $p_{c,r}$ is the instantaneous value of the difference in air pressure between the chamber and the atmosphere.

Finally, the equation of motion of the water column expressed by Eq. (4.19) is achieved [33].

$$(m_w + m_{add})\ddot{z} + \mathcal{B}\dot{z} + \rho_w g A_c z = \\ = A_c \rho_w g \eta_w \frac{\cosh(k(h-D)}{\cosh(kh))} + m_{add}\dot{v}_{z,w} - A_c p_{c,r} \tag{4.19}$$

The determination of the equation of motion of the heaving rigid piston leads to the solution of the hydrodynamics of the OWC chamber.

The thermodynamics and aerodynamics of the caisson have to be solved in addition to the hydrodynamics to determine the inlet conditions of the air delivered by the primary converter for the operation of the secondary converter. For this purpose, the mutual interactions between the oscillating water column and the above volume of air trapped inside the structure are considered.

The air volume inside the caisson in unperturbed conditions has to be sufficiently large to prevent the entry of seawater in the duct of the air turbine for the most critical wave conditions of the application site of the system. For example, the air volume ratio to the area of the horizontal cross-section of the chamber typically ranges from 3 to 8 m for systems with a fixed structure, depending on the tidal oscillations. Slightly increasing the value of this ratio does not cause significant reductions in the efficiency of the primary power transformation, while a marked enhancement determines a substantial decrease of the air pressure gradients, and the chamber becomes not capable of converting wave power. The increase of the air volume corresponds to the rise of the compressibility effects inside the caisson, which can be relevant for full-size devices [1].

Since the air volume is subject to an oscillating compression by the action of the water column, the density of the air varies based on the level of the water free surface inside the caisson.

The hypothesis applied for the solution of the thermodynamics of the chamber is the presence of adiabatic and isentropic transformations. Regarding the first assumption, the air temperature variations inside the caisson are small, and the duration of each flow phase is typically in the interval between 1 and 7 s, determining very limited heat exchanges with the seawater and the walls, compared to the energy flux in the air turbine [1]. Concerning the second assumption, the entropy variations of the airflow inside the chamber are negligible relative to the entropy changes owing to the viscous losses of the turbine. Thus, the entropy variations are related to the efficiency of the secondary converter [23, 1].

Therefore, in the model of the thermodynamics of the OWC chamber developed, the processes are considered adiabatic and isentropic. The control volume for the transformations of the air inside the caisson is represented in the scheme of Figure 4.5.

The hypothesis of isentropic processes implies that, from the general equation of state of perfect gasses stated in Eq. (4.20), the formulation of Eq. (4.21) can be obtained for the open system of the air inside the caisson.

$$p_c = \rho_c \mathcal{R} \mathcal{T}_c \tag{4.20}$$

$$\frac{p_c}{\rho_c^{\gamma_c}} = constant \tag{4.21}$$

where $p_c$, $\rho_c$, $\mathcal{R}$, $\mathcal{T}_c$, and $\gamma_c$ are the static pressure, density, temperature, gas constant, and specific heat capacity ratio of the air

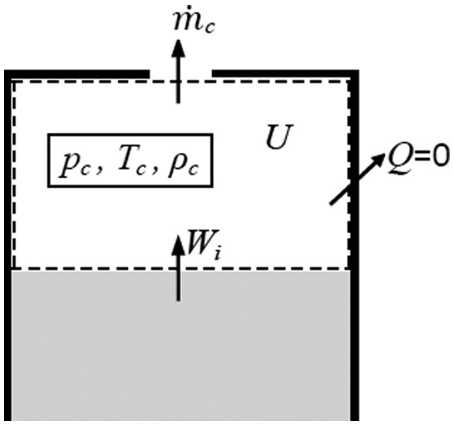


Figure 4.5: Scheme of the OWC chamber with dashed line representing the control volume for the analysis of the air thermodynamics [23].

inside the caisson, respectively.

The content of Eq. (4.21) can be reformulated by considering the air pressure in the caisson $p_c$ as the sum of the pressure in unperturbed conditions $p_{c,0}$ and the corresponding variations $p_{c,r}$ [216, 217, 218], as expressed by Eq. (4.22).

$$\frac{p_{c,0} + p_{c,r}}{\rho_c^{\gamma}} = \frac{p_{c,0}}{\rho_{c,0}^{\gamma}} \tag{4.22}$$

Subsequently, from Eq. (4.22) the formula of Eq. (4.23) is obtained [23].

$$\rho_c = \rho_{c,0}\left(1 + \frac{p_{c,r}}{p_{c,0}}\right)^{\frac{1}{\gamma}} \tag{4.23}$$

Under the hypothesis of significantly lower ratio of pressure variations $p_{c,r}$ to unperturbed pressure $p_{c,0}$, the linear formulation of the air density is achieved in Eq. (4.24).

$$\rho_c = \rho_{c,0}\left(1 + \frac{p_{c,r}}{\gamma p_{c,0}}\right) \tag{4.24}$$

Figure 4.6 indicates that the linearised equation of the air pressure is in excellent agreement with Eq. (4.24) for the interval of the pressure oscillations that may occur in an OWC chamber. Indeed, there is a difference lower than 0.2% corresponding to a pressure of 15000 Pa, which is much higher than the operating typically reached in this converter [23].

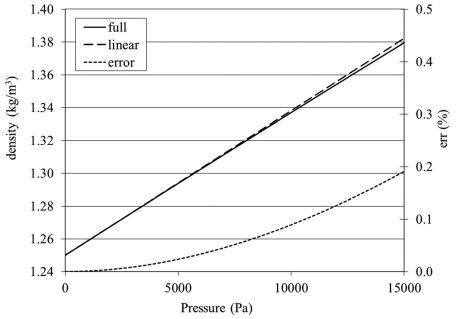


Figure 4.6: Air density variation inside an OWC caisson as a function of the air pressure [23].

In analogy, the air temperature varies as a function of the air pressure inside the chamber, as expressed by Eq. (4.25).

$$\mathcal{T}_c p_c^{\frac{1-\gamma}{\gamma}} = constant \tag{4.25}$$

Consequently, equations from Eq.(4.26) to (4.28) can be obtained lo linearise the formulation of the air temperature.

$$\mathcal{T}_c = \mathcal{T}_{c,0}\left(1 + \frac{p_{c,r}}{p_{c,0}}\right)^{\frac{\gamma-1}{\gamma}} \tag{4.26}$$

$$\mathcal{T}_c = \mathcal{T}_{c,0}\left(1 + \frac{\gamma - 1}{\gamma}\frac{p_{c,r}}{p_{c,0}}\right) \tag{4.27}$$

$$\mathcal{T}_c = \mathcal{T}_{c,0} + \mathcal{T}_{c,0}\frac{\gamma - 1}{\gamma}\frac{p_{c,r}}{p_{c,0}} \tag{4.28}$$

Therefore, the linear relation of the temperature variation of the air inner to the chamber is given by Eq. (4.29).

$$\mathcal{T}_{c,r} = \mathcal{T}_{c,0}\frac{\gamma - 1}{\gamma}\frac{p_{c,r}}{p_{c,0}} \tag{4.29}$$

Similarly to the case of the air density, Figure 4.7 denotes an excellent agreement of the non-linear and linearised formulations of the air temperature, with a maximum difference lower than 0.2% for the air pressure of 15000 Pa [23].

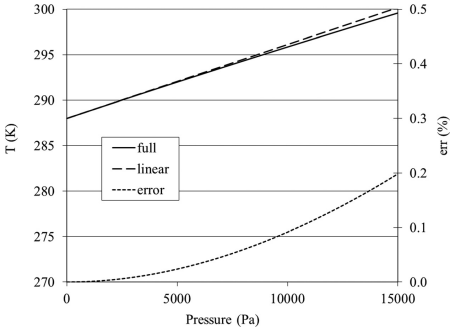


Figure 4.7: Air temperature variation inside an OWC caisson as a function of the air pressure [23].

The linear formulations of the air density and temperature provide suitable approximations and, thus, are applied in the developed model.

The time differential of the air pressure of Eq. (4.24) is expressed in Eq. (4.30).

$$\frac{d\rho_c}{dt} = \frac{1}{\gamma}\frac{\rho_{c,0}}{p_{c,0}}\frac{dp_{c,r}}{dt} \tag{4.30}$$

The sound speed of the air inside the chamber $s_c$ is given by Eq. (4.31) as a function of the specific heat capacity ratio, gas constant, and air temperature.

$$s_c = \sqrt{\gamma \mathcal{R} \mathcal{T}_{c,0}} \tag{4.31}$$

By combining Eqs. (4.30) and (4.31), the formula of Eq. (4.32) defining the instantaneous variation of the air density inside the chamber is achieved.

$$\frac{d\rho_c}{dt} = \frac{1}{s_c^2}\frac{dp_{c,r}}{dt} \tag{4.32}$$

Since the relative pressure of the air in the caisson $p_{c,r}$ is given by the difference between the chamber air pressure $p_c$ and the atmosphere air pressure $p_{amb}$, the equivalence of the derivatives of Eq. (4.33) can be written [202].

$$\frac{dp_c}{dt} = \frac{dp_{c,r}}{dt} \tag{4.33}$$

The mass airflow rate $\dot{m}_c$ provided by the chamber to the turbine is expressed by Eq. (4.34), where the sign is considered positive if the air exits the chamber during the outflow phase and negative vice versa during the inflow phase [35, 126, 33, 24].

$$\dot{m}_c = \frac{dm_c}{dt} = -\frac{d(\rho_c V_c)}{dt} = -\frac{d\rho_c}{dt}V_c + \rho_c\frac{dV_c}{dt} \tag{4.34}$$

The air volume in the caisson $V_c$ is given by Eq. (4.35) as a function of the chamber volume in unperturbed conditions $V_{c,0}$ and the velocity of the free surface of the water column.

$$V_c = V_{c,0} - A_c z = A_c(\hbar_{c,0} - z) = A_c \hbar_c \tag{4.35}$$

where $\hbar_c$ and $\hbar_{c,0}$ are the instant and unperturbed values of the height of the air domain inside the chamber, respectively.

The volume airflow rate $\dot{q}_c$ is given by the time derivative of the air volume of Eq. (4.36).

$$\dot{q}_c = \frac{dV_c}{dt} = A_c \frac{dz}{dt} = A_c \dot{z} \tag{4.36}$$

Considering the air compressibility expressed by Eq. (4.32), the final formulation of the mass airflow rate of Eq. (4.37) is achieved [35].

$$\dot{m}_c = \rho_c A_c \dot{z} - V_c \frac{1}{s_c^2} \frac{dp_{c,r}}{dt} = \rho_c A_c \dot{z} - (V_{c,0} + A_c z) \frac{1}{s_c^2} \frac{dp_{c,r}}{dt} \tag{4.37}$$

Therefore, the derivative of the difference in air pressure between the inside and outside of the OWC chamber is obtained with Eq. (4.38).

$$\frac{dp_{c,r}}{dt} = \frac{s_c^2 \rho_c}{V_c} A_c \dot{z} - \frac{s_c^2}{V_c} \dot{m}_c \tag{4.38}$$

Based on Eq. (4.31) and the assumption of linear variation of the air density with the air pressure, Eq. (4.38) can be reformulated as in Eq. (4.39).

$$\frac{dp_{c,r}}{dt} = \frac{\gamma p_c}{V_c} A_c \dot{z} - \frac{s_c^2}{V_c} \dot{m}_c \tag{4.39}$$

Subsequently, considering the two terms that constitute the formula of the chamber air pressure, Eq. (4.40) is achieved.

$$\frac{dp_{c,r}}{dt} = \frac{\gamma(p_{c,r} + p_{amb})}{V_c} A_c \dot{z} - \frac{s_c^2}{V_c} \dot{m}_c \tag{4.40}$$

Finally, the combination of Eqs. (4.40) and (4.35) leads to Eq. (4.41), which defines the pressure variation of the air inside the caisson. This ordinary differential equation provides the solution of the thermodynamics and aerodynamics of the oscillating water column chamber.

$$\dot{p}_{c,r} = \frac{dp_{c,r}}{dt} = \frac{\gamma(p_{c,r} + p_{amb})}{\hbar_c} \dot{z} - \frac{s_c^2}{A_c \hbar_c} \dot{m}_c \tag{4.41}$$

Under the assumption of small values of the volume $A_c z$ regarding the volume $V_{c,0}$, a simplified formulation of the chamber thermodynamics and aerodynamics may be obtained [35, 126, 33, 24]. In this case, the contribution of the former term becomes negligible, thus Eq. (4.37) can be simplified to Eq. (4.42).

$$\dot{m}_c = \rho_c A_c \dot{z} - V_{c,0} \frac{1}{s_c^2} \frac{dp_{c,r}}{dt} \tag{4.42}$$

From Eq. (4.42), the simplified version of the pressure variation of the air inside the chamber is defined by Eq. (4.43).

$$\dot{p}_{c,r} = \frac{dp_{c,r}}{dt} = \frac{\gamma(p_{c,r} + p_{amb})}{V_{c,0}} A_c \dot{z} - \frac{s_c^2}{V_{c,0}} \dot{m}_c \tag{4.43}$$

The formula of the air pressure variation of Eq. (4.41) can be achieved even with an alternative approach based on the application of the ideal gas law of Eq. (4.44) to the air inside the chamber [202, 122].

$$p_c V_c = m_c \mathcal{R} \mathcal{T}_c \tag{4.44}$$

The differential of Eq. (4.44) with respect to the time gives

Eq. (4.45).

$$p_c \frac{dV_c}{dt} + V_c \frac{dp_c}{dt} = \mathcal{R}\mathcal{T}_c \frac{dm_c}{dt} + m_c \mathcal{R} \frac{d\mathcal{T}_c}{dt} \tag{4.45}$$

Subsequently, dividing Eq. (4.45) by $V_c$ and utilising Eq. (4.44), the formula of Eq. (4.46) is obtained.

$$\frac{p_c}{V_c}\frac{dV_c}{dt} + \frac{dp_c}{dt} = \frac{\mathcal{R}\mathcal{T}_c}{V_c}\frac{dm_c}{dt} + \frac{p_c}{\mathcal{T}_c}\frac{d\mathcal{T}_c}{dt} \tag{4.46}$$

Since the compression and expansion of the air inside the caisson may be modelled as isentropic transformations, Eq. (4.47) can be written.

$$p_c V_c^{\gamma} = constant \tag{4.47}$$

By combining Eqs. (4.44) and (4.47), the relation of Eq. (4.48) is achieved.

$$p_c^{1-\gamma} \mathcal{T}_c^{\gamma} = constant \tag{4.48}$$

The application of the logarithmic differential to Eq.(4.48) provides the equations from Eq. (4.49) to Eq. (4.52).

$$p_c^{1-\gamma} \frac{d(\mathcal{T}_c^{\gamma})}{dt} + \mathcal{T}_c^{\gamma} \frac{d(p_c^{1-\gamma})}{dt} = 0 \tag{4.49}$$

$$\frac{1}{\mathcal{T}_c^{\gamma}} \frac{d(\mathcal{T}_c^{\gamma})}{dt} + \frac{1}{p_c^{1-\gamma}} \frac{d(p_c^{1-\gamma})}{dt} = 0 \tag{4.50}$$

$$\frac{\gamma}{\mathcal{T}_c}\frac{d\mathcal{T}_c}{dt} + \frac{1-\gamma}{p_c}\frac{dp_c}{dt} = 0 \tag{4.51}$$

$$\frac{p_c}{\mathcal{T}_c}\frac{d\mathcal{T}_c}{dt} = \frac{\gamma - 1}{\gamma}\frac{dp_c}{dt} \tag{4.52}$$

Substituting Eq.(4.52) into Eq. (4.46) gives Eq. (4.53).

$$\frac{p_c}{V_c}\frac{dV_c}{dt} + \frac{dp_c}{dt} = \frac{\gamma - 1}{\gamma}\frac{dp_c}{dt} + \frac{\mathcal{R}\mathcal{I}_c}{V_c}\frac{dm_c}{dt} \tag{4.53}$$

Then, Eq. (4.53) is rearranged to obtain Eq. (4.54).

$$\gamma\frac{p_c}{V_c}\frac{dV_c}{dt} + \frac{dp_c}{dt} = \frac{\gamma\mathcal{R}\mathcal{I}_c}{V_c}\frac{dm_c}{dt} \tag{4.54}$$

Combining Eq. (4.54) with the speed of sound expressed by Eq. (4.31), Eq. (4.55) is formulated.

$$\gamma\frac{p_c}{V_c}\frac{dV_c}{dt} + \frac{dp_c}{dt} = \frac{s_c^2}{V_c}\frac{dm_c}{dt} \tag{4.55}$$

In analogy with the other procedure described above, the mass flow rate of Eq. (4.34) is assumed positive when the air mass inside the chamber decreases during the exhalation phase. Thus, considering the equivalence of Eq. (4.33) regarding the pressure derivatives and the volume of the chamber air expressed by Eq. (4.35), the ordinary differential equation defining the air pressure variation inside the caisson is once again achieved. The formula is equal to Eq. (4.43) under the hypothesis of low ratio between the volume $A_c z$ and the volume $V_{c,0}$ as usually occurs.

The joint solution of Eq. (4.19) regulating the hydrodynamics of the OWC chamber with Eq. (4.41) or (4.43) expressing its thermodynamics and aerodynamics, allows the calculation of the flow conditions at the outlet of the caisson. Therefore, the system of ordinary differential equations with two variables of Eqs. (4.56) is composed by an equation of the second order and one of the first order [209, 126, 33].

$$\begin{cases} m_w\ddot{z} + \mathcal{B}\dot{z} + \rho_w g A_c z = A_c \rho_w g \eta_w \dfrac{\cosh(k(h-D))}{\cosh(kh))} \\ \qquad\qquad + m_{add}(\dot{v}_{z,w} - \ddot{z}) - A_c p_{c,r} \\ \dot{p}_{c,r} = \dfrac{dp_{c,r}}{dt} = -\dfrac{s_c^2}{V_{c,0}}\dot{m}_c + \dfrac{\gamma(p_{c,r} + p_{amb})}{V_{c,0}} A_c \dot{z} \end{cases} \tag{4.56}$$

The solution of the system of equations requires the definition of the boundary values listed below and the definition of the relation between the mass airflow rate $\dot{m}_c$ crossing the wave energy converter and the pressure difference $p_{c,r}$ delivered by the chamber for the operation of the air turbine.

- $z(t=0) = 0$.
- $\dot{z}(t=0) = 0$.
- $p_c(t=0) = p_{amb}$.

The relation connecting the airflow rate and the pressure variation is obtained through the imposition of the results of the turbomachine aerodynamics when the chamber model is used in stand-alone mode, while it is achieved through the iterative solution of the models of the single converters when the wave-to-wire modelling is utilised. In the latter case, the solution of the system of ordinary differential equations is performed jointly with that of the equations ruling the aerodynamics of the air turbine [209, 126], and, eventually, even of the dynamics of the electric generator [33, 24]. All the analytical utilise *MATLAB* and *Simulink* for performing calculations.

Furthermore, the rigid piston model is suitable for using calibrated porous media or orifices to mimic the secondary converter

through the imposition of a linear or a quadratic ideal law of pressure variation as a function of the volume airflow rate, respectively [202, 219, 36, 1, 122]. This simplification of the modelling may be considered reasonable for prototypes functioning in laboratory conditions or systems operating in real sea wave conditions at scales at least of 1:4 regarding the real size [1].

During the early stages of the development of the rigid piston model, analysis with calibrated openings were carried out to compare the results predicted by the analytical model of the chamber with numerical and experimental outcomes previously obtained by the *LABIMA*.

The function of the mass airflow rate versus the pressure drop through a calibrated porous medium is given by Eq. (4.57), expressing the law of Darcy [220].

$$\dot{m}_c = \frac{-\kappa \pi r_o^2}{\rho_c \mu_c} \frac{dp_c}{d\bar{t}_o} \tag{4.57}$$

where $r_o$, $\kappa$, and $\bar{t}_o$ are the radius, permeability, and thickness of the porous medium, respectively.

For calibrated orifices, the mass airflow rate is expressed by Eq. (4.58) as a function of the pressure variation [35].

$$\dot{m}_c = \mathcal{D}_o \pi r_o^2 \sqrt{2 \rho_c p_c} \tag{4.58}$$

where $\mathcal{D}_o$ is the discharge coefficient of the orifice.

A different approach to the one described above, relying on the solution of the air turbine aerodynamics, and applied in the present thesis, is typically utilised in the literature for obtaining a simplified analysis of an OWC system. This approach is based on using the damping coefficient $K$ to simulate the turbine impact

on the airflow made available by the chamber.

The damping coefficient is a function of the system flow coefficient $\Phi$ and the system pressure coefficient $\Psi$, defined by Eqs. (4.59) and (4.60).

$$\Phi = \frac{\dot{q}_a}{\Omega d_{tip}^3} \tag{4.59}$$

$$\Psi = \frac{p_{ta,in} - p_{a,out}}{\rho_{a,1} \Omega^2 d_{tip}^2} \tag{4.60}$$

where $\dot{q}_a$ is the airflow rate across the turbine, $\Omega$ is the angular velocity of the turbine rotor, $d_{tip}$ is the turbine diameter, $p_{ta,in}$ is the air total pressure at the turbine inlet, and $p_{a,out}$ is the air static pressure at the turbine outlet.

The continuity equation ensures the conservation of the airflow rate, thus $\dot{q}_a$ is equivalent to $\dot{q}_c$. The pressure drop across the turbine $p_{ta,in} - p_{a,out}$ depends upon the relative pressure between the chamber and the atmosphere $p_c$. The two values are ideally equivalent in the absence of pressure losses along the duct connecting the chamber with the environment.

The relation connecting the damping coefficient with the two non-dimensional parameters $\Phi$ and $\Psi$ is ideally expressed by Eqs. (4.61) and (4.62) for a Wells turbine and an impulse turbine, respectively. The relation can be approximated to linearity for the former, while for the latter, it can be considered nearly quadratic.

$$\Phi = K\Psi \tag{4.61}$$

$$\Phi = K\Psi^{\frac{1}{2}} \tag{4.62}$$

Therefore procedures for determining the mass airflow rate

of Wells and impulse turbines different from the direct solution of the turbomachine aerodynamics may be applied.

In particular, for a Wells turbine, the mass airflow rate may be calculated combining Eqs. (4.59), (4.60), and (4.61), obtaining Eqs. (4.63) and (4.64).

$$\frac{\dot{q}_a}{\Omega d_{tip}^3} = K \frac{p_{ta,in} - p_{a,out}}{\rho_{a,1} \Omega^2 d_{tip}^2} \tag{4.63}$$

$$\dot{m}_a = \frac{K d_{tip} (p_{ta,in} - p_{a,out})}{\Omega} \tag{4.64}$$

For the impulse turbine, the mass airflow rate can be computed combining Eqs. (4.59), (4.60), and (4.61), achieving Eqs. (4.65) and (4.66).

$$\frac{\dot{q}_a^2}{\Omega^2 d_{tip}^6} = K \frac{p_{ta,in} - p_{a,out}}{\rho_{a,1} \Omega^2 d_{tip}^2} \tag{4.65}$$

$$\dot{m}_a = \sqrt{K \rho_a d_{tip}^4 (p_{ta,in} - p_{a,out})} \tag{4.66}$$

In some cases the linearisation of the non-linear phenomena is required for applying this approach. The linearisation procedure consists in converting the non-linear representation of forces into a linear approximation, considering the real system conditions.

A source of non-linear effects is the drag force induced by viscous flow effects in the duct of oscillating water column systems due to effects like the friction on walls and the vortex shedding. The other source of non-linearities is the damping effect of the turbine.

The techniques proposed in 2021 by Brooklyn et al. to linearise the drag force and the damping effect can be applied. Different approaches are available for determining the performance of wave energy converters under regular or irregular wave

conditions.

## 4.2 Wells turbine analytical models

The analytical models for predicting the operation of Wells turbines are based on the blade element momentum (BEM) theory [21, 50, 221]. The turbine cascades are modelled as sets of blades, and each single blade is assumed to be comprised of a finite number of airfoils stacked in the radial direction (Figure 4.8). Each couple of adjacent airfoils defines an annular sector on the blade representing a single blade element, with its distinctive geometry and subject to specific flow conditions [126, 24, 31].

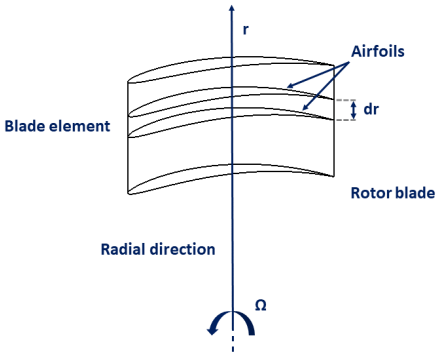


Figure 4.8: Scheme of the discretisation of a turbine blade applied by a BEM model.

The two main hypotheses of this method are the absence of aerodynamic interactions among the different blade elements comprising a blade along its span and the use of airfoil lift and drag coefficients for determining the forces acting on each blade element. The first hypothesis implies an adequate discretisation of the computational domain achievable by setting a sufficient

number of blade elements along the blade span; the second hypothesis makes the use of accurate lift and drag coefficients a key aspect of the modelling.

The two-dimensional cascade theory or the actuator disc theory may be applied to assess the flow field impacting the blade elements. The former assumes that the radial velocities are negligible upstream and downstream of the rotor and that for each annular region, the fluid dynamics is determined by the two-dimensional potential flow about a blade cascade of negligible thickness. The latter assumes that the radial velocity variation arises not only across the blade but even in the upstream and downstream regions, resulting in the variation of axial and tangential velocity along the axial and radial directions [50].

### 4.2.1 Two-dimensional cascade model of monoplane isolated Wells turbines

The first model developed for the analysis of a monoplane isolated Wells turbine is based on the two-dimensional cascade theory. The flow is steady, incompressible, irrotational, and axisymmetric, and the variations in the radial velocity may occur only across the blades. The hypothesis of null radial velocity is a condition for the validity of the two-dimensional analysis. It is satisfied if the incompressible and irrotational flow has a constant circulation around the blades. The radial equilibrium theory is applied both upstream and downstream of the rotor.

The isolated monoplane is the simplest configuration of a Wells turbine. It generally consists of a cascade of identical untwisted blades staggered at 90 degrees concerning the incoming

flow and equispaced in the circumferential direction (Figure 4.9).

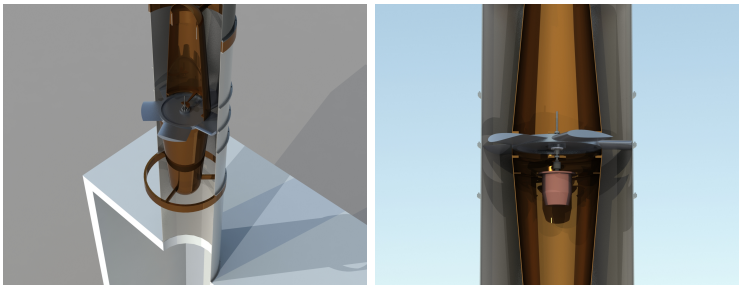

(a) Isometric view (b) Front view

Figure 4.9: Rendering of the **(a)** isometric and **(b)** front sections of the CAD model created for the system with the monoplane isolated Wells turbine.

The blade airfoils for this application are usually symmetric four-digit NACA00XX profiles with constant chord length, stacked in the radial direction (Figure 4.10).

Figure 4.10: Scheme of the blade-to-blade section of the cascade of a monoplane isolated Wells turbine.

A blade element code for the assessment of the fluid dynamics of an isolated monoplane Wells turbine was developed with *MATLAB* [222, 126, 24, 31]. The code can operate in standalone mode or integrated into a wave-to-wire model generated with *MATLAB* and *Simulink*.

The analytical model starts with the definition of the geometry and operating conditions, represented by the parameters listed below.

- ◇ Airfoil profile.
- ◇ Turbine tip radius $r_{tip}$.
- ◇ Rotor tip clearance gap $t$.
- ◇ Hub-to-tip ratio.
- ◇ Aspect ratio $AR$.
- ◇ Rotor solidity $\sigma$.
- ◇ Rotor inertia $J$.
- ◇ Rotor angular velocity $\Omega$.
- ◇ Turbine duct upstream length $\ell_{duct,up}$.
- ◇ Turbine duct downstream length $\ell_{duct,do}$.

Figure 4.11 shows a scheme of the straight annular turbine duct, including one single blade passage. The turbine duct length is given by the sum of the length of the duct upstream and downstream of the blade rotor, $\ell_{duct,up}$ and $\ell_{duct,up}$, respectively; the rotor is generally positioned at the centre of the turbine duct.

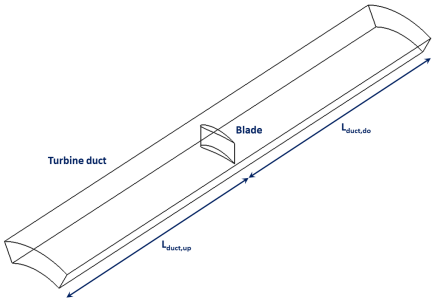


Figure 4.11: Scheme of the annular duct including one blade of the Wells turbine.

The properties of air are calculated based on the parameters reported in the following list.

- ◇ Atmospheric pressure $p_{amb}$.
- ◇ Atmospheric temperature $\mathcal{T}_{amb}$.
- ◇ Air specific gas constant $\mathcal{R}$.
- ◇ Air heat capacity ratio $\gamma$.
- ◇ Air kinematic viscosity $\mu$.

Subsequently, the airflow conditions at the inlet section far upstream of the rotor are imposed. Since the model is able to operate both individually and coupled with the model of the chamber, the inlet conditions can be assigned based on literature data or the outcomes of previous calculations, in the former case, or can be part of the iterative cycle connecting the models of the primary and secondary converters, in the latter case. In particular, in all these cases, the static pressure at the rotor inlet is not exactly known in advance, as it depends upon the pressure drop determined by the turbine (Section 4.1.1). Therefore, the pressure is initialised with the value obtained from literature data

or previous calculations or with the equation of state for ideal gases of Eq. (4.67).

$$p_{a1} = \rho_{a,amb} \mathcal{R}_a T_{a,amb} \tag{4.67}$$

where $p_a$, $\rho_a$, $T_a$, and $\mathcal{R}_a$ are the static pressure, density, temperature and gas constant of air, respectively, and subscripts *1* and *amb* refer to the turbine inlet section and the atmospheric conditions outside the OWC system, respectively.

An iterative procedure based on the two-dimensional cascade theory is applied to calculate the variables needed to determine the pressure difference across the rotor and, thus, the static pressure at the domain inlet. The resulting value is iteratively utilised in the complete computation of the analytical model to update the static pressure $p_{a1}$ starting from Eq. (4.68). This equation determines the air density at the turbine inlet $\rho_a$ under the hypothesis of negligible air temperature variation across the turbine duct.

$$\rho_a = \frac{p_{a1}}{\mathcal{R}_a T_{a,amb}} \tag{4.68}$$

For the momentum balance in the radial direction, in a system of cylindrical coordinates ($x$, $\theta$, $r$), the radial equilibrium implies through of Eq. (4.69) that the pressure force in the radial direction equals the centripetal acceleration.

$$\frac{1}{\rho_a} \frac{\partial p_a}{\partial r} = \frac{v_\theta^2}{r} \tag{4.69}$$

where $r$ is the turbine radius and $v_\theta$ is the tangential component of the absolute velocity.

The radial equilibrium of Eq. (4.69) is valid both upstream

and downstream of the cascade, where the streamlines define concentric cylinders. Radial displacements can occur only within the cascade [221].

The following step of a BEM analysis is determining the conditions of the flow impacting the blade elements. Each element has its distinctive geometry, moves with an assigned specific tangential speed, and is subject to different flow conditions. For these reasons, a sensitivity analysis was carried out to evaluate the number of sections needed for the domain discretisation. It was found that 51 sections are the optimal compromise between accuracy and computational time. Since the number of blade elements is reduced in size by one regarding the number of sections, as visible in Figure 4.8, 50 blade elements were set along the blade span to discretise the domain.

The incoming flow for a monoplane isolated Wells turbine is bounded by an inner and an outer coaxial cylindrical wall. The flow is axial and uniform for both the inflow and outflow phases. Due to the typical operating conditions of this turbomachine typology, the Kutta condition of finite velocity without shocks is imposed at either the blade leading edge and trailing edge [223, 224]. The inlet and outlet velocity triangles of each blade element $i$ of Figure 4.12 are determined by the procedure described below for the two flow phases.

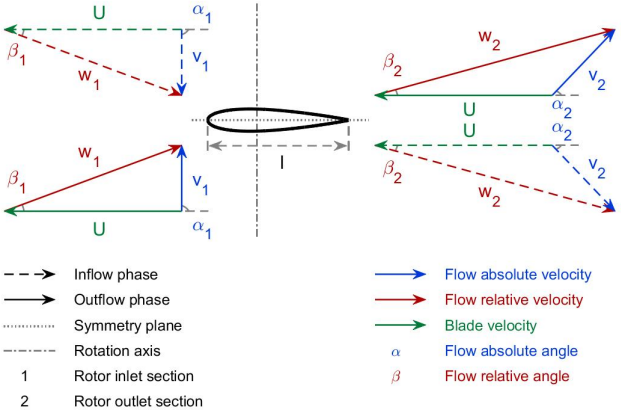


Figure 4.12: Scheme of the blade-to-blade section and velocity triangles of an isolated monoplane Wells turbine with NACA0015 profile [24].

The area of the turbine annulus $A_{ann}$ is defined based on the hub and tip radius through Eq. (4.70).

$$A_{ann} = \pi(r_{tip}^2 - r_{hub}^2) \tag{4.70}$$

The axial component of the inlet absolute velocity is imposed by the continuity equation of Eq. (4.71), and its circumferential component is null, as stated in Eq. (4.72).

$$v_{x1,i} = \frac{\dot{m}_{a1,i}}{\rho_{a,i} A_{ann,i}} = \frac{\dot{q}_{a1,i}}{A_{ann,i}} \tag{4.71}$$

$$v_{\theta 1,i} = 0 \tag{4.72}$$

where $v_{x1}$ and $v_{\theta 1}$ are the axial and tangential components of the absolute velocity at the rotor inlet, respectively, $\dot{m}_{a1}$ is the mass flow rate, $\dot{q}_{a1}$ is the volume flow rate, and subscript $i$ refers to the generic blade element.

Under the assumptions of inviscid and irrotational flow, the total pressure and flow rotation can be determined with Eqs. (4.73) and (4.74).

$$p_{ta1,i} = p_{a1,i} + \frac{\rho_{a,i}}{2}(v_{x1,i}^2 + v_{\theta 1,i}^2) \tag{4.73}$$

$$\mathcal{O}_{\theta 1,i} = \frac{\partial v_{r1,i}}{\partial x} - \frac{\partial v_{x1,i}}{\partial r} \tag{4.74}$$

where $p_t$ is the total pressure, $\mathcal{O}$ is the flow rotation, and $v_r$ is the radial component of the absolute velocity.

Since the circumferential flow velocity is null and the static pressure distribution along the span is constant for Eq. (4.69), the total inlet pressure is constant in the radial direction.

The flow circulation $\Gamma$ at the rotor inlet can be computed with Eq. (4.75), and it is null for monoplane isolated Wells turbines.

$$\Gamma_{1,i} = 2\pi r_i v_{\theta 1,i} \tag{4.75}$$

Furthermore, when radial equilibrium is connected with the hypothesis of constant inlet axial velocity in the flow field, the variation of flow circulation is null along blade span, and blades shed no vorticity in the axial direction.

Through Eqs. (4.71) and (4.72), and equations from Eq. (4.76) to Eq. (4.82) the velocity triangle at the rotor inlet can be determined. The flow coefficient $\phi$ is defined with Eq. (4.83) as the ratio of the flow axial velocity to the blade speed.

$$U_i = \Omega r_i \tag{4.76}$$

$$v_{1,i} = \sqrt{v_{x1,i}^2 + v_{\theta 1,i}^2} \tag{4.77}$$

$$w_{x1,i} = v_{x1,i} \tag{4.78}$$

$$w_{\theta 1,i} = v_{\theta 1,i} - U_i \tag{4.79}$$

$$w_{1,i} = \sqrt{w_{x1,i}^2 + w_{\theta 1,i}^2} \tag{4.80}$$

$$\alpha_{1,i} = \frac{\pi}{2} \tag{4.81}$$

$$\beta_{1,i} = \frac{w_{x1,i}}{w_{\theta 1,i}} \tag{4.82}$$

$$\phi_{1,i} = \frac{v_{x1,i}}{U_i} \tag{4.83}$$

where $U$ is the blade velocity, $v$ is the absolute velocity, $w$ is the relative velocity, $w_x$ and $w_\theta$ are its axial and tangential components, respectively, $\alpha$ is the absolute flow angle, and $\beta$ is the relative flow angle.

The flow crossing the turbine duct impacts the airfoils of the rotor blades with a specific angle of attack depending on the flow field and the airfoil geometry. An angle of attack different from zero determines a variation of the tangential component of the flow velocity between the inlet and outlet of the rotor. The difference in tangential velocity is responsible for the work exerted by the flow and the rotor blades [126, 24, 31]. Following the traditional practice in aerodynamics, the work may be expressed in terms of the composition of lift and drag forces through the

use of the lift coefficient $C_L$ and the drag coefficient $C_D$. These aerodynamic coefficients depend upon the airfoil shape and are functions of the angle of attack, the Reynolds number and the Mach number. The lift force $f_L$ is directed orthogonally to the direction of the relative flow velocity at the blade inlet $w_1$, while the drag force $f_D$ is coincident with this direction (Figure 4.13).

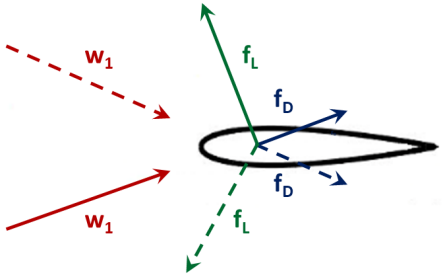


Figure 4.13: Scheme of the lift and drag forces acting on a NACA0015 airfoil.

A wide variety of numerical and experimental data of lift and drag coefficients are available in the literature for standard blade airfoils, like the ones of Wells turbines. In the present study, the *Sandia* tables were selected to obtain the values of lift and drag coefficients, as their use is widely consolidated in the practice of wind turbine design [225]. These coefficients arise from experimental campaigns performed on isolated blades inside wind tunnels.

For taking into account the decrease of the power output caused by the leakage of the airflow through the tip clearance, induced drag coefficients are added to the corresponding experimental values to calculate the equivalent drag coefficients $CD_{tc}$, as in Eq. (4.84). The induced drag is a function of the lift coef-

ficient, the tip clearance $t$, the aspect ratio $AR$, and the pitch $\mathfrak{t}$ calculated at the blade tip [51].

$$C_{Dtc,i} = C_{D,i} + 0.7\frac{C_{L,i}t}{AR\mathfrak{t}} \tag{4.84}$$

With Eqs. (4.85) and (4.86), the lift and drag forces can be resolved into their components in the axial and tangential directions to obtain the coefficients of the axial thrust and tangential force $C_x$ and $C_\theta$, respectively, acting on the airfoil.

$$C_{x,i} = C_{L,i}cos\beta_{1,i} + C_{Dtc,i}sin\beta_{1,i} \tag{4.85}$$

$$C_{\theta,i} = C_{L,i}sin\beta_{1,i} - C_{Dtc,i}cos\beta_{1,i} \tag{4.86}$$

The lift force and the drag force acting on an infinitesimal airfoil of chord length $l$ are calculated with Eqs. (4.87) and (4.88).

$$df_{L,i} = \frac{1}{2}\rho_{a,i}l_iC_{L,i}w_{1,i}^2dr \tag{4.87}$$

$$df_{D,i} = \frac{1}{2}\rho_{a,i}l_iC_{Dtc,i}w_{1,i}^2dr \tag{4.88}$$

The lift and drag forces can be composed to calculate the axial force $f_x$ and tangential force $f_\theta$ acting on the blade with Eqs. (4.89) and (4.90).

$$df_{x,i} = df_{L,i}cos\beta_{1,i} + df_{D,i}sin\beta_{1,i} = \frac{1}{2}\rho_{a,i}l_iC_{x,i}w_{1,i}^2dr \tag{4.89}$$

$$df_{\theta,i} = df_{L,i}cos\beta_{1,i} - df_{D,i}sin\beta_{1,i} = \frac{1}{2}\rho_{a,i}l_iC_{\theta,i}w_{1,i}^2dr \tag{4.90}$$

For symmetrical airfoils, like those generally used in Wells turbines, the direction of the tangential force is the same for both the positive and negative values of the angle of attack. As a result, if the lift force dominates over the drag force, the tangential force $f_\theta$ has the same sign of the circumferential velocity of the blade and provides a positive contribution to the work extraction. Conversely, if the drag force overcomes the lift force, the tangential force is opposite to the blade circumferential velocity, determining a negative work transfer to the rotor. Generally, the net work conversion from the flow to the rotor is positive during the inflow and outflow phases. Consequently, the rotor operation is bidirectional.

The torque $\tau_b$ exerted by the flow on a single blade is obtained from Eq. (4.90) and it is equal to Eq. (4.91).

$$d\tau_{b,i} = r_i df_{\theta,i} = \frac{1}{2}\rho_{a,i} l_i C_{\theta,i} w_{1,i}^2 r_i dr \tag{4.91}$$

The power $P_b$ transferred by the flow to a single rotating blade is given by the product of the angular velocity and the torque, as stated in Eq. (4.92).

$$dP_{b,i} = \Omega r_i df_{\theta,i} = \frac{1}{2}\rho_{a,i} l_i C_{\theta,i} w_{1,i}^2 \Omega r_i dr \tag{4.92}$$

The previous formulas determine the performance of a single blade under the hypothesis of negligible mutual interferences amongst blades of the same row. However, Wells turbines have high values of rotor solidity, typically ranging from 0.4 to 0.6 at blade midspan, for combining efficient and self-starting operation. A high solidity determines a mutual interference amongst the row blades caused by both inviscid and viscous effects. The inviscid effects are due to the velocities induced by every blade

on each other. The viscous effects are determined by the wakes produced at the trailing edge of a blade, which influence the flow field at the leading edge of the following blade. This interference is not only a function of the rotor solidity but also of the angle of attack of the flow. Since the operation of a monoplane Wells turbine is significantly affected by the aerodynamic interference between the row blades, a correction factor shall be introduced. The potential flow theory or a semi-empirical approach can be used, as explained in detail in Section 3.2.1.

In the present study, an approach based on the theory of the flow circulation of Kutta-Joukowski was utilised with the aim of minimising the differences between the predictions of the developed analytical model and the literature experimental models [226]. The force coefficients of Eqs. (4.85) and (4.86) are multiplied by the cascade interference factor of Eq. (3.4) to obtain the modified values of the axial and tangential force coefficients of Eqs. (4.93) and (4.94), respectively. A specific interference factor is obtained for each blade element, as they have their distinctive values of rotor solidity and force coefficients.

$$C_{xCIF,i} = \frac{1}{1-\sigma_i^2} C_{x,i} \tag{4.93}$$

$$C_{\theta CIF,i} = \frac{1}{1-\sigma_i^2} C_{\theta,i} \tag{4.94}$$

By using the values of the force coefficients of Eqs. (4.93) and (4.94) corrected with the interference factor instead of their original values, the performance of the Wells turbine can be determined without neglecting the cascade interference effects. Therefore, this method allows considering the interference effects both on the lift and drag forces.

As discussed in Section 3.2.1, Eqs. (4.93) and (4.94) indi-

cate that the aerodynamic forces acting on the blades and the pressure drop across the turbine significantly increase with rotor solidity. Conversely, the aerodynamic efficiency of the rotor, which is determined by the ratio between the peripheral and axial forces acting on the blades, is not strongly affected by solidity.

In order to calculate the velocity triangle at the rotor outlet, the absolute angle of the flow exiting the blade $\alpha_2$ has to be determined. Two approaches can be applied: one considers the flow deviation across the cascade as a function of only the rotor geometry in terms of blade chord length and rotor pitch, while the other takes into account even the effects of the conditions of the airflow fluid dynamics.

The first approach of Eq. (4.95) is based on the balance of the resulting forces acting on the blade elements and the variation of the momentum in the chordwise direction [50].

$$\cot \alpha_{2,i} = \cot \alpha_{1,i} + 2 \tan \frac{\pi l_i}{2\mathfrak{t}_i} \tag{4.95}$$

Instead, the semi-empirical approach applies the balance of the resulting torque on the blade elements and the change in the angular momentum through Eqs. (4.96) and (4.97) to compute the value of $\alpha_2$ at the rotor outlet section [221]. This approach was selected in the present study for modelling the aerodynamics of the Wells turbine.

$$\Gamma_{1,i} - \Gamma_{2,i} = \frac{Z l_i C_{\theta CIF,i} v_{x,i}}{2\beta_{1,i}} \tag{4.96}$$

$$\cot \alpha_{2,i} = \cot \alpha_{1,i} + \frac{Z l_i C_{\theta CIF,i}}{4\pi \beta_{1,i}} \tag{4.97}$$

The velocity triangle at the outlet of the rotor row is deter-

mined with equations ranging from Eq. (4.98) to Eq. (4.105).

$$\alpha_{2,i} = \operatorname{arccot}\left(\cot\alpha_{1,i} + \frac{Zl_i C_{\theta CIF,i}}{4\pi\beta_{1,i}}\right) \tag{4.98}$$

$$v_{x2,i} = v_{x1,i} \tag{4.99}$$

$$v_{\theta 2,i} = v_{x2,i}\cot\alpha_{2,i} \tag{4.100}$$

$$v_{2,i} = \sqrt{v_{x2,i}^2 + v_{\theta 2,i}^2} \tag{4.101}$$

$$w_{x2,i} = v_{x2,i} \tag{4.102}$$

$$w_{\theta 2,i} = v_{\theta 2,i} - U_i \tag{4.103}$$

$$w_{2,i} = \sqrt{v_{w2,i}^2 + w_{\theta 2,i}^2} \tag{4.104}$$

$$\beta_{2,i} = \arctan\frac{w_{2,i}}{w_{\theta 2,i}} \tag{4.105}$$

The torque $\tau$ exerted by the flow on all the airfoils of the rotor is obtained by multiplying Eq. (4.91) by the number of rotor blades and substituting the tangential force coefficient calculated on an isolated profile $C_\theta$ with the value $C_{\theta CIF}$ corrected using the cascade interference factor to consider the rotor blade interaction.

$$d\tau_i = \frac{1}{2}\rho_{a,i} l_i Z C_{\theta CIF,i} w_{1,i}^2 r_i dr \tag{4.106}$$

The power $P$ transferred to each rotor airfoil can be calcu-

lated with Eq. (4.107) by multiplying the torque of Eq. (4.106) by the rotational velocity.

$$dP_i = \frac{1}{2}\rho_{a,i} l_i Z C_{\theta CIF,i} w_{1,i}^2 \Omega r_i dr \tag{4.107}$$

The total power output of the rotor can be evaluated through numerical integration of Eq. (4.107) along the blade span.

The equilibrium of the axial momentum is imposed to determine the pressure drop across the rotor and the energy parameters of the turbine. In Eqs. (4.108) and (4.109), the axial force acting on the rotor, expressed in terms of force equilibrium by Eq. (4.89) is balanced by the pressure force acting on the flow [22].

$$(p_{a1,i} - p_{a2,i}) 2\pi r_i dr = \frac{1}{2}\rho_{a,i} l_i Z C_{xCIF,i} w_{1,i}^2 dr \tag{4.108}$$

$$\frac{p_{a1,i} - p_{a2,i}}{\frac{1}{2}\rho_{a,i} w_{1,i}^2} = \frac{l_i Z C_{xCIF,i}}{2\pi r_i} \tag{4.109}$$

By substituting the inlet relative velocity with the inlet absolute velocity, the static-to-static pressure drop across the rotor is obtained with Eq. (4.110).

$$p_{a1,i} - p_{a2,i} = \frac{\rho_{a,i} l_i Z C_{xCIF,i} v_{x1,i}^2}{4\pi r_i \sin^2 \beta_{1,i}} \tag{4.110}$$

Therefore, the total-to-static pressure drop within the rotor is expressed by Eq. (4.111). This quantity determines the pressure difference that the chamber has to provide to the turbine for the operation of the oscillating water column system.

$$p_{ta1,i} - p_{a2,i} = \frac{\rho_{a,i} l_i Z C_{xCIF,i} w_{1,i}^2}{4\pi r_i} + \frac{1}{2}\rho_{a,i} v_{1,i}^2 \tag{4.111}$$

The total-to-total pressure drop across the rotor can be calculated with Eq. (4.112) as a function of the axial force coefficient and, thus, of the lift and drag coefficients.

$$p_{ta1,i} - p_{ta2,i} = \frac{\rho_{a,i} l_i Z C_{xCIF,i} w_{1,i}^2}{4\pi r_i} + \frac{1}{2}\rho_{a,i} v_{1,i}^2 - \frac{1}{2}\rho_{a,i} v_{2,i}^2 \tag{4.112}$$

Since the kinetic power at the rotor outlet is considered as a loss, the total power entering the system $P_I$ is determined by Eq. (4.113) through the product of the total-to-total pressure drop and the volume flow rate.

$$dP_{I,i} = (p_{ta1,i} - p_{ta2,i}) d\dot{q}_{a,i} \tag{4.113}$$

The formulation of Eq. (4.113) can be made explicit by substituting Eq. (4.111) and the volume flow rate through the annulus. In this way, Eq. (4.114) is obtained.

$$\begin{aligned} dP_{I,i} &= \frac{\rho_{a,i} l_i Z C_{xCIF,i} v_{x1,i}^2}{4\pi r_i \sin^2 \beta_{1,i}} 2\pi r_i v_{x1,i} dr = \\ &= \frac{1}{2}\rho_{a,i} l_i Z C_{xCIF,i} w_{1,i}^2 v_{x1,i} dr \end{aligned} \tag{4.114}$$

The total power is comprised of the sum of the power output $P_O$ and the power dissipation due to viscous effects on the blades $P_V$, as indicated in Eq. (4.115).

$$dP_{I,i} = (p_{ta1,i} - p_{ta2,i})d\dot{q}_i = dP_{O,i} + dP_{V,i} \tag{4.115}$$

If the total-to-static pressure drop within the rotor is considered, Eq. (4.116) can be written by making explicit the contribution of the dissipation of kinetic power $P_K$.

$$(p_{ta1,i} - p_{a2,i})d\dot{q}_i = dP_{O,i} + dP_{V,i} + dP_{K,i} \tag{4.116}$$

The right side terms of Eq. (4.116) can be expressed through equations from Eq. (4.117) to Eq. (4.119).

$$dP_{O,i} = \frac{1}{2}\rho_{a,i} l_i Z C_{\theta CIF,i} w_{1,i}^2 U_i dr \tag{4.117}$$

$$dP_{V,i} = \frac{1}{2}\rho_{a,i} l_i Z C_{Dtc,i} w_{1,i}^3 dr \tag{4.118}$$

$$dP_{K,i} = \frac{1}{2}\rho_{a,i} v_{2,i}^2 d\dot{q}_i \tag{4.119}$$

Under the hypothesis of conservation of the absolute velocity imposed by the two-dimensional cascade theory, the power balance can be verified with the equations from Eq. (4.120) to Eq.(4.122) by substituting Eqs. (4.111), (4.117), (4.118), and (4.119) into Eq. (4.115).

$$\begin{aligned}(p_{ta1,i} - p_{a2,i})d\dot{q}_i = &\frac{1}{2}\rho_{a,i} l_i Z C_{\theta CIF,i} w_{1,i}^2 U_i dr + \\ &+ \frac{1}{2}\rho_{a,i} l_i Z C_{Dtc,i} w_{1,i}^3 dr + \frac{1}{2}\rho_{a,i} v_{2,i}^2 d\dot{q}_i\end{aligned} \tag{4.120}$$

$$\begin{aligned}&\frac{1}{2}\rho_{a,i} l_i Z C_{xCIF,i} w_{1,i}^2 v_{x1,i} dr = \\ &= \frac{1}{2}\rho_{a,i} l_i Z w_{1,i}^2 (C_{\theta CIF,i} U_i + C_{Dtc,i} w_{1,i}) dr\end{aligned} \tag{4.121}$$

$$C_{xCIF,i} v_{x1,i} - C_{\theta CIF,i} U_i = C_{Dtc,i} w_{1,i} \tag{4.122}$$

The formulation of Eq. (4.122) states the relation that links the velocity triangles with the force coefficients, connecting, in turn, the rotor angular velocity, the blade radii, the lift and drag coefficients, and the rotor solidity. The equation is always fulfilled for a monoplane isolated Wells turbine under the assumption of null velocity variations in the axial direction.

The blade element aerodynamic efficiency $\xi$ is defined in Eq. (4.123) by the ratio of the infinitesimal blade power output and the infinitesimal total power input of the corresponding channel sector.

$$\xi_i = \frac{dP_{O,i}}{dP_{I,i}} = \frac{dP_{O,i}}{dP_{O,i} + dP_{V,i} + dP_{K,i}} \tag{4.123}$$

The radially mass-averaged aerodynamic efficiency of the rotor is obtained with Eq. (4.124) by numerical integration along the blade span.

$$\xi_i = \frac{dP_{O,i}}{dP_{I,i}} = \frac{\int_{r_{hub}}^{r_{tip}} (dP_{O,i}}{\int_{r_{hub}}^{r_{tip}} dP_{O,i} + dP_{V,i} + dP_{K,i})} \tag{4.124}$$

The total pressure downstream of the rotor is calculated with Eq. (4.125).

$$p_{ta2,i} = p_{a2,i} + \frac{\rho_{a,i}}{2}(v_{x2,i}^2 + v_{\theta 2,i}^2) \tag{4.125}$$

By applying radial equilibrium, the total pressure distribution along the blade radius at the rotor outlet can be formulated with Eq. (4.126).

$$\frac{dp_{ta2,i}}{dr} = \frac{\rho_{a,i}}{2}\frac{d(v_{x2,i})^2}{dr} + \frac{\rho_{a,i}}{2r_i^2}\frac{d(rv_{\theta 2,i})^2}{dr} \tag{4.126}$$

With the assumption of constant total pressure along the blade span [22], Eq. (4.126) is reduced to Eqs. (4.127), (4.128) and finally to Eq. (4.129).

$$\frac{d(v_{x2,i})^2}{dr} = -\frac{1}{r_i^2}\frac{d(rv_{\theta 2,i})^2}{dr} \tag{4.127}$$

$$\frac{d(v_{x2,i})^2}{dr} = -\frac{1}{4\pi^2 r_i^2}\frac{d(2\pi rv_{\theta 2,i})^2}{dr} \tag{4.128}$$

$$\frac{d(v_{x2,i}^2)}{dr} = -\frac{1}{4\pi^2 r_i^2}\Gamma_{2,i}^2 \tag{4.129}$$

Under the hypothesis of constant work and blade circulation around the blades, thus of null circulation in the radial direction, the variation of the axial velocity in the radial direction upstream and downstream of the blade row is zero. This implies that the flow axial velocity is constant for each blade element for the two-dimensional cascade theory.

### 4.2.2 Actuator disc model of monoplane isolated Wells turbines

The concept of the actuator disc was first used by Rankine in 1865 in the theory of ship propeller design. Afterwards, actuator disc models have been widely used to date in turbomachinery. The main feature of the model is to consider a cascade of a turbomachine as an infinitely thin and permeable disc that mimics

the effect of the former in terms of energy exchange with the flow. The circular disc determines an axial resistance to the flow, which is considered uniform within the disc section, as the row is approximated as a set of infinite blades. The radial equilibrium condition is imposed far upstream and far downstream of the disc, although it is not necessarily respected in the area between these sections. This approach allows the development of a model based on the conservation of the mass and momentum, suitable for the assessment of the energy extraction by flows that are not subject to high vorticity and energy losses [21, 221]. The main assumptions of the theory are to consider a steady, axisymmetric, and inviscid flow.

The axial momentum theory applies the conservation laws in the axial direction inside an annular stream tube containing an actuator disc. Its main aim is to establish a relation between the axial velocity and the axial force acting on the disc. This is the result of the mass, axial momentum, and energy conservation at the inlet and the outlet of the stream tube. In an actuator disc model, the axial component of the velocity is not necessarily constant in both the axial and radial directions upstream and downstream of the blade row. Indeed, a redistribution of the mass flow is taken into account, as stated by experimental analyses carried out on axial turbomachines. The conservation of the axial momentum identifies that the axial force exerted by the flow on the actuator disc is equal to Eq. (4.130).

$$f_{x,i} = \dot{m}(v_{x1,i} - v_{x2,i}) = \rho_{a,i} v_{x\not{d},i} A_{ann,i}(v_{x1,i} - v_{x2,i}) \quad (4.130)$$

where $v_{x\not{d}}$ is the axial component of the absolute airflow velocity

at the actuator disc section.

The energy conservation determines that the axial power acting on the disc of Eq. (4.131) equals the power lost by the flow of Eq. (4.132).

$$\begin{aligned} P_{x,i} &= f_{x,i} v_{x\acute{d},i} = \dot{m}_i (v_{x1,i} - v_{x2,i}) v_{x\acute{d},i} = \\ &= \rho_{a,i} v_{x\acute{d},i}^2 A_{ann,i} (v_{x1,i} - v_{x2,i}) \end{aligned} \tag{4.131}$$

$$\begin{aligned} P_{x,i} &= \frac{1}{2} \dot{m}_i (v_{x1,i}^2 - v_{x2,i}^2) = \\ &= \frac{1}{2} \rho_{a,i} v_{x\acute{d},i} A_{ann,i} (v_{x1,i}^2 - v_{x2,i}^2) \end{aligned} \tag{4.132}$$

Therefore, the kinetic energy that is extracted from the flow is the same as the energy absorbed by the actuator disc. It follows that, combining Eqs. (4.131) and (4.132), the axial velocity within the disc $v_{x\acute{d}}$ is expressed by Eq. (4.133).

$$v_{x\acute{d},i} = \frac{1}{2} (v_{x1,i} + v_{x2,i}) \tag{4.133}$$

The actuator disc theory states that within the disc, at any given radius, the axial velocity is equal to the average of the undisturbed axial velocities at the same radius, far upstream and far downstream of the disc. Thus, the perturbations superimposed on the axial velocities of the far-field $v_{x1}$ and $v_{x2}$ right before and after the disc $v_{x1}^{'}$ and $v_{x2}^{'}$ in the upstream and downstream regions, can be written as in Eqs. (4.134) and (4.135), respectively.

$$v_{x1,i}^{'} = \frac{1}{2} (v_{x2,i} - v_{x1,i}) \tag{4.134}$$

$$v_{x2,i}^{'} = \frac{1}{2}(v_{x1,i} - v_{x2,i}) \tag{4.135}$$

From Eq. (4.133) and imposing the continuity and a constant tangential vorticity in the region between the far upstream inlet, where the condition of radial equilibrium is satisfied, and the disc, Eqs. (4.136) and (4.137) can be obtained [221].

$$\frac{\partial v_r}{\partial x} = \frac{\partial}{\partial r}(v_{x1} + v_{x1}^{'}) = -\frac{\partial v_{x1}}{\partial r} \tag{4.136}$$

$$\frac{\partial v_r}{\partial x} = \frac{\partial v_{x1}^{'}}{\partial r} \tag{4.137}$$

where $v_r$ is the radial component of the absolute airflow velocity.

Then, Eq. (4.137) can be generalised in Eq. (4.138) by including Eq. (4.135).

$$\frac{\partial v_r}{\partial x} = \frac{\partial v_{x1}^{'}}{\partial r} = \frac{\partial v_{x2}^{'}}{\partial r} = \frac{\partial v_{x}^{'}}{\partial r} \tag{4.138}$$

Therefore, the continuity equation can be written as in Eq. (4.139).

$$\frac{\partial v_{x}^{'}}{\partial x} + \frac{\partial v_r}{\partial r} + \frac{v_r}{r} = 0 \tag{4.139}$$

Substituting Eq. (4.137) into Eq. (4.139) and partially differentiating with respect to the radius, Eq. (4.140) is obtained [221].

$$\frac{\partial^2 v_r}{\partial x^2} + \frac{\partial^2 v_r}{\partial r^2} + \frac{1}{r}\frac{\partial^2 v_r}{\partial r^2} \tag{4.140}$$

By imposing the boundary condition of null radial velocity $v_r = 0$ both at hub and at tip, a solution of the differential Eq. (4.140) expressing the velocity perturbation can be obtained

[221], as expressed by Eq. (4.141).

$$v_x^{'} = \pm(v_{x2} - v_{x1})e^{\pm\frac{\pi x}{r_{tip}-r_{hub}}} \tag{4.141}$$

The important result of the axial momentum theory applied to the actuator disc is that the velocity perturbations decay exponentially away from the disc, both upstream and downstream.

The formula achieved for the decay rate in Eq. (4.142) is called settling-rate rule [221].

$$v_x = v_{x1} \pm (v_{x2} - v_{x1})e^{\pm\frac{\pi x}{r_{tip}-r_{hub}}} \tag{4.142}$$

The plus or minus signs in the above equations refer to the upstream and downstream flow regions, respectively. This approximate solution was proved to be consistent with the exact solution of the analysis [178].

The determination of the flow field with the actuator disc model is performed by means of an iterative procedure. Firstly, the law of the axial velocity variation of Eq. (4.129) and the continuity equation of Eq. (4.139) are utilised to calculate the radial distribution of the axial velocity at the domain outlet by assuming that, at the first step, the flow velocity in front of the disc is equal to that of the undisturbed flow. Then, with Eq. (4.133) the axial flow velocity across the disc is determined as the average between the values of the axial velocity far upstream and far downstream of the disc. For each blade element, the work produced, the work lost, the tangential component of the absolute velocity downstream of the disc, and the static and total values of pressure drop are calculated once again with the formulations presented in Section 4.2.1 and a new outlet distribution of the axial velocity is determined. The iterative procedure continues until the convergence criterion of differences in energy conserva-

tion lower than $10^{-4}$ is satisfied.

### 4.2.3 Actuator disc model of Wells turbines with guide vanes

The analytical model of monoplane Wells turbines with two rows of guide vanes positioned upstream and downstream of the rotor, as visible in Figures 4.14 and 4.15, assumes that the flow is steady, axisymmetric, and inviscid, and applies the Kutta condition. Therefore, the flow velocity is always finite at the sharp leading edge of the inlet guide vane. The flow approaching the leading edge of the inlet guide vane is completely axial, and it is deflected by the inlet guide vane to obtain an absolute flow angle $\alpha_1$ at the rotor inlet greater than 90 degrees and directed in the direction of rotation of the rotor.

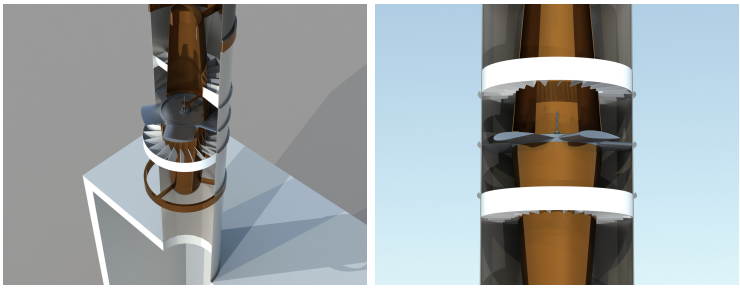

(a) Isometric view (b) Front view

Figure 4.14: Rendering of the **(a)** isometric and **(b)** front sections of the CAD model created for the system with a monoplane Wells turbine with guide vanes.

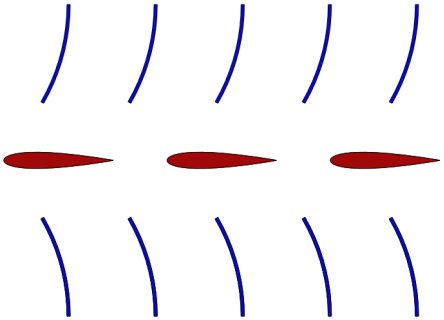

Figure 4.15: Scheme of the blade-to-blade section of the cascades of a monoplane Wells turbine with guide vanes.

Considering the two-dimensional potential flow about a blade cascade of negligible thickness, a simple approach to the design of the guide vanes is the application of Eq. (4.95) to balance the resulting forces acting on the blade elements and the variation of momentum in the chordwise direction. In Eq. (4.95), the angle $\alpha_1$ is imposed by the shape of the inlet guide vane, and the angle $\alpha_2$ depends on the geometry and operating conditions. Therefore, in ideal conditions, the flow absolute angles at the inlet and outlet of the rotor are supplementary, as stated by Eq. (4.143).

$$\alpha_{2,i} = \pi - \alpha_{1,i} \tag{4.143}$$

As a consequence, the guide vanes have to be symmetrical, and their angles are a function of only the rotor solidity [52]. Moreover, the flow exits the outlet guide vane without swirl, and the flow pattern of the two guide vanes is specular regarding the plane of symmetry of the turbine cascades. With this approach, the angle $\alpha_1$ can be determined through Eq. (4.144), and it is a function of only the chord to pitch ratio of the rotor, resulting

independent from the rotational speed and the flow rate.

$$\alpha_{1,i} = \frac{\pi}{2}\left(1 + \frac{l_i}{\mathfrak{t}_i}\right) \tag{4.144}$$

However, this approach has the limitation of neglecting the contribution of the drag force to the chordwise component of the force acting on the rotor.

A more accurate approach to determine the guide vane angles is based on the balance of the resulting torque on the blade elements and the change in the angular momentum of Eq. (4.97). The velocity triangle at the rotor inlet relates the absolute and relative flow angles $\alpha_1$ and $\beta_1$, respectively, through Eq. (4.145).

$$\cot\alpha_{1,i} + \cot\beta_{1,i} = \frac{\Omega r_i}{v_{x1,i}} \tag{4.145}$$

For specific values of flow rate, rotor geometry, and angular speed, the design geometry of the inlet guide vane is given by the equation of the distribution of the absolute flow angle $\alpha_1$ as a function of the radius. This determines in turn, the distributions of the relative flow angle $\beta_1$ and consequently of the tangential force coefficient $C_\theta$ along the radius. Therefore, the relation between the flow absolute angles at the inlet and outlet of the rotor becomes a direct function of the radius and Eq. (4.143) has to be satisfied for each airfoil along the blade span.

In the present work, the approach relying on the balance of the blade element torque and the change in the angular momentum was utilised. The procedure described in Sections 4.2.1 and 4.2.2 and Eqs. (4.143) and (4.145) was applied to determine the flow field in the axial and tangential directions and the performance of the monoplane Wells turbine with inlet and outlet guide vanes. The model begins with setting the geometrical

and operating states of the three turbomachine rows and with the computation of the inlet properties of the seawater and air according to the environmental conditions. Then, the airflow conditions at the section far upstream of the turbine duct are assigned on the basis of the literature results, achievements of previous calculations of the chamber model, or as part of the iterative cycle connecting the chamber and turbine models.

In analogy with the model of the monoplane isolated Wells turbine, the static pressure $p_0$ at the inlet of the upstream stator is initialised with the value obtained from the literature or the chamber model or through the application of the equation of state for ideal gases of Eq. (4.146).

$$p_0 = \rho_{amb} \mathcal{R} T_{amb} \tag{4.146}$$

Afterwards, an iterative procedure is used to determine the static pressure based on the pressure difference across the turbine, similarly to the monoplane isolated Wells turbine.

The air density at the inlet of the turbomachine $\rho_a$ is computed with Eq. (4.147) under the assumption of a negligible air temperature difference between the inlet and outlet of the turbine.

$$\rho_a = \frac{p_{a0}}{\mathcal{R}_a T_{a,amb}} \tag{4.147}$$

For the momentum balance in the radial direction, the radial equilibrium of Eq. (4.69) is applied upstream and downstream of the cascades. In particular, the flow approaching the inlet guide vane is assumed to be axial and uniform and Eqs. (4.148) and (4.149) are utilised to determine the velocity components of the airflow.

$$v_{x0,i} = \frac{\dot{m}_{a,i}}{\rho_{a,i} A_{ann,i}} = \frac{\dot{q}_{a,i}}{A_{ann,i}} \tag{4.148}$$

$$v_{\theta 0,i} = 0 \tag{4.149}$$

where $v_{x0}$ and $v_{\theta 0}$ are the axial and tangential components of the velocity at the inlet of the upstream stator, respectively. The flow is deflected by the inlet guide vane, thus the velocity components in this section are determined with Eqs. (4.150) and (4.151).

$$v_{x1,i} = v_{x0,i} \tag{4.150}$$

$$v_{\theta 1,i} = \frac{v_{x1,i}}{\tan \alpha_{1,i}} \tag{4.151}$$

The total pressure and the flow rotation can be calculated with Eqs. (4.152) and (4.153), under the assumptions of inviscid and irrotational flow.

$$p_{t0,i} = p_{0,i} + \frac{\rho_{0,i}}{2}(v_{x0,i}^2 + v_{\theta 0,i}^2) \tag{4.152}$$

$$\mathcal{O}_{\theta 0,i} = \frac{\partial v_{r0,i}}{\partial x} - \frac{\partial v_{x0,i}}{\partial r} \tag{4.153}$$

The flow circulation $\Gamma_1$ at the rotor inlet can be computed with Eq. (4.154) on the basis of the tangential velocity obtained through Eq. (4.151). For a Wells turbine with guide vanes, $\Gamma_1$ is not null, in contrast to the monoplane isolated configuration.

$$\Gamma_{1,i} = 2\pi r_i v_{\theta 1,i} \tag{4.154}$$

The velocity triangle and the flow coefficient at the inlet of the rotor are calculated with Eqs. (4.150) and (4.151) and the equations from Eq. (4.76) to Eq. (4.83). The equations from Eq. (4.85) to Eq. (4.90) are utilised to compute the lift, drag, and force coefficients and the forces acting on the rotor blades. Then, through Eqs. (4.93) and (4.94), the effect of the mutual interference between the rotor blades is included in the calculations. Subsequently, Eq. (4.98) is utilised to calculate the absolute flow angle exiting the rotor and the equations ranging from Eq. (4.99) and Eq. (4.105) are applied to determine the velocity triangle downstream of the rotor cascade. Afterwards, the torque and power exerted by the fluid on the turbine rotor are determined with Eqs. (4.106) and (4.107).

The static-to-static pressure drop across the turbine, which means between the inlet and outlet of the two guide vanes, is ideally equal to the static pressure variation across the rotor of Eq. (4.110). The total-to-static pressure drop through the turbine can be calculated by adding the specific kinetic energy at the entrance of the IGV, computed with Eq. (4.155) as a function of the flow velocity $v_{x0}$ at this section.

$$p_{t0,i} - p_{3,i} = \frac{\rho_{a,i} l_i Z C_{xCIF,i} w_{1,i}^2}{4\pi r_i} + \frac{1}{2}\rho_{a,i} v_{0,i}^2 \tag{4.155}$$

where $p_3$ is the static pressure at the exit of the outlet guide vane.

The inlet power of Eq. (4.156) is provided by the product of the total-to-static pressure variation across the turbomachine and the volume flow rate elaborated. The power entering the system equals the sum of the power output and the power dissipated for viscous and kinetic effects.

$$dP_{I,i} = (p_{t0,i} - p_{3,i})d\dot{q}_i = dP_{O,i} + dP_{V,i} + dP_{K,i} \tag{4.156}$$

The power output $P_O$ and the power dissipation due to viscous effects on the blades $P_V$ are determined by Eqs. (4.117) and (4.118), respectively. The dissipation of the kinetic power is given by Eq. (4.157), where the velocity term ideally coincides with the absolute axial velocity at the exit of the OGV. Indeed, the swirl component of the flow is ideally null both at the entrance and the exit of the guide vanes.

$$dP_{K,i} = \frac{1}{2}\rho_{a,i} v_{3,i}^2 d\dot{q}_i \tag{4.157}$$

The radially mass-averaged aerodynamic efficiency of the turbine is obtained with Eq. (4.124) by numerical integration of the power contributions along the blade span.

The total pressure downstream of the rotor is computed with Eq. (4.125), while its distribution along the blade radius at the rotor outlet is given by Eq. (4.126). The equations from Eq. (4.127) to Eq. (4.142) are applied to calculate the distributions of the axial and tangential velocity upstream and downstream of the rotor, modelled as an actuator disc.

The flow exiting the OGV is ideally axial, and its tangential component of the absolute velocity is null. Therefore, the total pressure at this section is determined through Eq. (4.158).

$$p_{t3,i} = p_{3,i} + \frac{1}{2}\rho_{a,i} v_{x3,i}^2 \tag{4.158}$$

The guide vanes used for the application with Wells turbines

may be defined by a fixed two-dimensional shape projected along the stator radius or may have a specific three-dimensional shape.

The design of guide vanes with a shape defined by two dimensions is based on applying the procedure described above to determine the optimal flow angle at the exit of the inlet guide vane that fulfils the conditions imposed by Eqs. (4.143) and (4.145) at the blade midspan section. The geometry of the guide vanes is imposed to obtain a value of the torque coefficient equal to the value calculated corresponding to the condition of maximum efficiency for the turbine without guide vanes [208].

For the guide vanes whose shape is defined by three dimensions, the geometry of the stators is designed to keep the angle of attack $\beta_1$ constantly equal to the value corresponding to the maximum efficiency point in the case of two-dimensional guide vanes [208].

The present model was developed to allow the choice of the design of two-dimensional or three-dimensional guide vanes.

The chord length of the guide vanes can be determined by applying the criterion of Zweifel for a specific number of vanes, set on the basis of experience and the design practice for turbomachinery [21]. Zweifel's criterion defines the optimal ratio between the real and ideal blade loading on a cascade to minimise the aerodynamic losses. The general formulation of the real blade loading on a generic airfoil is determined by Eq. (4.159).

$$\begin{aligned} \Gamma_i &= \rho_{a,i} \mathbf{t}_i v_{x,i} (v_{\theta in,i} + v_{\theta out,i}) = \\ &= \rho_{a,i} \mathbf{t}_i v_{x,i}^2 (\tan \alpha_{in,i} + \tan \alpha_{out,i}) \end{aligned} \tag{4.159}$$

where $\Gamma$ is the real blade loading and the subscripts *in* and *out* refer to the inlet and outlet sections of the cascade.

The ideal blade loading on a generic airfoil $i$ is expressed by Eq. (4.160).

$$\begin{aligned}\Gamma_{id,i} = (p_{tain,i} - p_{aout,i}) l_{x,i} = \frac{1}{2}\rho_{a,i}\mathfrak{t}_i v_{x,i}^2 l_{x,i} = \\ = \rho_{a,i}\mathfrak{t}_i v_{x,i}^2 \cos^2(\alpha_{out,i}) l_{x,i}\end{aligned} \tag{4.160}$$

The criterion of Zweifel states in Eq. (4.161) that the optimal value of the real to ideal blade loading ratio is 0.8 for a turbomachine row.

$$\frac{\Gamma_i}{\Gamma_{id,i}} = 2\frac{\mathfrak{t}_i}{l_{x,i}} \cos^2 \alpha_{out,i} (\tan \alpha_{in,i} + \tan \alpha_{out,i}) = 0.8 \tag{4.161}$$

The length of the axial chord of the stators is obtained from Eq. (4.162) by making explicit $l_{x,i}$ and substituting the values of the flow angles.

$$l_{x,i} = 2.5\mathfrak{t}_i \cos^2 \alpha_{1,i} (\tan \alpha_{0,i} + \tan \alpha_{1,i}) \tag{4.162}$$

The geometry and the chord length of the inlet and outlet guide vanes are identical; thus, even their axial chord length is equivalent. From this value, the chord length can be obtained by fixing the geometry of the guide vanes, which is typically represented by an arc of a circle [208].

### 4.2.4 Actuator disc model of biplane Wells turbines

The analytical model of biplane Wells turbines considers a machine composed of two rotor rows without guide vanes, as illustrated in Figures 4.16 and 4.17.

(a) Isometric view (b) Front view

Figure 4.16: Rendering of the **(a)** isometric and **(b)** front sections of the CAD model created for the system with the biplane Wells turbine.

Figure 4.17: Scheme of the blade-to-blade section of the cascades of a co-rotating Wells turbine.

The model applies a double actuator disc model to determine the aerodynamics of the turbomachine. The two co-rotating rotors are modelled as two coupled actuator discs to superimpose the effects of the cascades on the fluid dynamics of the entire turbine. As discussed in Section 3.2.3, the mutual interaction between the planes has a limited magnitude for the typical design parameters of biplane Wells turbines, as the gap to chord ratio is greater than the unit. Therefore, the effects of the interaction between planes, which are modelled, concern two aspects. The first is the air pressure at the inlet and outlet of the upstream rotor for the presence of the downstream rotor; the second is the modification of the velocity triangle of the downstream cascade

due to the flow distortion caused by the upstream cascade.

The analytical model starts with the definition of the geometric and operating conditions of the two rotor cascades. Moreover, the flow conditions at the turbine inlet are initialised based on available results or calculating the air properties and the static pressure at the rotor inlet through the equation of state for ideal gases of Eq. (4.67). Then, an iterative procedure relying on the two-dimensional cascade theory is applied to update the value of the static pressure on the basis of the calculated pressure difference across the entire turbine. The obtained value is utilised in the computations starting from the determination of the air density at the inlet of the upstream rotor with Eq. (4.68).

The equations in the interval between Eq. (4.69) and Eq. (4.75) are applied to impose the momentum balance in the radial direction and determine the flow characteristics at the inlet of the upstream cascade. Then, Eq. (4.163), the equations from Eq.(4.77) to Eq. (4.82), and Eq. (4.164) are calculated to determine the blade velocity of the upstream rotor.

$$\bar{U}_i = \bar{\Omega} r_i \tag{4.163}$$

$$\bar{\phi}_{1,i} = \frac{v_{x1,i}}{\bar{U}_i} \tag{4.164}$$

where the bar over the variables indicates the upstream rotor of the turbine.

The forces acting on this cascade and the related coefficients are calculated with equations from Eq. (4.165) to Eq. (4.170).

$$\bar{C}_{x,i} = \bar{C}_{L,i} cos\beta_{1,i} + \bar{C}_{D,i} sin\beta_{1,i} \tag{4.165}$$

$$\bar{C}_{\theta,i} = \bar{C}_{L,i} sin\beta_{1,i} - \bar{C}_{D,i} cos\beta_{1,i} \tag{4.166}$$

$$d\bar{f}_{L,i} = \frac{1}{2}\bar{\rho}_{a,i}\bar{l}_i\bar{C}_{L,i}w_{1,i}^2 dr \tag{4.167}$$

$$d\bar{f}_{D,i} = \frac{1}{2}\bar{\rho}_{a,i}\bar{l}_i\bar{C}_{D,i}w_{1,i}^2 dr \tag{4.168}$$

$$d\bar{f}_{x,i} = \frac{1}{2}\bar{\rho}_{a,i}\bar{l}_i\bar{C}_{x,i}w_{1,i}^2 dr \tag{4.169}$$

$$d\bar{f}_{\theta,i} = \frac{1}{2}\bar{\rho}_{a,i}\bar{l}_i\bar{C}_{\theta,i}w_{1,i}^2 dr \tag{4.170}$$

By combining the equations ranging from Eq. (4.165) to Eq. (4.170) with Eqs. (4.93) and (4.94), the effects of mutual interference amongst the rotor blades are introduced in the computation of the forces.

$$\bar{C}_{xCIF,i} = \frac{1}{1-\bar{\sigma}_i^2}\bar{C}_{x,i} \tag{4.171}$$

$$\bar{C}_{\theta CIF,i} = \frac{1}{1-\bar{\sigma}_i^2}\bar{C}_{\theta,i} \tag{4.172}$$

The torque $\bar{\tau}_i$ and power $\bar{P}_i$ transferred to every rotor airfoil are obtained with Eqs. (4.173) and (4.174).

$$d\bar{\tau}_i = \frac{1}{2}\bar{\rho}_{a,i}\bar{l}_i\bar{Z}\bar{C}_{\theta CIF,i}w_{1,i}^2 r_i dr \tag{4.173}$$

$$d\bar{P}_i = \frac{1}{2}\bar{\rho}_{a,i}\bar{l}_i\bar{Z}\bar{C}_{\theta CIF,i}w_{1,i}^2 \bar{\Omega} r_i dr \tag{4.174}$$

Subsequently, Eqs. (4.175) and (4.176) and the equations ranging from Eq. (4.99) to Eq. (4.105) are utilised to compute the velocity triangle at the outlet of the upstream rotor.

$$\cot \alpha_{2,i} = \cot \alpha_{1,i} + \frac{\bar{Z}\bar{l}_i\bar{C}_{\theta CIF,i}}{4\pi\beta_{1,i}} \tag{4.175}$$

$$\alpha_{2,i} = \operatorname{arccot}\left(\cot \alpha_{1,i} + \frac{\bar{Z}\bar{l}_i\bar{C}_{\theta CIF,i}}{4\pi\beta_{1,i}}\right) \tag{4.176}$$

The pressure variation across the upstream turbine is provided by Eqs. (4.177) and (4.178) in terms of static-to-static and total-to-static values, respectively.

$$p_{a1,i} - p_{a2,i} = \frac{\bar{\rho}_{a,i}\bar{l}_i\bar{Z}\bar{C}_{xCIF,i}w_{1,i}^2}{4\pi r_i} \tag{4.177}$$

$$p_{ta1,i} - p_{a2,i} = \frac{\bar{\rho}_{a,i}\bar{l}_i\bar{Z}\bar{C}_{xCIF,i}w_{1,i}^2}{4\pi r_i} + \frac{1}{2}\bar{\rho}_{a,i}v_{1,i}^2 \tag{4.178}$$

The power output $\bar{P}_O$, the power dissipation due to viscous effects on the blades $\bar{P}_V$, and the dissipation of kinetic power $\bar{P}_K$ for the upstream rotor are computed with Eqs. (4.179), (4.180), and (4.181), respectively.

$$d\bar{P}_{O,i} = \frac{1}{2}\bar{\rho}_{a,i}\bar{l}_i\bar{Z}\bar{C}_{\theta CIF,i}w_{1,i}^2\bar{U}_i dr \tag{4.179}$$

$$d\bar{P}_{V,i} = \frac{1}{2}\bar{\rho}_{a,i}\bar{l}_i\bar{Z}\bar{C}_{D,i}w_{1,i}^3 dr \tag{4.180}$$

$$d\bar{P}_{K,i} = \frac{1}{2}\bar{\rho}_{a,i}v_{2,i}^2 d\dot{q}_i \tag{4.181}$$

The relations of Eqs. (4.182) and Eqs. (4.183) and the equations in the interval from Eq. (4.127) to Eq. (4.129) are

utilised to determine the pressure and the axial velocity distribution along the blade radius at the outlet section of the upstream rotor. Then, the equations from Eq. (4.133) to Eq. (4.142) are calculated to apply the actuator disc approach based on the airflow velocity distribution at the same section.

$$p_{ta2,i} = p_{a2,i} + \frac{\bar{\rho}_{a,i}}{2}(v_{x2,i}^2 + v_{\theta 2,i}^2) \tag{4.182}$$

$$\frac{dp_{ta2,i}}{dr} = \frac{\bar{\rho}_{a,i}}{2}\frac{d(v_{x2,i})^2}{dr} + \frac{\bar{\rho}_{a,i}}{2r_i^2}\frac{d(rv_{\theta 2,i})^2}{dr} \tag{4.183}$$

An analogous procedure to that described for the upstream cascade is applied even for the downstream cascade. In particular, the static pressure at the inlet of the downstream row is initialised with the equation of state for ideal gases of Eq. (4.67), considering the pressure decrease through this single row. The velocity triangle at the inlet of the downstream rotor is identical to the one at the outlet of the upstream rotor, calculated with equations from Eq. (4.98) to Eq. (4.105). Afterwards, the same procedure used for the upstream row to determine the pressure variation and distribution and apply the actuator disc approach are imposed across the downstream rotor. In this case, the sections *1* and *2* at the inlet and outlet of the upstream rotor, respectively, are replaced by the sections *2* and *3* at the inlet and outlet of the downstream rotor, respectively.

The inlet power $P_{Ibp}$ of the biplane Wells turbine is given by the product of the total-to-static pressure drop across the entire turbine and the volume airflow rate passing through it, as written in Eq. (4.184).

$$dP_{Ibp,i} = (p_{ta1,i} - p_{a3,i})d\dot{q}_i \tag{4.184}$$

The power transformed by the blade elements of the two rotors, located at a specific radial position, is given by the sum of their contributions, as expressed in Eq. (4.185).

$$\begin{aligned} dP_{Obp,i} = & \frac{1}{2}\bar{\rho}_{a,i}\bar{l}_i\bar{Z}\bar{C}_{xCIF,i}w_{1,i}^2 v_{x1,i}dr + \\ & + \frac{1}{2}\bar{\bar{\rho}}_{a,i}\bar{\bar{l}}_i\bar{\bar{Z}}\bar{\bar{C}}_{xCIF,i}w_{2,i}^2 v_{x2,i}dr \end{aligned} \tag{4.185}$$

where the single bar and double bar subscripts indicate the upstream and downstream rotors, respectively.

The overall power output $P_{Obp}$ of the biplane turbine is provided by numerical integration of Eq. (4.185) along the radius from hub to tip, as expressed in Eq. (4.186).

$$\begin{aligned} P_{Obp} = & \int_{r_{hub}}^{r_{tip}} \frac{1}{2}\bar{\rho}_{a,i}\bar{l}_i\bar{Z}\bar{C}_{\theta 1CIF,i}w_{1,i}^2\bar{\Omega}r_i dr + \\ & + \int_{r_{hub}}^{r_{tip}} \frac{1}{2}\bar{\bar{\rho}}_{a,i}\bar{\bar{l}}_i\bar{\bar{Z}}\bar{\bar{C}}_{\theta 2CIF,i}w_{2,i}^2\bar{\bar{\Omega}}r_i dr \end{aligned} \tag{4.186}$$

where $w_3$ is the relative velocity of the airflow at the inlet of the downstream rotor.

The power loss $P_{Vbp}$ due to viscous effects on the blades of the two cascades is expressed by Eq. (4.187).

$$\begin{aligned} dP_{Vbp,i} = & \frac{1}{2}\bar{\rho}_{a,i}\bar{l}_i\bar{Z}\bar{C}_{D,i}w_{1,i}^3 dr + \\ & + \frac{1}{2}\bar{\bar{\rho}}_{a,i}\bar{\bar{l}}_i\bar{\bar{Z}}\bar{\bar{C}}_{D,i}w_{2,i}^3 dr \end{aligned} \tag{4.187}$$

The power loss $P_{Kbp}$ owing to the kinetic power of the flow

exiting the turbine is expressed by Eq. (4.188).

$$dP_{Kbp,i} = \frac{1}{2}\bar{\bar{\rho}}_{a,i} v_{3,i}^2 d\dot{q}_i \tag{4.188}$$

The radially mass-averaged value of the aerodynamic efficiency of a biplane Wells turbine is calculated with Eq. (4.189) through the ratio of the output power made available by the two biplane rotors and the inlet power entering the system.

$$\xi_{bp,i} = \frac{dP_{Obp,i}}{dP_{Ibp,i}} = \frac{\int_{r_{hub}}^{r_{tip}} dP_{Obp,i}}{\int_{r_{hub}}^{r_{tip}} (dP_{Obp,i} + dP_{Vbp,i} + dP_{Kbp,i})} \tag{4.189}$$

Therefore, the global efficiency of the biplane configuration depends upon the contributions of either the rotors comprising the turbomachine.

### 4.2.5 Actuator disc model of contra-rotating Wells turbines

The analytical model of contra-rotating Wells turbines investigates the aerodynamics of turbomachines comprised of two rotor cascades moving with opposite senses of rotation, in the absence of guide vanes, as shown in Figures 4.18 and 4.19.

(a) Isometric view (b) Front view

Figure 4.18: Rendering of the **(a)** isometric and **(b)** front sections of the CAD model created for the system with the contra-rotating Wells turbine.

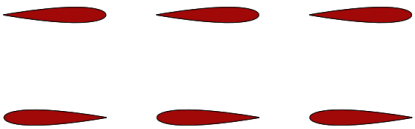

Figure 4.19: Scheme of the blade-to-blade section of the cascades of a contra-rotating Wells turbine.

The model implements a double actuator disc approach, coupling the effects of the two rows to evaluate the fluid dynamics of the entire turbine. As aforementioned in Section 3.2.4, the reciprocal interaction between the rotors is limited owing to the conventional design of contra-rotating Wells turbines, mainly as the ratio between the gap and the chord is greater than unitary. Thus, the influence between the cascades included in the modelling regards the effects of the downstream cascade on the pressure at the inlet and outlet of the upstream cascade and the modification of the velocity triangle of the downstream row owed to the flow distortion caused by the upstream row.

The actuator disc model of a contra-rotating Wells turbine has a similar structure to the biplane configuration. The same procedure explained in Section 4.2.4 is applied for both the upstream and downstream cascades. The main difference between the models is represented by the sign of the angular velocity of the two rows. In the case of contra-rotating rotors, the two cascades have opposite senses of rotation, which result in different signs for $\bar{U}$ and $\bar{\bar{U}}$.

## 4.3 Impulse turbine analytical model

The analytical model developed for the evaluation of the aerodynamics of axial-flow impulse turbines is an original code based on the design practice of axial turbomachines and relies on the blade element momentum theory [21, 221, 50].

As explained in detail in Section 3.3.1 and shown in Figure 4.20, the typical configuration of an axial-flow impulse turbine for wave energy converters relying on the oscillating water column technology has a single rotor cascade and a couple of stator cascades [24].

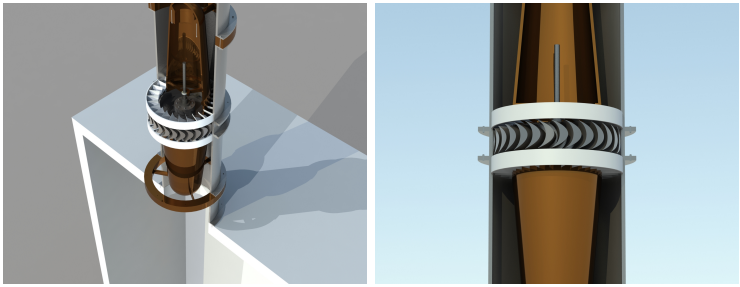

(a) Isometric view (b) Front view

Figure 4.20: Rendering of the **(a)** isometric and **(b)** front sections of the CAD model created for the system with the axial impulse turbine.

The blade-to-blade section of an axial impulse turbine depicted in Figure 4.21 defines the scheme of the airfoils of the three rows.

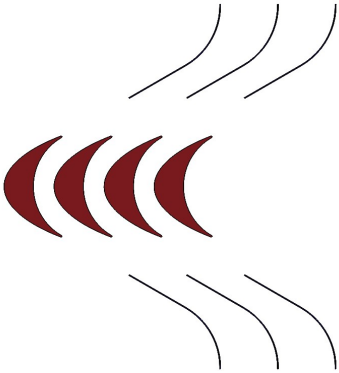

Figure 4.21: Scheme of the blade-to-blade section of the cascades of an axial impulse turbine.

The cascades are modelled as sets of blades, and each of them is considered as a finite number of airfoils stacked in the radial direction. Every couple of adjacent airfoils delineates a single

blade element, characterised by its distinct geometry and subject to peculiar flow conditions. The principal hypothesis of this method is the absence of mutual interactions amongst the different blade elements. This implies the need for an appropriate discretisation of the computational domain by utilising a sufficient number of blade elements in the radial direction.

The analytical model is based upon the application to the present case of the experimental correlations widely used for the design of axial turbomachines, in accordance with the similarities between these applications.

The model was developed with *MATLAB* and is capable of operating in stand-alone mode [227] or integrated into a wave-to-wire model created with *MATLAB* and *Simulink* [126, 33, 24].

A preliminary code for the analysis of axial impulse turbines for OWC systems was implemented at the *Sustainable Energy Research Group* (*SERG*) of the *University of Florence*. This code used a mean line approach based on consolidated correlations for the design of turbomachine cascades and compared the effects of various loss formulations on the prediction of turbine aerodynamics to select the most suited ones for this kind of application [228]. More recently, another preliminary version of the model was implemented in the framework of the present research. This code applied a blade element momentum approach, introducing the analysis of the aerodynamic losses along the blade span for the selected loss correlations. The model considered only a limited range of turbine geometric parameters and operating conditions [210].

Both the other models could only investigate the outflow phase and were decoupled from the OWC chamber. Therefore,

a separate calculation of the primary and secondary converters was necessary to assign the air conditions at the domain inlet of the impulse turbine. For these reasons, the current version of the model is fully automated and generated to allow the joint operation with the models of the primary and tertiary converters. Moreover, it is capable of investigating all the reasonable configurations of geometric parameters and operating conditions.

### 4.3.1 Flow distribution analysis

The arrangement of the rotor blades and stator vanes and the ideal velocity triangles of the air passing through an axial impulse turbine during the inflow and outflow phases are illustrated in Figure 4.22. The inlet guide vane operates as an accelerating row, while the outlet guide vane functions as a diffusive cascade.

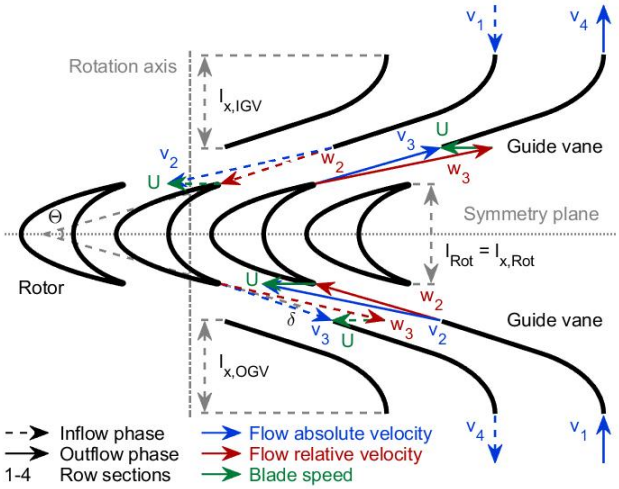


Figure 4.22: Scheme of the blade-to-blade section and ideal velocity triangles of an axial impulse turbine.

The velocity triangles of Figure 4.22 illustrate the ideal trajectories of the flow crossing an axial impulse turbine. Moreover, a scheme of the composition of the ideal velocity triangles and flow angles is presented in Figure 4.23 for the inflow and outflow phases.

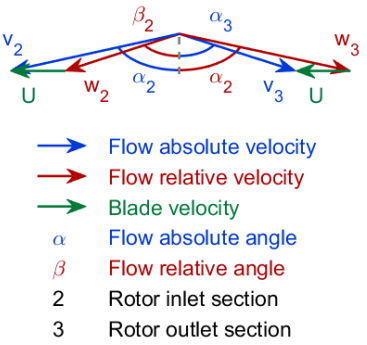


Figure 4.23: Ideal velocity triangles at the inlet and outlet of the turbine rotor of an axial impulse turbine.

In the developed model, the flow deviations from the ideal directions are determined by applying the criterion of Carter and Hughes for the inlet guide vane and rotor and the criterion of Howell for the outlet guide vane.

The approach implemented provides the actual direction of the flow exiting a cascade based on its conditions and the cascade geometry. Since the metal angles of the cascades are designed to perfectly guide the flow in ideal conditions, its deviation implies a misalignment between the flow at the outlet of the upstream row and the inlet of the downstream row. This aspect is particularly important between the rotor and the outlet guide vane, as it is responsible for significant flow blockage and relevant stagnation losses. These effects increase with the magnitude of the

absolute flow deflection imposed by the inlet guide vane and rotor. Thus, the inlet guide vanes are usually designed to have low values of the metal angle at their trailing edge or a movable geometry to reduce the flow blockage at the rotor outlet, and the corresponding losses [229, 32, 230]. Other factors of reduction of these losses are the use of rotor profiles generated by a circular arc and an elliptic arc and the control of flow deflection through the rotor cascade [229, 32, 230]. However, a low metal angle at the trailing edge of the IGV and a small flow deflection through the rotor reduce the net energy transferred by the airflow to the rotor and the turbine efficiency [231]. Instead, the utilisation of movable guide vanes requires a relevant complication of turbine manufacturing and maintenance.

The effects of the misalignment between the direction of the flow exiting the rotor and the outlet guide vane is depicted in Figure 4.24.

The code starts by defining the geometry and operation of the turbomachine, which are provided by the parameters of the following list.

- ◇ Stator and rotor profiles.
- ◇ Metal angles of the stator and rotor cascades.
- ◇ Turbine tip radius.
- ◇ Rotor tip clearance gap.
- ◇ Hub-to-tip ratio.
- ◇ Stator and rotor blade number.
- ◇ Camber line shape.

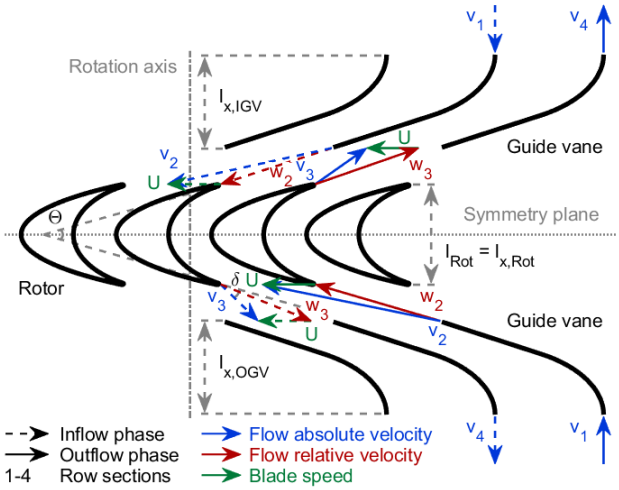


Figure 4.24: Scheme of the blade-to-blade section and the velocity triangles influenced by the flow misalignment between the rotor and outlet guide vane of an axial impulse turbine.

- ◇ Ratio of thickness to chord length.
- ◇ Rotor inertia.
- ◇ Rotor angular velocity.

In particular, a profile created by a circular arc and a straight line is utilised for the stators, and a profile generated by a circular arc and an elliptic arc is used for the rotor. The best-suited angles of the stator and rotor profiles are selected from literature experimental and numerical analyses to optimise the aerodynamics, as explained in detail in Section 3.3.1. The angle of 60 degrees regarding the direction of the machine rotation axis was set at the exit of the IGV and the entrance of the OGV, and at the rotor entrance and exit to promote the correct development of the boundary layer [232, 208, 32].

The definition of the turbine geometry is based on the use of the metal angles of the cascades as input data, as they represent a key design parameter for impulse turbines. This approach allows the operation of the code with fixed geometries of the guide vanes and the fast implementation of the analysis of adjustable geometries for these cascades. In addition, the blade numbers of rotor and stators were assigned as input parameters instead of the chord length, as they are fundamental design parameters affecting the aeroelasticity and aeroacoustics of turbomachines. The use of these parameters as input data allows the possible integration of the model with the outcomes of aeroelastic and aeroacoustic analyses.

Moreover, the environmental conditions and the parameters listed below are assigned to compute the air properties.

- ◇ Atmospheric pressure $p_{amb}$.
- ◇ Atmospheric temperature $\mathcal{T}_{amb}$.
- ◇ Air specific gas constant $\mathcal{R}$.
- ◇ Air heat capacity ratio $\gamma$.
- ◇ Air kinematic viscosity $\mu$.

The airflow conditions at the inlet and outlet sections of the turbine duct are imposed far upstream and downstream of the IGV and OGV, respectively. Since the model is capable of operating either in stand-alone mode and coupled with the model of the caisson, the inlet conditions can be assigned based on literature results or the achievements of former computations or may arise from the iterative cycle coupling the models of the primary and secondary converters.

Regarding the absolute velocity at the domain inlet, its axial component is obtained by imposing the flow continuity with equation Eq. (4.190) and its circumferential component of Eq. (4.191) is null, as the flow is considered uniform and homogeneous.

$$v_{x1,i} = \frac{\dot{m}_{a1,i}}{\rho_{a,i} A_{ann,i}} = \frac{\dot{q}_{a1,i}}{A_{ann,i}} \tag{4.190}$$

$$v_{\theta 1,i} = 0 \tag{4.191}$$

As concerns the camber line shape, the requirement of profile symmetry relative to the flow phases discussed in Section 3.3.1 has to be fulfilled. The possible choices are represented by the circular and parabolic outlines. The latter solution was selected as it allows to reduce the deviation of the flow exiting the blade.

The control of the deviation, which is the difference between the blade and flow angles, is paramount for a rotor cascade imposing a deflection similar to that of axial impulse turbines. The approach widely established in the literature was applied [208, 32, 94].

The maximum ratio of thickness to chord length was set to 0.3 for the rotor and 0.007 for the stators, based on the design practice of this typology of turbomachines [208, 32, 94]. Even for the thickness distribution, the condition of symmetry was respected.

The complete establishment of the geometry of the two stators and the rotor requires calculating the blade chord length for each cascade. Since the blade number and profile shape of all rows are imposed, the chord length of the blades is achieved through the iterative procedure described below.

Regarding the inlet guide vane and the rotor, the blade chord length is computed with an iterative process that applies the criterion of Zweifel and the criterion of Carter and Hughes.

Zweifel's criterion of Eq. (4.161) defines as 0.8 the optimal ratio between the real and ideal blade loading on turbine cascades in order to minimise the aerodynamic losses. From Eq. (4.161), the axial chord length of the two stators is calculated with Eq. (4.192) based on the stator pitch and the absolute flow angles at the inlet and outlet of the cascade, considering that the airflow at the turbine inlet is completely axial.

$$l_{x\mathcal{S},i} = 2.5\mathfrak{t}_{\mathcal{S},i} \cos^2 \alpha_{2,i} (\tan \alpha_{1,i} + \tan \alpha_{2,i}) \tag{4.192}$$

In analogy, the length of the axial chord length of the rotor is computed with Eq. (4.193) as a function of the rotor pitch and the absolute flow angles corresponding to its inlet and outlet sections.

$$l_{x\mathcal{R},i} = 2.5\mathfrak{t}_{\mathcal{R},i} \cos^2 \beta_{3,i} (\tan \beta_{2,i} + \tan \beta_{3,i}) \tag{4.193}$$

The deviation expresses the difference between the angle of the flow exiting a cascade and the metal angle of the cascade blades, as stated by Eqs. (4.194) and (4.195) for a stator and a rotor, respectively.

$$\delta_{\mathcal{S},i} = \alpha_{out,i} - \gamma_{out,i} \tag{4.194}$$

$$\delta_{\mathcal{R},i} = \alpha_{out,i} - \theta_{out,i} \tag{4.195}$$

where $\gamma$ and $\theta$ are the blade angles of the stator and rotor, respectively, and subscript *out* refers to the outlet of a generic

cascade.

The deviation is directed in the sense that it determines the reduction of the flow deflection. Since the magnitude of this parameter may be significant, especially for cascades with large camber angle and pitch to chord ratio, its proper determination during the design stage is a relevant aspect.

The criterion of Carter and Hughes applies Eq. (4.196) to determine the flow deviation across a cascade, based on its geometry in terms of blade shape and camber, pitch to chord ratio and stagger angle.

$$\delta_i = M_{CH,i}\Theta_i\left(\frac{\mathfrak{t}_i}{l_i}\right)^{\mathfrak{m}} \tag{4.196}$$

where $\delta$ is the flow deviation, $M_{CH}$ is a coefficient function of the stagger angle, $\Theta$ is the camber angle, which is the change in angle between the leading and trailing edges of a blade depicted in Figure 4.22, and $\mathfrak{m}$ is a coefficient related to the machine typology, that assumes value 1 for a turbine and value 1/2 for a compressor cascade.

The nominal flow deviation coefficient $M_{CH}$ for parabolic arc camber lines can be determined from Figure 4.25 based on the stagger angle of the stator or rotor.

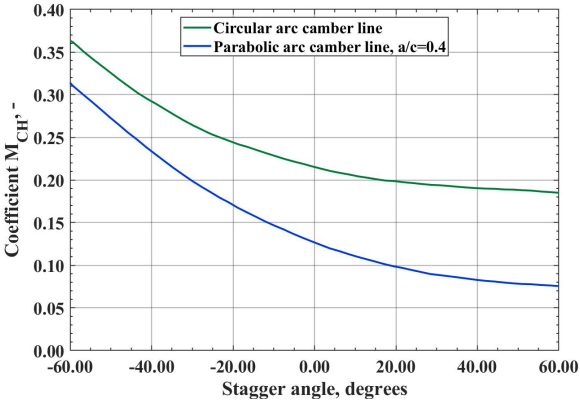


Figure 4.25: Nominal flow deviation coefficient as a function of the stagger angle for circular arc and parabolic arc camber lines.

By substituting the corresponding values of the nominal flow deviation coefficient and the geometric parameters, Eqs. (4.197) and (4.198) are obtained for the IGV and the rotor, respectively.

$$\delta_{IGV,i} = M_{CHIGV,i}\Theta_{IGV,i}\sqrt{\frac{\mathrm{t}_{IGV,i}}{l_{IGV,i}}} \tag{4.197}$$

$$\delta_{\mathcal{R},i} = M_{CH\mathcal{R},i}\Theta_{\mathcal{R},i}\frac{\mathrm{t}_{\mathcal{R},i}}{l_{\mathcal{R},i}} \tag{4.198}$$

The first step of the iterative procedure is the application of the Zweifel′s criterion to initialise the values of the chord length of the cascades based on their geometric angles. Thus, the hypothesis of perfectly guided flow without deviation through the cascades is initially applied. Subsequently, the criterion of Carter and Hughes is utilised to calculate the flow deviation across the cascades, and the criterion of Zweifel is again imposed to determine the chord length of the rows, removing the assumption of perfectly guided flow. The convergence criterion of the iterative

procedure is set to $10^{-3}$ for the length of the chord.

The chord length of the blades of the three cascades can be obtained once the axial chord length is computed. Regarding the rotor, the two values are coincident as its profile is symmetrical, as visible in Figure 4.22, while concerning the stators, the length of the chord depends upon their geometry. By setting the ratio between the length of the circular arc and the straight line defining the shape of the stator, the chord length can be determined from the value of its axial component, as illustrated in Figure 4.26.

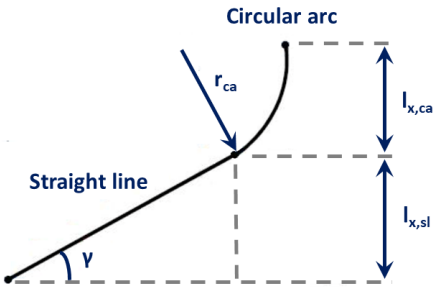


Figure 4.26: Scheme of the blade-to-blade section of a guide vane of an impulse turbine showing the shape defined by a circular arc and a straight line.

A sensitivity analysis to the guide vane shape was performed for an impulse turbine at a laboratory scale: an optimal value of 35% and 65% for the axial chord length of the circular arc and straight line portions, respectively, was determined for the machine efficiency under wave conditions with height and period typical of a moderate Mediterranean wave climate [210].

The flow velocity at the inlet of the impulse turbine is as-

signed by Eqs. (4.190) and (4.191) and the flow trajectories across the IGV and rotor are determined through the iterative process applying the criterion of Zweifel and the criterion of Carter and Hughes described above. Therefore, the velocity triangles upstream and downstream of the inlet guide vane and the rotor are completely defined, as shown in Figure 4.23. The absolute flow angle at the outlet of the IGV is expressed by Eq. (4.199) based on its outlet angle of metal $\gamma_{2,i}$ and the flow deviation $\delta_{IGV,i}$.

$$\alpha_{2,i} = \gamma_{2,i} - \delta_{IGV,i} \tag{4.199}$$

The axial component of the absolute flow velocity is assumed constant through the turbine, according to the consolidated practice in the design of axial-flow action turbomachines [21], thus Eq. (4.200) is obtained. From the axial component of the absolute flow velocity at the outlet of the inlet guide vane, the tangential component and the absolute flow velocity are determined with Eqs. (4.201) and (4.202) by considering the absolute flow angle.

$$v_{x,i} = v_{x1,i} = v_{x2,i} \tag{4.200}$$

$$v_{\theta 2,i} = v_{x,i} \tan \alpha_{2,i} \tag{4.201}$$

$$v_{2,i} = \frac{v_{x,i}}{\cos \alpha_{2,i}} \tag{4.202}$$

The blade velocity is calculated with Eq. (4.203) based on the radius of the blade element considered and the rotor angular velocity.

$$U_i = \Omega r_i \tag{4.203}$$

The flow coefficient is determined with Eq. (4.204) from the axial component of the absolute flow velocity and the blade velocity.

$$\phi_i = \frac{v_{x,i}}{U_i} \tag{4.204}$$

The tangential component of the relative flow velocity is computed with Eq. (4.205) as a function of the absolute flow velocity in the tangential direction and the blade speed.

$$w_{\theta 2,i} = v_{\theta 2,i} - U_i \tag{4.205}$$

The relative flow angle at the exit of the IGV is given by Eq. (4.206). Then, this value and the axial component of the absolute flow velocity are utilised in Eq. (4.207) to calculate the relative flow velocity at this section.

$$\beta_{2,i} = \arctan\left(\frac{w_{\theta 2,i}}{v_{x,i}}\right) = \arctan\left[\tan(\alpha_{2,i} - \phi_i^{-1})\right] \tag{4.206}$$

$$w_{2,i} = \frac{v_{x,i}}{\cos\beta_{2,i}} \tag{4.207}$$

The relative flow angle at the exit of the rotor is determined by the angle of the trailing edge of the rotor blades and the flow deviation at the rotor exit, as expressed by Eq. (4.208).

$$\beta_{3,i} = \gamma - \delta_{\mathcal{R},i} \tag{4.208}$$

By applying equations from Eq. (4.209) to Eq. (4.213), the velocity triangle at the rotor outlet is achieved.

$$w_{3,i} = \frac{v_{x,i}}{\cos \beta_{3,i}} \tag{4.209}$$

$$w_{\theta 3,i} = v_{x,i} \tan \beta_{3,i} \tag{4.210}$$

$$v_{\theta 3,i} = w_{\theta 3,i} - U_i \tag{4.211}$$

$$\alpha_{3,i} = \arctan\left(\frac{v_{\theta 3,i}}{v_{x,i}}\right) = \arctan\left[\tan(\beta_{3,i} - \phi_i^{-1})\right] \tag{4.212}$$

$$v_{3,i} = \frac{v_{x,i}}{\cos \alpha_{3,i}} \tag{4.213}$$

After determining the velocity triangles upstream and downstream of the inlet guide vane and the rotor cascade, an iterative procedure is applied to calculate the flow deviation downstream of the outlet guide vane to define the velocity triangle at the turbine outlet. The OGV is a decelerating and diffusive cascade. Indeed, it reduces the flow velocity and recovers the pressure. For these reasons, the correlations typically applied for assessing the flow through compressor rows were applied.

The empirical rule formulated by Howell in Eq. (4.214) is utilised to estimate the nominal deviation of the flow from the camber angle and pitch to chord ratio of the outlet guide vane [21].

$$\delta_i^* = M_{HW,i} \Theta_i \sqrt{\frac{\mathrm{t}_i}{l_i}} \tag{4.214}$$

where $\delta^*$ is the nominal flow deviation and $M_{HW}$ is a coefficient that depends upon the shape of the camber line and the flow deflection across the cascade.

The iterative process starts with the initialisation of the nominal value of the absolute flow angle at the exit of the OGV $\alpha^*_{4,i}$ with the angle of metal of the cascade $\gamma_{4,i}$, as expressed in Eq. (4.215).

$$\alpha^*_{4,i} = \gamma_{4,i} \tag{4.215}$$

The coefficient $M_{HW}$ is a function of the camber line shape and blade setting. For a diffusing flow, as in the case of the outlet guide vane of an impulse turbine, its value is given by Eq. (4.216). An iterative process is applied to determine $M_{HW}$ by initialising the value of $\alpha^*_{4,i}$ through Eq. (4.215).

$$M_{HW} = 0.232\left(\frac{\mathfrak{a}_{LE}}{l_i}\right)^2 + \frac{\alpha^*_{4,i}}{500} \tag{4.216}$$

where $\mathfrak{a}_{LE}$ is the distance from the leading edge corresponding to the maximum difference between the camber line and the chord.

By substituting Eq. (4.216) into Eq. (4.214), the value of the flow deviation is obtained with Eq. (4.217) at the first step of the iterations.

$$\delta^*_i = \left[0.232\left(\frac{\mathfrak{a}_{LE}}{l_i}\right)^2 + \frac{\alpha^*_{4,i}}{500}\right]\Theta_i\sqrt{\frac{\mathfrak{t}_i}{l_i}} \tag{4.217}$$

The absolute flow angle at the exit of the OGV is computed at the first step of the procedure with Eq. (4.218) based on the blade angle at the exit of the OGV and the value of the flow deviation at the first iterative step.

$$\alpha^*_{4,i} = \gamma_{4,i} - \delta^*_i \tag{4.218}$$

The calculation of Eqs. (4.217) and (4.218) is iterated until

the convergence criterion of $10^{-3}$ is reached for the outlet flow angle.

Subsequently, the flow deflection across the outlet guide vane has to be determined. For this purpose, the low-speed correlation of Eq. (4.219) formulated by Howell was applied [25]. The correlation expresses the nominal value of the flow deflection across a diffusing cascade $\epsilon^*$ as the 80% of the stalling flow deflection $\epsilon_{st}$.

$$\epsilon^* = 0.8\epsilon_{st} \tag{4.219}$$

The formula is, therefore, a correlation of stalling deflection, as more directly noticeable in Eq. (4.220).

$$\epsilon_{st} = 1.25\epsilon^* \tag{4.220}$$

The relation of Eq. (4.219) was determined from experiments performed on low-speed compressors for a wide variety of geometries, operating conditions, and intervals of flow incidence. The correlation has been widely applied for the design of axial-flow compressors, and it is a compromise between conservative and optimistic predictions [21]. The nominal values of the flow deflection for different configurations of compressor rows depend upon the pitch to chord ratio, the nominal absolute flow angle at the cascade outlet, and the Reynolds number [25, 21], as expressed by Eq. (4.221).

$$\epsilon^* = f\left(\frac{\mathsf{t}}{l}, \alpha^*_{out}, Re\right) \tag{4.221}$$

The formula is independent of the cascade camber angle for the typical values of the parameter used in turbomachinery de-

sign, which are comprised in the range between 20 and 40 degrees. The dependency on the Reynolds number is limited for values lower than $3 \cdot 10^5$ calculated based on the blade chord length [21, 25].

The nominal flow deflection to the vary of the nominal outlet angle of the correlation of Howell is represented in Figure 4.27 for typical values of the pitch to chord ratio [21, 25].

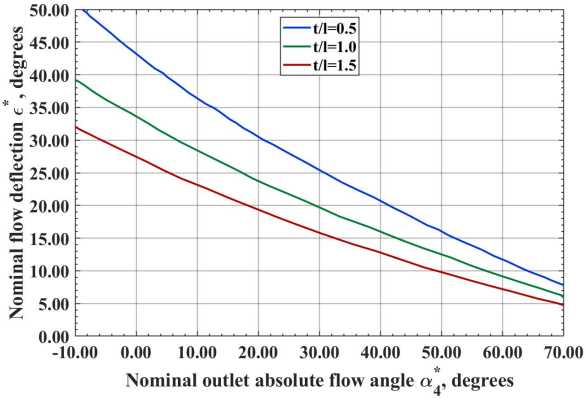


Figure 4.27: Nominal flow deflection as a function of the nominal outlet absolute flow angle for typical values of the pitch to chord ratio, adapted from Howell [25].

For the nominal values of the absolute flow angle between 0 and 40 degrees, the tangent-difference rule of Eq. (4.222) determined by Howell could be applied to obtain an approximation of the data of Figure 4.27 during the preliminary design stages. The formula expresses the flow deviation as a function of the pitch to chord ratio [25, 21].

$$\tan \alpha_{3,i}^* - \tan \alpha_{4,i}^* = \frac{1.55}{1 + 1.5 \frac{t_i}{l_i}} \tag{4.222}$$

In the model of the impulse turbine developed, the nominal flow deflection is obtained by interpolating the curves of Figure 4.27 using as input data the nominal value of the absolute flow angle at the exit of the OGV determined with the iterative procedure previously described. Then, the value of $\alpha_4^*$ is utilised to determine the nominal flow deflection across the row $\epsilon^*$. From these parameters, the nominal value of the absolute flow angle at the entrance of the OGV is determined with Eq. (4.223).

$$\alpha_{3,i}^* = \epsilon^* - \alpha_{4,i}^* \tag{4.223}$$

The nominal value of the incidence angle of the flow entering the outlet guide vane $\mathrm{i}_{3,i}^*$ can be computed with Eq. (4.224), while the effective value of the incidence angle $\mathrm{i}_{3,i}$ is provided by Eq. (4.225).

$$\mathrm{i}_{3,i}^* = \alpha_{3,i}^* - \gamma_{3,i} \tag{4.224}$$

$$\mathrm{i}_{3,i} = \alpha_{3,i} - \gamma_{3,i} \tag{4.225}$$

The difference between the effective and nominal values of the flow incidence $\mathrm{i}_{3,i} - \mathrm{i}_{3,i}^*$ and the nominal value of the flow deflection $\epsilon^*$ are utilised to determine the effective deflection of the flow across the outlet guide vane. The relation expressing the off-design operation of a compressor row obtained by Howell in Figure 4.28 is applied to determine the effective flow deflection [21, 25].

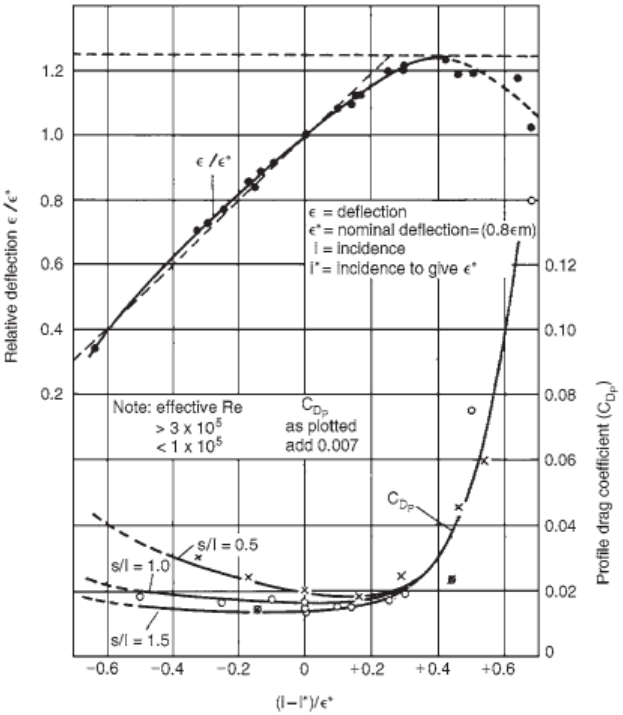


Figure 4.28: Curves of the off-design performance of a compressor row [21].

From the relative deflection $\epsilon/\epsilon^*$ obtained with Figure 4.28, the effective flow deflection can be easily determined based on the nominal value of the parameter of Eq. (4.219). The absolute flow angle at the exit of the guide vanes is provided by Eq. (4.226).

$$\alpha_{4,i} = \alpha_{3,i} - \epsilon_i \tag{4.226}$$

Therefore, the velocity triangle at the turbine outlet is obtained with Eqs. (4.227) and (4.228).

$$v_{\theta 4,i} = v_{x,i} \tan \alpha_{4,i} \tag{4.227}$$

$$v_{4,i} = \frac{v_{x,i}}{\cos \alpha_{4,i}} \tag{4.228}$$

The specific work $L_{b,i}$ exerted by the flow on each blade element of the rotor is determined with Euler′s theorem for turbomachinery of Eq. (4.229), based on the velocity triangles upstream and downstream of the rotor row.

$$L_{b,i} = U_i(v_{\theta 2,i} + v_{\theta 3,i}) \tag{4.229}$$

The power $P_{b,i}$ exchanged between the flow and a blade element of the rotor is obtained with Eq. (4.230) through Euler′s theorem, which relates the specific work to the velocity triangles of the rotor.

$$P_{b,i} = \dot{m}_{a,i} L_{b,i} = \rho_{a,i} A_{ann,i} v_{x,i} U_i (v_{\theta 2,i} + v_{\theta 3,i}) \tag{4.230}$$

The power transformed by the rotor blades is achieved with Eq. (4.231) by numerical integration in the spanwise direction of the contributions of all the blade elements.

$$P_b = \int_{r_{hub}}^{r_{tip}} \rho_{a,i} A_{ann,i} v_{x,i} \Omega (v_{\theta 2,i} + v_{\theta 3,i}) dr \tag{4.231}$$

From Eq. (4.230), the torque of each blade element $\tau_{b,i}$ is calculated with Eq. (4.232) by diving the rotor power for its rotational speed.

$$\tau_{b,i} = \frac{P_{b,i}}{\Omega} \tag{4.232}$$

The torque acting on rotor blades $\tau_b$ is provided by Eq. (4.233) based upon the integral form of rotor blade power.

$$\tau_b = \frac{P_b}{\Omega} \tag{4.233}$$

### 4.3.2 Loss determination

The analysis of the performance of an impulse turbine requires the estimation of the aerodynamic losses. Generally, all the causes of efficiency reduction of a turbomachine addressable to the flow are considered in this category.

During the preliminary phases of the modelling, the most widespread approaches for evaluating machine losses were considered and compared to determine the best solutions for the analysis of axial impulse turbines for oscillating water column wave energy converters. In particular, for the accelerating cascades, represented by the inlet guide vane and the rotor, the loss correlation of Soderberg and the correlation of Ainley and Mathieson, with the corrections proposed by Dunham and Came, Kacker and Okapuu, and Moustapha, were considered. Concerning the diffusing cascade, the correlations of Howell and Lieblein were taken into account. All these formulations were obtained from experimental campaigns performed on a wide variety of turbine and compressor cascades and represent the common practice in turbomachinery design [21].

After the preliminary analysis of the effects of the different approaches, the model of Ainley and Mathieson was chosen for the accelerating row, and the model of Howell was selected for the diffusing row. In particular, the correlation of Ainley and Mathieson provides a more accurate prediction of the losses of the IGV and rotor regarding the correlation of Soderberg, which neglects the effects of the profile shape of the cascades and the

level of reaction of the turbomachine. As concerns the OGV, the correlation of Howell was chosen to overcome the limitations imposed by the range of validity of the correlation of Lieblein, which considers only the positive values of the incidence angle. This limit is in contrast with the bidirectional airflow characterising the operation of oscillating water column systems. An extensive analysis of the effects of these loss formulations can be found in the mean line model initially proposed by the *SERG* [228].

The power losses that occur in turbomachine cascades are typically classified as listed below based on their effects on the flow field [233].

- ◇ Profile losses.
- ◇ Endwall losses.
- ◇ Tip leakage losses.

The contribution of the above categories to the total flow losses of a turbomachine depends upon its typology and geometry, mainly in terms of the aspect ratio of the blades and the type and size of the tip gap. A general assessment of these phenomena considers a comparable influence of the three categories on the turbine performance, with everyone responsible for approximately 1/3 of the overall flow losses [233]. The losses determine an increase of the entropy, occurring due to three transformations of thermo-fluid dynamics: viscous friction in the free shear layers and boundary layers, heat exchanges, and non-equilibrium processes arising with shock waves or sudden expansions [233].

In Figure 4.29 a general representation of the main vortices characterising the airflow in a turbomachine is provided.

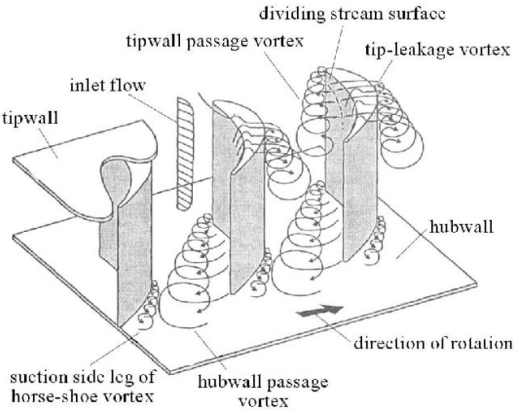


Figure 4.29: Scheme of the main vortices present in a rotating cascade of a turbomachine [26].

The profile losses consider the power dissipations caused by the formation of boundary layers on the surfaces of turbomachine vanes or blades far from endwalls. The viscous forces acting on the fluid in the boundary layer determine its velocity reduction and entropy rise regarding the free shear flow. This implies the growth of the entropy for a flow exiting a cascade relative to its inlet conditions. For a particular flow rate, the result is an increase of the pressure variation across a row regarding an isentropic flow. Since the pressure difference disposable at the turbine is determined for a specific machine configuration and peculiar operating conditions, the profile losses determine the decrease of the flow rate and the rise of the entropy. Consequently, the rotor power and the cascade efficiency lowering.

The parameters affecting the profile losses concern the flow in terms of Reynolds number and Mach number, and the vane or blade in terms of surface roughness and trailing edge thickness [233].

The endwall losses are determined by the flow velocity com-

ponents that do not belong to the blade-to-blade section of a turbomachine cascade. Since this is the main plane of the machine, these flows are usually referred to as secondary flows, and the related losses are typically categorised as secondary losses, as they include all the losses that are not otherwise considered. Therefore, the secondary flow is defined as the difference between the actual flow crossing a cascade and the ideal axisymmetric flow.

Several effects provide the complete secondary motion of a flow: the cascade secondary flow due to the turning of the mainstream, the mainstream secondary flow inside the passage owing to vortices developing from blades, the secondary flow at the tip of vanes and blades, the cross flows in the annulus boundary layer due to rotation and blade scraping effect, and the inward or outward radial flows owing to radial pressure gradients for stators or blade rotation for rotors [234].

The boundary layers of the endwall are transported inwards along the blade suction side by the action of the mainstream crossing the vane. This causes a disruption of the flow field, and it is responsible for relevant total pressure losses, determining the decrease of flow rate across a machine, for a given pressure drop, regarding an isentropic flow.

The secondary losses include, in particular, the skin friction losses related to the formation of boundary layers on the surfaces of the annulus walls of a turbomachine, which depend on the Reynolds number, the Mach number, and the wall roughness.

The tip leakage losses are causes of power decay owing to the pressure difference between the pressure side and suction side at the tip of rotor blades, as illustrated in Figure 4.30.

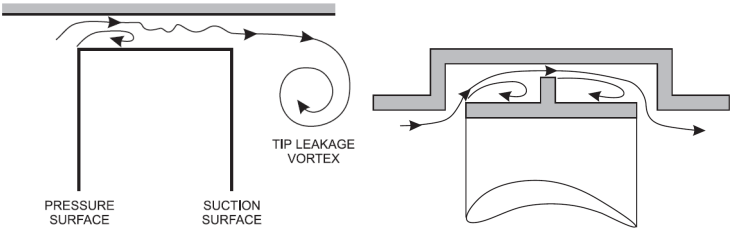


(a) Unshrouded blade (b) Shrouded blade

Figure 4.30: Scheme of the flow leakage at the tip of rotor blades [27]

The difference in the pressure is determined by the rotation of the cascade and forces the flow to pass through the thin gap between the blade tip and the annulus outer wall, without exchange of angular momentum with the blade. Therefore, the tip leakage causes the reduction of power transfer and the decrease of rotor efficiency. Moreover, this phenomenon has a complex interaction with the mainstream flow and the secondary flows. The parameters affecting the tip leakage losses are the typology of the gap between the blade tip and annulus wall, the tip gap size, the rotor angular velocity, the difference between the values of the magnitude and direction of the leakage flow and mainstream velocity, the flow turning in a cascade, and the inlet flow angle [27]. The types of clearance gaps mainly depend on the presence of unshrouded or shrouded blades and smooth or grooved walls.

The Mach number of the flow is significantly lower than 0.5 in the present application. Therefore, the air compressibility effects are negligible for the secondary converter. Moreover, the heat exchange and temperature variation across the cascades are negligible. Consequently, these two aspects are not considered

in the modelling.

The losses of the inlet guide vane and rotor were estimated by applying the correlations formulated by Ainley and Mathieson. In this approach, the global values of the total pressure losses of turbomachines in design and off-design conditions are determined by the profile, tip clearance, and secondary losses. Relevant improvements of the methodology were proposed by Dunham and Came in 1970, by Kacker and Okapuu in 1981, and by Moustapha et al. in 1990. The first two advancements regard the formulation of the profile, secondary, and tip clearance loss coefficients in design conditions, while the third advancement concerns the off-design operation.

For evaluating the cascade losses, the profile loss coefficient $\Upsilon$ is defined in Eq. (4.234) as the ratio of the total pressure difference across the cascade to the difference between the total and static values of the pressure at the cascade outlet.

$$\Upsilon = \frac{p_{t,in} - p_{t,out}}{p_{t,out} - p_{out}} \tag{4.234}$$

Since the air compressibility effects are negligible in the current application, Eq. (4.234) can be simplified to Eq. (4.235).

$$\Upsilon = \frac{p_{t,in} - p_{t,out}}{\frac{1}{2}\rho v_{out}^2} \tag{4.235}$$

Therefore, Eq. (4.236) is obtained for the inlet guide vane, while Eq. (4.237) is achieved for the rotor.

$$\Upsilon_{IGV} = \frac{p_{t1} - p_{t2}}{\frac{1}{2}\rho v_2^2} \tag{4.236}$$

$$\Upsilon_{\mathcal{R}} = \frac{p_{t2} - p_{t3}}{\frac{1}{2}\rho w_3^2} \tag{4.237}$$

The correlation of Ainley and Mathieson expresses the profile losses to the change of the absolute flow angles at the cascade inlet and outlet, the chord to pitch ratio of the row, and the maximum thickness to chord ratio of the blades. For cascades with $t/l = 0.2$ and flows with $Re = 2 \cdot 10^5$ and $Ma < 0.5$, the variation of the profile losses determined for nozzles and blade rows are represented in Figures 4.31a and 4.31b, respectively, as against the pitch to chord ratio, for different values of the absolute flow angle at the cascade outlet [28].

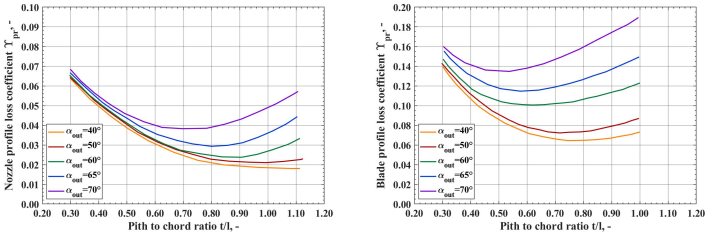


(a) Stator cascade (b) Impulse rotor cascade

Figure 4.31: Profile loss coefficient at null flow incidence angle for (**left**) nozzle cascades and (**right**) rotor cascades, adapted from Ainley and Mathieson [28]

By comparing the two cases, it is noticeable that the profile loss coefficient is significantly lower for nozzle blades than for rotor blades.

For intermediate configurations in terms of flow angles and maximum thickness to chord length ratio, Eqs. (4.238) and (4.239) provide the linear interpolation formula of the correlation of Ainley and Mathieson of Figure 4.31 for the two cascade typologies [235].

$$\Upsilon_{pr,(\mathrm{i}=0)} = \left\{ \Upsilon_{pr,(\alpha_{in}=0)} + \left( \frac{\alpha_{in}}{\alpha_{out}} \right)^2 \right.$$
$$\left. [\Upsilon_{pr,(\alpha_{in}=\alpha_{out})} - \Upsilon_{pr,(\alpha_{in}=0)}] \right\} \left( 5 \frac{\bar{t}_{h,max}}{l} \right)^{\frac{\alpha_{in}}{\alpha_{out}}} \tag{4.238}$$

$$\Upsilon_{pr,(\mathrm{i}=0)} = \left\{ \Upsilon_{pr,(\beta_{in}=0)} + \left( \frac{\beta_{in}}{\alpha_{out}} \right)^2 \right.$$
$$\left. [\Upsilon_{pr,(\beta_{in}=\alpha_{out})} - \Upsilon_{pr,(\beta_{in}=0)}] \right\} \left( 5 \frac{\bar{t}_{h,max}}{l} \right)^{\frac{\beta_{in}}{\alpha_{out}}} \tag{4.239}$$

where $\alpha_{in}$ and $\beta_{in}$ are the absolute and relative flow angles at the inlet of the nozzle and cascade, respectively, $\alpha_{out}$ is the absolute flow angle at the outlet of the cascade, $\bar{t}_{h,max}$ is the maximum blade thickness, $\Upsilon_{pr,(\alpha_{in}=0)}$, $\Upsilon_{pr,(\beta_{in}=0)}$, $\Upsilon_{pr,(\alpha_{in}=\alpha_{out})}$, and $\Upsilon_{pr,(\beta_{in}=\alpha_{out})}$ are the profile loss coefficients of equivalent cascades with axial flow and perfectly symmetric flow, expressed to the change of the pitch to chord ratio, according to Figure 4.31.

The correlation of Eq. (4.238) is valid in the range $0.15 \leq \bar{t}_{h,max}/l \leq 0.25$ because a correction for the effect of the blade thickness to chord ratio is included in the correlation. For values external to the interval, the loss can be approximated to that of a cascade with blades with ratio equal to the closest limit [28].

When in Eq. (4.239) the inlet absolute flow angle is zero and the blade thickness to chord ratio is equal to 0.2, the loss coefficient for stator nozzles $\Upsilon_{pr,(\alpha_{in}=0)}$ at null flow incidence of Figure 4.31a is obtained. In analogy, when in Eq. (4.239) the in-

let and outlet absolute flow angles are equivalent and the blade thickness to chord ratio is equal to 0.2, the loss coefficient for rotor blades $\Upsilon_{pr,(\alpha_{in}=\alpha_{out})}$ at null flow incidence of Figure 4.31b is achieved [21].

The correlation of Ainley and Mathieson is formulated to determine the profile losses for a cascade with null flow incidence. For values of incidence different from zero, a procedure for correcting the profile losses is applied based on an equivalent cascade with the value of 0.75 for the pitch to chord ratio. The first step of the process is the use of Figure 4.32 for determining the ratio of the outlet absolute flow angles of the investigated and equivalent cascades $\alpha_{out}/\alpha_{out(t/l=0.75)}$ with pitch to chord ratio $t/l$ assigned.

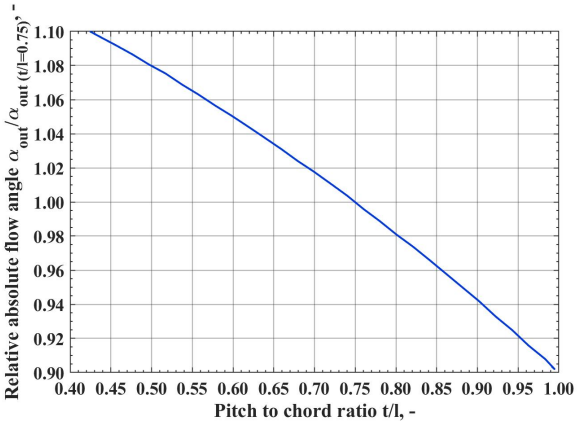


Figure 4.32: Ratio of outlet absolute flow angles as a function of the pitch to chord ratio, adapted from Moustapha et al. [29].

Subsequently, Figure 4.33 is applied to obtain the flow incidence angle in stall conditions of the equivalent row based on its inlet absolute flow angle and outlet absolute flow angle, deter-

mined with the previous step. The stall incidence is defined as the condition corresponding to a value of $\Upsilon_{pr}/\Upsilon_{pr,(i=0)} = 2$ for the profile loss coefficients.

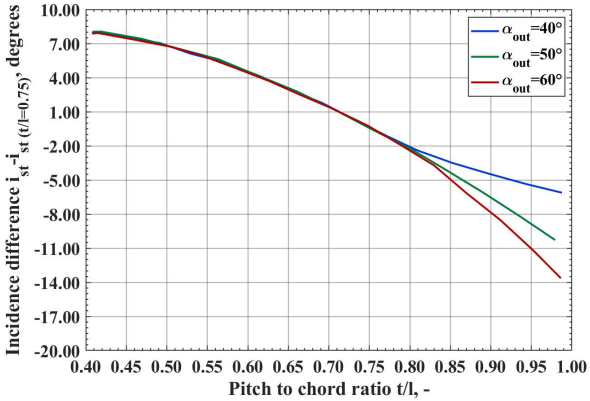


Figure 4.33: Stall incidence angle of the equivalent cascade with $t/l = 0.75$ as against its ratio of inlet and outlet absolute flow angles, for several values of $\alpha_{out}$, adapted from Moustapha et al. [29].

At the following step, the pitch to chord ratio is utilised to determine the difference in incidence stall angle for the investigated row and the equivalent row through Figure 4.34 with the pitch to chord ratio and the outlet absolute flow angle of the analysed row as input parameters.

Finally, the effective profile loss coefficient of the investigated cascade is achieved with Figure 4.35, which provides the multiplication factor to be applied to the reference profile losses of the equivalent cascade with zero stalling incidence.

In general, Figure 4.35 defines the profile loss coefficient of a wide interval of flow incidence angles regarding the profile loss coefficients at an incidence equal to zero, as a function of the

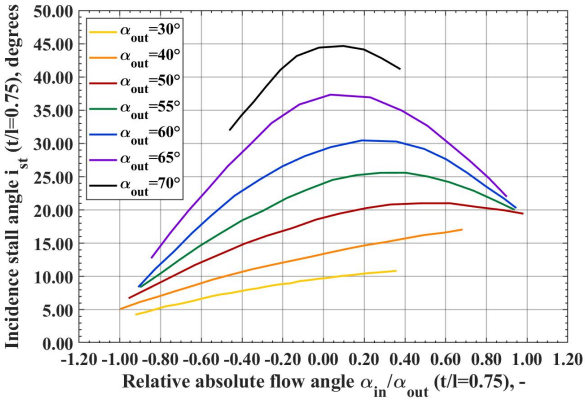


Figure 4.34: Difference in incidence stall angle for the analysed and equivalent rows to the change of the pitch to chord ratio, for several values of $\alpha_{out}$, adapted from Moustapha et al. [29].

ratio between the effective and stall incidence angles.

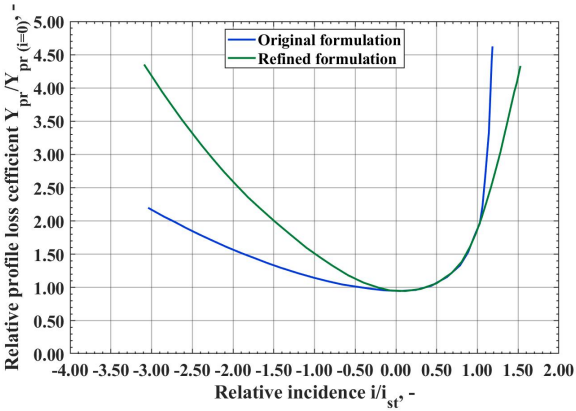


Figure 4.35: Profile loss coefficient ratio as a function of the flow incidence ratio, adapted from Moustapha et al. [29].

Ainley and Mathieson achieved the formulation of the pro-

file loss coefficient from experiments conducted with a flow with Reynolds number equal to $2 \cdot 10^5$ referred to the mean chord length and outlet flow conditions. For lower values of the Reynolds number, down to $5 \cdot 10^4$, the correction of Eq. (4.240) has to be applied to the total-to-total stage efficiency [21].

$$(1 - \xi_{tt}) \propto Re^{-0.2} \tag{4.240}$$

The secondary losses are caused by the non-uniformity of the complex three-dimensional flow field inside turbomachine nozzles and vanes. According to the approach of Ainley and Mathieson, the drag coefficient of Eq. (4.241) is defined to account for these losses based on the parameter $\lambda$, which depends on the acceleration of the flow crossing the cascade.

$$C_{D,se} = \frac{l}{\mathfrak{t}} \lambda C_L^2 \tag{4.241}$$

The drag coefficient related to secondary losses can be written in the form of Eq. (4.242) by considering the definitions of the loss coefficient for incompressible flows of Eq.(4.235) and the drag coefficient [21].

$$C_{D,se} = \frac{\mathfrak{t}}{l} \frac{p_{t,in} - p_{t,out}}{\frac{1}{2}\rho_{av} v_{av}^2} \frac{\cos^3 \alpha_{av}}{\cos^2 \alpha_{out}} \tag{4.242}$$

where the subscript $av$ refers to the average between the inlet and outlet of the cascade.

Therefore, the formulation of the secondary loss coefficient of Eq. (4.243) is obtained.

$$\Upsilon_{se} = \frac{l}{\mathfrak{t}} \frac{C_{D,se} \cos^2 \alpha_{out}}{\cos^3 \alpha_{av}} \tag{4.243}$$

By substituting Eq.(4.241) into Eq. (4.243), the secondary loss coefficient can be expressed even in terms of aerodynamic

loading coefficient $\Gamma_{ae}$ through Eq. (4.244).

$$\Upsilon_{se} = \lambda \left( \frac{l}{\mathfrak{t}} \right)^2 \frac{C_L^2 \cos^2 \alpha_{out}}{\cos^3 \alpha_{av}} = \lambda \Gamma_{ae} \tag{4.244}$$

The average value of the absolute flow angle $\alpha_{av}$ and the lift coefficient $C_L$ of Eq. (4.244) are provided by Eqs. (4.245) and (4.246), respectively.

$$\alpha_{av} = \arctan \left( \frac{v_{\theta,av}}{v_{x,av}} \right) \tag{4.245}$$

$$C_L = 2 \frac{\mathfrak{t}}{l} (\tan \alpha_{in} + \tan \alpha_{out}) \cos(\alpha_{av}) + C_{D,se} \tan \alpha_{av} \tag{4.246}$$

The flow acceleration coefficient $\lambda$ is determined through Figure 4.36 relying on the geometric coefficient $C_{\mathfrak{g}}$ defined in Eq. (4.247).

$$C_{\mathfrak{g}} = \frac{\left( \frac{A_{ann,out}}{A_{ann,in}} \right)^2}{1 + \frac{r_{hub}}{r_{tip}}} \tag{4.247}$$

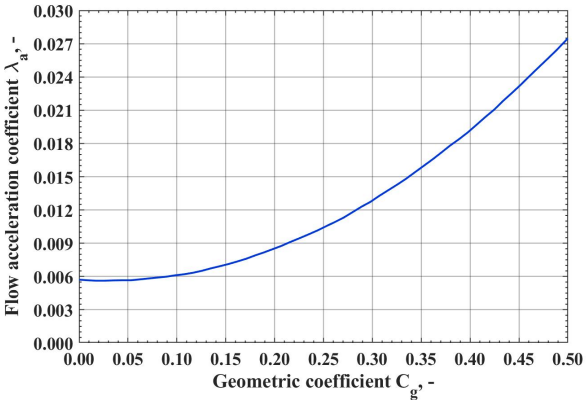


Figure 4.36: Distribution of the flow acceleration coefficient as a function of the geometric coefficient.

Dunham and Came proposed the correction approach of Eqs. (4.248) and (4.249) for both the profile and secondary loss coefficients, based on the sum of the two loss contributions and the Reynolds number [236].

$$\Upsilon_{pr} + \Upsilon_{se} \propto Re^{-0.2} \tag{4.248}$$

$$f(Re) = \begin{cases} \left(\dfrac{Re}{2 \cdot 10^5}\right)^{-0.4} & if\ Re \leq 2 \cdot 10^5 \\ 1 & if\ 2 \cdot 10^5 < Re \leq\ 1 \cdot 10^6 \\ \left(\dfrac{Re}{1 \cdot 10^6}\right)^{-0.2} & if\ Re > 1 \cdot 10^6 \end{cases} \tag{4.249}$$

where $f(Re)$ is the corrective factor depending on the Reynolds number formulated by Dunham and Came.

The tip clearance losses are related to the flow leakage through the gap between the blade tip and the inner surface of the turbine casing. To determine this effect, the tip clearance loss coefficient $\Upsilon_{tc}$ defined in Eq. (4.250) is utilised.

$$\Upsilon_{tc} = \mathfrak{B}\frac{t}{b}C_L^2\left(\frac{l}{\mathfrak{t}}\right)^2\cos^2(\alpha_{out})\cos^3(\alpha_{av}) \tag{4.250}$$

where the coefficient $\mathfrak{B}$ depends on the typology of tip clearance gap, and it assumes a value of 0.25 for unshrouded blades and 0.5 for shrouded blades.

The overall loss coefficient of an accelerating cascade is calculated as the sum of the tip clearance loss coefficient and the product between the corrective factor based on the Reynolds number and the sum of the profile and secondary loss coefficients. Through this procedure, the loss coefficients of the inlet guide vane and rotor are achieved with Eqs. (4.251) and (4.252), respectively.

$$\Upsilon_{AM,IGV} = (\Upsilon_{pr,IGV} + \Upsilon_{se,IGV})f(Re) + \Upsilon_{tc,IGV} \tag{4.251}$$

$$\Upsilon_{AM,\mathcal{R}} = (\Upsilon_{pr,\mathcal{R}} + \Upsilon_{se,\mathcal{R}})f(Re) + \Upsilon_{tc,\mathcal{R}} \tag{4.252}$$

As regards the outlet guide vane, the evaluation of the aerodynamic losses was achieved by applying the correlation of Howell [21, 25]. This correlation relies upon experimental data measured on diffusive profiles of compressors. The correlation subdivides the cascade losses in profile losses on the blade surfaces, skin friction losses on the annulus walls, and secondary losses for the contributions not included in the previous categories. The

estimation of the losses of Equation (4.253) is based on an equivalent overall drag coefficient $C_{D,HW}$ given by the sum of the effects of the profile, skin friction, and secondary drag coefficients, indicated as $C_{D,pr}$, $C_{D,sf}$, and $C_{D,se}$, respectively.

$$CD_{HW} = CD_{pr} + CD_{sf} + CD_{se} \tag{4.253}$$

The value of $C_{D,pr}$ is obtained from Figure 4.28, while $C_{D,sf}$ and $C_{D,se}$ are calculated with Eqs. (4.254) and (4.255), respectively [25].

$$CD_{sf} = 0.02\frac{\mathfrak{t}}{b} \tag{4.254}$$

$$CD_{se} = 0.018C_L \tag{4.255}$$

The equivalent overall drag coefficient is related to the total-to-total pressure drop across the cascade by Eq. (4.256).

$$C_{D,HW} = \frac{\mathfrak{t}}{l}\frac{(p_{t,3} - p_{t,4})\cos\alpha_{av,O\mathcal{GV}}}{\frac{1}{2}\rho v^2_{av,O\mathcal{GV}}} \tag{4.256}$$

The explicit form of the total pressure at the entrance of the OGV is obtained in Eq. (4.257) based on the formulation of the equivalent overall drag coefficient of Eq. (4.256).

$$p_{t,3} = p_{t,4} + \frac{l}{\mathfrak{t}}\frac{C_{D,HW}\frac{1}{2}\rho v^2_{av,O\mathcal{GV}}}{\cos\alpha_{av,O\mathcal{GV}}} \tag{4.257}$$

The total pressure at the inlet of the rotor is obtained with Eq. (4.258) by making explicit the pressure from Eq. (4.237).

$$p_{t,2} = p_{t,3} + \Upsilon_{\mathcal{R}}\frac{1}{2}\rho w_3^2 \tag{4.258}$$

In analogy, the total pressure at the entrance of the inlet

guide vane is provided by Eq. (4.259) by rearranging Eq. (4.236).

$$p_{t,1} = p_{t,2} + \Upsilon_{IGV} \frac{1}{2} \rho v_2^2 \tag{4.259}$$

The infinitesimal power input of each blade element of the turbine is given by Eq. (4.260) as the product of the total-to-static pressure drop across the turbine and the volume flow rate.

$$dP_{I,i} = (p_{t1,i} - p_{4,i}) d\dot{q}_{,i} \tag{4.260}$$

The aerodynamic efficiency of every blade element $\xi$ is defined in Eq. (4.261) by the ratio of the infinitesimal blade power output and the corresponding infinitesimal power input.

$$\xi_i = \frac{dP_{O,i}}{dP_{I,i}} \tag{4.261}$$

The radially mass-averaged aerodynamic efficiency of the rotor is achieved by numerical integration along the blade span with Eq. (4.262).

$$\xi_i = \frac{\int_{r_{hub}}^{r_{tip}} \rho_{a,i} A_{ann,i} v_{x,i} \Omega (v_{\theta 2,i} + v_{\theta 3,i}) dr}{\int_{r_{hub}}^{r_{tip}} (p_{t1,i} - p_{4,i}) d\dot{q}_{,i}} \tag{4.262}$$

## 4.4 Electric generator analytical model

The model of the OWC system includes the coupling of the turbine aerodynamics and dynamics with the electric generator dynamics through the control strategy. Indeed, the system operation depends upon the interaction of the secondary and tertiary converters, besides the primary converter, represented by the chamber.

The mechanical torque produced by the turbine is transmitted to the electric generator by a mechanical coupling at the

shaft. Since a simplified control system was implemented, this aspect was modelled by neglecting the aerodynamic friction torque caused by the wind losses [33, 24]. Thus, the relation can be expressed through Eq. (4.263).

$$J\dot{\Omega} = \tau_{\mathfrak{t}} - \tau_{\mathfrak{g}} \tag{4.263}$$

where $J$ is the rotational inertia of the rotor, $\dot{\Omega}$ is the rotor angular acceleration, and $\tau_{\mathfrak{t}}$ and $\tau_{\mathfrak{g}}$ are the torque of the turbine and generator, respectively.

The control system implemented is based on the monitoring of the instantaneous values of the rotor torque and rotational speed in design conditions. When the rotor torque is negative, the generator is disconnected from the rotor, which decelerates according to its inertia. On the contrary, when the torque is positive, the logic of the system of equations of Eq. (4.264) is pursued [33, 24].

$$\begin{cases} \Omega \geq \Omega_o \rightarrow \tau_{\mathfrak{g}} = \tau_{\mathfrak{t}} \\ \Omega < \Omega_o \rightarrow \tau_{\mathfrak{g}} = 0 \end{cases} \tag{4.264}$$

where $\Omega_o$ is the design angular velocity of the rotor.

For positive values of the turbine torque, the rotor is free to accelerate, and the generator is disconnected until the design angular velocity is reached; once the rotational speed equals or exceeds the design speed, the electric load is instantly connected [33, 24].

The electrical power made available by the generator is finally calculated with Eq. (4.265) by multiplying the turbine power $P_b$ for the organic efficiency $\xi_o$ and the electrical efficiency $\xi_e$ of the

generator. Both these efficiencies are assumed equal to 0.97 for taking into account the typical values of the losses.

$$P_e = \xi_o \xi_e P_b \tag{4.265}$$

# Chapter 5

# Computational fluid dynamics modelling

*The theoretical aspects of the computational fluid dynamics are analysed in the light of the models of the turbomachines developed. The conservation laws leading to the governing equations applied for solving aerodynamics with numerical methods are described. The main computational schemes are discussed, focusing on the effects of the selection of the turbulence models and the approaches for modelling the rotation of the turbine rotor.*

## 5.1 Conservation laws

The laws governing fluid flow rely on conservation laws. The principle of conservation of fluid dynamics imposes the balance between the accumulation of a certain fluid quantity inside a control volume and the difference between the flux of the quantity through the volume surface and the transformation of that quantity within the volume. The fluxes are determined by bulk con-

vection, responsible for directed mass flows and diffusion, which causes fluid motion without prevalent directionality [237].

In Figure 5.1, a generic volume $V$ contained inside a surface of area $A$ is depicted. The volume and the area are fixed in an inertial reference system. Considering an infinitesimal area, the normal vector to this area $d\mathbf{A}$ is conventionally pointed outwards to indicate as positive the fluxes exiting the volume.

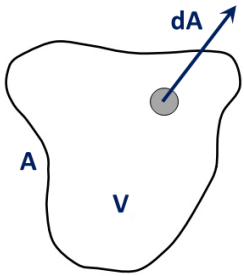


Figure 5.1: Generic control volume $V$ contained inside a surface of area $A$ with vector normal to an infinitesimal area $d\mathbf{A}$.

Indicating with $\boldsymbol{\mathcal{F}}$ the flux of an arbitrary quantity $\varphi$ in the absence of fluid transport, the transport flux is given by the product of the quantity and the velocity vector $\mathbf{u}$. Representing with $\mathcal{S}$ a source or sink of the arbitrary quantity, the law of conservation of $\varphi$ is expressed by Eq. (5.1).

$$\frac{d}{dt}\int_V \varphi dV = -\int_{\mathcal{S}} \left(\boldsymbol{\mathcal{F}} + \varphi\mathbf{u}\right)\cdot d\mathbf{A} + \int_V \mathcal{S} dV \qquad (5.1)$$

The negative sign indicates that an outward flux determines a reduction of the quantity inside the control volume. By applying the Gauss′s theorem, Eq. (5.1) can be reformulated as in Eq. (5.2).

$$\int_{\mathcal{S}} \left(\boldsymbol{\mathcal{F}} + \varphi \mathbf{u}\right) \cdot d\mathbf{A} = -\int_{V} \nabla \cdot \left(\boldsymbol{\mathcal{F}} + \varphi \mathbf{u}\right) dV \tag{5.2}$$

Since the reference system is inertial, the time derivative is equivalent to the local time derivative, as expressed by Eq. (5.3).

$$\frac{d}{dt}\int_{V} \varphi dV = \int_{V} \frac{\partial \varphi}{\partial t} dV \tag{5.3}$$

Including Eqs. (5.2) and (5.3) into Eq. (5.1) leads to Eq. (5.4).

$$\int_{V} \left[\frac{\partial \varphi}{\partial t} \nabla \cdot \left(\boldsymbol{\mathcal{F}} + \varphi \mathbf{u}\right) - \mathcal{S}\right] dV = 0 \tag{5.4}$$

Since the control volume is arbitrary, Eq. (5.4) is completely satisfied only if the term in square brackets is null in the entire domain. This condition is stated by Eq. (5.5), providing the general formulation of the conservation law [238, 226].

$$\frac{\partial \varphi}{\partial t} + \nabla \cdot \left(\boldsymbol{\mathcal{F}} + \varphi \mathbf{u}\right) - \mathcal{S} = 0 \tag{5.5}$$

## 5.2 Computational fluid dynamics mathematical model

The computational fluid dynamics models for the analysis of the aerodynamics of Wells and impulse turbines for oscillating water column wave energy converters were created with the releases *19.1* and *20.2* of the commercial software *ANSYS*. The software is a two-dimensional and three-dimensional viscous and inviscid code based on the solution of Reynolds averaged Navier-Stokes equations in steady and unsteady formulations (RANS and URANS, respectively).

In the most general form, the governing equations for the mass, the momentum, and the energy are achieved from Eq. (5.5) by substituting the variables representing the generic quantity, the flux, and the source or sink [238].

The mass conservation equation is obtained from Eq. (5.5) using the density as quantity considered, and imposing null values for $\mathcal{F}$ and $\mathcal{S}$ as the flux may vary only for transport processes and the mass cannot be created or destroyed. Hence, Eq. (5.6) can be written.

$$\frac{\partial \rho}{\partial t} + \nabla \cdot (\rho \mathbf{u}) = 0 \tag{5.6}$$

Regarding mass conservation, the specific momentum per unit volume is given by the product of the density and the velocity vector.

The variations of the momentum of the control volume are determined by the action of forces. In particular, pressure forces and stress forces are responsible for fluxes changing the momentum, while body forces, as those determined by gravity, are sources or sinks [237]. Therefore, the momentum conservation equation is expressed by Eq. (5.7).

$$\frac{\partial \rho \mathbf{u}}{\partial t} + \nabla \cdot (\rho \mathbf{u}\mathbf{u}) = -\nabla p + \nabla \cdot \boldsymbol{\tau} + \rho \mathbf{g} \tag{5.7}$$

where $\boldsymbol{\tau}$ is the stress tensor.

Concerning the energy conservation, the quantity considered is represented by the product of the density and the specific total energy $\mathfrak{h}_0$. The energy variations are given by the pressure variation and the energy fluxes due to the heat transfer and the changes in velocity. Thus, the energy conservation equation is

given by Eq. (5.8).

$$\frac{\partial(\rho \mathfrak{h}_0)}{\partial t} + \nabla \cdot (\rho \mathbf{u} \mathfrak{h}_0) = \frac{\partial p}{\partial t} + \nabla \cdot (\mathfrak{k} \nabla \mathcal{T} + \boldsymbol{\tau} \cdot \mathbf{u}) \tag{5.8}$$

where $\mathfrak{k}$ is the effective thermal conductivity.

The total specific enthalpy is defined in Eq. (5.9) as the sum of the specific enthalpy $\mathfrak{h}$ and the specific kinetic energy, which is a function of the air velocity magnitude $u$.

$$\mathfrak{h}_0 = \mathfrak{h} + \frac{u^2}{2} \tag{5.9}$$

The total specific energy $\mathfrak{E}$ is defined by Eq. (5.10) based on the specific enthalpy, pressure, density, and specific kinetic energy.

$$\mathfrak{E} = \mathfrak{h} - \frac{p}{\rho} + \frac{u^2}{2} \tag{5.10}$$

In the steady-state computations, the time derivatives in equations from Eq. (5.6) to Eq. (5.8) are neglected.

The Navier-Stokes equations provide one equation for mass conservation, three equations for momentum conservation, and one equation for energy conservation. The main unknowns are the pressure, the three components of the velocity vector, and the temperature. This gives a total of 5 equations and 6 unknowns. The sixth relation necessary for the solution of the set is the equation of state [226].

## 5.3 Turbulence modelling

Turbulence is a physical phenomenon determined by the fast and random variations of the local values of the pressure and velocity of a fluid. This unpredictability of the dynamics of a flow represents a critical issue for numerical modelling. Indeed, the possible ways to overcome this problem are represented by direct resolution and modelling turbulence. The former approach is applied by the direct numerical simulation (DNS), while the latter is utilised by the large eddy simulation (LES) and the Reynolds averaged Navier-Stokes method methods [237, 238, 226].

In the present thesis, the turbulence was modelled with RANS and URANS methods to achieve a suitable compromise between the accuracy of prediction and computational requirements. The mean values of fluid quantities are determined with an ensemble averaging operator, considering that a variable can be averaged as the result of a finite set of independent realisations of the same flow [239]. The Reynolds ensemble operator leads to the decomposition of the flow quantity, whereby an instantaneous quantity is decomposed into its time-averaged and fluctuating components, as expressed by Eq. (5.11).

$$\varphi(x,t) = \overline{\varphi}(x,t) + \varphi'(x,t) \tag{5.11}$$

where $\overline{\varphi}(x,t)$ indicates the mean component of a quantity obtained with the Reynolds averaging operator and $\varphi'(x,t)$ represents its fluctuating component.

It is worth noticing that the Reynolds averaged value of the fluctuations of a flow quantity is null.

The Reynolds averaging is imposed on the scalar and vec-

torial quantities of the governing equations. Consequently, the continuity equation may be expressed as in Eq. (5.12).

$$\nabla \cdot \overline{\mathbf{u}} = 0 \tag{5.12}$$

In analogy, the momentum equation may be reformulated as in Eq. (5.13).

$$\rho \frac{\partial \overline{\mathbf{u}}}{\partial t} + \rho \nabla \cdot (\overline{\mathbf{u}\mathbf{u}}) = -\nabla p + \mu \nabla^2 \overline{\mathbf{u}} \nabla \cdot \boldsymbol{\tau}^{Re} + \rho \mathbf{g} \tag{5.13}$$

where $\boldsymbol{\tau}^{Re}$ indicates the Reynolds stress tensor.

The Reynolds stress tensor models the additional stresses caused by the turbulent mixing of the fluid induced by the velocity fluctuations. The elements composing the tensor of Eq. (5.14) are the density and the components of the fluctuations of the velocity vectors in the x, y, and z coordinate directions of a Cartesian reference system.

$$\begin{bmatrix} \rho\overline{u_1' u_1'} & \rho\overline{u_1' u_2'} & \rho\overline{u_1' u_3'} \\ \rho\overline{u_2' u_1'} & \rho\overline{u_2' u_2'} & \rho\overline{u_2' u_3'} \\ \rho\overline{u_3' u_1'} & \rho\overline{u_3' u_2'} & \rho\overline{u_3' u_3'} \end{bmatrix} \tag{5.14}$$

The Reynolds stress tensor is determined by an average dyadic product of the velocity oscillations. The tensor is a symmetric matrix and its elements may be expressed with Eq. (5.15).

$$\overline{u_i' u_j'} = \overline{u_j' u_i'} \tag{5.15}$$

The Reynolds stress tensor introduces 6 additional variables to the set of unknowns, represented by the pressure, the velocity vector, and the temperature. This circumstance is named the

closure problem as it is necessary introducing additional equations to solve the set of equations. These equations are provided by the turbulence models, which are based on assumptions regarding the velocity oscillations.

The main approach to the closure problem developed for Reynolds averaged Navier-Stokes methods is the Boussinesq analogy. This approach, even named Boussinesq hypothesis, is based on the assumption that the components of the Reynolds stress tensor have a linear dependence upon the gradients of the average velocity vector, as expressed by Eq. (5.16).

$$\tau_{i,j} = \rho(u_i' u_j') = \mu_t \left( \frac{\partial u_i}{\partial x_j} + \frac{\partial u_j}{\partial x_i} \right) - \frac{2}{3} \rho \mathfrak{k} \delta_{i,j} \tag{5.16}$$

where $\mu_t$ is the turbulent viscosity coefficient, $\kappa$ is the turbulence kinetic energy, and $\delta_{i,j}$ is the Kronecker delta.

The turbulent viscosity or eddy viscosity is defined as the coefficient expressing the proportionality between the Reynolds stress tensor and the mean strain rate of the flow. The turbulence kinetic energy is computed based on the contribution of the flow velocity fluctuations through Eq.(5.17).

$$\kappa = \frac{1}{2} \left( u_1'^2 + u_2'^2 + u_3'^2 \right) \tag{5.17}$$

The Boussinesq analogy assumes that the turbulence has an isotropic behaviour. This formulation allows for the development of robust and computationally efficient turbulence models for the solution of the Navier-Stokes equations. Therefore, this approach is particularly appropriate for the analysis of cases not affected by significant turbulence anisotropy, mostly due to strong adverse pressure gradients and boundary layer separation, swirling

effects, and fast variations in fluid strain rate [240].

When the above effects are significant, the Reynolds stress models need to be applied. These models introduce an additional equation for the direct calculation of the Reynolds stress tensor. Moreover, they differ for modelling the turbulence kinetic energy as the eddy viscosity hypothesis of the Boussinesq analogy is not utilised. However, the Reynolds stress approach is significantly more demanding from a computational point of view. Thus, their application is suggested for the cases where the aforementioned flow characteristics are significant.

The main turbulence models generally implemented in Reynolds averaged Navier-Stokes methods are resumed in the following list.

- ◇ Algebraic Baldwin-Lomax model.
- ◇ Cebeci-Smith model.
- ◇ Prandtl mixing length model.
- ◇ Spalart-Allmaras single transport equation model.
- ◇ Two-equations $\kappa - \epsilon$ model in the standard version.
- ◇ Two-equations $\kappa - \epsilon$ model in the realisable version.
- ◇ Two-equations Wilcox $\kappa - \omega$ model in the high Reynolds version.
- ◇ Two-equations Wilcox $\kappa - \omega$ model in the low Reynolds version.
- ◇ Two-equations Menter transitional shear stress transport model (SST) $\kappa - \omega$ model.

- ◇ Four-equations Langtry-Menter transitional shear stress transport model (SST) transition model.
- ◇ Reynolds stress model.

The literature regarding the numerical modelling of oscillating water column systems for wave energy converters demonstrated that RANS and URANS models based on $\kappa - \epsilon$ and $\kappa - \omega$ turbulence models provide the most suited compromise between result accuracy and computational requirements. For this reason, this approach was applied in the present thesis.

A brief characterisation of the fundamental equations of the turbulence models utilised is provided in Appendix A.

## 5.4 Modelling of rotor motion

The computational fluid dynamics models of the Wells and impulse turbines require the modelling of the kinematic of the turbine. The motion of the investigated turbines is represented by the rotation of the rotor, as all the cascades were considered with a fixed pitch angle.

The software *ANSYS Fluent* typically solves the governing equations of fluid dynamics in an inertial reference frame. Although, it is also possible to solve the equations in a non-inertial reference frame. The movement can be modelled as the combination of translation and rotation. Focusing on the methods for modelling rotation, five main alternatives are present in computational fluid dynamics: the single reference frame (SRF) or multiple reference frame (MRF) with moving reference, mixing plane (MP), sliding mesh (SM), dynamic mesh (DM), and overset mesh (OM).

In the present thesis, the multiple reference frame with moving reference method, the mixing plane method, and the sliding mesh method were applied for modelling rotor movement.

The MRF approach, also called the frozen rotor approach, is a steady-state approximation of movement based on different reference frames for the steady and rotating cell zones. The governing equations of the stationary cell zones are computed in a stationary reference frame, while the equations of the rotating cell zones are solved in a rotating reference frame by including the centrifugal and the Coriolis forces in the momentum equation. At the interface of stationary and rotating cell zones, a local reference frame transformation is done to enable the use of the flow variables of one zone for the computation of the fluxes at the boundary of the adjacent zone. This process can be applied under the assumptions of a steadily rotating frame, and steady flow conditions at the interfaces between steady and rotating reference frames [34].

The SRF approach with moving reference is a particular case of the MRF approach with moving reference in which the entire computational domain has a single non-inertial reference frame.

The main advantages of the SRF and MRF methods are the reduced computational time compared to the other methods for modelling rotation and the possibility of performing steady-state computations.

The determination of the rotation in the rotating cell zones is achieved by modifying the equation of the flow velocity. A coordinate system moving with steady rotation with angular speed $\boldsymbol{\Omega}$ regarding a stationary inertial reference frame is considered. The origin of the rotating coordinate system is positioned at a distance $\mathfrak{a}_o$ from the stationary coordinate system; an arbitrary

point of the CFD domain is positioned at a distance $\mathfrak{a}$ from the origin of the rotating frame. The flow velocity in the rotating frame is obtained from the velocity in the stationary frame through the transformation imposed by Eq. (5.18) based on the rotational speed [34].

$$\mathbf{u}_r = \mathbf{u} - \mathbf{v}_r \tag{5.18}$$

where $\mathbf{u}_r$ is the relative velocity of the fluid regarding the moving frame, $\mathbf{u}$ is its absolute velocity in the stationary frame, and $\mathbf{v}_r$ is the velocity relative to the rotating frame.

From Eq. (5.18), the relative velocity of the moving frame $\mathbf{v}_r$ can be expressed with Eq. (5.19) relying on the translational velocity of the frame $\mathbf{u}_{tr}$ and the angular velocity vector $\mathbf{\Omega}$.

$$\mathbf{v}_r = \mathbf{u}_{tr} + \mathbf{\Omega} \times \mathfrak{a} \tag{5.19}$$

The general form of the governing equations can be reformulated on the basis of Eq. (5.19) by applying the absolute or the relative velocity formulation. The former approach utilises the absolute velocity as the dependent variable in the momentum equation, while the latter uses the relative velocity. The pressure-based solvers allow the application of either formulation, whereas the density-based solvers always apply the absolute velocity formulation [34].

Since the absolute velocity formulation was applied in the present thesis, the modified governing equations of the flow for a steadily rotating frame are reported. The equation of the mass conservation is provided by Eq. (5.20).

$$\frac{\partial \rho}{\partial t} + \nabla \cdot (\rho \mathbf{u}_r) = 0 \tag{5.20}$$

The equation of the momentum conservation is expressed by Eq. (5.21).

$$\frac{\partial(\rho\mathbf{u})}{\partial t}+\nabla\cdot(\rho\mathbf{u}_r\mathbf{u})+[\rho\boldsymbol{\Omega}\times(\mathbf{u}-\mathbf{u}_{tr})]=-\nabla p+\nabla\cdot\boldsymbol{\tau}+\rho\mathbf{g} \quad (5.21)$$

In the absolute velocity formulation of the motion with the constant rotation of the reference frame, the effects of the centrifugal and Coriolis forces are collapsed into the single term $\rho\boldsymbol{\Omega}\times(\mathbf{u}-\mathbf{u}_{tr})$.

The equation of the energy conservation is given by Eq. (5.22).

$$\frac{\partial(\rho\mathfrak{h}_0)}{\partial t}+\nabla\cdot(\rho\mathbf{u}_r\mathfrak{h}_0+p\,(\boldsymbol{\Omega}\times\mathfrak{a})=\frac{\partial p}{\partial t}+\nabla\cdot(\mathfrak{k}\nabla\mathcal{T}+\boldsymbol{\tau}\cdot\mathbf{u}) \quad (5.22)$$

The multiple reference frame model provides a physically meaningful solution if the flow at the interface between adjacent stationary and moving cell zones is approximately uniform. Conversely, if the effects of the non-uniformities are significant, the use of a mixing plane method or a sliding mesh method is required. When the application of the sliding mesh model is not convenient, or it is not possible, the mixing plane model may be a cost-effective alternative [34].

The mixing plane method differs from the frozen rotor method as the variables computed for a cell zone are not directly transferred to the adjacent cell zone. Indeed, the fluid dynamic quantities are considered as boundary conditions at the interface, and they are passed between adjacent zones after a process of spatial averaging that may be in the axial or radial direction based on the mixing plane geometry. Subsequently, the axial or ra-

dial profiles of the averaged variables are utilised to update the boundary conditions along the two zones of the mixing plane interface. The mixing of the data at the interfaces determines the removal of unsteady phenomena related to circumferential variations of the flow field, like wakes, shock waves, and separated flow effects. This implies that the computed results are in a steady-state. Even though the mixing plane method introduces relevant simplifications, it provides suitable approximations of the time-averaged fluid dynamics for a wide variety of turbomachinery applications [34].

The mixing plane pair is the procedure of coupling between an upstream outlet boundary zone with a downstream inlet boundary zone. The possible combinations that can be assigned are resumed in Table 5.1.

| Upstream outlet boundary | Downstream inlet boundary |
|---|---|
| Pressure outlet | Pressure inlet |
| Pressure outlet | Velocity inlet |
| Pressure outlet | Mass flow inlet |

Table 5.1: Possible combinations of the mixing plane pairs [34].

In the present application, an upstream pressure outlet and a downstream mass flow inlet were utilised to ensure rigorous conservation of the mass flow through the mixing plane. This approach may cause a discontinuity in the total pressure at the interface, which is nonetheless very low regarding the total pressure variations in the rest of the flow field.

The mixing of the variables is performed by applying three methodologies: area-weighted averaging, mass averaging, and mixed-out averaging.

The area-weighted averaging is carried out with Eq. (5.23) to calculate the mean value of a generic variable $\overline{\varphi}$ based on the area. This is the simplest method for mixing the variables at the interface, but it may cause the computation of values of the pressure and temperature that are not representative of the momentum and energy of the flow [34].

$$\overline{\varphi} = \frac{1}{A} \int_A \varphi \ dA \tag{5.23}$$

The mass averaging is computed through Eqs. (5.24) and (5.25) to achieve a more accurate calculation of the total quantities compared to the area-weighted averaging method [34].

$$\overline{\varphi} = \frac{1}{\dot{m}} \int_A \varphi \ \rho \mathbf{u} \cdot \hat{n} dA \tag{5.24}$$

$$\dot{m} = \int_A \rho \mathbf{u} \cdot \hat{n} dA \tag{5.25}$$

The mixed-out averaging method relies upon the conservation of the mass, momentum, and energy through the equations from Eq. (5.26) to Eq. (5.30).

$$\overline{\varphi}_c = \int_A \rho \left( \mathbf{u} \cdot \hat{n} \right) dA \tag{5.26}$$

$$\overline{\varphi}_{m1} = \int_A \rho \left( \mathbf{u} \cdot \hat{n} \right) u dA + \int_A \mathcal{P} \left( \hat{e}_x \cdot \hat{n} \right) dA \tag{5.27}$$

$$\overline{\varphi}_{m2} = \int_A \rho \left( \mathbf{u} \cdot \hat{n} \right) v dA + \int_A \mathcal{P} \left( \hat{e}_y \cdot \hat{n} \right) dA \tag{5.28}$$

$$\overline{\varphi}_{m3} = \int_A \rho \left( \mathbf{u} \cdot \hat{n} \right) w dA + \int_A \mathcal{P} \left( \hat{e}_z \cdot \hat{n} \right) dA \tag{5.29}$$

$$\overline{\mathfrak{E}} = \frac{\gamma \mathcal{R}}{(\gamma - 1)} \int_A \rho \left( \mathbf{u} \cdot \hat{n} \right) \mathcal{T} dA + \\ + \frac{1}{2} \int_A \rho \left( \mathbf{u} \cdot \hat{n} \right) \left( u^2 + v^2 + w^2 \right) dA \tag{5.30}$$

where $\mathbf{u}$ is the flow velocity vector, $u$, $v$, and $w$ are its components, and $\hat{e}_x$, $\hat{e}_y$, and $\hat{e}_z$ are the energy components along the coordinate axes.

Furthermore, the conditions of the conservation of the swirl and total enthalpy across the mixing plane were included in the modelling.

The third approach for modelling the rotor motion is the sliding mesh method. This method allows the achievement of time-accurate solutions of the flow instead of the time-averaged obtainable with the multiple reference frame and mixing plane methods. As the main advantage, the SM model is the most accurate approach to simulate fluids in multiple moving reference frames. This is particularly important, for instance, in the modelling of the interaction between stator and rotor cascades in turbomachinery. However, its computational requirements are significantly higher than the two approaches aforementioned.

For flows not subject to an interaction between parts with relative movement, the use of the MRF or MP methods is more efficient, as in the case of monoplane isolated Wells turbines, comprised of a single rotor cascade. If such an interaction is present, these models provide a steady approximation of the phenomenon. The sliding mesh model has to be applied to determine a transient interaction. Since the flow is inherently unsteady, a time-dependent computation is needed [34].

In this case, the rotating cell zones move relative to the adjacent zones along the mesh interface with discrete steps as rigid bodies. Indeed, the volume of the cells is constant for both the stationary and moving cell zones. Since the flow is inherently unsteady, only full transient simulations can be performed. At the interfaces between the zones, two overlapping faces, one for each zone, are created as this approach involves mesh motion. The interaction among adjacent zones is modelled by interpolating the information across the faces.

Considering the generic control volume $V$, the equation of conservation for a generic scalar variable $\varphi$ is provided by Eq. (5.31).

$$\begin{aligned} &\frac{d}{dV}\int_V \rho\varphi dV + \int_{\partial V} \varphi\left(\mathbf{u}-\mathbf{u}_m\right) d\mathbf{A} \\ &= \int_{\partial V} \Gamma\nabla\varphi \cdot d\mathbf{A} + \int_V \mathcal{S}_\varphi dV \end{aligned} \tag{5.31}$$

where $\mathbf{u}_m$ is the speed of the sliding mesh, $\mathbf{A}$ is the face area vector, $\Gamma$ is the diffusion coefficient, $\mathcal{S}_\varphi$ is the source term, and $\partial V$ is the boundary of the control volume.

The dynamic mesh model allows imposing the movement of the domain boundaries to freely modify with time the shape of the computational domain. This model may even be applied for steady cases if moving the mesh in the steady-state solver is needed. The mesh movement may be imposed in terms of linear or angular velocity, or it may be not imposed if the movement at the following time step is given by the solution at the current time.

The solution of analyses relying on the dynamic mesh requires high computational time and power, which is generally greater than the other approaches.

The overset mesh model permits the separate definition of numerical grids and their combination in a single computational domain through overlapping interfaces. Generally, the mesh is comprised of a background grid that extends over the entire domain, and one or smaller foreground grids positioned adjacent to moving boundaries and related to moving components. This approach usually simplifies the meshing procedure and may be beneficial in cases involving large relative motion between components. The computational requirements are lower than the dynamic mesh model and comparable to the sliding mesh model, as the interfaces are modelled with an analogous approach.

# Chapter 6

# Individual converter results

*The models of the individual converters were applied to determine the stages of the energy conversion of oscillating water column systems. The hydrodynamics, thermodynamics, and aerodynamics of the fixed and detached chamber were solved under typical conditions of a moderate wave climate. The analytical and CFD models of the Wells and impulse turbines were compared among themselves and with analytical and experimental data of literature to validate the proposed solutions. The model of the control strategy was defined to enhance the annual energy conversion of the oscillating water column systems by regulating the coupling between the turbomachine and the electric generator.*

## 6.1 Primary converter results

The chamber constitutes the primary converter of an oscillating water column system. The modelling of this converter relies on

the linear wave theory, which assumes that the fluid flow is inviscid, incompressible, and irrotational. The theoretical aspects of the model are explained in detail in Section 4.1.1 for a chamber detached and fixed with reference to the sea bottom.

The caisson considered for presenting the results of the single converter is subject to the action of unidirectional waves moving in seawater with a constant depth of 25 m. Therefore, the only possible motion mode is the heave oscillation of the water column. The hydrodynamics, thermodynamics, and aerodynamics were solved by applying the rigid piston concept, as the dimensions of the structure are small regarding the wavelength of the incident waves analysed.

For the results presented in this Section, the properties and hydrodynamic coefficients of the chamber were determined through correlative procedures with the aim of applying a completely analytical model. This allows the fast evaluation of a wide set of system configurations and wave conditions, which is paramount in the preliminary phases of the design of an OWC system. A refinement of this approach would be the application of a boundary element code of numerical type for determining these parameters. However, they strongly depend on the geometry of the chamber and the frequency of the waves. Thus, the calculation of a broad set of parameters considering all the possible configurations would be needed, with relevant effects on the overall computational power and time.

The geometry of the chamber was determined through an optimisation procedure, based on computational fluid dynamics, previously carried out at the *Maritime Engineering Laboratory* of the *University of Florence* [35] and subsequently applied for a preliminary application of the wave-to-wire model [126]. The

main geometric specifications are listed in Table 6.1.

| Chamber Inner Length | Chamber Inner Breadth | Chamber Inner Height | Front Wall Draught Length | Front Wall Freeboard Length |
|---|---|---|---|---|
| $W$, m | $B_c$, m | $G$, m | $D$, m | $F_c$, m |
| 9.5 | 10 | 22.5 | 3.5 | 7.5 |

Table 6.1: Optimal values of the main geometric parameters of the primary converter determined through numerical optimisation at the *LABIMA* [35].

The value of the added mass of the water column for the caisson analysed was determined with Eq. (6.1), considering this parameter equal to that of a hemisphere of equivalent radius $r_{eq}$ [202].

$$m_{add} = \frac{2}{3}\rho_w \pi r_{eq}^3 = 356631\ kg \tag{6.1}$$

Two sea wave conditions were considered to present the results of the primary converter model. The first sea state is defined by a couple of significant wave height $H_{m0}$ and wave energy period $T_{m-1,0}$ of 2 m and 6 s, respectively, while the second state has values of 2.5 m and 7 s, respectively. These conditions were selected as representative of the highest contributions to the annual average energy transport by sea waves in a moderate wave climate of the Mediterranean Sea.

The chamber was coupled with either a Wells turbine or an axial impulse turbine regarding the secondary converter. The force balance and the dynamics of the water column were analysed for both configurations and compared amongst themselves. The main geometric parameters and operating conditions of the turbines are resumed in Table 6.2. They were chosen to anal-

yse two well-suited configurations with comparable functioning. Therefore, two possible configurations of coupling between the primary and secondary converters were analysed.

| Parameter | Wells turbine | Impulse turbine |
|---|---|---|
| Rotational speed, rpm | 900 | 300 |
| Turbine casing radius, m | 1.00 | 0.85 |
| Hub-to-tip ratio, - | 0.50 | 0.70 |
| Rotor blade aspect ratio, - | 1.10 | 0.76 |
| Stator blade number, - | - | 26 |
| Rotor blade number, - | 5 | 30 |
| Tip clearance, % | 1.00 | 1.00 |
| Rotational inertia, $m^2$ kg | 25.61 | 104.12 |

Table 6.2: Geometry and rotor angular velocity of the Wells and impulse turbines applied as secondary converters.

The balance of the forces acting on the rigid piston is provided by Eq. (4.6). The equation may be reformulated as in Eq. (6.2) to make explicit the inertial force of the internal volume of seawater.

$$m_w \ddot{z} = f_{rdp} + f_{hst} + f_{exc} + f_{add} + f_{pto} \tag{6.2}$$

The formula of the added mass force of Eq. (4.15) may be written as in Eq. (6.3) to separate the contributions of the inertial force depending on the acceleration of the free surface of the water column and the velocity of the water particles.

$$f_{add} = m_{add}\dot{v}_{z,w} - m_{add}\ddot{z} = f_{par} - m_{add}\ddot{z} \tag{6.3}$$

In turn, the force determined by the velocity of the water particles $f_{par}$ is expressed by Eq. (6.4).

$$f_{par} = m_{add}\dot{v}_{z,w} \tag{6.4}$$

By substituting Eq. (6.3) into Eq. (6.2), the total inertial force of the internal volume of water may be written in explicit form through Eq. (6.5).

$$(m_w + m_{add})\ddot{z} = f_{rdp} + f_{hst} + f_{exc} + f_{par} + f_{pto} = f_{tot} \tag{6.5}$$

From the above equation, the acceleration of the oscillating water column is achieved with Eq. (6.6), as explained in detail in Section 4.1.

$$\ddot{z} = \frac{f_{rdp} + f_{hst} + f_{exc} + f_{par} + f_{pto}}{(m_w + m_{add})} \tag{6.6}$$

Considering now the results achieved with the analytical model of the primary converter, the time series of the sinusoidal position and acceleration of the free surface of the incident sea waves are presented in Figure 6.1. The heave motion of the wave was imposed as an inlet condition. A duration of two periods was taken into account, starting from the rest position of the sea waves, when their free surface level coincides with the still water level.

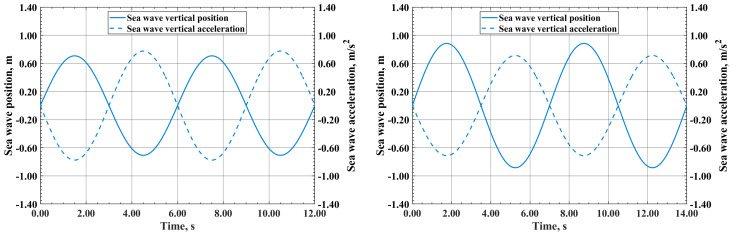


(a) Hs=2 m and Te=6 s (b) Hs=2.5 m and Te=7 s

Figure 6.1: Time series of the sea wave position and acceleration for the two investigated conditions with **(a)** $H_{m0}$=2 m and $T_{m-1,0}$=6 s and **(b)** $H_{m0}$=2.5 m and $T_{m-1,0}$=7 s.

In Figure 6.2, the excitation force $f_{exc}$ acting at the bottom of the water column for the effect of the hydrodynamic pressure of the incident sea wave is shown as a function of time.

The excitation force depends on the characteristics of the incident wave through the wave height, seawater density, and wavenumber, on the geometry of the chamber as regards the area of the horizontal cross-section and the draught length, and on the location concerning the seawater depth and gravitational acceleration. Therefore, the force exerted on the oscillating water column is identical for either the configurations investigated for a specific wave condition.

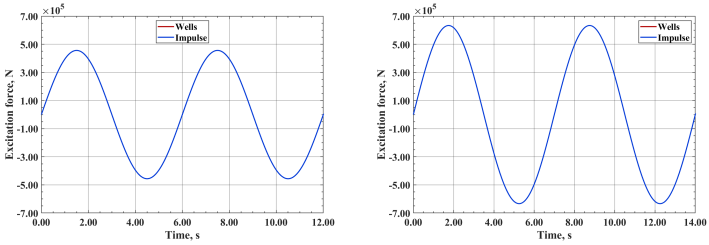


(a) Hs=2 m and Te=6 s (b) Hs=2.5 m and Te=7 s

Figure 6.2: Time series of the excitation force exerted by the hydrodynamic pressure of the incident sea wave with **(a)** $H_{m0}$=2 m and $T_{m-1,0}$=6 s and **(b)** $H_{m0}$=2.5 m and $T_{m-1,0}$=7 s.

The excitation force acting on the water column under the action of the wave conditions of Figure 6.1a is lower regarding the conditions of Figure 6.1b owing to the smaller wave height. In either case, the force has the same frequency and phase of the incident sea wave, as noticeable from the comparison of Figures 6.1 and 6.2.

The hydrostatic force $f_{hst}$ exerted by the hydrostatic pressure of the water column is presented in Figure 6.3 by varying the time.

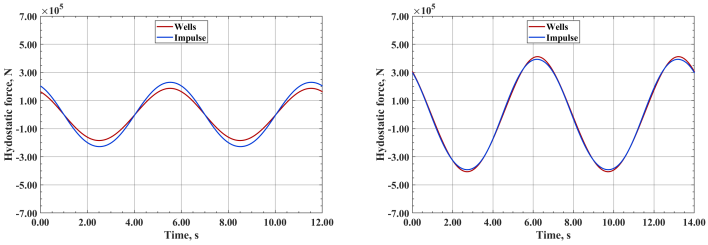


(a) Hs=2 m and Te=6 s (b) Hs=2.5 m and Te=7 s

Figure 6.3: Time series of the hydrostatic force exerted by the hydrostatic pressure of the water column for sea waves with **(a)** $H_{m0}$=2 m and $T_{m-1,0}$=6 s and **(b)** $H_{m0}$=2.5 m and $T_{m-1,0}$=7 s.

The hydrostatic force depends upon the displacement of the free surface of the water inside the chamber, the area of the horizontal cross-section of the caisson, the seawater density, and the gravitational acceleration. The time series of the free surface level of the water column is shown in Figure 6.4.

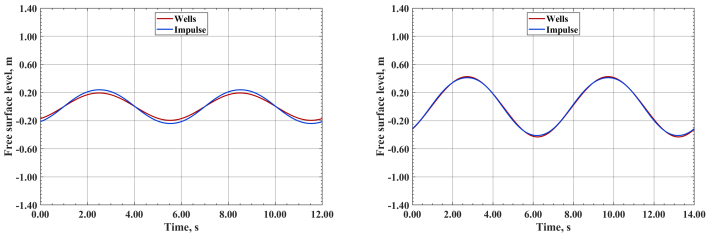


(a) Hs=2 m and Te=6 s (b) Hs=2.5 m and Te=7 s

Figure 6.4: Time series of the free surface level of the oscillating column inside the chamber for sea waves with **(a)** $H_{m0}$=2 m and $T_{m-1,0}$=6 s and **(b)** $H_{m0}$=2.5 m and $T_{m-1,0}$=7 s.

From the comparison of Figures 6.3 and 6.4, it is visible that the hydrostatic force is negative when the free surface displace-

ment is positive and vice versa.

For sea waves with a significant height of 2 m and an energy period of 6 s, the hydrostatic force of the configuration with the Wells turbine reaches smaller absolute values at the extremes of the flow phases regarding the configuration with the impulse turbine. This is due to the lower amplitude of the free surface displacements. Conversely, for sea waves with a significant height of 2.5 m and an energy period of 7 s, the absolute values of the extremes of the configuration with the Wells turbine are greater owing to the higher magnitude of water oscillation. The maximum difference is about 23% for the former wave conditions and around 5% for the latter.

In Figure 6.5, the radiating damping force $f_{rdp}$ is depicted as a function of time. This force is provided by the product of the velocity of the water column and the radiating damping coefficient, which in turn depends on the hydrostatic restoring coefficient, the oscillating water column mass, and the added mass.

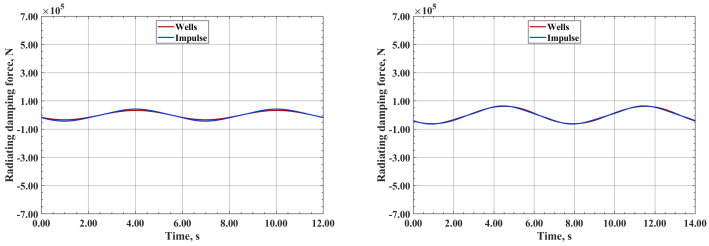


(a) Hs=2 m and Te=6 s (b) Hs=2.5 m and Te=7 s

Figure 6.5: Time series of the radiating damping force exerted by the hydrostatic pressure of the water column for sea waves with **(a)** $H_{m0}$=2 m and $T_{m-1,0}$=6 s and **(b)** $H_{m0}$=2.5 m and $T_{m-1,0}$=7 s.

The velocity of the water column and the radiating damping coefficient are time-dependent parameters, as visible in Figures 6.6 and 6.7.

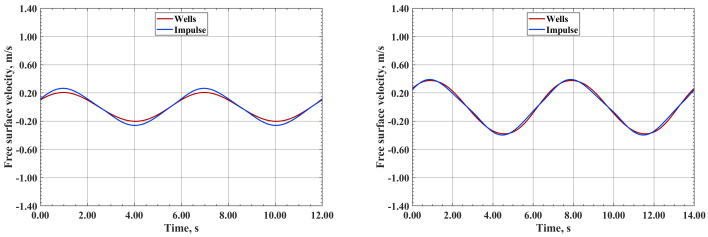


(a) Hs=2 m and Te=6 s (b) Hs=2.5 m and Te=7 s

Figure 6.6: Time series of the free surface velocity of the oscillating column inside the chamber for sea waves with **(a)** $H_{m0}$=2 m and $T_{m-1,0}$=6 s and **(b)** $H_{m0}$=2.5 m and $T_{m-1,0}$=7 s.

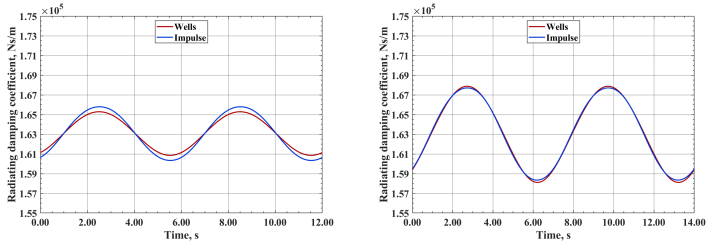


(a) Hs=2 m and Te=6 s (b) Hs=2.5 m and Te=7 s

Figure 6.7: Time series of the radiating damping coefficient for sea waves with **(a)** $H_{m0}$=2 m and $T_{m-1,0}$=6 s and **(b)** $H_{m0}$=2.5 m and $T_{m-1,0}$=7 s.

The absolute values of the peaks of the radiating damping force reached by the configuration with the impulse turbine are higher for both the investigated wave conditions. The reason is the higher velocity of the water column. The maximum dif-

ference is approximately 29% and 5% for the two wave states, respectively.

The time series of the force associated with the velocity of the seawater particles $f_{par}$ is depicted in Figure 6.8.

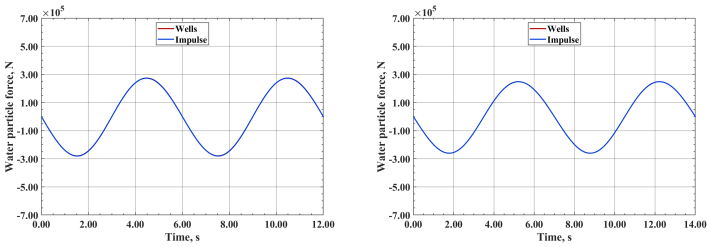


(a) Hs=2 m and Te=6 s (b) Hs=2.5 m and Te=7 s

Figure 6.8: Time series of the water particle force for sea waves with **(a)** $H_{m0}$=2 m and $T_{m-1,0}$=6 s and **(b)** $H_{m0}$=2.5 m and $T_{m-1,0}$=7 s.

The curves of the force calculated for the two configurations are almost coincident for both the wave conditions, as the only different value assumed by the parameters is the free water level and its influence on the function is low.

The force $f_{pto}$ acting on the top of the water column for the action of the compression and expansion of the air inside the caisson is presented as a function of time in Figure 6.9.

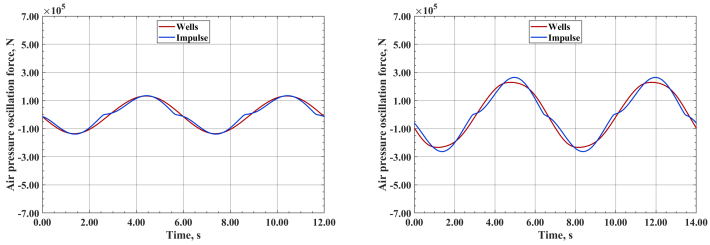


(a) Hs=2 m and Te=6 s (b) Hs=2.5 m and Te=7 s

Figure 6.9: Time series of the air pressure oscillation force for sea waves with **(a)** $H_{m0}$=2 m and $T_{m-1,0}$=6 s and **(b)** $H_{m0}$=2.5 m and $T_{m-1,0}$=7 s.

This force depends on the free surface velocity of the water column and the pressure drop imposed by the power take-off, which is depicted in Figure 6.10 as a function of time.

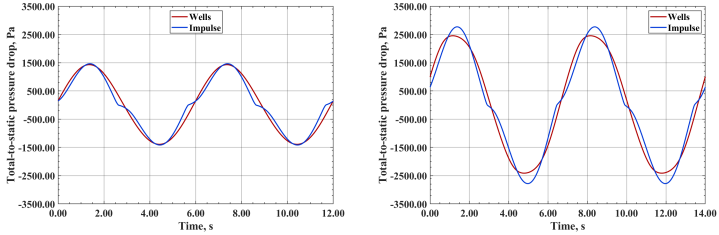


(a) Hs=2 m and Te=6 s (b) Hs=2.5 m and Te=7 s

Figure 6.10: Time series of the total-to-static pressure drop across the power take-off for sea waves with **(a)** $H_{m0}$=2 m and $T_{m-1,0}$=6 s and **(b)** $H_{m0}$=2.5 m and $T_{m-1,0}$=7 s.

Since the intervals of the air pressure difference required for the operation of the two turbines are similar for the first wave state analysed, the corresponding curves of the air pressure oscillation force reach values close to each other at the extremes of the flow phases. For the second wave state, the configuration

with the impulse turbine is subject to a higher air pressure force as the turbine operation requires a greater pressure difference between its inlet and outlet.

The total mass of the water column, comprising the mass of the seawater and the added mass, is depicted in Figure 6.11 by varying the time.

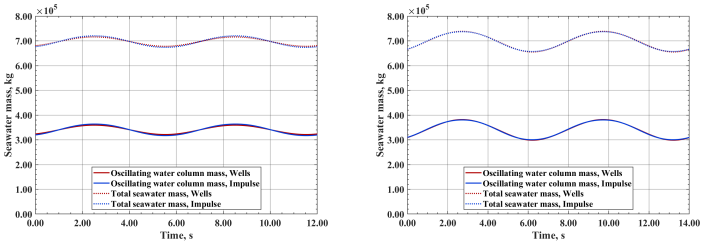


(a) Hs=2 m and Te=6 s (b) Hs=2.5 m and Te=7 s

Figure 6.11: Time series of the mass and total mass of the oscillating water column for sea waves with **(a)** $H_{m0}$=2 m and $T_{m-1,0}$=6 s and **(b)** $H_{m0}$=2.5 m and $T_{m-1,0}$=7 s.

The maximum and minimum values of the seawater mass depend upon the displacements of the oscillating water column of Figure 6.4, while the value of the added mass is constant for a specific chamber geometry and seawater density.

The solution of the hydrodynamics of the primary converter provides the position, velocity, and acceleration of the oscillating water column. Coupling these parameters with the solution of the thermodynamics of the chamber, the volume airflow rate made available by the primary converter at its outlet was determined. The time series of this quantity is depicted in Figure 6.12.

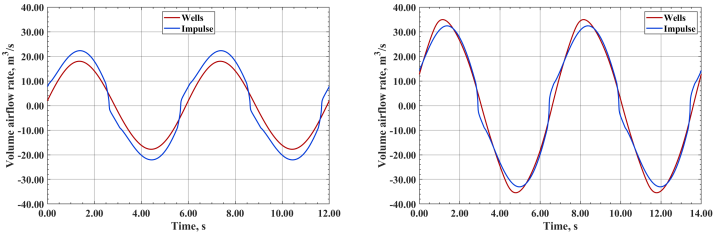


(a) Hs=2 m and Te=6 s (b) Hs=2.5 m and Te=7 s

Figure 6.12: Time series of the volume airflow rate processed by the chamber for sea waves with **(a)** $H_{m0}$=2 m and $T_{m-1,0}$=6 s and **(b)** $H_{m0}$=2.5 m and $T_{m-1,0}$=7 s.

Based on the geometric parameters of the secondary converter, the time series of the airflow velocity crossing the turbine rotor of Figure 6.13 was achieved for the configurations and wave conditions investigated.

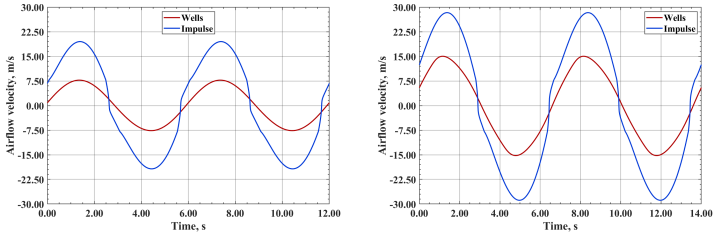


(a) Hs=2 m and Te=6 s (b) Hs=2.5 m and Te=7 s

Figure 6.13: Time series of the volume airflow rate crossing the turbine rotor for sea waves with **(a)** $H_{m0}$=2 m and $T_{m-1,0}$=6 s and **(b)** $H_{m0}$=2.5 m and $T_{m-1,0}$=7 s.

By comparing Figures 6.12 and 6.13, it is noticeable that the lower passage area of the flow crossing the rotor of the impulse turbine determines a significantly higher absolute axial velocity of the airflow. This allows the functioning of the turbomachine

on a wider operating range with higher variations of the flow coefficient during the flow phases.

## 6.2 Secondary converter results

The secondary converter of an oscillating water column system consists of the air turbine. The most widely used and promising technologies for this kind of application are Wells and impulse turbines. In the present Section, several configurations of monoplane isolated Wells turbines, and the axial-flow impulse turbine are analytically and numerically investigated. The operation of the individual converters was evaluated and the results of the analytical and CFD models were compared between themselves and with literature experimental data. The aim was to validate the single models for their application in the wave-to-wire model developed.

### 6.2.1 Monoplane isolated Wells turbine

A monoplane isolated Wells turbine for oscillating water column systems was studied with an analytical approach and computational fluid dynamics to evaluate the aerodynamics of the airflow and determine the operating curves, the power conversion, and the performance parameters.

The analytical model applies the actuator disc theory and the blade element momentum theory, and it is described in detail in Sections 4.2.1 and 4.2.2. Through this approach, a turbomachine row is modelled as an infinitely thin disc simulating the former in terms of energy exchange with the flow through the imposition of mass and momentum conservation. The flow is assumed to be

steady, axisymmetric, and inviscid.

The creation of the computational domain of the CFD analyses, constituted by the straight annular duct embedding the turbine, and its spatial discretisation were achieved with *ANSYS ICEM 19.1*, the analyses were solved with *ANSYS Fluent 19.1* and the results were assessed with *ANSYS CFD Post 19.1*, developing a completely automated procedure. Either steady and unsteady Reynolds-averaged Navier-Stokes (RANS and u-RANS, respectively) equations were applied as governing equations, and the closure problem was solved with both the realisable $\kappa$-$\epsilon$ model with enhanced wall functions and the $\kappa$-$\omega$ stress transport model with low Reynolds number correction to the turbulent viscosity [30, 31]. The motion of the turbine rotor was modelled with two different approaches: multiple reference frame with moving reference frame and sliding mesh. The theoretical aspects of the CFD models are discussed in detail in Chapter 5.

Two-dimensional models were generated in the preliminary phases of the model development to quickly assess the parameters of the computational domain and the numerical settings for the three-dimensional models.

#### 6.2.1.1 Numerical domain

A monoplane isolated Wells turbine comprised of a single rotor cascade with symmetrical blades staggered around the central hub was considered. The rotor blades are symmetrically positioned on a plane orthogonal to the rotation axis and therefore at 90 degrees regarding the incoming flow (Figure 6.14). The blade airfoils are symmetrical NACA0015 profiles with constant stacking in the radial direction. This is one of the most effective profiles together with the NACA0012, NACA0018, and

NACA0021 [22, 44].

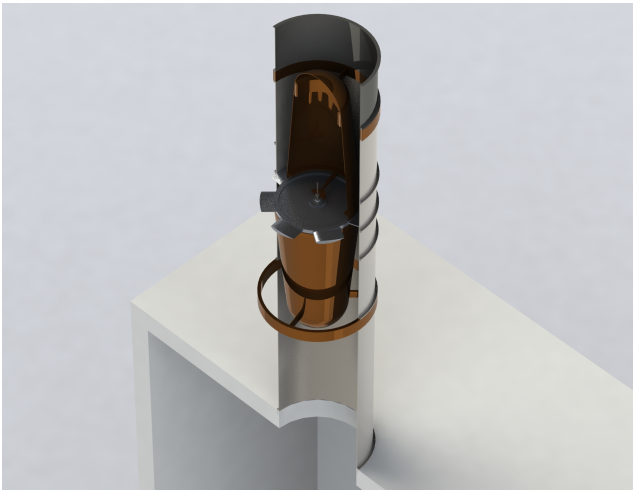

Figure 6.14: Section of the rendering of an OWC system showing the monoplane isolated Wells turbine analytically and numerically investigated.

The main geometric specifications and operating conditions of the Wells turbine analysed are listed in Table 6.3 based on the reference literature data [241, 242]. For the computations performed by imposing a sinusoidal law as a function of time for the inlet velocity, a wave period of 7 s was selected to consider typical conditions of a moderate climate of the Mediterranean Sea [30, 31].

| Parameter | Description |
|---|---|
| Turbine typology | Isolated monoplane |
| Blade profile | NACA0015 |
| Blade number | 7 |
| Turbine casing diameter | 0.50 m |
| Hub-to-tip ratio | 0.75 |
| Chord length | 0.117 m |
| Rotational speed | 3600 rpm |
| Inflow velocity amplitude | 14.91 $^{m}/_{s}$ |
| Outflow velocity amplitude | 15.73 $^{m}/_{s}$ |
| Airflow period | 7 s |

Table 6.3: Main geometric specifications and operating conditions of the Wells turbine analytically and numerically investigated.

The flow conditions and the geometry of the straight annular duct and the turbine are axisymmetric in function to the number of rotor blades [243, 81, 84]. Therefore, the model is periodic in the circumferential direction. This enables to perform simulations on a computational domain comprising $^{1}/_{7}$ of the turbine annulus, including one blade passage instead of analysing the full annulus. As a consequence, the computational time and power required are significantly reduced. The domain is bounded by the inlet and outlet boundaries, the periodic surfaces, the annulus walls and the blade walls (Figure 6.15). The extension of the gap determines the implications of this geometric parameter on the turbine performance. In particular, the decrease of

its dimension enhances the turbine efficiency due to the reduction of the leakage losses but advances the aerodynamic stall [30, 31]. Therefore, the gap is typically defined between around 1% and 2% of the blade chord length to achieve a good compromise between these opposing effects. For such values, the gap influence on the operating curves of the turbomachine is limited [243, 68, 69, 70].

The computational domain was subdivided into three cell zones disposed along the rotation axis: upstream duct, rotor, and downstream duct. The first and the last zones model the stationary parts of the duct and are steady, while the second zone is a rotating region modelling the motion of the turbine rotor. The cell zones are symmetrically arranged regarding the axial direction, as the operation of the self-rectifying machine was analysed considering a bidirectional airflow. For this purpose, full transient simulations with a sinusoidal inlet velocity were conducted in addition to steady-state and unsteady simulations with fixed inlet velocity. The length in the axial direction of either the upstream and downstream zones was set to 6 times the length of the blade chord to ensure the full development of the flow before impacting the rotor and to analyse the outlet flow field after the interaction with the blades [244, 81, 245]. For the rotating zone, the axial dimension was defined as equal to about the length of the blade chord according to the sensitivity analysis explained in Section 6.2.1.5 for ensuring mesh independence [30, 31].

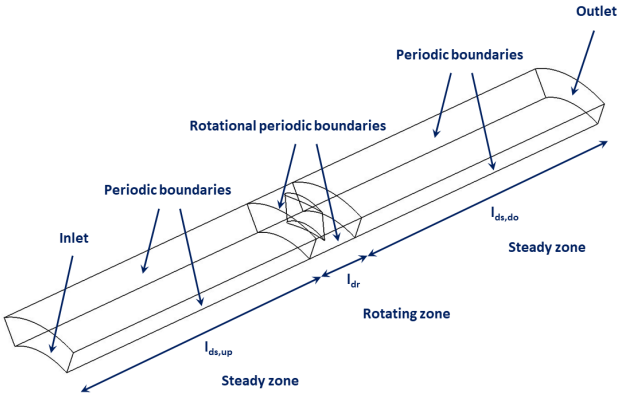


Figure 6.15: Scheme of the computational domain of the monoplane isolated Wells turbine.

#### 6.2.1.2 Numerical grid

The creation of the computational domain and its spatial discretisation were obtained with *ANSYS ICEM 19.1* generating a fully mapped mesh of hexahedral elements. A multi-block technique was applied to generate a C-type mesh topology in the region surrounding the blade to capture the complex boundary layer flow, and H-type mesh topologies were utilised in the rest of the domain (Figure 6.16).

The numerical grid consists of 3.85 million nodes and about 3.76 million elements. Since the aim was to investigate different CFD models, a fine grid with high accuracy was selected while limiting the computational time. The mesh fulfils the convergence criteria of the mass conservation within $10^{-3}$ and maximum order of the root mean squares residuals of $10^{-6}$ for the continuity, momentum, turbulence, and energy equations [30, 31].

In the circumferential direction, 300 nodes were distributed around the blade profile, and 70 nodes were positioned in the

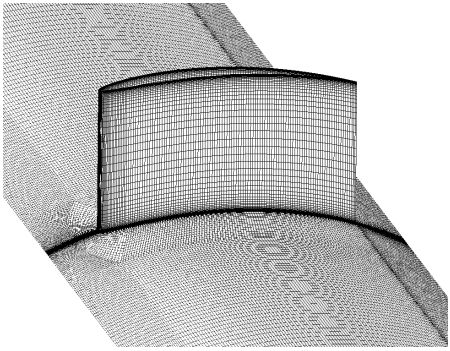

Figure 6.16: Isometric view of the blade and hub wall mesh of the Wells turbine [30, 31].

blade passage with 30 nodes upstream of the leading edge and 40 downstream of the trailing edge (Figure 6.17).

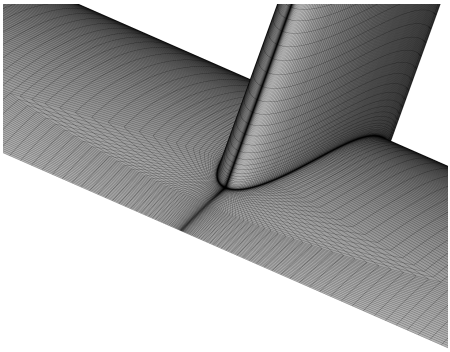

Figure 6.17: Mesh close-up at the hub leading edge of the isolated monoplane Wells turbine [30, 31].

In the radial direction, 80 nodes were set along the blade span. In the axial direction, 80 nodes were located in the stationary regions, and 100 nodes were established in the rotating region. The dimension of the boundary layer cells in the direction normal to the wall boundary was defined to achieve values

of $y^+$ between 30 and 90 for the simulations carried out with the κ-ϵ turbulence model and lower than 1 for the simulations performed with the κ-ω turbulence model. The cell growth ratio was set to 1.05 at all the wall boundaries with a maximum value of 1.2 in the other parts of the domain (Figure 6.18).

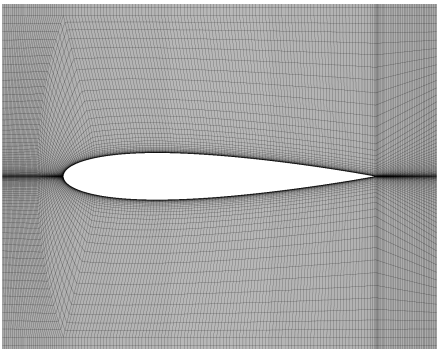

Figure 6.18: Mesh close-up around the blade tip of the Wells turbine [30, 31].

#### 6.2.1.3 Mathematical modelling

Steady and unsteady Reynolds averaged Navier-Stokes equations were solved with *ANSYS Fluent 19.1* for a compressible ideal gas. The conservation equations for the continuity, momentum and energy are provided by Eqs. (5.6), (5.7), and (5.8), respectively, as discussed in Section 5.2. The air density, the thermal conductivity, and the dynamic viscosity were defined as functions of the temperature.

The Navier-Stokes equations were discretised with a second-order scheme for the pressure and a second-order upwind scheme for the density, momentum, energy, turbulent kinetic energy, and specific dissipation rate. The coupled method was utilised to re-

late the velocity and pressure corrections. The least-squares and cell-based method was applied for computing the variable gradients [30, 31]. Since the relative Reynolds number based upon the blade chord ranges from approximately $2 \cdot 10^4$ to nearly $3 \cdot 10^6$, the turbulence was modelled [243, 81, 246] with second-order discretisation through the application of the realisable $\kappa$-$\epsilon$ model with enhanced wall functions for the near-wall treatment [247] or the $\kappa$-$\omega$ stress transport model [248] with low Reynolds number correction to the turbulent viscosity [34]. The equations were implicitly solved with a pressure-based approach, as the Mach number of the flow is lower than 0.4 for all the investigated cases.

During the realisation of the thesis, the effects of the application of numerical methods different from the coupled method, as the SIMPLE (Semi-Implicit Method for Pressure-Linked Equations) and the SIMPLEC (Semi-Implicit Method for Pressure-Linked Equations-Consistent), were investigated. Relevant variations of the achieved results were not found. The coupled method was finally selected as it ensures more robust modelling.

#### 6.2.1.4 Boundary conditions

The conditions applied to the boundaries of the computational domain are listed in Table 6.4.

| Boundary | Condition |
|---|---|
| Inlet | Velocity, turbulent intensity, length scale, and temperature |
| Outlet | Static pressure, radial equilibrium, and turbulent intensity, length scale, and temperature of the back-flow |
| Blade and walls | No-slip |
| Rotor circumferential side-walls | Rotational periodicity |
| Duct circumferential side-walls | Periodicity |

Table 6.4: Boundary conditions applied in the CFD models of the Wells turbine.

For all the numerical configurations, uniform distributions of the flow velocity and uniform and constant temperature distributions were assigned at the inlet boundary. At the domain outlet, uniform and constant distributions of the static pressure with radial equilibrium condition and a constant back-flow temperature were imposed [30, 31]. The values of the range of the inlet velocity and rotational speed designated are provided in Table 6.3, while the static gauge pressure and the temperature were set to 0 Pa and 288.15 K, respectively.

The turbulence intensity $ti$ was determined with Eq. (6.7) on the basis of the relative Reynolds number $Re_{hd}$ calculated depending upon the hydraulic diameter of the annular duct [34].

$$ti = 0.16 Re_{hd}^{-0.125} \tag{6.7}$$

The turbulent length scale $\mathfrak{l}$ was computed with Eq. (6.8) with respect to the characteristic length of the flow opening $\mathfrak{L}$ [34].

$$\mathfrak{l} = 0.07\mathfrak{L} \tag{6.8}$$

On the walls of the annulus and blade, no-slip boundary conditions were imposed. Periodic and rotationally periodic boundary conditions were assigned to the circumferential side-walls of the stationary and rotating regions, respectively.

Regarding the uniform distributions of the inlet flow velocity, two different approaches were defined. Indeed, the effects of applying a discrete set of constant values covering the entire operating range and values varying with a sinusoidal function in the same range were analysed. The first approach was used for both steady and unsteady simulations, while the second requires unsteady analyses.

The rotating motion of the rotor was modelled by using the multiple reference frame with moving frame and the sliding mesh models. Fixed values of the rotational speed were analysed. The MRF model limits the computational requirements and provides time-averaged solutions that are physically meaningful when the flow at the interface between adjacent stationary and moving cell zones is nearly uniform. The SM model allows the achievement of time-dependent solutions of the fluid dynamics, increasing the accuracy of the simulation of fluids in reference frames subject to reciprocating motion.

#### 6.2.1.5 CFD sensitivity analysis

The development of a computational fluid dynamics model requires sensitivity analyses to spatial and temporal discretisation. The former type of investigation concerns the element number and distribution of the computational grid, and it is needed for all the simulations; the latter analysis regards the time step size and is necessary only for transient simulations.

With the aim of assessing the computational mesh independence, a mesh sensitivity analysis was carried out comparing the results of several different grids with node number ranging from 0.5 to 9.5 million. The finer and coarser meshes were derived through homogeneous variations of the node number relative to the selected mesh comprising 3.85 million nodes. The minimum values of node number around the blade airfoil and along its span were set to 200 and 50, respectively [30, 31].

The mesh sensitivity analysis consists of three steps. Firstly, the effects of the number of elements and their distribution on the calculated values were assessed over the entire computational domain. Subsequently, the influence of the extension in the axial direction of the rotating cell zone was evaluated to determine the minimum value ensuring the mesh independence. During the final step, an extensive mesh sensitivity analysis regarding the element number and distribution was performed for the grids fulfilling the requirements of the previous steps [30, 31].

The number and the arrangement of elements are fundamental features, in particular for the rotating cell zone. The static-to-static pressure drop and the torque exerted on the rotor blades were considered for evaluating the grid influence as they are the most important parameters for the selection of Wells turbines. The graphs of the mesh sensitivity analysis are depicted for the maximum value of the inlet flow velocity equal to 15.73 $^{m}/_{s}$ and

an intermediate value, equivalent to 8 $^{m}/_{s}$, both referred to the outflow phase. The values are presented for the steady-state computations with the κ-ω turbulence model and the multiple reference frame method for modelling rotation. The selected quantities, flow conditions and numerical settings are representative of the effects of the investigated grid parameters for all the CFD analyses performed [30, 31].

Figures 6.19 and 6.20 indicate that the mesh dependence is more pronounced for the highest value of the flow axial velocity compared to the intermediate value. As concerns the axial dimension of the rotating cell zone, Figures 6.19a and 6.19b denote that the independence of the grid from the parameter $l_{dr}$ is achieved corresponding to an axial length of the rotating cell zone of at least around one chord.

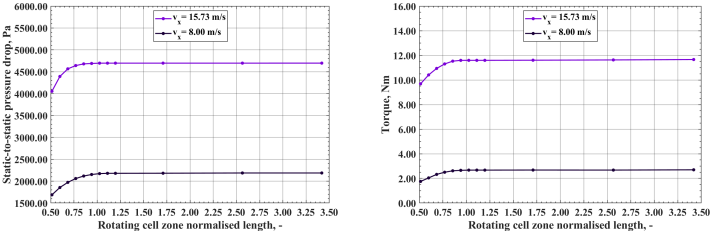


(a) Static-to-static pressure drop (b) Blade torque

Figure 6.19: **(a)** Static-to-static pressure drop and **(b)** blade torque for different inlet flow velocities as a function of the axial dimension of the rotating cell zone normalised relative to the blade chord length.

For a mesh with about 0.5 million nodes, the maximum difference in computed static-to-static pressure drop and torque is approximately 5.4% and 5.8%, respectively, relative to the finest mesh with 9.5 million nodes, as visible in Figures 6.20a and 6.20b. The variations of both the quantities decrease to nearly 1% for a

grid with approximately 1.6 million nodes. By further increasing the node number, the discrepancies become slight and for a mesh with 3.85 million nodes are negligible [30, 31].

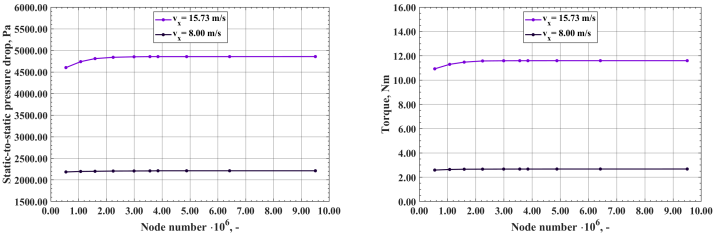


(a) Static-to-static pressure drop (b) Blade torque

Figure 6.20: **(a)** Static-to-static pressure drop and **(b)** blade torque for different inlet flow velocities as a function of the number of nodes.

A non-dimensional parameter called computational time ratio $\mathfrak{tr}$ was defined to provide information concerning the time required for solving the CFD analyses. The parameter is calculated with Eq. (6.9) as the ratio of the computational time $t$ of each case to the computational time $t_{ref}$ of the reference case. For the steady-state analyses, the reference time is given by the case with 3.85 million nodes using the MRF scheme and the $\kappa$-$\omega$ turbulence model. For the transient analyses, the case with the same mesh, turbulence model, and rotational scheme, and the time-step size of $5 \cdot 10^{-3}$ s is considered as the reference for normalisation [30, 31].

$$\mathfrak{tr} = \frac{t}{t_{ref}} \tag{6.9}$$

In Figure 6.21, the trade-off between the accuracy of the calculation of the torque acting on the rotor blades and the computational time is presented by varying the grid size. The results

are presented for the maximum flow inlet velocity during the outflow phase.

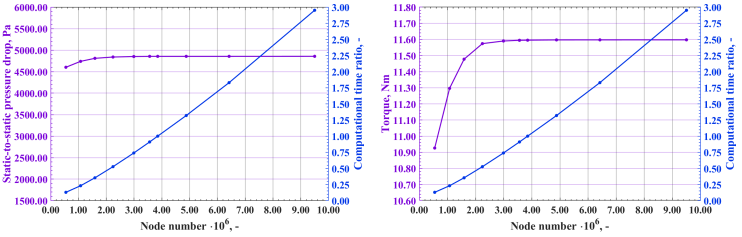


(a) Static-to-static pressure drop (b) Blade torque

Figure 6.21: Compromise between the computational time and the accuracy of the calculated quantity for **(a)** the static-to-static pressure drop and **(b)** the blade torque.

From a perusal of Figure 6.21 it is noticeable that a mesh with at least about 1.6 million nodes ensures a good accuracy of torque prediction with limited requirements of computational time. A similar option may be recommended if the target of the analysis is investigating a wide variety of cases. The mesh with 3.85 million nodes provides higher accuracy and requires a computational time that is about three times higher regarding the former mesh. This choice may be recommended if the aim of the study is the accurate analysis of a selected set of cases.

The definition of the values of the time step for the fully transient models requires a sensitivity analysis. The objective is to evaluate the effects of the magnitude of the time step for determining the highest value that ensures slight or negligible variations of the computed quantities. Even in these cases, the static-to-static pressure drop and the torque are shown as representative of all the quantities of the analyses conducted. Figures

6.22 and 6.23 indicate that values of the time step size equal or lower than $1 \cdot 10^{-2}$ s provide a satisfactory prediction of the static-to-static pressure variation and the torque during the entire computations for the analyses performed with the multiple reference frame model. For the sliding mesh model, such value of the time step size entails fluctuations of the computed quantities corresponding to the extremes of the inflow and outflow phases. The fluctuations are avoided by a time step equivalent or inferior to $8 \cdot 10^{-3}$. A further decrease of the time step size to at least $5 \cdot 10^{-3}$ is needed for obtaining reasonable independence of the computed results from this parameter.

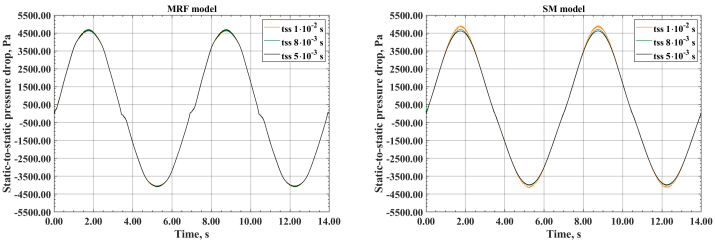


(a) MRF model (b) SM model

Figure 6.22: Sensitivity analysis of the static-to-static pressure drop to the time step size for **(a)** the MRF and **(b)** the SM models.

A time step of $5 \cdot 10^{-3}$ s results in maximum variations of the static-to-static pressure variation across the turbine duct lower than 0.22% and 0.37% for the multiple reference frame and siding mesh models, respectively.

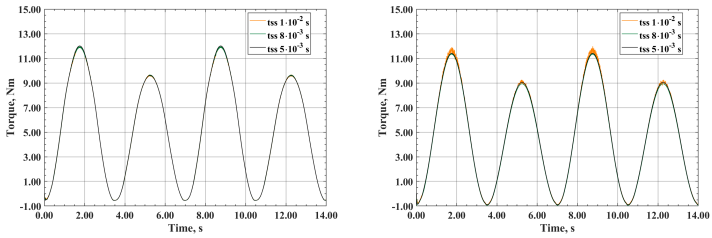


(a) MRF model (b) SM model

Figure 6.23: Sensitivity analysis of the blade torque to the time step size for **(a)** the MRF model and **(b)** the SM model.

The maximum variations of the torque acting on the blades of the rotor are less than 0.25% and 0.40% for the multiple reference frame and sliding mesh models, respectively, when the time step size is equal to $5 \cdot 10^{-3}$ s. For these reasons, such value of the time step size was utilised to simulate in time the transient CFD models for all the turbulence approaches and the methods for modelling rotation.

From a perusal of Figure 6.24, it is noticeable that the computational time required by the SM model is higher compared to the MRF model. In particular, the computational time is approximately 19% greater for the time step size of $5 \cdot 10^{-3}$ s.

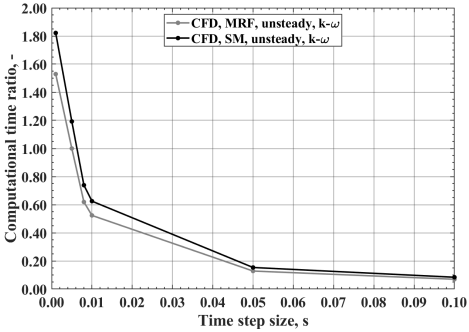


Figure 6.24: Computational time ratio for the MRF and SM models as a function of the time step size [30, 31].

#### 6.2.1.6 Analytical and numerical results

The results of the aerodynamics of the Wells turbine achieved with the BEM model and the CFD models are presented in terms of non-dimensional and dimensional parameters, following the traditional practice in turbomachinery [21]. The non-dimensional parameters are the flow coefficient, the input and torque coefficients $C_A$ and $C_T$, and the efficiency, defined in equations from Eq. (6.10) to Eq. (6.13), respectively. The dimensional parameters are the static-to-static pressure drop across the computational domain, the rotor torque, and the rotor power.

$$\phi_m = \frac{v_{x,m}}{U_m} \tag{6.10}$$

$$C_{A,m} = \frac{(p_{t,in} - p_{out})\dot{q}}{\frac{1}{2}\rho_{in}(v_{x,m}^2 + U_m^2)blZv_{x,m}} \tag{6.11}$$

$$C_{T,m} = \frac{\tau}{\frac{1}{2}\rho_{in}(v_{x,m}^2 + U_m^2)blZr_m} \tag{6.12}$$

$$\xi = \frac{\Omega\tau}{(p_{t,in} - p_{out})\dot{q}} = \frac{C_{T,m}}{\phi_m C_{A,m}} \tag{6.13}$$

where $p_{t,in}$ is the total pressure at the domain inlet, $p_{out}$ is the static pressure at the domain outlet, $\rho_{in}$ is the air density at the domain inlet, and subscript $m$ refers to the blade midspan.

The operating curves are presented as functions of the turbine volume flow rate or flow coefficient calculated at blade midspan. During the inflow phase, the airflow enters the device and the values of the flow coefficient and flow rate are considered negative; conversely, during the outflow phase, the airflow exits the device and the values are regarded as positive. Generally, the parameters reach higher values to parity of flow coefficient during the outflow for the greater air density due to the higher inlet pressure of the airflow originating in the caisson. The inlet airflow is in atmospheric conditions during the inflow phase, while during the outflow phase, its conditions are dependent upon the pressure variation in the caisson.

Except for the curves of efficiency, the values of all the performance parameters presented in Figures 6.25 and 6.26 monotonically rise with the absolute value of the flow coefficient of the volume flow rate.

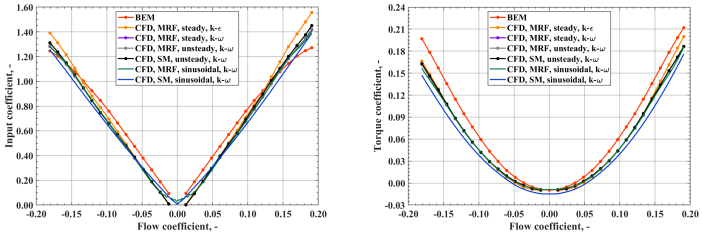


(a) Input coefficient (b) Torque coefficient

Figure 6.25: **(a)** Input coefficient and **(b)** torque coefficient versus flow coefficient at the blade midspan [31].

Figure 6.25a shows that the input coefficient has a linear relation with the flow coefficient and deviates from this trend only at the extremes of the operating range. The deviation is very slight for the CFD simulations with the κ-ω turbulence model, while it is more marked for the cases with the κ-ϵ model due to the prediction of greater pressure drops across the turbine duct. For the analytical model, the linear relation discrepancy is higher owing to the lower values of the pressure variation [30, 31].

In Figure 6.25b, the torque coefficient is negative for low incidence angles, corresponding to the values of $\phi_m$ between approximately -0.05 and 0.05. This occurs as the opposite contribution of the viscous forces prevails on that of the pressure forces acting on the rotor blade surfaces. For higher flow incidence angles, the torque coefficient is positive, as the contribution of the pressure forces is dominant. The BEM model provides higher levels of the torque coefficient regarding the CFD models due to the greater blade torque predicted [30, 31]. The higher values of the torque coefficient predicted by the BEM model regarding all the numerical models are mainly due to the determination of greater values of the lift coefficient compared to the drag coefficient, which re-

sult in a greater tangential force coefficient and a higher blade torque.

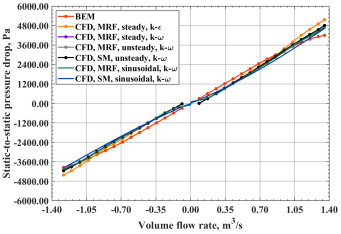


(a) Static-to-static pressure drop

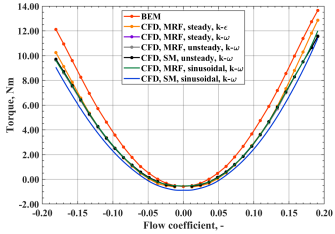


(b) Blade torque

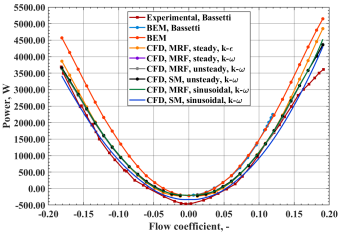


(c) Blade power

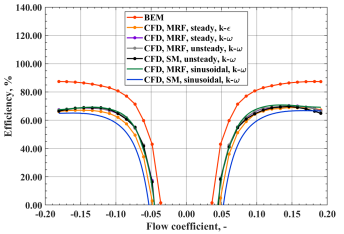


(d) Efficiency

Figure 6.26: **(a)** Static-to-static pressure drop versus volume airflow rate and **(b)** torque, **(c)** power, and **(d)** efficiency as functions of the flow coefficient at the blade midspan [31]

Figure 6.26a shows the static-to-static pressure drop between the turbine inlet and outlet as a function of the volume airflow rate. The relation is linear and deviates from linearity only at the extremes of the flow phases.

The torque acting on the rotor blades is presented in Figure 6.26b by varying the midspan flow coefficient. As the related torque coefficient, the torque increases with the rise of the absolute value of the flow coefficient and thus of the incidence angle of the flow.

In Figure 6.26c, the power transferred by the flow to the

blades is shown. Since the rotational velocity is constant, the power curves have the same trend as those of the torque. It is noticeable that the results of the CFD models are in close agreement with the experimental literature results for the whole inflow phase and the majority of the outflow phase. Conversely, at the extreme of the outflow phase, the experimental curve of the power is subject to a reduction of the growth speed, which is not shown by the CFD models [49,50]. The $\kappa$-$\omega$ turbulence model predicts power values closer to the experimental results than the $\kappa$-$\epsilon$ model. The overestimation of the power of the numerical models can be addressed to the absence of mechanical losses and, for the CFD models, even of the tip clearance. The analytical model provides results in excellent agreement with the analytical literature model and has a broader range of applicability than this reference, as it considers both the inflow and outflow phases. Either the analytical models overestimate the rotor power [30, 31].

The curves of efficiency are depicted in Figure 6.26d. The efficiency of the turbine increases with the absolute value of the flow coefficient up to a specific value, after which it declines. The peak efficiency is reached during the outflow phase and is nearly 87% for the analytical model and ranges between 69% and 71% for the CFD models. The CFD models based on applying a sinusoidal function for the inlet velocity and the $\kappa$-$\omega$ turbulence model were selected for further analyses as they provide the closest results to the experimental data [30, 31]. The higher peak efficiency achieved with the analytical model compared to the numerical models is mainly due to the greater torque determined, while the influence of the differences in the values of pressure variation are lower.

The CFD models based on applying a sinusoidal function for the inlet velocity and the κ-ω turbulence model were selected to examine further the modelling, as they provide the closest results to the experimental data.

In Figure 6.27, the variation of the absolute tangential velocity of the airflow is analysed. Since the flow entering the turbine duct is assumed to be perfectly axial, this quantity coincides with the tangential component of the absolute velocity in the downwind section. In particular, for the analytical model, the variation is calculated between the inlet and outlet sections positioned far upstream and downstream of the rotor. The maximum average value of the change in the absolute tangential velocity inside the computational domain is considered for the CFD models. This value is reached right downwind of the rotor blades, as moving towards the outlet the swirl reduces.

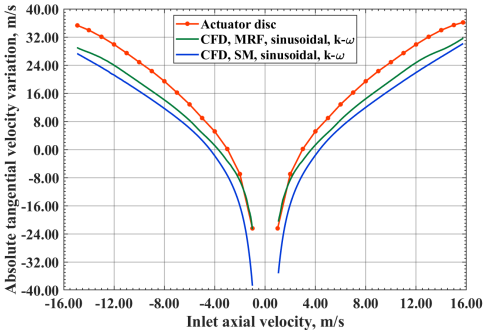


Figure 6.27: Variation of the absolute tangential velocity predicted by the analytical and numerical models [31].

The variations of the absolute tangential velocity achieved with the BEM model are generally higher regarding the CFD models in the entire operating range, except at the lowest abso-

lute values of the flow coefficient for the case of the MRF model. The differences in the outcomes are due to the overprediction by the analytical model of the tangential force acting on the rotor blades. This, in turn, depends on the overestimation of the lift force regarding the drag force.

The computational fluid dynamics analyses of the monoplane isolated Wells turbines provide the details of the flow field crossing the turbine duct and impacting the rotor. The results achieved allow the determination of the operating curves and performance of the turbomachine.

At first, the influence of the potential effect on the rotor blades was investigated. This aspect is particularly important as the analyses were performed on a section of the turbine annulus by imposing circumferential periodicity boundary conditions instead of solving the computations for the full annulus. The flow fields of the static-to-static pressure variation across the turbine duct were considered to analyse the potential effect caused by the interaction of the wake at the trailing edge of each blade with the leading edge of the following blade of the row. The images from Figure 6.28 to Figure 6.31 are close-ups of the distributions of the relative static pressure in the region around a rotor blade, in correspondence with evenly spaced surfaces positioned with a constant radius at 25%, 50% and 75% of the blade span. The inflow and outflow phases are shown for the MRF and SM models corresponding to the intermediate and maximum values of the inlet velocity magnitude. Since the potential effect is limited for both the numerical models and all the investigated velocities, the use of the circumferential periodicity boundary conditions on a section of the annulus is a reasonable approach instead of performing full annulus analyses [30, 31].

In Figure 6.28 the relative static pressure flow field calculated with the MRF model is depicted for the extremes of the inflow and outflow phases. The difference in relative pressure between the upstream and downstream of the rotor is higher when the flow exits the system to parity of the axial flow velocity. This is due to the different conditions of the inlet air, which are atmospheric during the inflow, while they depend upon the pressure variation along the turbine duct during the outflow. Moving from the blade hub to the blade tip, the magnitude of the pressure variation increases. This is mainly determined by the rise of the maximum values and the reduction of the minimum values of the static pressure close to the leading edge.

(a) Inflow, 25% span (b) Inflow, 50% span (c) Inflow, 75% span

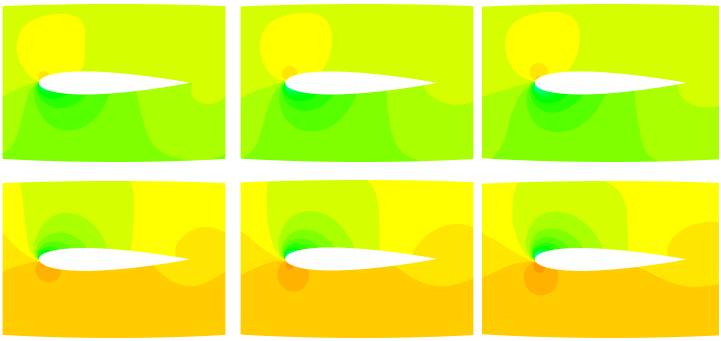

(d) Outflow, 25% span (e) Outflow, 50% span (f) Outflow, 75% span


Figure 6.28: Flow fields of the relative static pressure computed with the MRF model at the extremes of the inflow and outflow phases.

The comparison between the relative static pressure predicted by the multiple reference frame and the sliding mesh in Figures 6.28 and 6.29, respectively, indicates that similar distributions

are obtained with the two methods for modelling rotation during the inflow and outflow phases and along the blade radius.

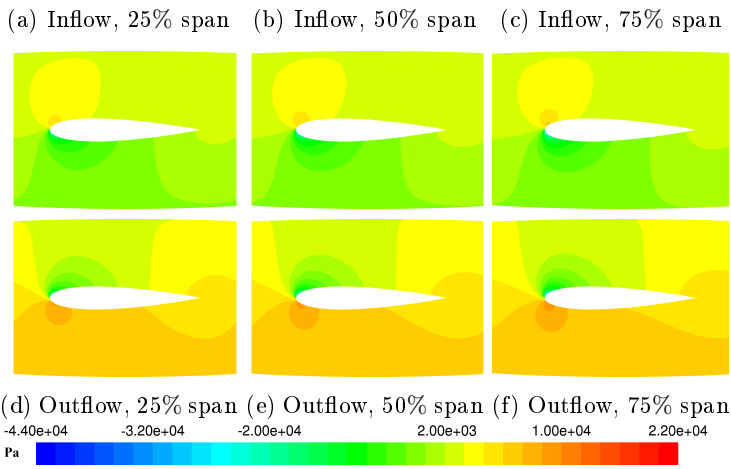


Figure 6.29: Flow fields of the relative static pressure computed with the SM model at the extremes of the inflow and outflow phases.

In Figure 6.30 the flow fields of the relative static pressure obtained with the MRF model are illustrated along the blade span for the intermediate value of the range of the inlet axial velocity analysed, which is equal to 8 m/s. The computed distributions denote lower values of the variation of the relative static pressure across the rotor row regarding the case with the maximum inlet velocity magnitude. For both the flow phases, the same volume flow rate through the rotor is obtained.

Even for the intermediate values of the inlet velocity, using the multiple reference frame model or the sliding mesh model leads to analogous flow fields of the relative static pressure.

In Figure 6.32, the flow fields of the absolute tangential velocity around the blade computed with the MRF model are depicted

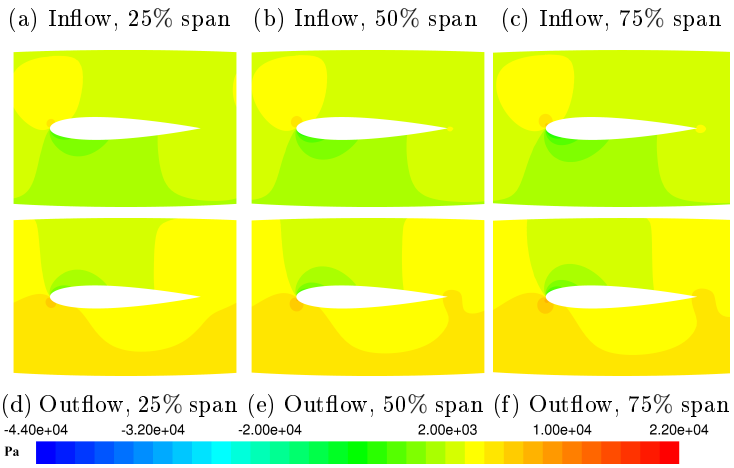


Figure 6.30: Flow fields of the relative static pressure computed with the MRF model corresponding to the inlet velocity magnitude of 8 m/s.

on evenly spaced surfaces with a constant radius at 25%, 50%, and 75% of the blade span for the inflow and outflow phases corresponding to the highest inlet velocity magnitude. The flow is attached to the blade from the hub (a, d) to the tip (c, f) for the inflow and outflow phases. Higher velocities can be noticed at the blade tip, in particular close to the leading edge, due to the higher peripheral speed [30, 31]. The greatest values of tangential velocity occur at the leading edge on the pressure side, while the lowest values are located at the leading edge on the suctions side and in the wake at the trailing edge, especially on the pressure side. The trailing edge wake is significantly distorted by the interaction between the blades composing the cascade.

(a) Inflow, 25% span (b) Inflow, 50% span (c) Inflow, 75% span

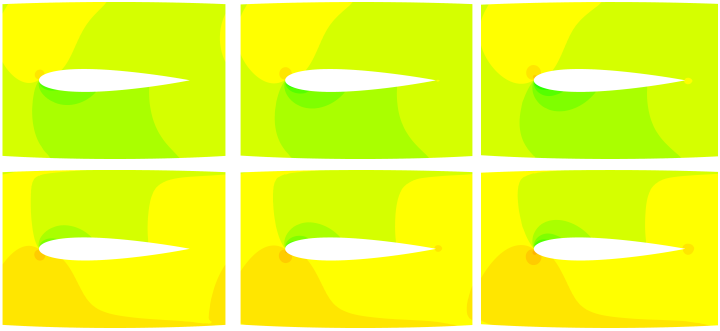

(d) Outflow, 25% span (e) Outflow, 50% span (f) Outflow, 75% span


Figure 6.31: Flow fields of the relative static pressure computed with the SM model corresponding to the inlet velocity magnitude of 8 m/s.

(a) Inflow, 25% span (b) Inflow, 50% span (c) Inflow, 75% span

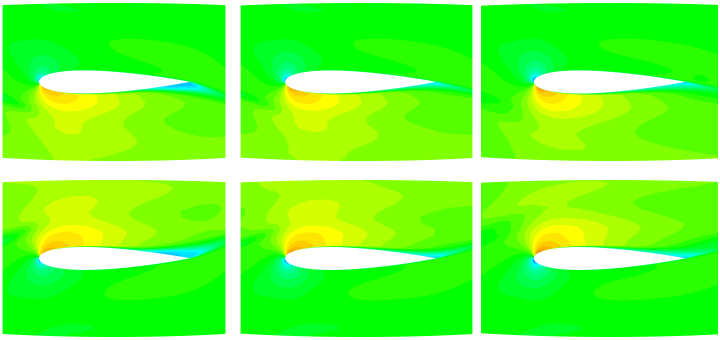

(d) Outflow, 25% span (e) Outflow, 50% span (f) Outflow, 75% span


Figure 6.32: Flow fields of the absolute tangential velocity calculated with the MRF model at the extremes of the inflow and outflow phases [30, 31].

The distributions of the absolute tangential velocity of Figure 6.33 obtained with the sliding mesh model are in strict accordance with the distributions of Figure 6.32 calculated with the multiple reference frame model.

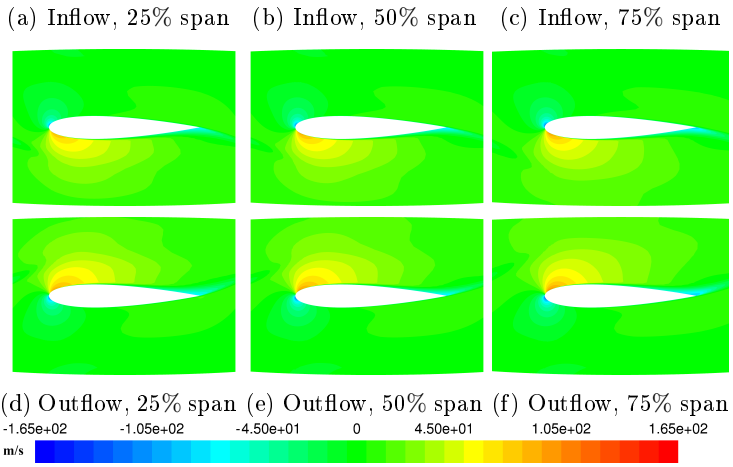


Figure 6.33: Flow fields of the absolute tangential velocity calculated with the SM model at the extremes of the inflow and outflow phases [31].

The flow fields of the absolute tangential velocity are depicted even for the intermediate values of the inlet axial velocity, which are equivalent to -8 m/s and 8 m/s during the inflow and outflow phases, respectively. The distributions of this quantity calculated with the MRF and SM models are illustrated in Figures 6.34 and 6.35.

The reduction of the absolute tangential velocity in the wake at the outlet of the blade is presented in Figures from 6.36 to 6.39 on sections evenly spaced in the circumferential direction, in correspondence with three radial positions equal to 25%, 50%, and 75% of the blade span. Moving away from the blade, from

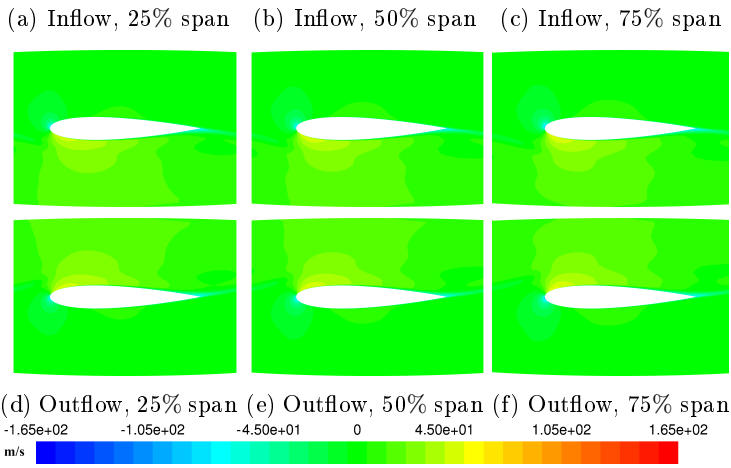


Figure 6.34: Flow fields of the absolute tangential velocity calculated with the MRF model corresponding to the inlet velocity magnitude of 8 m/s.

line 1 to line 5, the influence of the wake is reduced, the wake tends to mix with the surrounding flow, and it is deflected in the downstream direction. For the selected control lines, the effects of the wake enhance moving towards the blade hub. The consequences of the wake presence are more pronounced during the outflow than the inflow owing to the different inlet air conditions [31].

(a) Inflow, 25% span (b) Inflow, 50% span (c) Inflow, 75% span

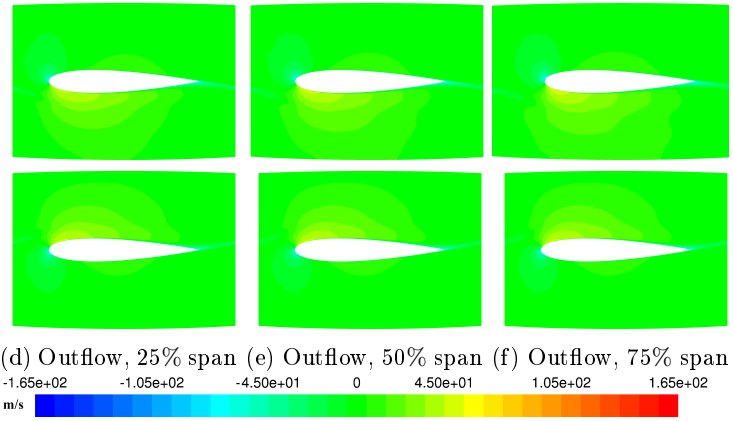


(d) Outflow, 25% span (e) Outflow, 50% span (f) Outflow, 75% span

Figure 6.35: Flow fields of the absolute tangential velocity calculated with the SM model corresponding to the inlet velocity magnitude of 8 m/s.

(a) Inflow, 25% span (b) Inflow, 50% span (c) Inflow, 75% span

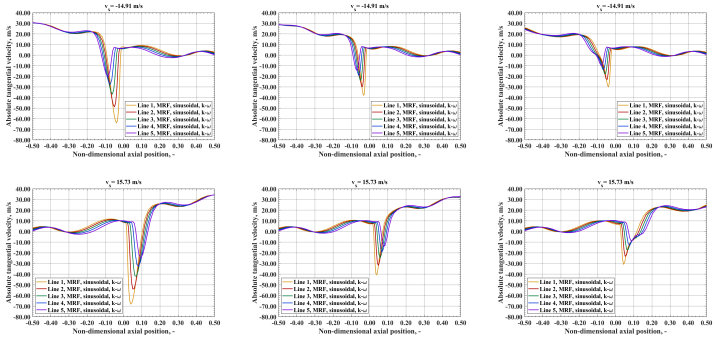

(d) Outflow, 25% span (e) Outflow, 50% span (f) Outflow, 75% span

Figure 6.36: Absolute tangential velocity in the trailing edge region computed with the MRF model at the extremes of **(a, b, c)** the inflow and **(d, e, f)** outflow phases.

By comparing the two rotational models, the predicted trend of the absolute tangential velocity is similar, although the variations obtained with the MRF model are higher regarding the SM model.

(a) Inflow, 25% span (b) Inflow, 50% span (c) Inflow, 75% span

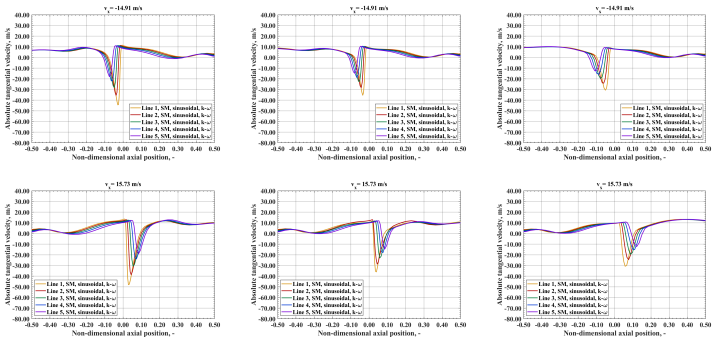


(d) Outflow, 25% span (e) Outflow, 50% span (f) Outflow, 75% span

Figure 6.37: Absolute tangential velocity in the trailing edge region computed with the SM model at the extremes of **(a, b, c)** the inflow and **(d, e, f)** outflow phases.

Considering the intermediate values of the inlet velocity, the decrease of the absolute tangential velocity in the wake has the same trend observed at the extremes of the inflow and outflow phases. However, the effects are significantly lower in magnitude.

(a) Inflow, 25% span (b) Inflow, 50% span (c) Inflow, 75% span

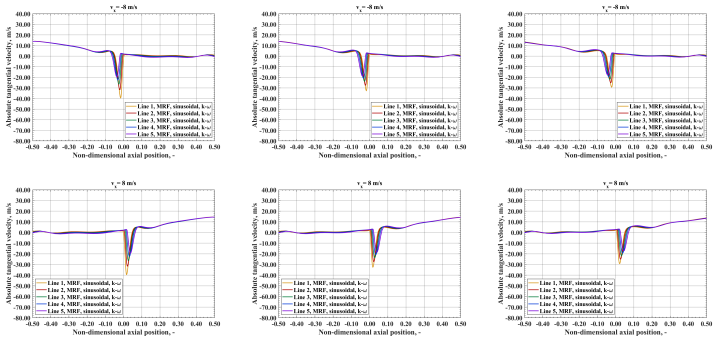


(d) Outflow, 25% span (e) Outflow, 50% span (f) Outflow, 75% span

Figure 6.38: Absolute tangential velocity in the trailing edge region computed with the MRF model for the axial velocity magnitude of 8 m/s during **(a, b, c)** the inflow and **(d, e, f)** outflow.

(a) Inflow, 25% span (b) Inflow, 50% span (c) Inflow, 75% span

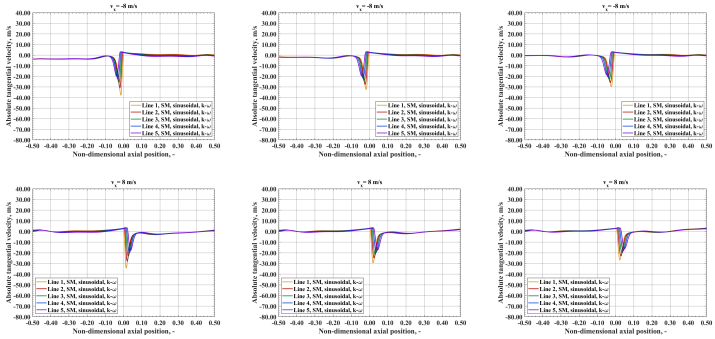


(d) Outflow, 25% span (e) Outflow, 50% span (f) Outflow, 75% span

Figure 6.39: Absolute tangential velocity in the trailing edge region computed with the SM model for the axial velocity magnitude of 8 m/s during **(a, b, c)** the inflow and **(d, e, f)** outflow.

The distributions of the relative static pressure and the isentropic Mach number are plotted in the graphs of Figure 6.40 and 6.41 by varying the normalised curvilinear abscissa along the blade surface on the pressure side and the suction side of the rotor blade. The graphs are referred to curves with constant radial coordinates equal to 25%, 50%, and 75% of the blade span. The results are depicted for both the outflow phase (continuous line) and the inflow phase (dashed line) and consider the extremes and the two selected intermediate values of the flow phases [31].

The isentropic Mach number is obtained with Eq. (6.14) by applying the isentropic flow relations.

$$Ma_{is} = \sqrt{\left(\left(\frac{p_{t,fr}}{p}\right)^{\frac{\gamma-1}{\gamma}} - 1\right)\frac{2}{\gamma-1}} \qquad (6.14)$$

where $p_{t,fr}$ is the reference total pressure calculated in the free stream based on the inlet static pressure and the inlet velocity computed in the rotating reference frame.

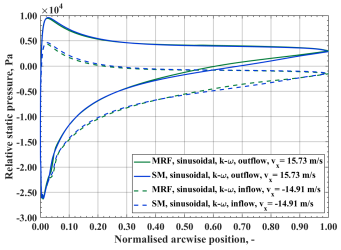


(a) Static pressure, 75% span

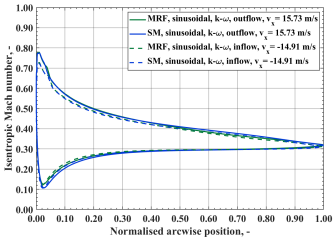


(b) Isentropic Mach, 75% span

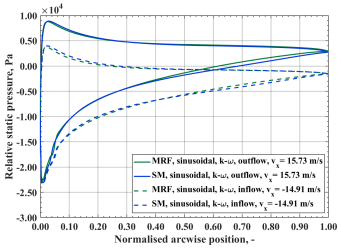


(c) Static pressure, 50% span

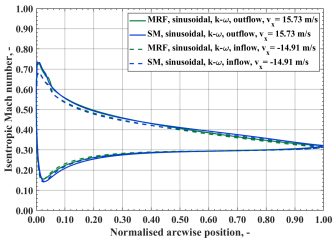


(d) Isentropic Mach, 50% span

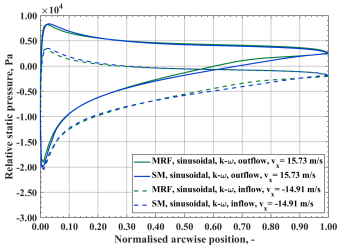


(e) Static pressure, 25% span

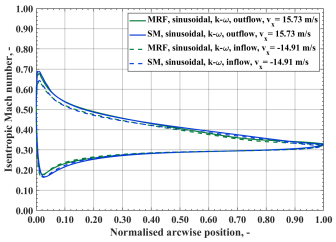


(f) Isentropic Mach, 25% span

Figure 6.40: Distribution of the relative static pressure and isentropic Mach number along the pressure side and suction side of a rotor blade calculated with the MRF and SM models.

At the leading edge of the suction side, the flow has a rapid acceleration and quickly reaches the maximum isentropic Mach number in correspondence with the minimum of the static pressure. Afterwards, the flow experiences a smooth deceleration to its lowest value due to the shape of the airfoil. On the pressure

side, the flow firstly decelerates and then accelerates with a very gradual trend in the region subject to the slow reduction of the static pressure. During the inflow, the static pressure values on the blade surfaces are lower regarding the outflow and result in smaller variations of the isentropic Mach number [31].

The static pressure and the isentropic Mach number on the blade surface computed at the intermediate values of the inlet velocity have analogous distributions to those obtained corresponding to the extremes of the flow phases. The main difference is represented by the average lower values and the significantly smaller peaks reached, especially in the leading edge region.

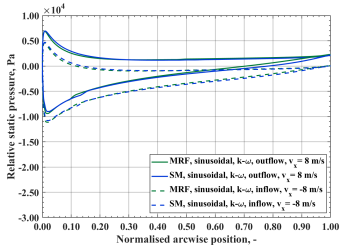


(a) Static pressure, 75% span

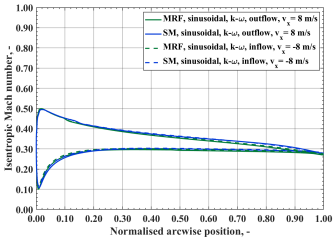


(b) Isentropic Mach, 75% span

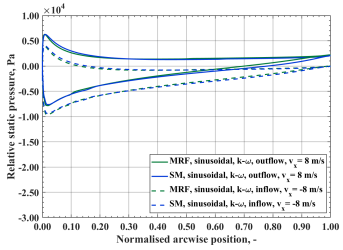


(c) Static pressure, 50% span

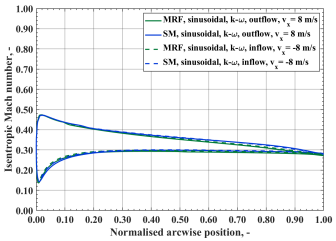


(d) Isentropic Mach, 50% span

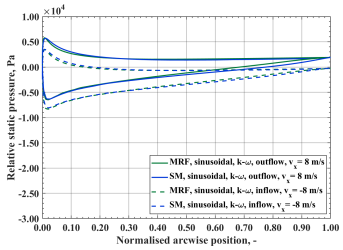


(e) Static pressure, 25% span

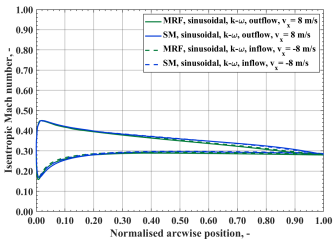


(f) Isentropic Mach, 25% span

Figure 6.41: Distribution of the relative static pressure and isentropic Mach number along the pressure side and suction side of a rotor blade calculated with the MRF and SM models.

Figure 6.42 indicates the variation of the specific enthalpy between the inlet and outlet of the turbine duct as a function of the specific entropy obtained at the extremes of the flow phases. The variation in the specific total enthalpy equals the difference between the specific work exchanged by the flow with the rotor

blades and the specific work lost for the friction with the other wall boundaries. The specific total enthalpy drop during the outflow is greater than during the inflow, resulting in a higher power transferred from the airflow to the rotor. Considering the entire operating range, the variation in the specific total enthalpy leads to the calculation of an average value of the power acting on the rotor blades that is 6.09% lower for the SM model regarding the MRF model [31].

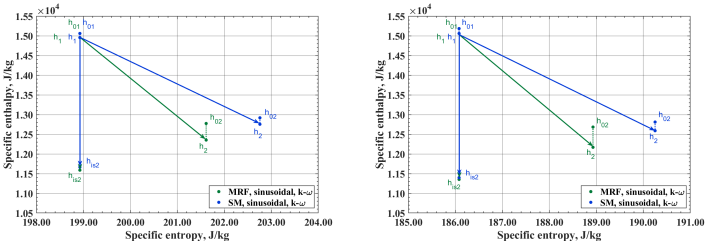


(a) Input coefficient (b) Torque coefficient

Figure 6.42: Specific enthalpy variation versus specific entropy generation calculated across the turbine duct calculated with **(a)** the MRF model and **(b)** the SM model [31].

The power transferred from the flow to the turbine and the efficiency computed with the BEM model and the CFD models are compared in Table 6.5 considering the extremes of the flow phases [31].

| Quantity | Inflow | | | Outflow | | |
|---|---|---|---|---|---|---|
| | BEM | MRF | SM | BEM | MRF | SM |
| $v_{x1}$, m/s | -14.91 | -14.91 | -14.91 | 15.73 | 15.73 | 15.73 |
| $\dot{m}$, kg/s | -1.57 | -1.57 | -1.57 | 1.73 | 1.73 | 1.73 |
| $P_I$, W | 5244 | 5367 | 5252 | 5915 | 6542 | 6454 |
| $P_b$, W | 4568 | 3625 | 3411 | 5147 | 4528 | 4300 |
| $\xi$, % | 87.12 | 67.54 | 64.95 | 87.00 | 69.22 | 66.63 |

Table 6.5: Power conversion and efficiency computed with the analytical and CFD models [31].

Finally, the time series of the power converted by the monoplane isolate Wells turbine are presented in Figure 6.43 for the CFD models with sinusoidal function for the inlet velocity [31].

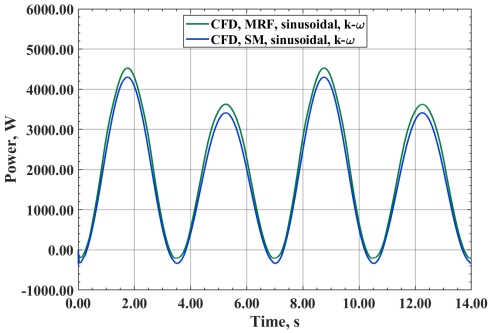


Figure 6.43: Time series of the power exerted by the airflow on the rotor blades for the MRF and SM models [31].

The computational model providing the closest results to the experimental data applies the sliding mesh scheme and the κ-ω turbulence model and assigns a sinusoidal function for the inlet velocity. This configuration and the use of a mesh with around 3.85 million nodes and a time step of $5 \cdot 10^{-3}$ s are sug-

gested to achieve the highest accuracy. Moreover, time-variant inlet boundary conditions allow the analysis of the flow quantities and the performance parameters in the time domain, making the CFD model suitable for coupling with the models of the primary and tertiary converters. Conversely, when the objective of the analysis is comparing a wide variety of cases, the frozen rotor approximation (MRF model) is a cost-effective approach to evaluating the machine operation and a mesh with about 1.6 million nodes and time step size up to $1 \cdot 10^{-2}$ s may be utilised. For further speeding up the computations, the use of incompressible gas formulations is recommended.

### 6.2.2 Axial impulse turbine

An impulse turbine for oscillating water column systems was investigated with an analytical approach and computational fluid dynamics to assess the aerodynamics of the airflow and obtain the operating curves, power conversion, and performance parameters.

The analytical model applies the blade element momentum theory and is described in detail in Sections 4.3. It is based on the application to the present case of the experimental correlations, which are widely used for the design of axial turbomachines, in accordance with the similarities between these applications. With this approach, the turbine cascades are modelled as sets of blades, formed by a finite number of airfoils stacked in the radial direction. The flow is assumed to be steady, axisymmetric, and inviscid [33].

For the CFD model, the generation of the computational domain, represented by the straight annular duct embedding the

inlet and outlet guide vanes and the rotor, and its spatial discretisation were obtained with *ANSYS ICEM 20.2*. The simulations were performed with *ANSYS Fluent 20.2* and the results were processed with *ANSYS CFD Post 20.2*. A completely automated procedure was developed for the entire model. Either RANS and u-RANS analyses were conducted using the $\kappa$-$\omega$ stress transport model with low Reynolds number correction to the turbulent viscosity. The motion of the turbine rotor was modelled with the mixing plane approach.

Even for the impulse turbine, two-dimensional models were created during the preliminary phases of the study to quickly evaluate the parameters of the computational settings.

#### 6.2.2.1 Numerical domain

An axial-flow impulse turbine for wave energy converters was analysed. As explained in detail in Section 3.3, an impulse turbine is constituted by one rotor row and two stator rows, which alternate in the function of inlet and outlet guide vanes. The stators are symmetrically positioned with respect to the plane of symmetry of the three cascades and are orthogonal to the rotation axis. The nozzles of the stators and the blades of the rotor have a symmetrical shape and are staggered around the central hub of the machine.

The geometry and the operating conditions of the analysis were defined based on the turbine experimentally studied by Setoguchi [208, 32]. The scheme of the blade-to-blade section of the impulse turbine is shown in Figure 6.44.

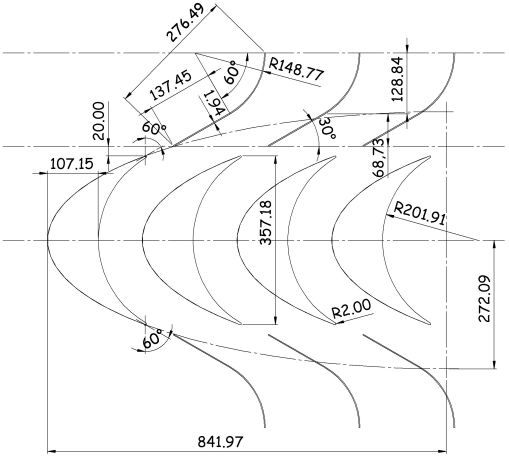


Figure 6.44: Scheme of the blade-to-blade section of the axial impulse turbine with the indication of the main geometric parameters.

The principal characteristics of the turbine are shown in Figure 6.44 and are listed in Table 6.6.

The flow conditions and the geometry of the straight annular duct and the turbine are axisymmetric. Therefore, the model is periodic in the circumferential direction, even for the case of the impulse turbine. Hence, the computational domain was created to enclose a single rotor blade and a single vane of each stator cascade. Three cell zones were defined along the axial direction: inlet guide vane, rotor, and outlet guide vane. The first and the last cell zones are stationary parts, and each one embeds a single stator vane, while the second zone is a rotating region modelling the rotor movement and includes a single rotor blade (Figure 6.45). The rotor region has a circumferential extension of $1/30$ of the turbine annular duct, while for the stator regions, the extension is equal to $1/26$ of the duct. This allowed performing

| Parameter | Description |
|---|---|
| Turbine typology | Axial-flow |
| Blade profile | Circular-elliptic |
| Rotor blade number | 30 |
| Stator blade number | 26 |
| Turbine casing diameter | 0.30 m |
| Hub to tip ratio | 0.70 |
| Stator chord length | 0.054 m |
| Rotor chord length | 0.070 m |
| Rotational speed | 600 rpm |
| Maximum velocity magnitude | 19.7 $^{m}/_{s}$ |

Table 6.6: Main geometric specifications and operating conditions of the impulse turbine analytically and numerically investigated.

the calculations on single blade passages without the need for full annulus simulations. As a consequence, the computational effort required was markedly reduced.

The computational domain of the turbomachine is defined by the inlet and outlet boundaries, the periodic surfaces, the annulus walls, and the walls of the stator and rotor blades. Even for the impulse turbine, the tip clearance was not modelled for limiting the computational requirements. Considering the typical dimensions of the clearance gap, the effects of neglecting the presence of this geometrical feature are limited for the purposes of the present modelling.

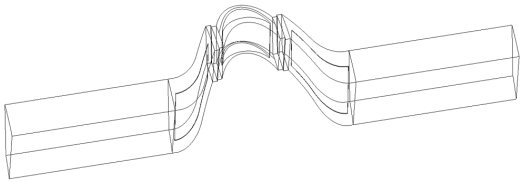

Figure 6.45: Scheme of the computational domain and the boundaries of the impulse turbine.

#### 6.2.2.2 Numerical grid

The computational domain and its spatial discretisation were generated with *ANSYS ICEM 20.2*. A fully mapped mesh of hexahedral elements was created by applying a multi-block technique. A C-type mesh topology was defined in the regions around the rotor blade and the stator blades to analyse in detail the boundary layer flow, while in the other parts of the domain, H-type mesh topologies were applied (Figure 6.46).

Figure 6.46: Isometric view of the wall mesh of the impulse turbine.

The numerical grid is defined by 6.78 million nodes and 6.58 million elements. The fine mesh satisfies the convergence crite-

ria of the mass conservation within $10^{-3}$ and maximum order of the root mean squares residuals of $10^{-6}$ for the continuity, momentum, turbulence, and energy equations.

A total of 400 nodes were distributed around the profile of the rotor, and 50 nodes were set both at the leading edge and trailing edge.

In the axial direction, 200 nodes were defined in the rotating region, and 180 nodes were positioned in the stationary regions, of which 100 were set close to the stator blades and 80 in the other parts of the duct. In the radial direction, 80 nodes were distributed along the blade span.

The dimension of the boundary layer cells in the direction normal to the wall was defined to achieve values of $y^+$ lower than the unit to perform simulations with the $\kappa$-$\omega$ turbulence model. The growth ratio of the cells was imposed equal to 1.05 at all the wall boundaries and was increased to 1.2 in the remaining parts of the domain (Figure 6.47).

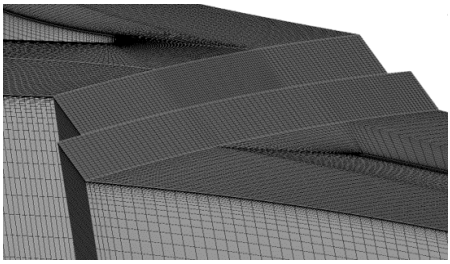

Figure 6.47: Mesh close-up at the interface between the rotor and stator cell zones of the impulse turbine.

#### 6.2.2.3 Mathematical modelling

The solution of the fluid dynamics of the impulse turbine was achieved with steady and unsteady Reynolds averaged Navier-

Stokes analyses performed with *ANSYS Fluent 20.2* for a compressible ideal gas. The governing equations of the mass, momentum, and energy conservation are discussed in Section 5.2 and are provided by Eqs. (5.6), (5.7), and (5.8), respectively. The air density, the thermal conductivity, and the dynamic viscosity were calculated based on the air temperature.

The description of the mathematical modelling is analogous to the case of the CFD model of the Wells turbine of Section 6.2.1.3.

#### 6.2.2.4 Boundary conditions

The boundary conditions for the definition of the numerical settings of the impulse turbine were defined in analogy with the model of the Wells turbine 6.2.1.4.

At the inlet, the flow velocity, turbulent intensity, length scale, and temperature were imposed, while at the outlet, the static pressure, radial equilibrium, and turbulent intensity, length scale, and temperature of the back-flow were assigned. No-slip conditions were set on the blade and walls. Rotational periodicity and periodicity conditions were defined for the circumferential side-walls of the rotating and stationary parts, respectively.

#### 6.2.2.5 CFD sensitivity analysis

A mesh sensitivity analysis was performed to ensure the independence of the computational grid. The predictions of several different meshes with a number of nodes ranging between 1.5 and 9.5 million were compared. The grids created for the comparison with the selected mesh were generated by homogeneously varying the element number of the grid blocks. During this pro-

cedure, the minimum number of nodes around the rotor blade and stator blades was fixed to 300 and 50, respectively, while it was fixed to 60 in the spanwise direction.

The selected mesh fulfils the requirements of variation within 0.1% for both the blade torque and the pressure drop across the turbine.

#### 6.2.2.6 Analytical and numerical results

The analytical and CFD models of the impulse turbine developed were validated through the comparison with literature experimental data obtained at a laboratory scale [32].

Figure 6.48 reports the comparison between the outcomes of the literature experiments and the results of the models developed for the same impulse turbine and operating conditions. The performance parameters that were considered are the input coefficient, the torque coefficient, and the turbine efficiency.

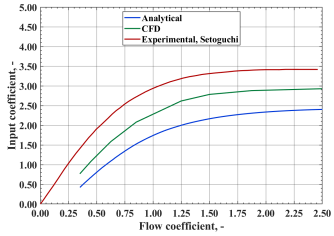


(a) Input coefficient

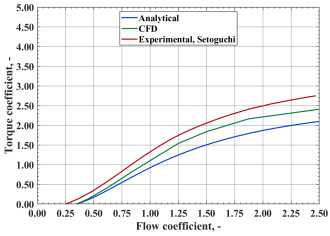


(b) Torque coefficient

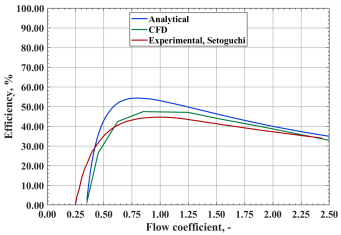


(c) Efficiency

Figure 6.48: Comparison of the results of the analytical and CFD models with the experimental data obtained by Setoguchi [32] in terms of **(b)** input coefficient, **(b)** torque coefficient, and **(c)** efficiency.

Upon examining the results, it is noticeable that all the curves of the analytical and CFD models, and of the literature experimental model have similar trends. The discrepancies with the experiments are higher for the analytical data than for the numerical data.

In Figure 6.48a, both the analytical and CFD models underestimate the input coefficient for all the values of the flow coefficient. This is due to the prediction of lower values of the total-to-static pressure drop across the turbine regarding the experiments.

The slight discrepancies between the analytical, numerical,

and experimental results visible in Figure 6.48b can be addressed to the underestimation by the developed models of the torque exerted by the airflow on the rotor, owing to the determination of lower values of flow angle variation across the rotor cascade.

Figure 6.48c indicates that efficiency is underestimated by the analytical model at the very small values of the flow coefficient owing to the lower torque prediction compared with the experiments. For the remaining part of the operating range, the analytical model overestimates efficiency as the differences in the predictions of the pressure drop prevail on those of the torque. The numerical model provides slightly lower values of efficiency for the entire flow phase.

The results achieved with the analytical and CFD models are considered very promising within the limitations discussed above.

Figure 6.49 shows the relative static pressure flow field on evenly spaced surfaces with a constant radius at 25%, 50%, and 75% of the blade span. The distributions were computed corresponding with the maximum absolute values of the inlet axial velocity during the inflow and outflow phases.

During the outflow phase, the difference in the relative pressure across the rotor is slightly higher to parity of the axial flow velocity, mainly due to the different inlet conditions of the air. The magnitude of the pressure difference rises moving from the hub to the tip of the blade.

Moreover, it is noticeable that the potential effect is limited, allowing the application of circumferential periodicity boundary conditions instead of performing full annulus analyses.

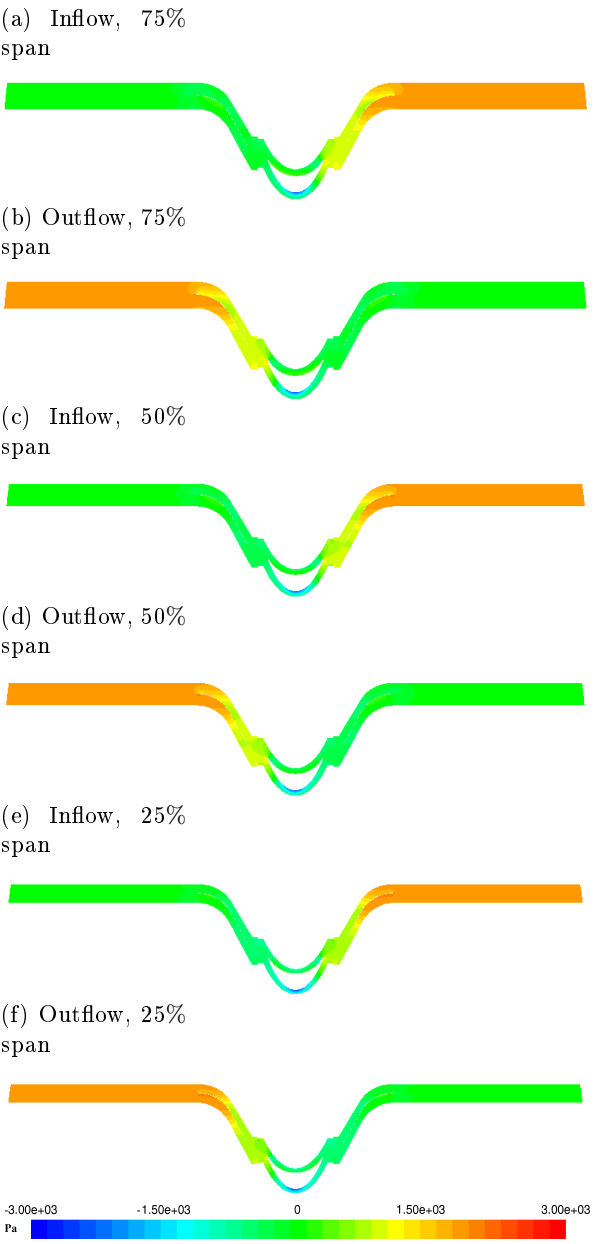


Figure 6.49: Flow fields of the relative static pressure computed corresponding with the maximum absolute values of the inlet velocity during the inflow and outflow phases.

The flow fields of the absolute tangential velocity are presented in Figure 6.50. The flow is attached to the blade for all the values of the span. The maximum levels of this quantity are achieved downstream of the rotor, between its blade and the outlet guide vane. After the passage through this stator row, the flow is straightened and becomes nearly axial at the outlet section.

(a) Inflow, 75% span

(b) Outflow, 75% span

(c) Inflow, 50% span

(d) Outflow, 50% span

(e) Inflow, 25% span

(f) Outflow, 25% span

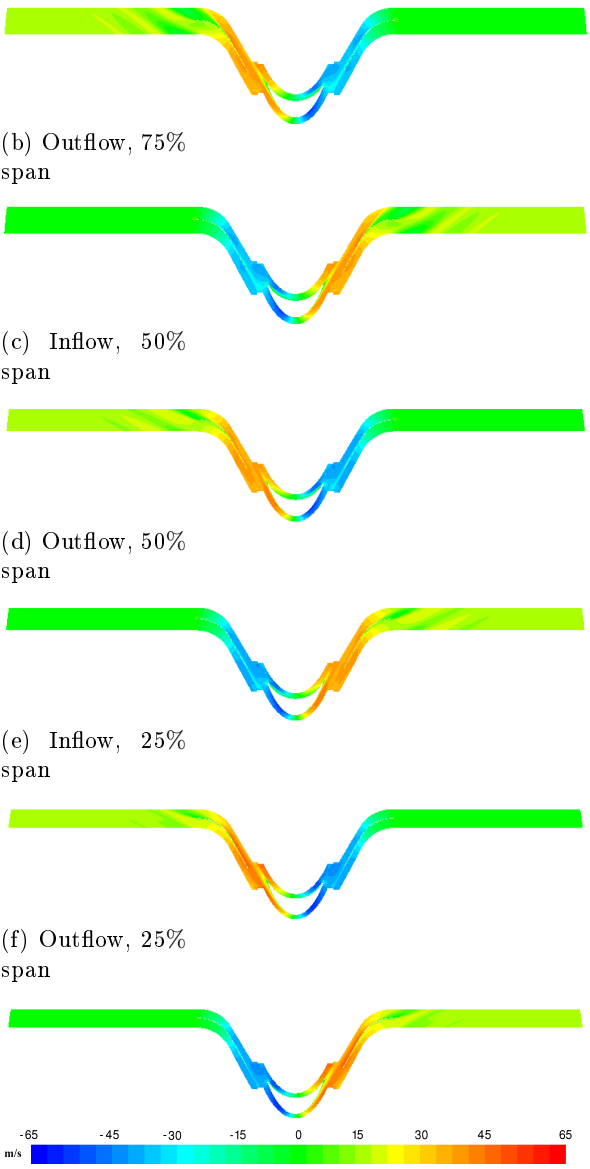


Figure 6.50: Flow fields of the absolute tangential velocity calculated corresponding with the maximum value of the inlet velocity during the inflow and outflow phases.

Focusing now on the operating curves predicted with the analytical model, Figures 6.51 and 6.52 denote that the performance parameters monotonically increase with the rise of the absolute values of the flow coefficient or the volume flow rate during either the flow phases, apart from the efficiency.

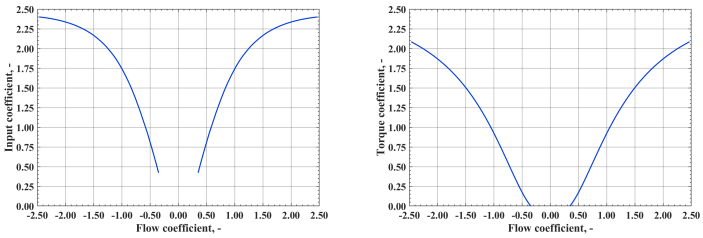


(a) Input coefficient (b) Torque coefficient

Figure 6.51: **(a)** Input coefficient and **(b)** torque coefficient versus flow coefficient at the blade midspan.

Figure 6.51a presents the input coefficient as a function of the flow coefficient for the entire operating range of the impulse turbine. The speed of variation of the curves is higher for the lowest absolute values of the flow coefficient and significantly decreases at the extremes of the flow phases.

In Figure 6.51b, the torque coefficient is negative for values of the flow coefficient ranging between -0.34 and 0.34 due to the low incidence angles. This determines the predominance of the viscous forces on the pressure forces exerted on the blade surfaces. Increasing the absolute values of the flow coefficient, the pressure forces are dominant, and the torque coefficient is positive.

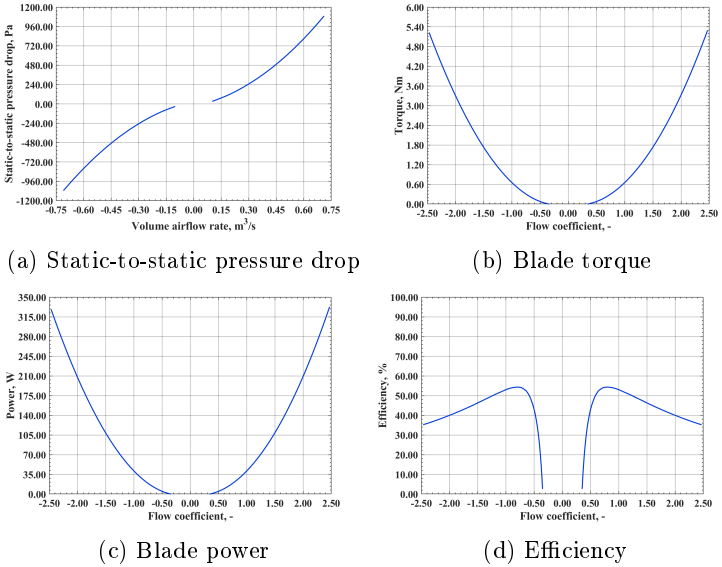


(a) Static-to-static pressure drop

(b) Blade torque

(c) Blade power

(d) Efficiency

Figure 6.52: **(a)** Static-to-static pressure drop versus volume airflow rate and **(b)** torque, **(c)** power, and **(d)** efficiency as functions of the flow coefficient at the blade midspan

Figure 6.52a shows the relation between the static-to-static pressure drop across the turbine and the volume flow rate. The graph indicates that the relation is quadratic in the entire operating range, as typical of axial impulse turbines

Figure 6.52b indicates that the torque is positive for a significant part of the operating conditions. This allows for suitable energy conversion under the flow conditions analysed.

The power transferred from the airflow to the rotor is presented in Figure 6.52d. The curve has the same trend of the torque as the angular velocity of the rotor is constant.

Figure 6.52 denotes that the peaks of the efficiency of energy conversion are around 54% for both the flow phases. These values are reached for relatively low absolute values of the flow

coefficient of around 0.80 indicating that the turbine operates with limited efficiency corresponding to the extremes of the flow phases.

## 6.3 Tertiary converter results

The control algorithm of the coupling between the turbine and the electric generator is explained in detail in Section 4.4. It relies regulating the instantaneous values of the rotor angular velocity and the torque transmission between the turbomachine and the generator. The generator is disconnected from the rotor when the turbine torque is negative, which decelerates based on its inertia. On the contrary, when the torque is positive, the logic applied depends on the comparison between the design and actual values of the rotational speed. If the actual value is equal or greater than the design value, the electric load is connected, and the torque is transmitted from the turbine to the generator. If the actual value is lower than the design value, the mechanical transmission is interrupted until the design speed is reached, thus allowing the rotor to accelerate.

For the application cases presented in Section 6.1, the use of the control strategy increases the energy harvesting. For the system operating with the Wells turbine, the annual energy converted rises of 10.48%, while the increase is 3.51% for configuration with the axial impulse turbine. The enhancement of the conversion achieved with a control strategy regulating the instant rotor angular velocity and torque is significantly greater for the former machine.

The energy conversion and aerodynamic efficiency of an air turbine for OWC systems are strongly affected by the rapid de-

crease of the net torque transferred by the flow to the rotor, especially at the extremes of their operating range. This is due to the low ratio of the tangential force to the axial force acting on the blade, determined by high absolute values of the flow coefficient.

Since Wells turbines have a narrow operating compared to impulse turbines, they function for longer periods in off-design conditions. This implies the higher effects of the control system on the energy conversion end efficiency. Conversely, the wider operating range of impulse turbines determines smoother variations of these parameters for the different conditions of the wave spectrum of the sea.

# Chapter 7

# Wave-to-wire model results

*The wave-to-wire model was developed and applied to analyse the functioning of wave energy converters based on the oscillating water column technology. Two highly energetic points located near the coasts of Italy were selected for evaluating the possible future installation of the systems in wave conditions typical of moderate Mediterranean wave climates. With this aim, optimisation procedures were performed to establish the system configurations that maximise the annual energy harvesting from waves to wire. The geometry and properties of the chamber were obtained from laboratory experiments conducted to optimise the efficiency of pneumatic energy transformation for moderate Mediterranean wave states. The optimal geometry and functioning conditions of either monoplane isolated Wells turbines and axial impulse turbines were determined by investigating the operating maps of a wide set of configurations. The operating curves, performance parameters, and energy extraction were achieved on an annual*

*basis for the selected application sites and system layouts. Finally, the possibility of enhancing the power output was analysed by considering different design values of rotational speed during the four seasons of the year.*

## 7.1 Application site selection

The analytical wave-to-wire model was applied to real sea wave conditions with the aim of assessing the operation of wave energy converters functioning with the oscillating water column principle. A preliminary analysis was carried out on a broad set of locations to identify the most suitable ones for installing OWC systems. All the wave conditions and the corresponding energy transport and frequency of occurrence were determined for each of them. The wave spectra of all the locations considered are typical of moderate Mediterranean wave climates. Two sites were selected from the entire set as wave energy hotspots of different regions of Italy [49, 33, 24].

The selected points are located on a water depth of 50 m close to the coast. The first point (P1) is situated in the central sea of Tuscany and its WGS84–UTM32 coordinates are latitude 4826150 m N and longitude 587255 m E (Figure 7.1). The average specific power transported by sea waves during one year is 3.3 kW/m regarding the wavefront. The second point (P2) is positioned in front of the north-west coast of Sardinia with WGS84–UTM32 coordinates: latitude 4509971 m N and longitude: 424733 m E (Figure 7.1). This site is characterised by an average annual wave power of 10.5 kW/m regarding the wavefront, which is remarkably higher compared to the first point [33, 24].

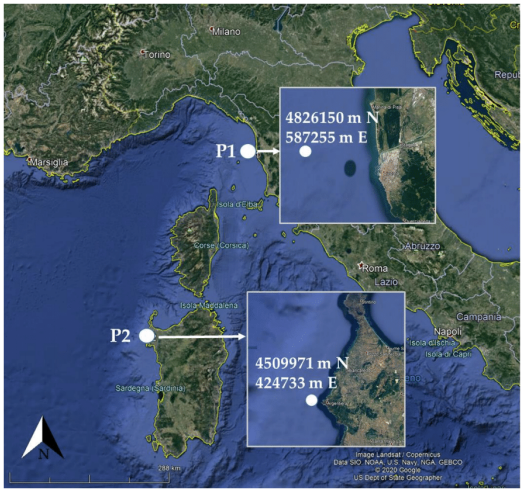


Figure 7.1: Geographical map and coordinates of the sites with highly energetic wave climate selected to apply the wave-to-wire model [33].

The evaluation of the energy potential of the sea waves of the two sites is based upon a wave hindcasting dataset for a period of 20 years, achieved by using the third-generation spectral wave model WAVEWATCH III [249]. The dataset, developed and validated by the *LABIMA* at the *University of Florence*, provides wave data for the whole Mediterranean Sea for the period from 2000 to 2019 with hourly sampling [250]. The spectral domain of the numerical model is set to 25 frequencies in the interval between 0.042 and 0.410 Hz, and the grid resolution is set to 0.05° in both latitude and longitude. Every sea state is defined by a couple of values of significant wave height $H_{m0}$ and wave energy period $T_{m-1,0}$ using the JONSWAP spectrum. The corresponding deep-water power for meter of wavefront length $P_w$, is obtained through Eq. (7.1). The use of this formula may introduce some approximations, especially for the longest waves, due

to the partial dissipation of energy in propagating from deep waters to the depth of 50 m. However, this effect is very limited in the present case and the related approximations are considered acceptable for the purpose of the research.

$$P_w = \frac{1}{64}\frac{g^2}{\pi}\rho_w H_{m,0}^2 T_{m-1,0} \tag{7.1}$$

The average annual values of sea wave power achieved with the hindcast datasets of the two locations differ for less than 15% from the results of a work previously conducted by the *LABIMA* [250]. This study was based on a 5-year-long dataset obtained by the *French Research Institute for Exploitation of the Sea* with the *MED6MIN* model. The distribution of the yearly wave energy $AE$, resulting from combining the specific wave power of Eq. (7.1) and the frequency of the event of every wave condition, is reported in Figure 7.2 for either the selected sites.

| P1 | | $T_{m-1,0}$ [s] | | | | | | | | | | |
|---|---|---|---|---|---|---|---|---|---|---|---|---|
| AE [kWh/m] | | <3 | 3-4 | 4-5 | 5-6 | 6-7 | 7-8 | 8-9 | 9-10 | 10-11 | 11-12 | > 12 |
| $H_{m0}$ [m] | > 9 | 0 | 0 | 0 | 0 | 0 | 0 | 0 | 0 | 0 | 0 | 0 |
| | 8-9 | 0 | 0 | 0 | 0 | 0 | 0 | 0 | 0 | 0 | 0 | 0 |
| | 7-8 | 0 | 0 | 0 | 0 | 0 | 0 | 0 | 0 | 0 | 0 | 0 |
| | 6-7 | 0 | 0 | 0 | 0 | 0 | 0 | 0 | 31 | 79 | 0 | 0 |
| | 5-6 | 0 | 0 | 0 | 0 | 0 | 0 | 65 | 481 | 32 | 0 | 0 |
| | 4-5 | 0 | 0 | 0 | 0 | 0 | 50 | 1171 | 322 | 70 | 0 | 0 |
| | 3-4 | 0 | 0 | 0 | 0 | 18 | 1842 | 1770 | 384 | 85 | 25 | 0 |
| | 2-3 | 0 | 0 | 0 | 22 | 1300 | 3398 | 1500 | 493 | 183 | 7 | 0 |
| | 1-2 | 0 | 14 | 276 | 2045 | 4233 | 2892 | 1365 | 351 | 34 | 0 | 0 |
| | < 1 | 90 | 1153 | 1129 | 692 | 318 | 119 | 42 | 7 | 1 | 0 | 0 |

| P2 | | $T_{m-1,0}$ [s] | | | | | | | | | | |
|---|---|---|---|---|---|---|---|---|---|---|---|---|
| AE [kWh/m] | | <3 | 3-4 | 4-5 | 5-6 | 6-7 | 7-8 | 8-9 | 9-10 | 10-11 | 11-12 | > 12 |
| $H_{m0}$ [m] | > 9 | 0 | 0 | 0 | 0 | 0 | 0 | 0 | 0 | 0 | 53 | 0 |
| | 8-9 | 0 | 0 | 0 | 0 | 0 | 0 | 0 | 0 | 135 | 401 | 0 |
| | 7-8 | 0 | 0 | 0 | 0 | 0 | 0 | 0 | 41 | 1379 | 263 | 0 |
| | 6-7 | 0 | 0 | 0 | 0 | 0 | 0 | 0 | 1772 | 2601 | 123 | 0 |
| | 5-6 | 0 | 0 | 0 | 0 | 0 | 0 | 816 | 6316 | 1491 | 62 | 0 |
| | 4-5 | 0 | 0 | 0 | 0 | 0 | 324 | 7570 | 5834 | 718 | 65 | 0 |
| | 3-4 | 0 | 0 | 0 | 0 | 277 | 5733 | 10390 | 3057 | 323 | 29 | 4 |
| | 2-3 | 0 | 0 | 0 | 338 | 4468 | 10345 | 5334 | 1227 | 75 | 5 | 6 |
| | 1-2 | 0 | 9 | 923 | 5550 | 6829 | 3047 | 609 | 34 | 4 | 0 | 0 |
| | < 1 | 21 | 708 | 1033 | 499 | 99 | 6 | 1 | 0 | 0 | 0 | 0 |

Figure 7.2: Scatter matrices of the average annual values of specific wave energy $AE$ for classes of different significant wave height $H_{m0}$ and wave energy period $T_{m-1,0}$.

The rigid piston model is applied for every wave status considering a regular wave with height $H$ and a period $T$ conveying the same energy of the related irregular wave motion. Hence, the relations of Eq. (4.1) and Eq. (4.2) were assigned.

This modelling is a good approximation of real random waves with a narrow-band frequency spectrum, while it leads to some inaccuracies in the case of a wide-band frequency spectrum. Considering the huge amount of system configurations that must be simulated for preforming the turbine optimisation, this approach has been applied to limit the computational efforts.

The average annual values of specific wave energy and frequency of occurrence of each wave condition used in the computations were extracted from the scatter matrices of Figure 7.2. The data were obtained by limiting the maximum wave height

to 5 m to avoid seawater entry in the turbine duct. Despite the reduction of data regarding the complete scatter matrices, this selection allows considering approximately 90% and 83% of the energy exploitable from the sea waves for the application sites located in Tuscany and Sardinia, respectively [33]. The wave conditions imposed in the wave-to-wire model are resumed in the scatter matrices reported in Tables 7.1 and 7.2 for Tuscany and in Tables 7.3 and 7.4 for Sardinia.

| $AE$, kWh/m | | $T_{m-1,0}$, s | | | | | | | | | | |
|---|---|---|---|---|---|---|---|---|---|---|---|---|
| | | 2.5 | 3.5 | 4.5 | 5.5 | 6.5 | 7.5 | 8.5 | 9.5 | 10.5 | 11.5 | 12.5 |
| $H_{m0}$, m | 4.5 | 0 | 0 | 0 | 0 | 0 | 50 | 1171 | 322 | 70 | 0 | 0 |
| | 3.5 | 0 | 0 | 0 | 0 | 18 | 1842 | 1770 | 384 | 85 | 25 | 0 |
| | 2.5 | 0 | 0 | 0 | 22 | 1300 | 3398 | 1500 | 493 | 183 | 7 | 0 |
| | 1.5 | 0 | 14 | 276 | 2045 | 4233 | 2892 | 1365 | 351 | 34 | 0 | 0 |
| | 0.5 | 90 | 1153 | 1129 | 692 | 318 | 119 | 42 | 7 | 1 | 0 | 0 |

Table 7.1: Scatter matrix of the annual specific wave energy $AE$ distribution of the wave conditions in Tuscany, for classes of significant wave height $H_{m0}$ and energy period $T_{m-1,0}$ [33].

| $rf$, % | | $T_{m-1,0}$, s | | | | | | | | | | |
|---|---|---|---|---|---|---|---|---|---|---|---|---|
| | | 2.5 | 3.5 | 4.5 | 5.5 | 6.5 | 7.5 | 8.5 | 9.5 | 10.5 | 11.5 | 12.5 |
| $H_{m0}$, m | 4.5 | 0 | 0 | 0 | 0 | 0 | 0.01 | 0.16 | 0.04 | 0.01 | 0 | 0 |
| | 3.5 | 0 | 0 | 0 | 0 | 0.01 | 0.48 | 0.41 | 0.08 | 0.02 | 0 | 0 |
| | 2.5 | 0 | 0 | 0 | 0.02 | 0.76 | 1.73 | 0.67 | 0.20 | 0.07 | 0 | 0 |
| | 1.5 | 0 | 0.04 | 0.65 | 3.94 | 6.90 | 4.09 | 1.70 | 0.39 | 0.03 | 0 | 0 |
| | 0.5 | 3.44 | 31.44 | 23.94 | 12.00 | 4.67 | 1.51 | 0.47 | 0.07 | 0.01 | 0 | 0 |

Table 7.2: Scatter matrix of the annual relative frequency $rf$ distribution of the wave conditions in Tuscany, for classes of significant wave height $H_{m0}$ and energy period $T_{m-1,0}$ [33].

| $AE$, kWh/m | | $T_{m-1,0}$, s | | | | | | | | | | |
|---|---|---|---|---|---|---|---|---|---|---|---|---|
| | | 2.5 | 3.5 | 4.5 | 5.5 | 6.5 | 7.5 | 8.5 | 9.5 | 10.5 | 11.5 | 12.5 |
| $H_{m0}$, m | 4.5 | 0 | 0 | 0 | 0 | 0 | 324 | 7570 | 5834 | 718 | 65 | 0 |
| | 3.5 | 0 | 0 | 0 | 0 | 277 | 5733 | 10390 | 3057 | 323 | 29 | 4 |
| | 2.5 | 0 | 0 | 0 | 338 | 4468 | 10345 | 5334 | 1227 | 75 | 5 | 6 |
| | 1.5 | 0 | 9 | 923 | 5550 | 6829 | 3047 | 609 | 34 | 4 | 0 | 0 |
| | 0.5 | 21 | 708 | 1033 | 499 | 99 | 6 | 1 | 0 | 0 | 0 | 0 |

Table 7.3: Scatter matrix of the annual specific wave energy $AE$ distribution of the wave conditions in Sardinia, for classes of significant wave height $H_{m0}$ and energy period $T_{m-1,0}$ [33, 24].

| $rf$, % | | $T_{m-1,0}$, s | | | | | | | | | | |
|---|---|---|---|---|---|---|---|---|---|---|---|---|
| | | 2.5 | 3.5 | 4.5 | 5.5 | 6.5 | 7.5 | 8.5 | 9.5 | 10.5 | 11.5 | 12.5 |
| $H_{m0}$, m | 4.5 | 0 | 0 | 0 | 0 | 0 | 0.05 | 1.05 | 0.72 | 0.08 | 0.01 | 0 |
| | 3.5 | 0 | 0 | 0 | 0 | 0.08 | 1.49 | 2.38 | 0.63 | 0.06 | 0 | 0 |
| | 2.5 | 0 | 0 | 0 | 0.23 | 2.62 | 5.26 | 2.39 | 0.49 | 0.03 | 0 | 0 |
| | 1.5 | 0 | 0.03 | 2.17 | 10.70 | 11.14 | 4.31 | 0.76 | 0.04 | 0 | 0 | 0 |
| | 0.5 | 0.79 | 19.31 | 21.90 | 8.66 | 1.46 | 0.08 | 0.01 | 0 | 0 | 0 | 0 |

Table 7.4: Scatter matrix of the annual relative frequency $rf$ distribution of the wave conditions in Sardinia, for classes of significant wave height $H_{m0}$ and energy period $T_{m-1,0}$ [33, 24].

For either application sites, the seasonal scatter matrices of specific wave energy and relative frequency were obtained by determining their average distributions during the four seasons of the year.

The seasonal values of $AE$ and $rf$ defining the wave conditions of the site positioned in Tuscany are expressed in Tables from 7.5 to 7.12 as functions of the significant wave height and energy period.

| $AE$, kWh/m | | $T_{m-1,0}$, s | | | | | | | | | | |
|---|---|---|---|---|---|---|---|---|---|---|---|---|
| | | 2.5 | 3.5 | 4.5 | 5.5 | 6.5 | 7.5 | 8.5 | 9.5 | 10.5 | 11.5 | 12.5 |
| $H_{m0}$, m | 4.5 | 0 | 0 | 0 | 0 | 0 | 35 | 590 | 166 | 22 | 0 | 0 |
| | 3.5 | 0 | 0 | 0 | 0 | 4 | 639 | 766 | 219 | 3 | 18 | 0 |
| | 2.5 | 0 | 0 | 0 | 6 | 380 | 833 | 643 | 223 | 133 | 4 | 0 |
| | 1.5 | 0 | 11 | 102 | 608 | 1071 | 958 | 650 | 182 | 23 | 0 | 0 |
| | 0.5 | 33 | 218 | 229 | 170 | 100 | 46 | 20 | 3 | 0 | 0 | 0 |

Table 7.5: Scatter matrix of the winter specific wave energy $AE$ distribution of the wave conditions in Tuscany, for classes of significant wave height $H_{m0}$ and energy period $T_{m-1,0}$.

| $rf$, % | | $T_{m-1,0}$, s | | | | | | | | | | |
|---|---|---|---|---|---|---|---|---|---|---|---|---|
| | | 2.5 | 3.5 | 4.5 | 5.5 | 6.5 | 7.5 | 8.5 | 9.5 | 10.5 | 11.5 | 12.5 |
| $H_{m0}$, m | 4.5 | 0 | 0 | 0 | 0 | 0 | 0.02 | 0.33 | 0.08 | 0.01 | 0 | 0 |
| | 3.5 | 0 | 0 | 0 | 0 | 0 | 0.68 | 0.72 | 0.18 | 0 | 0.01 | 0 |
| | 2.5 | 0 | 0 | 0 | 0.02 | 0.91 | 1.73 | 1.18 | 0.37 | 0.20 | 0 | 0 |
| | 1.5 | 0 | 0.14 | 0.98 | 4.79 | 7.14 | 5.53 | 3.31 | 0.83 | 0.09 | 0 | 0 |
| | 0.5 | 5.08 | 24.27 | 19.82 | 12.03 | 5.96 | 2.41 | 0.91 | 0.13 | 0.01 | 0 | 0 |

Table 7.6: Scatter matrix of the winter relative frequency $rf$ distribution of the wave conditions in Tuscany, for classes of significant wave height $H_{m0}$ and energy period $T_{m-1,0}$.

| $AE$, kWh/m | | $T_{m-1,0}$, s | | | | | | | | | | |
|---|---|---|---|---|---|---|---|---|---|---|---|---|
| | | 2.5 | 3.5 | 4.5 | 5.5 | 6.5 | 7.5 | 8.5 | 9.5 | 10.5 | 11.5 | 12.5 |
| $H_{m0}$, m | 4.5 | 0 | 0 | 0 | 0 | 0 | 4 | 131 | 73 | 11 | 0 | 0 |
| | 3.5 | 0 | 0 | 0 | 0 | 4 | 457 | 476 | 53 | 42 | 7 | 0 |
| | 2.5 | 0 | 0 | 0 | 6 | 259 | 1083 | 449 | 158 | 33 | 0 | 0 |
| | 1.5 | 0 | 1 | 68 | 474 | 1209 | 815 | 319 | 83 | 8 | 0 | 0 |
| | 0.5 | 252 | 315 | 201 | 82 | 32 | 13 | 3 | 1 | 0 | 0 | 0 |

Table 7.7: Scatter matrix of the spring specific wave energy $AE$ distribution of the wave conditions in Tuscany, for classes of significant wave height $H_{m0}$ and energy period $T_{m-1,0}$.

| $rf$, % | | $T_{m-1,0}$, s | | | | | | | | | | |
|---|---|---|---|---|---|---|---|---|---|---|---|---|
| | | 2.5 | 3.5 | 4.5 | 5.5 | 6.5 | 7.5 | 8.5 | 9.5 | 10.5 | 11.5 | 12.5 |
| $H_{m0}$, m | 4.5 | 0 | 0 | 0 | 0 | 0 | 0 | 0.07 | 0.04 | 0 | 0 | 0 |
| | 3.5 | 0 | 0 | 0 | 0 | 0 | 0.47 | 0.43 | 0.04 | 0.03 | 0 | 0 |
| | 2.5 | 0 | 0 | 0 | 0.02 | 0.60 | 2.17 | 0.79 | 0.25 | 0.05 | 0 | 0 |
| | 1.5 | 0 | 0.01 | 0.63 | 3.60 | 7.76 | 4.53 | 1.57 | 0.36 | 0.03 | 0 | 0 |
| | 0.5 | 2.40 | 27.06 | 26.27 | 13.70 | 4.73 | 1.61 | 0.56 | 0.14 | 0.03 | 0 | 0 |

Table 7.8: Scatter matrix of the spring relative frequency $rf$ distribution of the wave conditions in Tuscany, for classes of significant wave height $H_{m0}$ and energy period $T_{m-1,0}$.

| $AE$, kWh/m | | $T_{m-1,0}$, s | | | | | | | | | | |
|---|---|---|---|---|---|---|---|---|---|---|---|---|
| | | 2.5 | 3.5 | 4.5 | 5.5 | 6.5 | 7.5 | 8.5 | 9.5 | 10.5 | 11.5 | 12.5 |
| $H_{m0}$, m | 4.5 | 0 | 0 | 0 | 0 | 0 | 0 | 31 | 0 | 0 | 0 | 0 |
| | 3.5 | 0 | 0 | 0 | 0 | 0 | 166 | 100 | 0 | 0 | 0 | 0 |
| | 2.5 | 0 | 0 | 0 | 3 | 230 | 691 | 131 | 8 | 0 | 0 | 0 |
| | 1.5 | 0 | 0 | 30 | 369 | 1037 | 548 | 137 | 8 | 0 | 0 | 0 |
| | 0.5 | 11 | 371 | 334 | 161 | 53 | 14 | 2 | 0 | 0 | 0 | 0 |

Table 7.9: Scatter matrix of the summer specific wave energy $AE$ distribution of the wave conditions in Tuscany, for classes of significant wave height $H_{m0}$ and energy period $T_{m-1,0}$.

| $rf$, % | | $T_{m-1,0}$, s | | | | | | | | | | |
|---|---|---|---|---|---|---|---|---|---|---|---|---|
| | | 2.5 | 3.5 | 4.5 | 5.5 | 6.5 | 7.5 | 8.5 | 9.5 | 10.5 | 11.5 | 12.5 |
| $H_{m0}$, m | 4.5 | 0 | 0 | 0 | 0 | 0 | 0 | 0.02 | 0 | 0 | 0 | 0 |
| | 3.5 | 0 | 0 | 0 | 0 | 0 | 0.17 | 0.09 | 0 | 0 | 0 | 0 |
| | 2.5 | 0 | 0 | 0 | 0.01 | 0.53 | 1.38 | 0.23 | 0.01 | 0 | 0 | 0 |
| | 1.5 | 0 | 0 | 0.28 | 2.80 | 6.66 | 3.05 | 0.67 | 0.03 | 0 | 0 | 0 |
| | 0.5 | 1.58 | 39.82 | 27.84 | 10.99 | 3.08 | 0.68 | 0.07 | 0 | 0 | 0 | 0 |

Table 7.10: Scatter matrix of the summer relative frequency $rf$ distribution of the wave conditions in Tuscany, for classes of significant wave height $H_{m0}$ and energy period $T_{m-1,0}$.

| $AE$, kWh/m | | $T_{m-1,0}$, s | | | | | | | | | | |
|---|---|---|---|---|---|---|---|---|---|---|---|---|
| | | 2.5 | 3.5 | 4.5 | 5.5 | 6.5 | 7.5 | 8.5 | 9.5 | 10.5 | 11.5 | 12.5 |
| | 4.5 | 0 | 0 | 0 | 0 | 0 | 12 | 419 | 83 | 38 | 0 | 0 |
| | 3.5 | 0 | 0 | 0 | 0 | 10 | 580 | 428 | 112 | 39 | 0 | 0 |
| $H_{m0}$, m | 2.5 | 0 | 0 | 0 | 7 | 431 | 792 | 278 | 104 | 17 | 4 | 0 |
| | 1.5 | 0 | 2 | 76 | 594 | 915 | 572 | 260 | 78 | 3 | 0 | 0 |
| | 0.5 | 31 | 312 | 252 | 160 | 83 | 26 | 8 | 1 | 0 | 0 | 0 |

Table 7.11: Scatter matrix of the fall specific wave energy $AE$ distribution of the wave conditions in Tuscany, for classes of significant wave height $H_{m0}$ and energy period $T_{m-1,0}$.

| $rf$, % | | $T_{m-1,0}$, s | | | | | | | | | | |
|---|---|---|---|---|---|---|---|---|---|---|---|---|
| | | 2.5 | 3.5 | 4.5 | 5.5 | 6.5 | 7.5 | 8.5 | 9.5 | 10.5 | 11.5 | 12.5 |
| | 4.5 | 0 | 0 | 0 | 0 | 0 | 0.01 | 0.24 | 0.04 | 0.02 | 0 | 0 |
| | 3.5 | 0 | 0 | 0 | 0 | 0.01 | 0.61 | 0.40 | 0.09 | 0.03 | 0 | 0 |
| $H_{m0}$, m | 2.5 | 0 | 0 | 0 | 0.02 | 1.02 | 1.63 | 0.50 | 0.17 | 0.02 | 0 | 0 |
| | 1.5 | 0 | 0.02 | 0.73 | 4.63 | 6.04 | 3.27 | 1.31 | 0.35 | 0.01 | 0 | 0 |
| | 0.5 | 4.78 | 34.42 | 21.62 | 11.25 | 4.95 | 1.36 | 0.36 | 0.02 | 0 | 0 | 0 |

Table 7.12: Scatter matrix of the fall relative frequency $rf$ distribution of the wave conditions in Tuscany, for classes of significant wave height $H_{m0}$ and energy period $T_{m-1,0}$.

The seasonal data regarding the energy transport and frequency of occurrence of the wave conditions that characterise the wave climate of the application site located in Sardinia are presented in Tables from 7.13 to 7.20.

| $AE$, kWh/m | | $T_{m-1,0}$, s | | | | | | | | | | |
|---|---|---|---|---|---|---|---|---|---|---|---|---|
| | | 2.5 | 3.5 | 4.5 | 5.5 | 6.5 | 7.5 | 8.5 | 9.5 | 10.5 | 11.5 | 12.5 |
| | 4.5 | 0 | 0 | 0 | 0 | 0 | 185 | 3935 | 2959 | 335 | 65 | 0 |
| | 3.5 | 0 | 0 | 0 | 0 | 178 | 2440 | 3958 | 1600 | 193 | 29 | 4 |
| $H_{m0}$, m | 2.5 | 0 | 0 | 0 | 185 | 1743 | 3031 | 2113 | 657 | 45 | 6 | 6 |
| | 1.5 | 0 | 4 | 294 | 1530 | 1736 | 1070 | 284 | 12 | 1 | 0 | 0 |
| | 0.5 | 3 | 98 | 187 | 98 | 22 | 1 | 0 | 0 | 0 | 0 | 0 |

Table 7.13: Scatter matrix of the winter specific wave energy $AE$ distribution of the wave conditions in Sardinia, for classes of significant wave height $H_{m0}$ and energy period $T_{m-1,0}$ [24].

| $rf$, % | | $T_{m-1,0}$, s | | | | | | | | | | |
|---|---|---|---|---|---|---|---|---|---|---|---|---|
| | | 2.5 | 3.5 | 4.5 | 5.5 | 6.5 | 7.5 | 8.5 | 9.5 | 10.5 | 11.5 | 12.5 |
| | 4.5 | 0 | 0 | 0 | 0 | 0 | 0.12 | 2.21 | 1.49 | 0.15 | 0.03 | 0 |
| | 3.5 | 0 | 0 | 0 | 0 | 0.22 | 2.57 | 3.68 | 1.33 | 0.14 | 0.02 | 0 |
| $H_{m0}$, m | 2.5 | 0 | 0 | 0 | 0.52 | 4.15 | 6.26 | 3.85 | 1.07 | 0.07 | 0.01 | 0.01 |
| | 1.5 | 0 | 0.05 | 2.81 | 11.96 | 11.49 | 6.14 | 1.44 | 0.06 | 0 | 0 | 0 |
| | 0.5 | 0.46 | 10.83 | 16.09 | 6.91 | 1.34 | 0.07 | 0 | 0 | 0 | 0 | 0 |

Table 7.14: Scatter matrix of the winter relative frequency $rf$ distribution of the wave conditions in Sardinia, for classes of significant wave height $H_{m0}$ and energy period $T_{m-1,0}$ [24].

| $AE$, kWh/m | | $T_{m-1,0}$, s | | | | | | | | | | |
|---|---|---|---|---|---|---|---|---|---|---|---|---|
| | | 2.5 | 3.5 | 4.5 | 5.5 | 6.5 | 7.5 | 8.5 | 9.5 | 10.5 | 11.5 | 12.5 |
| | 4.5 | 0 | 0 | 0 | 0 | 0 | 57 | 1493 | 1162 | 208 | 0 | 0 |
| | 3.5 | 0 | 0 | 0 | 0 | 30 | 1480 | 2390 | 727 | 75 | 0 | 0 |
| $H_{m0}$, m | 2.5 | 0 | 0 | 0 | 51 | 1060 | 2751 | 1557 | 361 | 13 | 0 | 0 |
| | 1.5 | 0 | 3 | 219 | 1459 | 1867 | 860 | 140 | 11 | 3 | 0 | 0 |
| | 0.5 | 4 | 156 | 253 | 144 | 35 | 2 | 1 | 0 | 0 | 0 | 0 |

Table 7.15: Scatter matrix of the spring specific wave energy $AE$ distribution of the wave conditions in Sardinia, for classes of significant wave height $H_{m0}$ and energy period $T_{m-1,0}$ [24].

| $rf$, % | | $T_{m-1,0}$, s | | | | | | | | | | |
|---|---|---|---|---|---|---|---|---|---|---|---|---|
| | | 2.5 | 3.5 | 4.5 | 5.5 | 6.5 | 7.5 | 8.5 | 9.5 | 10.5 | 11.5 | 12.5 |
| | 4.5 | 0 | 0 | 0 | 0 | 0 | 0.04 | 0.82 | 0.57 | 0.09 | 0 | 0 |
| | 3.5 | 0 | 0 | 0 | 0 | 0.04 | 1.52 | 2.17 | 0.59 | 0.05 | 0 | 0 |
| $H_{m0}$, m | 2.5 | 0 | 0 | 0 | 0.14 | 2.47 | 5.55 | 2.77 | 0.58 | 0.02 | 0 | 0 |
| | 1.5 | 0 | 0.04 | 2.04 | 11.16 | 12.08 | 4.82 | 0.69 | 0.05 | 0.01 | 0 | 0 |
| | 0.5 | 0.67 | 16.84 | 21.28 | 9.91 | 2.03 | 0.10 | 0.03 | 0 | 0 | 0 | 0 |

Table 7.16: Scatter matrix of the spring relative frequency $rf$ distribution of the wave conditions in Sardinia, for classes of significant wave height $H_{m0}$ and energy period $T_{m-1,0}$ [24].

| $AE$, kWh/m | | $T_{m-1,0}$, s | | | | | | | | | | |
|---|---|---|---|---|---|---|---|---|---|---|---|---|
| | | 2.5 | 3.5 | 4.5 | 5.5 | 6.5 | 7.5 | 8.5 | 9.5 | 10.5 | 11.5 | 12.5 |
| | 4.5 | 0 | 0 | 0 | 0 | 0 | 11 | 381 | 271 | 0 | 0 | 0 |
| | 3.5 | 0 | 0 | 0 | 0 | 6 | 483 | 1412 | 82 | 0 | 0 | 0 |
| $H_{m0}$, m | 2.5 | 0 | 0 | 0 | 6 | 589 | 2214 | 583 | 27 | 0 | 0 | 0 |
| | 1.5 | 0 | 0 | 112 | 1139 | 1585 | 462 | 43 | 0 | 0 | 0 | 0 |
| | 0.5 | 8 | 278 | 320 | 127 | 17 | 2 | 1 | 0 | 0 | 0 | 0 |

Table 7.17: Scatter matrix of the summer specific wave energy $AE$ distribution of the wave conditions in Sardinia, for classes of significant wave height $H_{m0}$ and energy period $T_{m-1,0}$ [24].

| $rf$, % | | $T_{m-1,0}$, s | | | | | | | | | | |
|---|---|---|---|---|---|---|---|---|---|---|---|---|
| | | 2.5 | 3.5 | 4.5 | 5.5 | 6.5 | 7.5 | 8.5 | 9.5 | 10.5 | 11.5 | 12.5 |
| | 4.5 | 0 | 0 | 0 | 0 | 0 | 0.01 | 0.21 | 0.13 | 0 | 0 | 0 |
| | 3.5 | 0 | 0 | 0 | 0 | 0.01 | 0.50 | 1.28 | 0.07 | 0 | 0 | 0 |
| $H_{m0}$, m | 2.5 | 0 | 0 | 0 | 0.02 | 1.37 | 4.46 | 1.04 | 0.04 | 0 | 0 | 0 |
| | 1.5 | 0 | 0 | 1.05 | 8.70 | 10.25 | 2.59 | 0.21 | 0 | 0 | 0 | 0 |
| | 0.5 | 1.23 | 30.03 | 26.91 | 8.76 | 1.00 | 0.09 | 0.02 | 0 | 0 | 0 | 0 |

Table 7.18: Scatter matrix of the summer relative frequency $rf$ distribution of the wave conditions in Sardinia, for classes of significant wave height $H_{m0}$ and energy period $T_{m-1,0}$ [24].

| $AE$, kWh/m | | $T_{m-1,0}$, s | | | | | | | | | | |
|---|---|---|---|---|---|---|---|---|---|---|---|---|
| | | 2.5 | 3.5 | 4.5 | 5.5 | 6.5 | 7.5 | 8.5 | 9.5 | 10.5 | 11.5 | 12.5 |
| | 4.5 | 0 | 0 | 0 | 0 | 0 | 70 | 1761 | 1443 | 174 | 0 | 0 |
| | 3.5 | 0 | 0 | 0 | 0 | 63 | 1330 | 2630 | 648 | 56 | 0 | 0 |
| $H_{m0}$, m | 2.5 | 0 | 0 | 0 | 97 | 1076 | 2349 | 1081 | 182 | 17 | 0 | 0 |
| | 1.5 | 0 | 2 | 298 | 1422 | 1641 | 655 | 141 | 10 | 0 | 0 | 0 |
| | 0.5 | 5 | 177 | 273 | 130 | 25 | 1 | 0 | 0 | 0 | 0 | 0 |

Table 7.19: Scatter matrix of the fall specific wave energy $AE$ distribution of the wave conditions in Sardinia, for classes of significant wave height $H_{m0}$ and energy period $T_{m-1,0}$ [24].

| $rf$, % | | $T_{m-1,0}$, s | | | | | | | | | | |
|---|---|---|---|---|---|---|---|---|---|---|---|---|
| | | 2.5 | 3.5 | 4.5 | 5.5 | 6.5 | 7.5 | 8.5 | 9.5 | 10.5 | 11.5 | 12.5 |
| $H_{m0}$, m | 4.5 | 0 | 0 | 0 | 0 | 0 | 0.04 | 0.98 | 0.72 | 0.08 | 0 | 0 |
| | 3.5 | 0 | 0 | 0 | 0 | 0.08 | 1.39 | 2.42 | 0.53 | 0.04 | 0 | 0 |
| | 2.5 | 0 | 0 | 0 | 0.27 | 2.53 | 4.80 | 1.95 | 0.29 | 0.02 | 0 | 0 |
| | 1.5 | 0 | 0.02 | 2.82 | 11.00 | 10.74 | 3.71 | 0.71 | 0.04 | 0 | 0 | 0 |
| | 0.5 | 0.80 | 19.32 | 23.19 | 9.02 | 1.46 | 0.07 | 0 | 0 | 0 | 0 | 0 |

Table 7.20: Scatter matrix of the fall relative frequency $rf$ distribution of the wave conditions in Sardinia, for classes of significant wave height $H_{m0}$ and energy period $T_{m-1,0}$ [24].

## 7.2 Added mass determination with free decay experiments

The assessment of the operation of the chamber with the analytical model required the determination of the added mass of the oscillating water column, as explained in detail in Section 4.1.1. This parameter was obtained from free decay laboratory tests performed on a fixed, bottom-detached model of an OWC caisson with a prismatic shape. The tests were performed at a 1:50 scale in the wave flume of the *LABIMA* at the *University of Florence* [36].

A scheme of the investigated chamber and an image of the experimental model installed in the test rig are shown in Figures 7.3 and 7.4, respectively.

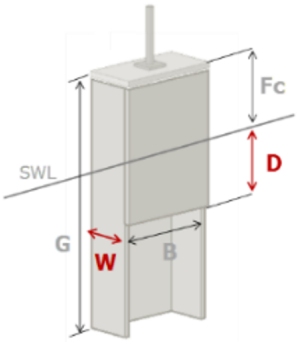


Figure 7.3: Scheme of the OWC chamber tested with small-scale experiments at the *LABIMA*.

The device could be conceived as integrated into an offshore construction, as a tension-leg platform or a very large floating structure [36]. Indeed, OWC systems that are fixed and detached regarding the sea bottom are often studied in the literature with reference to intermediate or deep-water conditions [251, 252, 253, 254].

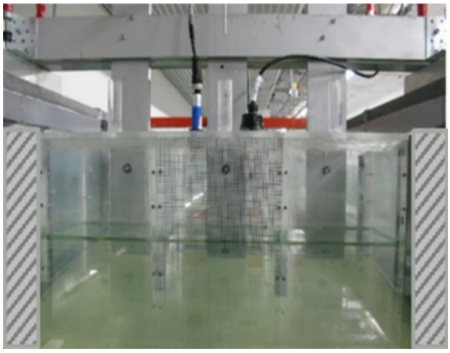

Figure 7.4: Image of the experimental model of the OWC chamber tested in the wave flume of the *LABIMA*.

The geometry of the caisson considered for the estimation of

$m_{add}$ is the one associated with the tested model that provided the highest efficiency of pneumatic energy conversion during the laboratory tests [36]. The maximum primary efficiency of about 73% was achieved with waves with a fixed significant height of 2 m and an energy period of 7 s using a chamber with the geometrical parameters listed in Table 7.21. The model was tested in a water depth of 0.5 m and its PTO was simulated by using a calibrated circular vent tube with a diameter of 0.03 m and a length of 0.1 m located on the top cover of the chamber [33].

| Chamber Outer Section | Chamber Inner Section | Chamber Height | Front Wall Draught Length | Front Wall Freeboard Section |
|---|---|---|---|---|
| $A_{c,ext}$, $m^2$ | $A_c$, $m^2$ | $G$, m | $D$, m | $F_c$, m |
| 0.040 | 0.033 | 0.290 | 0.090 | 0.160 |

Table 7.21: Main geometric parameters of the chamber optimising the primary efficiency determined with laboratory experiments carried out at the *LABIMA* [36, 33].

As a first approximation, the added mass was assumed independent from the frequency of waves [122].

The tests were performed by imposing an initial water level of the inner free surface of the model higher regarding the still water level and sampling the resulting free surface oscillation. The water motion inside the chamber was measured considering the displacements of the free surface, as noticeable in Figure 7.5. A procedure based on the analysis of the decay of the free surface oscillations was implemented to estimate the added mass [33].

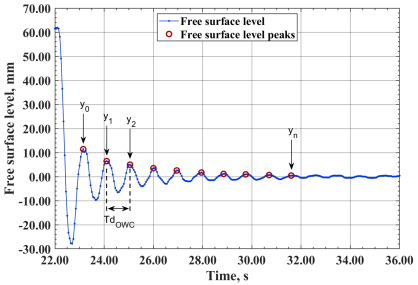


Figure 7.5: Time series of the free surface oscillation inside the oscillating water column chamber in the free decay tests [33].

From the decay response of the damped oscillating system, the logarithmic decrement $\varsigma$ may be determined with Eq. (7.2).

$$\varsigma = \frac{1}{n} \ln \left( \frac{\chi(t_o)}{\chi(t_n)} \right) \tag{7.2}$$

where $n$ is the number of peaks considered and $\chi(t_o)$ and $\chi(t_n)$ are the surface displacements corresponding to the first peak and the last peak, respectively.

The damping ratio $\zeta$ is obtained from the logarithmic decrement by applying Eq. (7.3).

$$\zeta = \frac{\varsigma}{4\pi^2 + \varsigma^2} \tag{7.3}$$

The damped natural frequency $\omega_{dn}$ is associated by Eq. (7.4) to the natural period $T_{dn,owc}$ calculated as the average time elapsed between consecutive peaks of the signal.

$$\omega_{dn} = \frac{2\pi}{T_{dn,owc}} \tag{7.4}$$

The undamped natural frequency $\omega_{un}$ is computed through Eq. (7.5) based on the damped natural frequency and the damp-

ing ratio.

$$\omega_{un} = \frac{\omega_{dn}}{\sqrt{1-\zeta^2}} \tag{7.5}$$

The undamped natural period of the chamber $T_{un,owc}$ is given by Eq. (7.6) based on the undamped natural frequency.

$$T_{un,owc} = \frac{2\pi}{\omega_{un}} \tag{7.6}$$

Finally, the added mass $m_{add}$ is estimated with Eq. (7.7) from the undamped natural frequency $\omega_{un}$ [125, 255].

$$m_{add} = \frac{\rho_a g A_c}{\omega_{un}^2} - m_0 \tag{7.7}$$

where $m_0$ is the initial value of the water mass.

The values of the added mass and undamped natural frequency computed for the optimised chamber, defined through the experimental campaign, are listed in Table 7.22.

| Added Mass | Undamped Natural Frequency |
|---|---|
| $m_{add}$, kg | $\omega_{un}$, rad/s |
| 4.28 | 6.70 |

Table 7.22: Added mass and undamped natural frequency calculated for the chamber optimised through experiments [33].

## 7.3 Turbine selection

A procedure for selecting a Wells and an impulse turbine was performed with the aim of providing a preliminary design of the wave energy converters for a possible future installation in the

selected sites located in Tuscany and Sardinia. Four sets of parametric analyses were performed, maximising the objective function represented by the overall annual energy harvested by the system.

The characteristics of the wave climate investigated are indicated in the scatter matrices of Tables 7.1 and 7.2 for Tuscany and Tables 7.3 and 7.4 for Sardinia in terms of annual wave specific energy and frequency of occurrence, for different classes of equivalent wave height $H_{m0}$ and wave energy period $T_{m-1,0}$.

For all the investigated configurations of the system, the geometry and properties of the chamber were considered constant. They were defined based on the laboratory experiments described in Section 7.2 and carried out for optimising the primary efficiency of the system for wave conditions characteristic of a moderate state of the Mediterranean Sea. Therefore, they can be considered representative of the specific application site with reasonable approximation [126]. The rules of similitude analysis was applied to scale up by a factor of 50 the data of the prototype tested at the laboratory scale [36]. The geometric parameters of the real-scale chamber utilised in the analytical wave-to-wire model are resumed in Table 7.23.

| Chamber Outer Section | Chamber Inner Section | Chamber Height | Front Wall Draught Length | Front Wall Freeboard Section |
|---|---|---|---|---|
| $A_{c,ext}$, $m^2$ | $A_c$, $m^2$ | $G$, m | $D$, m | $F_c$, m |
| 100.0 | 82.5 | 14.5 | 4.5 | 8.0 |

Table 7.23: Main geometric parameters of the chamber utilised for the computations with the wave-to-wire model [33, 24].

The added mass and undamped natural frequency of the chamber at the real scale were calculated by applying the procedure described in Section 7.2 based on the geometric parameters of Table 7.23. The value of the added mass and undamped natural frequency obtained are listed in Table 7.24.

| Added Mass | Undamped Natural Frequency |
|---|---|
| $m_{add}$, kg | $\omega_{un}$, rad/s |
| 535000 | 0.95 |

Table 7.24: Added mass and undamped natural frequency calculated for the chamber utilised for the computations with the wave-to-wire model [33, 24].

The scale effects are modifications in the physical behaviour of a phenomenon arising at different geometric scales. They occur for the difficulty of keeping the force ratio constant when using a scaling approach as the Froude′s scaling law.

Literature numerical analyses conducted on chambers reduced in dimensions up to a factor 50 regarding the real case were considered for evaluating the scaling effects. The results obtained by applying the similitude law of Froude indicated that the scaling influence on the chamber performance is negligible when the assumption of air incompressibility is imposed [256]. Moreover, the impact of the Reynolds effects due to the increasing importance of viscous forces regarding inertial forces and the influence of the Weber effects connected to the rising relevance of surface tension forces compared to inertial forces are negligible for a scale ratio up to 1:50 like that of the current case [257]. The most relevant aspect to be considered is air compressibility. This parameter can be neglected without marked repercussions on the chamber

dynamics for models scaled of factor 10 or higher, while it has to be regarded for lower values of the scale factor up to the full-scale [256]. The absence of the modelling of the air compressibility at full-scale determines the overestimation of about 10-15% of the air pressure in the chamber and the subsequent air volume flux, but less than 10% for the capture width ratio [257].

In the present application, the scaling effects may arise during the determination of the properties of the real-scale chamber based on the free decay experiments performed with the laboratory model. Since the magnitude of the influence is limited and involves only the properties of the caisson, the approximation is considered acceptable [257].

The parametric analyses for the optimisation procedures of the monoplane isolated Wells turbine and the axial impulse turbine were performed by varying the geometrical features and the operating conditions according to the ranges reported in Table 7.25. The intervals were defined based on the existing prototypes of these turbomachines to investigate an effective test plan for a preliminary selection of the secondary converter [55, 44, 43, 92, 32, 104]. A constant tip clearance equal to 1% of the blade height was considered.

Once the best-suited parameters of the test plan of Table 7.25 were determined, the analysis of the optimal design angular velocity on a yearly basis was further refined. A range of 300 rpm centred around the value of the rotational speed previously obtained was examined with intervals of 25 rpm for either the machines and both the application sites.

For the case of Tuscany, energy extraction was increased by reducing the rotational speed to 875 rpm and 275 rpm for the Wells and impulse turbine, respectively. For the case of Sardinia,

| Parameter | Wells Turbine | | | Impulse Turbine | | |
|---|---|---|---|---|---|---|
| | Min. | Max. | Int. | Min. | Max. | Int. |
| Rotational Speed, rpm | 300 | 1200 | 300 | 300 | 1200 | 300 |
| Turbine Case Radius, m | 0.50 | 1.00 | 0.05 | 0.50 | 1.00 | 0.05 |
| Hub-to-tip ratio, - | 0.50 | 0.70 | 0.05 | 0.60 | 0.70 | 0.05 |
| Rotor blade aspect ratio, - | 0.50 | 1.50 | 0.10 | - | - | - |
| Stator blade number, - | - | - | - | 26 | 30 | 2 |
| Rotor blade number, - | 5 | 12 | 1 | 30 | 40 | 2 |

Table 7.25: Design space of the parametric analyses performed on the Wells and impulse turbines [24].

the angular velocity was increased to 950 rpm for the Wells turbine, while for the impulse turbine, the value of 300 rpm was confirmed.

The geometry and rotational speed of the Wells and impulse turbines of the test plan leading to the maximisation of the annual energy harvesting for Tuscany are resumed in Table 7.26.

From a perusal of Table 7.26, it can be observed that the angular velocity of the rotor of the selected Wells turbine is 3.18 times greater, and the radius of the turbine casing is 25.00% bigger with respect to the impulse turbine, leading to a blade speed ratio of 3.98. Therefore, the aerodynamic acoustic emissions of the Wells turbine are markedly higher.

| Parameter | Wells Turbine | Impulse Turbine |
|---|---|---|
| Rotational speed, rpm | 875 | 275 |
| Turbine casing radius, m | 1.00 | 0.80 |
| Hub-to-tip ratio, - | 0.50 | 0.65 |
| Rotor blade aspect ratio, - | 1.40 | 0.85 |
| Stator blade number, - | - | 26 |
| Rotor blade number, - | 6 | 30 |
| Tip clearance, % | 1.00 | 1.00 |
| Rotational inertia, $m^2$ kg | 23.24 | 79.28 |

Table 7.26: Rotor angular velocity and geometry of the Wells and impulse turbines selected for the operation in Tuscany.

The inertia of the two turbines was determined considering the rotors made of marine grade aluminium EN AW 5083 to ensure corrosion resistance while limiting the production costs [32]. The greater inertia of the impulse turbine has two opposite effects: it increases the forces required to run up the rotor at the design speed and levels the oscillations of power conversion owing to the flywheel energy storage.

The significant lower dimensions and values of rotational speed of the impulse turbines regarding the Wells turbine provide significant advantages even in terms of increase of specific component life and, consequently, of the reduction of manufacturing and maintenance costs. Moreover, the rotational speed of the impulse turbine may have positive effects on the coupled operation with the electric generators.

The geometrical parameters and angular velocity of the tested

Wells and impulse turbines maximising annual energy conversion for Sardinia are listed in Table 7.27.

| Parameter<br>Turbine | Wells Turbine | Impulse |
|---|---|---|
| Rotational speed, rpm | 950 | 300 |
| Turbine casing radius, m | 1.00 | 0.85 |
| Hub-to-tip ratio, - | 0.50 | 0.70 |
| Rotor blade aspect ratio, - | 1.10 | 0.76 |
| Stator blade number, - | - | 26 |
| Rotor blade number, - | 5 | 30 |
| Tip clearance, % | 1.00 | 1.00 |
| Rotational inertia, $m^2$ kg | 25.61 | 104.12 |

Table 7.27: Rotor angular velocity and geometry of the Wells and impulse turbines selected for the operation in Sardinia [24].

The ratio of the rotational speed of the selected Wells turbine to that of the impulse turbine is 3.17 and the turbine casing radius is approximately 17.65% bigger for the former turbine regarding the latter, determining a ratio of around 3.73 between the blade speeds. Consequently, even for this application site, the acoustic emissions due to aerodynamics are significantly higher for the Wells turbine, while the inertia is markedly greater for the impulse turbine.

## 7.4 Operating maps

The operating maps were obtained from the design space of Table 7.25 by considering an annual energy extraction scenario.

The analysis aims to identify the most relevant parameters regulating the turbine functioning and evaluate their effects on the performance of the wave energy converters. The annual energy harvesting ratio $\Sigma_{d,y}$ was defined in Eq. (7.8) to distinguish the best configurations and rank their performance. For each turbine typology, this parameter is the ratio of the annual energy transformed by a specific configuration to the maximum energy converted amongst the configurations examined. Therefore, the annual energy harvesting ratio of the best-suited layout investigated is unitary for either Wells and impulse turbines [24].

$$\Sigma_{d,y} = \frac{E_{d,y}}{E_{max,y}} \tag{7.8}$$

where $E$ is the energy harvested, subscript $d$ refers to the device configuration examined, subscript $max$ indicates the optimal configuration maximising energy extraction, and subscript $y$ refers to the year.

The blade velocity of the turbomachines investigated requires to be limited to values corresponding to a maximum Mach number of 0.47 at the blade tip, calculated based on the flow relative velocity [44]. Indeed, it is necessary to avoid aerodynamic losses caused by transonic flow and shock waves, which could occur around the blade tip at high velocities. Therefore, only the data obtained for turbine configurations operating below the critical speed were included in the results.

For the Wells turbines, in addition to the requirement of operation below the critical speed, the condition of self-starting functioning was applied for presenting the achieved results. The ability to autonomously run up to the operational speed is critical for this kind of machine.

### 7.4.1 Operating maps of Tuscany

The operating maps of all the configurations of the wave energy converters investigated for the sea wave conditions of the site located in Tuscany are shown for relating the annual energy harvesting ratio to the main design parameters.

In Figures 7.6 and 7.7, the maps of energy harvesting ratio $\Sigma_{d,y}$ of the Wells and impulse turbines, respectively, are presented as functions of the hub-to-tip ratio and the turbine casing radius for different values of rotor angular speed.

From a perusal of the maps of the Wells turbine shown in Figure 7.6, it is noticeable that for values of rotational speed between 300 and 600 rpm, increasing the turbine radius allows for greater energy extraction due to the higher mass flow rate. Conversely, for the velocity values between 900 and 1200 rpm, the effects of the variation of the tip radius depend upon the radius. In particular, a turbine casing radius of 1 m leads to maximising energy extraction in the ranges of the test plan.

The hub-to-tip ratio has a relevant influence on $\Sigma_{d,y}$ for all the values of rotor angular velocity investigated, apart from the lowest one. Reducing this geometrical parameter to 0.5 increases energy harvesting, as it determines the rise of the flow rate. Moreover, low values of the hub-to-tip ratio require lower values of the rotor solidity to ensure the ability to run up independently to a certain rotational speed. In turn, limiting the solidity reduces the blockage of the flow across the rotor cascade and thus the requirement of primary energy availability. The solidity calculated at the rotor tip ranges from 0.30 to 0.45 for the most-suited configurations.

As reported in Table 7.26, the Wells turbine requires a relatively high rotational speed of 875 rpm for properly exploiting the resource. Values of rotor speed lower than 600 rpm and

higher than 1200 rpm determine a significant reduction of the performance for the present application.

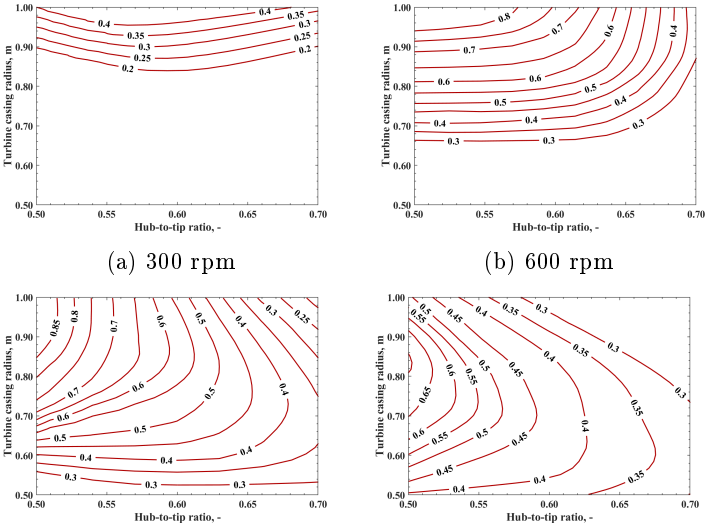


(a) 300 rpm (b) 600 rpm

(c) 900 rpm (d) 1200 rpm

Figure 7.6: Energy ratio as a function of the hub-to-tip ratio and turbine casing radius for rotor angular velocities equal to **(a)** 300, **(b)** 600, **(c)** 900, and **(d)** 1200 rpm for the Wells turbines operating in Tuscany.

Figure 7.7 shows the maps of the annual energy harvesting ratio of systems functioning with impulse turbines. The turbine radius has relevant effects on energy harnessing. All the maps indicate that an excessive increase of this parameter determines a reduction of energy conversion. In particular, a casing diameter of around 1.6 m maximises energy harvesting.

The hub-to-tip ratio significantly influences the operation of the system corresponding with the rotational speed equal to 300 rpm, while the effects are limited for the other velocities. The

most-suited configurations have a value of hub-to-tip ratio near 0.65.

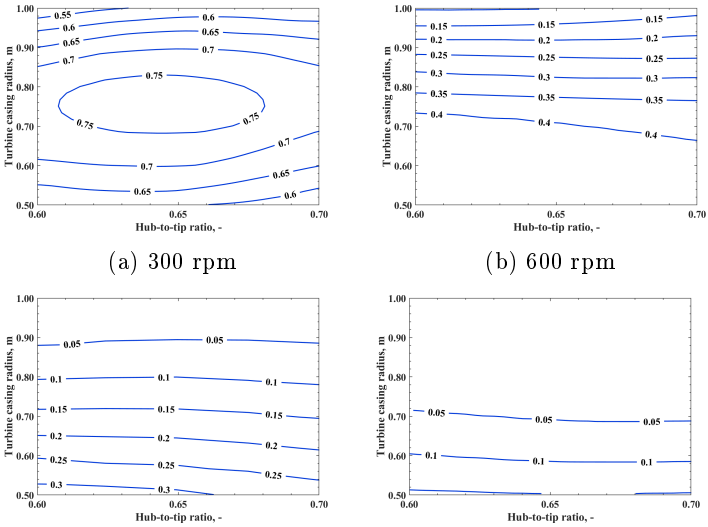


(a) 300 rpm (b) 600 rpm

(c) 900 rpm (d) 1200 rpm

Figure 7.7: Energy ratio as a function of the hub-to-tip ratio and turbine casing radius for rotor angular velocities equal to **(a)** 300, **(b)** 600, **(c)** 900, and **(d)** 1200 rpm for the impulse turbines operating in Tuscany.

The aspect ratio of the rotor blades was imposed as a boundary parameter for the Wells turbine according to the interval of the test plan of Table 7.25. Conversely, it was defined based on the length of the chord determined with the criterion of Zweifel for the impulse turbine. This criterion imposes an optimal value for the ratio of the real and ideal blade loading for each configuration. The values of the aspect ratio of the rotor blades maximising energy extraction range between 1.10 and 1.50 for the Wells turbine and from 0.75 to 1.25 for the impulse turbine.

For further development of the analysis of the main geometric parameters, the evaluation of the trade-off between aerodynamic performance and costs should be carried out, especially for the selection of the turbine diameter.

### 7.4.2 Operating maps of Sardinia

The operating maps of the configurations of the oscillating water column systems analysed under the sea wave conditions of the site selected in Sardinia are analysed to determine the effects of the main design parameters on the annual energy harnessing.

In Figure 7.8, the maps of energy harvesting ratio $\Sigma_{d,y}$ are shown to varying of the hub-to-tip ratio and the turbine casing radius for different values of rotational speed.

Even for the wave conditions of Sardinia, the Wells turbine needs a relatively high rotational speed of around 900 rpm for properly exploiting the resource. In particular, energy harnessing is maximised with a speed of 950 rpm, as reported in Table 7.27. For the cases with 300 and 600 rpm, the increase of the turbine radius determines a positive variation of annual energy extraction for all the levels of hub-to-tip ratio due to the rise of the flow rate crossing the turbomachine. At the speed of 900 rpm, the increase of the turbine casing radius has a positive effect on the performance for the lowest values of hub-to-tip ratio analysed, while for the highest values, the impact of an excessive increase of the radius is negative. In particular, a value of 1 m maximises energy extraction for the ranges of the test plan. For the velocity of 1200 rpm, the magnitude of the turbine radius enhancing the performance raises with the reduction of the ratio between the hub radius and the tip radius [24].

The hub-to-tip ratio has significant effects on energy extrac-

tion for the two highest velocity values analysed. A reduction of this geometrical parameter generally enhances the performance, as it increases the airflow rate. Especially, a value of 0.5 maximises the annual energy harvesting for the design space. Furthermore, reducing the hub-to-tip ratio decreases the rotor solidity required to run up independently the rotor to a specific rotational speed. This is beneficial to the system operation, as limiting solidity diminishes the blockage of the airflow across the turbine and thus the requirement of pneumatic power from the primary converter. The rotor solidity calculated at blade tip ranges from 0.35 to 0.45 for the best-suited configurations [24].

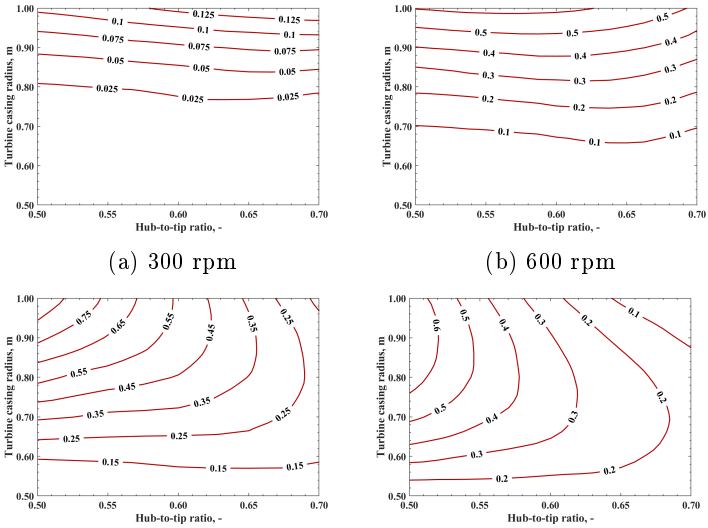


(a) 300 rpm (b) 600 rpm

(c) 900 rpm (d) 1200 rpm

Figure 7.8: Energy ratio as a function of the hub-to-tip ratio and turbine casing radius for rotor angular velocities equal to **(a)** 300, **(b)** 600, **(c)** 900, and **(d)** 1200 rpm for the Wells turbines operating in Sardinia.

The maps of the annual energy harvesting ratio of Figure 7.9 indicate that impulse turbines harvest the maximum energy at the rotational speed of 300 rpm. The turbine casing radius has significant effects for all the achieved maps. For the two lowest values of velocity, the system performance decreases with an excessive rise of the radius, while for the two highest velocities increasing this parameter determines the reduction of energy conversion in the entire design space. In particular, a radius of 0.85 m maximises the energy extracted during one year [24].

Regarding the hub-to-tip ratio, the effects on the system operation are mainly noticeable for the two lowest values of rotational velocity. This geometric parameter is between 0.65 and 0.70 for the best-suited configurations [24].

Even for the case of Sardinia, the aspect ratio of the rotor blades was assigned for the Wells turbine, while it depends on the length of the blade chord determined by applying the criterion of Zweifel for the impulse turbine. Energy harvesting is maximised with values of the aspect ratio of the rotor blades ranging from 1.00 to 1.20 for the former turbomachine and between 0.75 and 1.15 for the latter. The most suited values of the aspect ratio of the stators are between 1.00 and 1.50 for the impulse turbine.

## 7.5 Primary energy conversion

The solution of the hydrodynamics, thermodynamics, and aerodynamics of the chamber determines the primary power conversion stage of an oscillating water column system. The time series of the forces acting on the rigid piston, the water column motion, and the main quantities of the fluid dynamics of the airflow were considered to analyse the power transformations from sea waves to the duct embedding the air turbine duct.

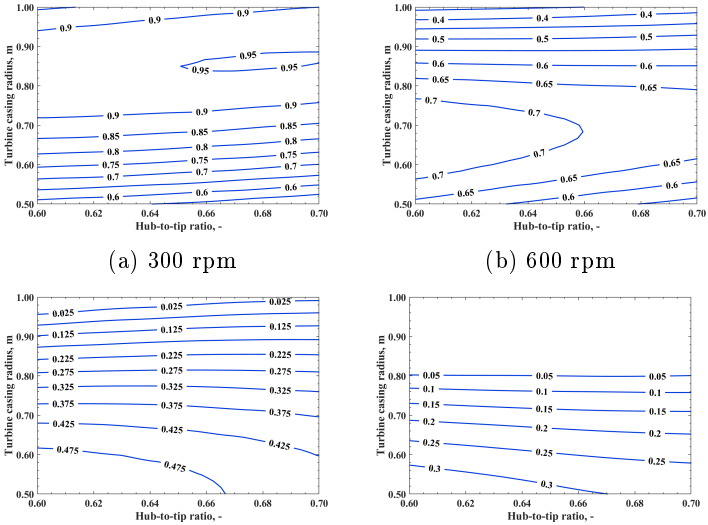


(a) 300 rpm (b) 600 rpm

(c) 900 rpm (d) 1200 rpm

Figure 7.9: Energy ratio as a function of the hub-to-tip ratio and turbine casing radius for rotor angular velocities equal to **(a)** 300, **(b)** 600, **(c)** 900, and **(d)** 1200 rpm for the impulse turbines operating in Sardinia.

The results achieved with the analytical model of the primary converter for Tuscany and Sardinia are presented corresponding with the distinctive wave conditions maximising annual energy harnessing of the specific application site.

### 7.5.1 Primary energy conversion for Tuscany

The wave status maximising annual energy conversion in Tuscany has a significant wave height of 1.5 m and a wave energy period of 5.5 s for the system configurations operating with the selected Wells and impulse turbines. The time series of either

the position and acceleration of the incident sea wave are depicted in Figure 7.10 for a duration of two periods starting from the position corresponding to the still water level. The height of the sea wave is determined from the significant wave height through Eq. (4.1), while the wave period is equivalent to the energy period, as stated in Section 4.1.1.

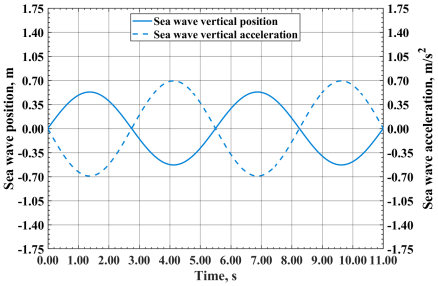


Figure 7.10: Time series of the sea wave position and acceleration for the wave class with $H_{m0}$=1.5 m and $T_{m-1,0}$=5.5 s maximising annual energy harvesting in Tuscany.

The excitation force determined by the action of the hydrodynamic pressure of the incident sea wave on the bottom of the water column is presented as a function of time in Figure 7.11. The excitation force is dependent upon the features of the incident wave, the seawater depth, and the caisson geometry. Thus, the force exerted on the rigid piston is identical for the two selected configurations of the system. The incident sea wave and the exciting force have the same period and phase, as visible comparing Figures 7.10 and 7.11.

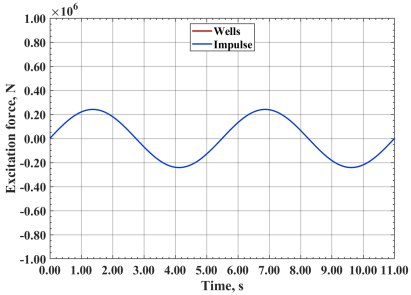


Figure 7.11: Time series of the excitation force exerted by the hydrodynamic pressure of the incident sea wave with $H_{m0}$=1.5 m and $T_{m-1,0}$=5.5 s in Tuscany.

The time series of the hydrostatic force determined by the hydrostatic pressure of the water column is presented in Figure 7.12a. This force is a function of the displacement of the free surface level of the water column, which is shown in Figure 7.12b. The hydrostatic force is positive when the free surface displacement is negative and vice versa. The magnitude of this force depends on the area of the chamber horizontal cross-section, the seawater density, and the gravitational acceleration.

The hydrostatic force is greater for the case of the impulse turbine owing to the higher displacements of the oscillating water column.

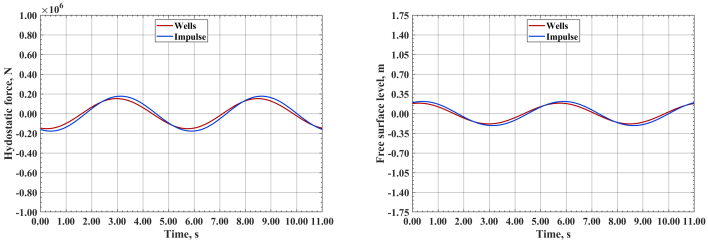


(a) Hydrostatic force (b) Free surface level

Figure 7.12: Time series of **(a)** the hydrostatic force and **(b)** the free surface level inside the chamber for the sea wave with $H_{m0}$=1.5 m and $T_{m-1,0}$=5.5 s in Tuscany.

The radiating damping force is determined by the product of the radiating damping coefficient and the water column velocity, which are depicted in Figure 7.13 as functions of time. This force is higher for the configuration with the impulse turbine as both the radiating damping coefficient and the speed of the seawater free surface are greater concerning the Wells turbine.

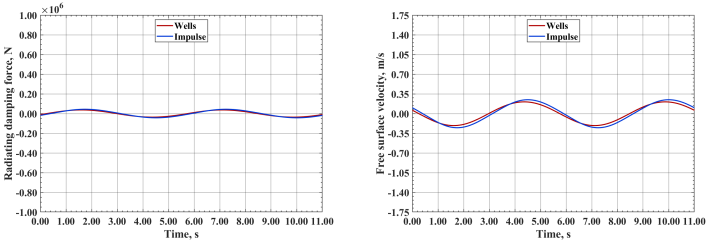


(a) Radiating damping force (b) Free surface velocity

Figure 7.13: Time series of **(a)** the radiating damping force and **(b)** the velocity of the free surface inside the chamber for the sea wave with $H_{m0}$=1.5 m and $T_{m-1,0}$=5.5 s in Tuscany.

The radiating damping coefficient of Figure 7.14a is a function of the hydrostatic restoring coefficient and the total seawater

mass, given by the sum of the oscillating water column mass and the added mass, which is a constant, as shown in Figure 7.14b. The oscillating water column mass depends upon the vertical displacements of the water column of Figure 7.12b. The added mass was determined with the free decay tests described in Section 7.2, and it is constant for the selected chamber.

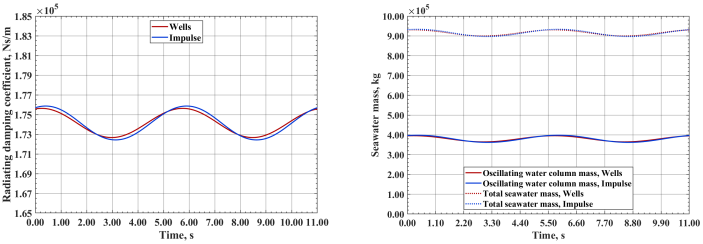


(a) Radiating damping coefficient (b) Seawater mass

Figure 7.14: Time series of **(a)** the radiating damping coefficient and **(b)** the oscillating water column mass and total water mass for the sea wave with $H_{m0}$=1.5 m and $T_{m-1,0}$=5.5 s in Tuscany.

The alternate compression and expansion of the air inside the chamber determine the action of an alternate pressure force on the top of the water column. The time series of the air pressure oscillation force and the total-to-static pressure variation imposed by the power take-off are shown in Figure 7.15.

The pressure difference required for the chamber to function with the impulse turbine is lower than the Wells turbine due to the lower damping imposed by the secondary converter on the primary converter. This implies that the power take-off force acting on the oscillating water column is greater for the latter configuration.

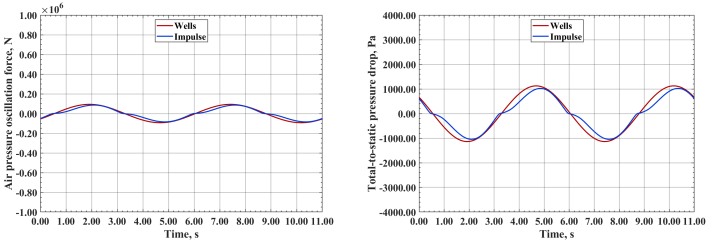


(a) Air pressure force (b) Total-to-static pressure drop

Figure 7.15: Time series of **(a)** the air pressure oscillation force and **(b)** the total-to-static pressure drop across the power take-off for the sea wave with $H_{m0}$=1.5 m and $T_{m-1,0}$=5.5 s in Tuscany.

The volume airflow rate processed by the system and the air velocity at the inlet of the secondary converter achieved with the solution of the hydrodynamics, thermodynamics, and aerodynamics of the primary converter are shown in Figure 7.16.

The volume airflow rate made available by the caisson is greater when the secondary converter is the impulse turbine due to the higher displacements of the free water surface. The difference in the axial velocity driving the secondary converter is significantly enhanced by the lower passage area realisable for the impulse turbine owing to its markedly smaller dimensions regarding the Wells turbine.

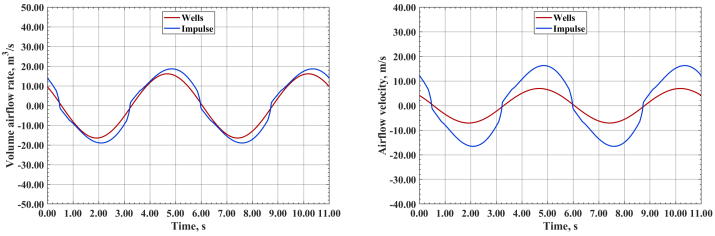


(a) Volume airflow rate (b) Airflow axial velocity

Figure 7.16: Time series of **(a)** the volume airflow rate and **(b)** turbine axial inlet velocity for the sea wave with $H_{m0}$=1.5 m and $T_{m-1,0}$=5.5 s in Tuscany.

### 7.5.2 Primary energy conversion for Sardinia

The main contribution to the annual energy harvesting for the application site located in Sardinia is provided by waves with a significant height of 3.5 m and a period of 8.5 s. In Figure 7.17, the vertical position and acceleration of the sea wave incident on the chamber are presented for two periods starting at the point corresponding to the still water level. Even in this case, the wave height was calculated with Eq. (4.1) based on the significant wave height and the wave period is equal to the energy period.

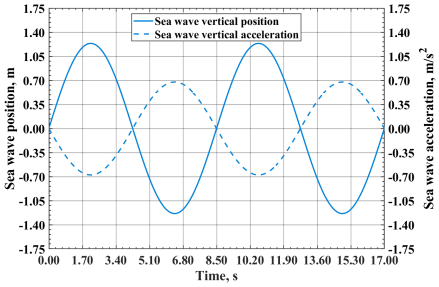


Figure 7.17: Time series of the sea wave position and acceleration for the wave class with $H_{m0}$=3.5 m and $T_{m-1,0}$=8.5 s maximising annual energy harvesting in Sardinia.

The time series of the excitation force exerted on the bottom of the water column by the action of the hydrodynamic pressure of the incident sea wave is depicted in Figure 7.18. For either system configuration, this force is equivalent and has the same period and phase of the sea wave displacement, as aforementioned.

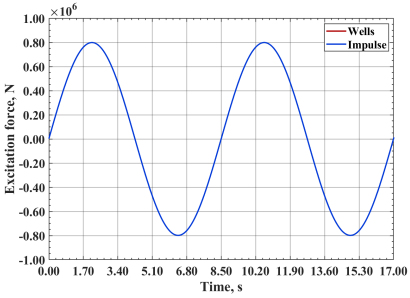


Figure 7.18: Time series of the excitation force exerted by the hydrodynamic pressure of the incident sea wave with $H_{m0}$=3.5 m and $T_{m-1,0}$=8.5 s in Sardinia.

The hydrostatic force depends upon the hydrostatic pressure of the water column determined by the displacement of the free

surface level of the water inside the caisson. As visible from their time series of Figure 7.19, the hydrostatic force and the water displacement have opposite signs.

For the wave maximising energy conversion in Sardinia, the hydrostatic force is higher for the configuration with the Wells turbine for the greater displacements of the seawater inside the chamber.

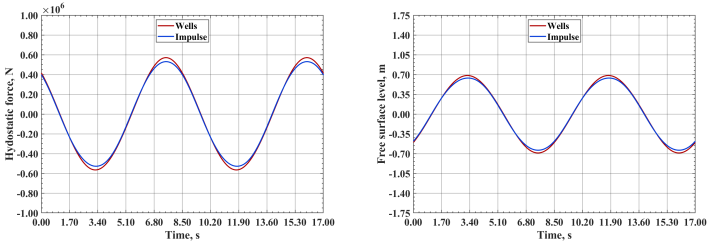


(a) Hydrostatic force (b) Free surface level

Figure 7.19: Time series of **(a)** the hydrostatic force and **(b)** the free surface level inside the chamber for the sea wave with $H_{m0}$=3.5 m and $T_{m-1,0}$=8.5 s in Sardinia.

The radiating damping force and the velocity of the vertical motion of the free surface inside the caisson are shown in Figure 7.20 by varying time. The maximum values of this force are greater for the system operating with the Wells turbine.

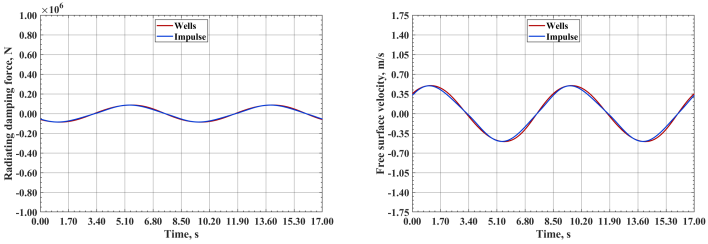


(a) Radiating damping force (b) Free surface velocity

Figure 7.20: Time series of **(a)** the radiating damping force and **(b)** the velocity of the free surface inside the chamber for the sea wave with $H_{m0}$=3.5 m and $T_{m-1,0}$=8.5 s in Sardinia.

The radiating damping coefficient, the oscillating water column mass, and the total mass of the seawater are depicted as functions of time in Figure 7.21.

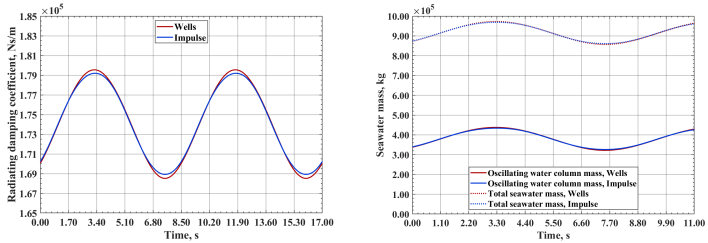


(a) Radiating damping coefficient (b) Seawater mass

Figure 7.21: Time series of **(a)** the radiating damping coefficient and **(b)** the oscillating water column mass and total water mass for the sea wave with $H_{m0}$=3.5 m and $T_{m-1,0}$=8.5 s in Sardinia.

The time series of the alternate air pressure force determined by the oscillating compression and expansion of the air inside the caisson and the pressure drop occurring in the duct embedding the air turbine are presented in Figure 7.22.

The difference in air pressure needed for the operation of the

impulse turbine is higher relative to the Wells turbine for the wave conditions and systems maximising energy extraction in Sardinia. As a consequence, the pressure force imposed by the power take-off is lower for the latter wave energy converter.

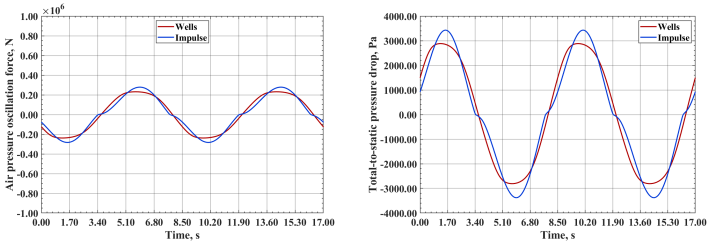


(a) Air pressure force (b) Total-to-static pressure drop

Figure 7.22: Time series of **(a)** the air pressure oscillation force and **(b)** the total-to-static pressure drop across the power take-off for the sea wave with $H_{m0}$=3.5 m and $T_{m-1,0}$=8.5 s in Sardinia.

The joint solution of the hydrodynamics, thermodynamics, and aerodynamics of the chamber provides the volume airflow rate crossing the system and the air velocity at the inlet of the secondary converter, which are depicted in Figure 7.23.

The volume airflow rate crossing the Wells turbine is higher owing to the greater amplitude of the free surface displacements of the water column. However, the airflow speed is higher for the case of the impulse turbine as the passage area of the flow is lower for this configuration.

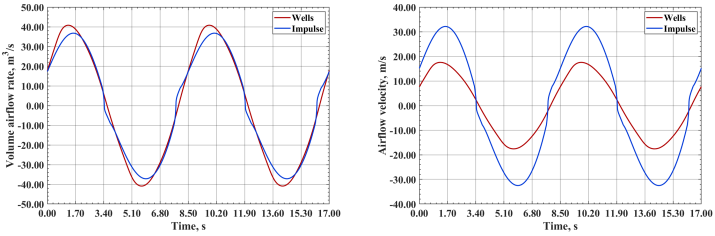


(a) Volume airflow rate (b) Airflow axial velocity

Figure 7.23: Time series of **(a)** the volume airflow rate and **(b)** turbine axial inlet velocity for the sea wave with $H_{m0}$=3.5 m and $T_{m-1,0}$=8.5 s in Sardinia.

## 7.6 Operating curves and maps

The aerodynamics of the air turbines determined by the wave-to-wire model is presented using the non-dimensional and dimensional parameters traditionally applied in turbomachinery [21] and described in Section 6.2.1.6. The non-dimensional parameters are the turbine flow coefficient, the input coefficient, the torque coefficient, and the turbine efficiency. The dimensional parameters are the static-to-static pressure variation between the inlet and outlet of the turbine and the torque and power acting on the rotor.

For each application site, the operating curves of the two selected wave energy converters are presented for the wave status that yields the greatest contribution to global energy harvesting every year. This allows to evaluate and compare the system performance in design conditions for either configuration.

The maps of the annual distributions of energy ratio and

efficiency ratio were analysed for the two wave energy converters. For each system configuration, the annual energy ratio of each wave condition $\Sigma_{ij,y}$ was obtained with Eq. (7.9) by dividing the computed values of energy conversion for the global energy transformed by the system in one year. In analogy, the annual efficiency ratio $\Xi_{ij,y}$ is defined in Eq. (7.10) considering the values of energy conversion efficiency of each wave condition and the overall yearly efficiency of the system [24].

$$\Sigma_{ij,y} = \frac{E_{ij,y}}{E_y} \tag{7.9}$$

$$\Xi_{ij,y} = \frac{\xi_{ij,y}}{\xi_y} \tag{7.10}$$

where subscripts $i$ and $j$ are the indices of the rows and columns of the scatter matrices used to indicate a specific wave status.

The energy extracted during each season is compared with the corresponding overall annual value through the seasonal energy ratio $\Sigma_{ij,s}$ for the two selected systems. For each of them, this parameter is defined in Eq. (7.11) as the ratio of the seasonal energy harvested for every point of the scatter matrix to the corresponding energy conversion computed over the year [24].

$$\Sigma_{ij,s} = \frac{E_{ij,s}}{E_{ij,y}} \tag{7.11}$$

where subscript $s$ relates to the season considered.

The comparison of the efficiency of energy conversion between a specific season and the year is performed through the seasonal efficiency ratio $\Xi_{ij,s}$ for either the selected systems. For each configuration, Eq. (7.12) defines this parameter as the ratio of

the efficiency of energy conversion computed for every point of the scatter matrix to the global efficiency of the entire year [24].

$$\Xi_{ij,s} = \frac{\xi_{ij,s}}{\xi_y} \tag{7.12}$$

### 7.6.1 Annual system operation in Tuscany

The operating curves of the turbomachine are presented in terms of the non-dimensional and dimensional parameters defined in Section 6.2.1.6, expressed as functions of the volume airflow rate or the flow coefficient determined at the midspan of rotor blades.

The performance parameters generally achieve greater values to parity of flow coefficient during the outflow phase, as the airflow has a higher inlet pressure and thus a greater density. Moreover, except for the efficiency of the impulse turbine, the values of all the presented parameters monotonically rise with the absolute value of the volume airflow rate or the flow coefficient for the entire operating range of either the system configurations.

All the operating curves indicate that the functioning range of the impulse turbine is significantly wider when compared to that of the Wells turbine.

In Figure 7.24a, the relation between the input coefficient and the flow coefficient is presented. This performance parameter expresses the primary energy necessary for the turbine functioning relative to its geometry and operating conditions. The curves of the impulse turbine are on average greater than the Wells turbine and reach higher maximum values with a lower speed of rise. Indeed, the impulse turbine requires a greater input power to parity of conditions.

The torque coefficient of Figure 7.24b is significantly higher for the impulse turbine regarding the Wells turbine. This is due to the greater torque exerted on the rotor blades compared to

the functioning and geometric parameters of the machine. The torque coefficient has a negative sign for low values of the flow coefficient as the flow incidence angle is small and viscous forces prevail on pressure forces. The torque coefficient is null if the two opposite actions are equivalent, while it is positive when the impact of pressure forces predominates over viscous forces, as occurs increasing the flow incidence angle.

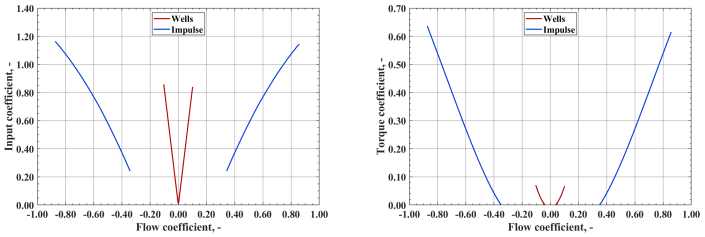


(a) Input coefficient (b) Torque coefficient

Figure 7.24: **(a)** Input coefficient and **(b)** torque coefficient as functions of the midspan flow coefficient, for the wave status maximising energy harvesting in Tuscany.

Figure 7.25 shows the static-to-static pressure drop between the turbine inlet and outlet as a function of the volume airflow rate. For the Wells turbine, the relation is linear in the entire operating range. For the impulse turbine, the relation is quadratic, even if the deviation from linearity is limited under the investigated wave conditions, especially for the low and intermediate absolute values of volume flow rate. The amplitude of the pressure oscillation required to the chamber for the operation of the former turbine is more significant than for the latter. For both turbomachines, the caisson needs to provide greater pressure differences to parity of volume flow rate during the outflow than during the inflow, owing to the higher air density.

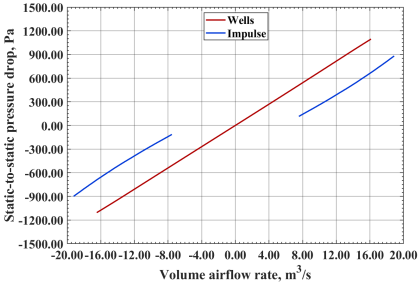


Figure 7.25: Static-to-static pressure drop as a function of the volume airflow rate for the wave status maximising energy harvesting in Tuscany.

The analysis of Figure 7.26 indicates that the rotor torque has a negative sign for small absolute values of the flow coefficient as the viscous forces dominate over the pressure forces exerted on the rotor blade surfaces. The torque is null if the two opposite actions are equivalent and it is positive when the impact of the pressure forces prevails, as it occurs increasing the flow incidence angle. Comparing the two selected configurations, the system operating with the impulse turbine achieves significantly higher maximum values of the torque, but the speed of rise is lower regarding the case of the Wells turbine.

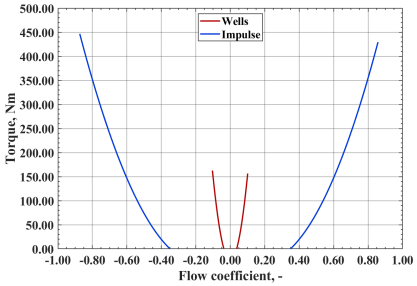


Figure 7.26: Turbine torque as a function of the midspan flow coefficient for the wave status maximising energy harvesting in Tuscany.

The curves of the rotor power output of Figure 7.27 denote that the average values and the peaks are higher for the Wells turbine in comparison to the impulse turbine, owing to the greater rotational speed. The former turbine has a narrower operating range and functions longer with a slightly higher average value of power exerted by the airflow on the rotor.

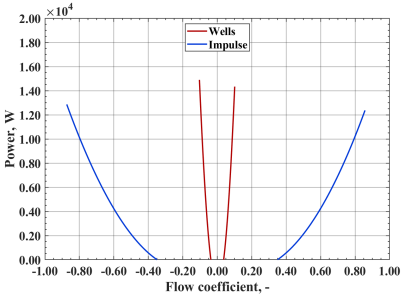


Figure 7.27: Turbine power as a function of the midspan flow coefficient for the wave status maximising energy harvesting in Tuscany.

In Figure 7.28, the curves of aerodynamic efficiency are positive when the flow incidence angle leads to the predominance of

the pressure forces over the viscous forces. For the Wells turbine, the efficiency has a monotonous trend in the entire operating range. For the impulse turbine, the efficiency very slightly decreases at the extremes of the flow phases. The system operating with the former turbomachine has greater values of efficiency.

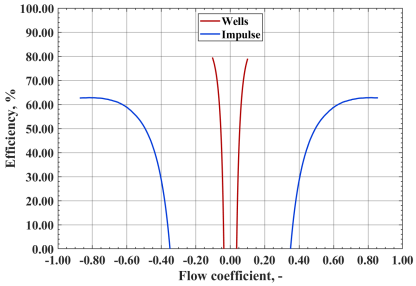


Figure 7.28: Aerodynamic efficiency as a function of the volume airflow rate for the wave status maximising energy harvesting in Tuscany.

For a better understanding of the power transformed by the turbine rotor for the two configurations of the OWC system, the time series of the rotor power is presented in Figure 7.29. The graph highlights the greater power transformation of the system operating with the Wells turbine regarding the impulse turbine for the wave status with a significant wave height of 1.5 m and an energy period of 5.5 s.

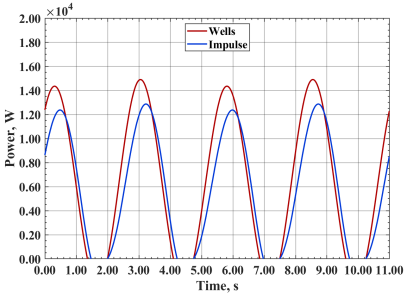


Figure 7.29: Time series of the rotor power for the systems operating with the selected Wells and the impulse turbines in Tuscany.

Regarding the global results, the two OWC wave energy converters operating with the selected Wells and impulse turbines harvest 14.47 MWh and 13.94 MWh during one year, respectively. These values were obtained using the annual wave scatter matrices of Tables 7.1 and 7.2 for the wave distribution of the selected site located in Tuscany. The control strategy enhances the yearly energy harvesting of 30.27% and 3.78% for the two configurations, respectively. The effect is significantly greater for the case of the Wells turbine as its operation is subject to higher variations of power and efficiency in off-design conditions. Moreover, the latter turbines would determine a negative contribution to the power conversion for a wider number of wave classes in the absence of a control strategy.

The calculated efficiency of the power transformation from the resource to the grid is 5.81% for the system operating with the Wells turbine and 5.60% for the device working with the impulse turbine. The values of efficiency calculated for the main stages of power transformation of the two OWC systems are reported in Table 7.28.

| Parameter | Wells system | Impulse system |
|---|---|---|
| Chamber, % | 10.10 | 10.93 |
| Turbine with control, % | 61.18 | 54.48 |
| Organic, % | 97.00 | 97.00 |
| Electric, % | 97.00 | 97.00 |

Table 7.28: Main values of efficiency computed for the two WECs selected for the operation in Tuscany.

The values of efficiency reduce to 5.25% and 5.05%, respectively, regarding the overall energy transported by the sea.

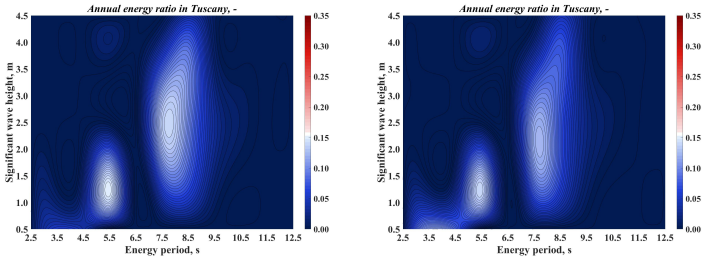


(a) Wells turbine (b) Impulse turbine

Figure 7.30: Maps of annual energy ratio distribution for the two systems operating in Tuscany with the **(a)** Wells and **(b)** impulse turbines for sets of significant wave height and energy period.

Figures 7.30a and 7.30b show that the functioning of the two systems has two regions with high peaks of energy harvesting. The first region belongs to the lowly energetic wave classes with significant wave height ranging from 0.75 to 2 m and energy period between 5 and 6 s. The second region is identified by

the highly energetic wave classes, which have $H_{m0}$ between 1.5 and 4 m and $T_{m-1,0}$ from 7 s to 8.5 s. The relevant energy transformation is determined by the high frequency of occurrence for the former region, while it is regulated by the great power conveyed by waves for the latter region. For the other wave conditions, the system performance reduces significantly.

By comparing the two selected wave energy converters, the one functioning with the Wells turbine reaches greater peaks of energy harnessing, while the one with the impulse turbine has a smoother operation.

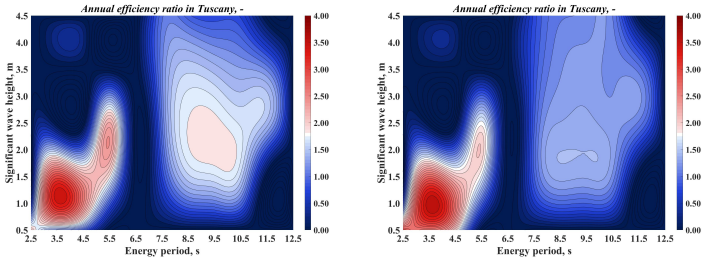


(a) Wells turbine (b) Impulse turbine

Figure 7.31: Maps of annual efficiency ratio distribution for the two systems operating in Tuscany with the **(a)** Wells and **(b)** impulse turbines for sets of significant wave height and energy period.

From a perusal of Figures 7.31a and 7.31b it is noticeable that the efficiency of the annual energy conversion of the two systems reaches the highest values for the less energetic wave classes. For the highly energetic wave classes, the systems operate with limited values of efficiency. This characteristic is more marked for the impulse turbine than for the Wells turbine.

### 7.6.2 Annual system operation in Sardinia

The performance parameters of the selected turbines are shown to changes of the turbine flow coefficient and volume flow rate, in analogy with the case of Tuscany presented in Section 7.6.1. Even in this case, the values of the performance parameter are typically lower during the inflow phase to parity of flow coefficient for the lower pressure and density of air at the inlet.

Either during the inflow and outflow, the curves rise monotonically with the absolute value of the volume airflow rate or flow coefficient for the configurations investigated, apart from the efficiency curves.

The input coefficient is presented in Figure 7.32a as a function of the flow coefficient at the midspan of the rotor blades. The speed of rise and the maximum values are lower for the impulse turbine than for the Wells turbine. This is due to the lower input power required for the functioning of the former turbomachine to parity of geometric parameters and operating conditions.

The curves of the torque coefficient are depicted in Figure 7.32b by varying the midspan flow coefficient. The speed of rise of the torque coefficient is faster for the Wells turbine, while the maximum values reached by the impulse turbine are significantly higher. The curves indicate that the torque exerted by the airflow on the turbine blades is significantly greater to parity of operating conditions for the system operating with the impulse turbine.

In Figure 7.33, the static-to-static pressure drop across the turbine duct is presented as a function of the volume airflow rate. For the Wells turbine, the relation is linear and slightly deviates from linearity only for relatively high absolute values of the airflow rate. Conversely, for the impulse turbine, the curve is

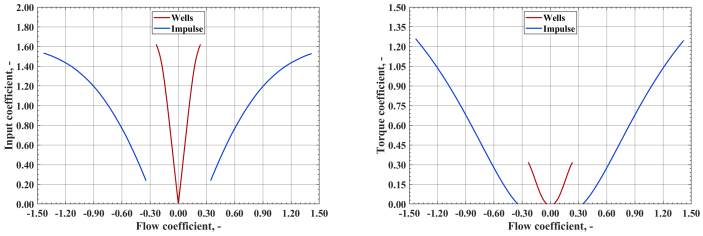


(a) Input coefficient (b) Torque coefficient

Figure 7.32: **(a)** Input coefficient and **(b)** torque coefficient as functions of the midspan flow coefficient, for the wave status maximising energy harvesting in Sardinia.

quadratic during the whole functioning. Regarding the comparison of the two selected configurations, the Wells turbine requires a greater pressure oscillation from the primary converter for operating. Moreover, the pressure difference needed is higher during the outflow concerning the inflow due to the greater density of the airflow.

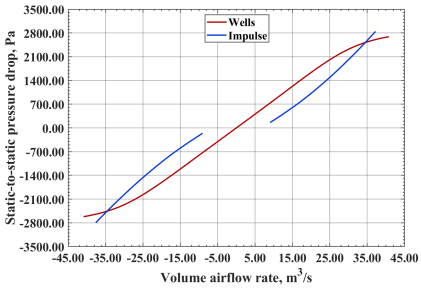


Figure 7.33: Static-to-static pressure drop as a function of the volume airflow rate for the wave status maximising energy harvesting in Sardinia.

In Figure 7.34, the curves of the torque exerted on the rotor blades by the action of the airflow denote that the Wells turbine

achieves significantly lower maximum values but has a higher speed of rise regarding the impulse turbine. For both the selected system configurations, the torque is negative corresponding to the lowest absolute values of the flow coefficient owing to the small incidence angle of the flow on the blades.

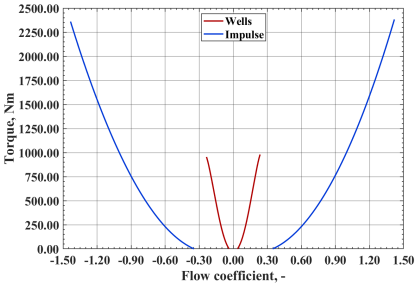


Figure 7.34: Turbine torque as a function of the volume airflow rate for the wave status maximising energy harvesting in Sardinia.

Figure 7.35 shows that the power output of the rotor blades is more remarkable for the Wells turbine regarding the impulse turbine due to the higher angular velocity. The former turbomachine has a narrower interval of operation and it is subject for longer to a higher average value of power transferred from the airflow to the rotor.

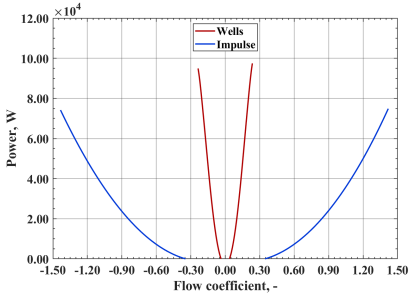


Figure 7.35: Turbine power as a function of the volume airflow rate for the wave status maximising energy harvesting in Sardinia.

The curves of the aerodynamic efficiency of Figure 7.36 are positive corresponding with the flow incidence angle determining the predominance of the pressure forces over the viscous forces. During either the flow phases, the efficiency rises up to reaching the maximum values and afterwards reduces for both the machines. Thus, the curves are not monotonous at the extremes of the inflow and outflow. This trend is more prominent for the impulse turbine when compared to the Wells turbine.

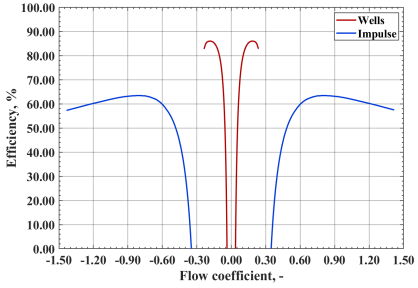


Figure 7.36: Aerodynamic efficiency as a function of the volume airflow rate for the wave status maximising energy harvesting in Sardinia.

The time series of the power converted by the blades of the turbine rotor is shown in Figure 7.37. Corresponding to the wave class with a significant wave height of 3.5 m and an energy period of 8.5 s, the power transformation of the system operating with the Wells turbine is higher.

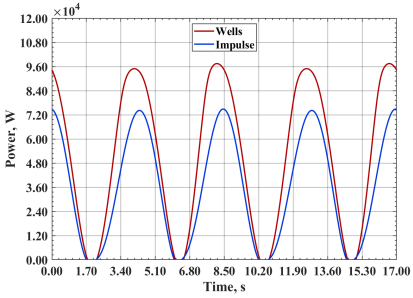


Figure 7.37: Time series of the rotor power for the systems operating with the selected Wells and the impulse turbines in Sardinia.

Focusing now on the global results, the annual energy converted by the two configurations of the OWC wave energy converters operating with the selected Wells and impulse turbines in Sardinia is 47.20 MWh and 40.97 MWh, respectively. These values were obtained using the annual wave scatter matrices of Tables 7.3 and 7.4 for the wave distribution of the selected site located in Sardinia. The control strategy enhances the yearly energy harvesting of 11.30% and 3.46% for the two configurations, respectively. This marked difference is due to the lower variations of the power output and efficiency of the impulse turbine in off-design conditions regarding the Wells turbine.

The calculated efficiency of the power transformation from the resource to the grid is 6.88% for the system operating with the Wells turbine and 5.98% for the device working with the

impulse turbine. The efficiencies of the principal stages of power conversion are reported in Table 7.29.

| Parameter | Wells system | Impulse system |
|---|---|---|
| Chamber, % | 10.61 | 10.75 |
| Turbine with control, % | 68.96 | 59.06 |
| Organic, % | 97.00 | 97.00 |
| Electric, % | 97.00 | 97.00 |

Table 7.29: Main values of efficiency computed for the two WECs selected for the operation in Sardinia.

The values of efficiency reduce to 5.71% and 4.96%, respectively, regarding the overall energy transported by the sea.

The maps of the annual distributions of energy ratio $\Sigma_{ij,y}$ and efficiency ratio $\Xi_{ij,y}$ are shown in Figures 7.38 and 7.39, respectively, for the two configurations of the wave energy converters selected for the application in Sardinia.

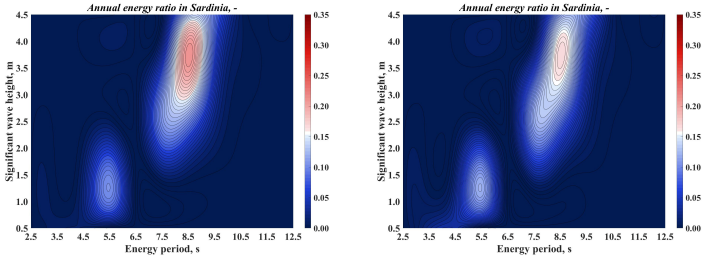


(a) Wells turbine (b) Impulse turbine

Figure 7.38: Maps of annual energy ratio distribution for the two systems operating in Sardinia with the **(a)** Wells and **(b)** impulse turbines for sets of significant wave height and energy period.

Figures 7.38a and 7.38b indicate that the two systems reach the maximum energy extraction for wave conditions with a significant wave high of around 3.5 m and an energy period of about 8.5 s. Energy conversion markedly decreases for wave conditions outside the highly energetic range, which has an energy period between 7.5 and 9.5 s and a significant height between 2.5 and 4.5 m. A lower peak of energy extraction is present for either the systems for wave conditions with $H_{m0}$ in the range from 1 to 1.5 m and $T_{m-1,0}$ equal to 5.5 s. The system with the Wells turbine reaches higher maximum values, while the system with the impulse turbine has a smoother operation [24]. Therefore, the former turbine is more suited for energy conversion from a narrow range of wave conditions.

For the application site located in Sardinia, the difference in annual global energy conversion of the two configurations is bigger regarding Tuscany due to the capability of the Wells turbine of converting great levels of energy from the highly energetic wave classes. The frequency of occurrence of these wave conditions is markedly higher for the case of Sardinia.

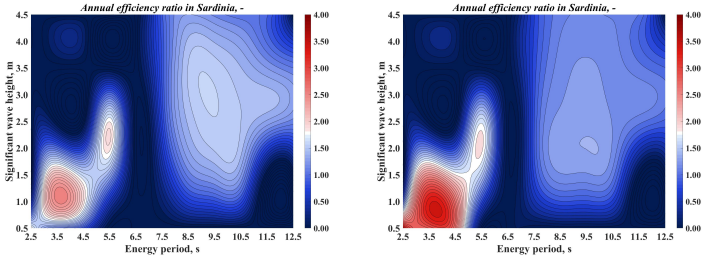


(a) Wells turbine (b) Impulse turbine

Figure 7.39: Maps of annual efficiency ratio distribution for the two systems operating in Sardinia with the **(a)** Wells and **(b)** impulse turbines for sets of significant wave height and energy period.

From a perusal of Figure 7.39, it is noticeable that both the configurations convert wave energy with higher efficiency for waves with low energy period and significant wave height. This feature is stronger for the impulse turbine than for the Wells turbine [24].

### 7.6.3 Seasonal system operation in Tuscany

The operation of the two wave energy converters was investigated also considering the seasonal wave conditions of the selected application sites.

In Figures 7.40 and 7.41, it is noticeable that the distributions of the seasonal energy ratio of the systems operating with the Wells and impulse turbines are strongly dependent on the specific season of the year. For both configurations, energy harnessing is maximum during winter owing to the significantly higher energy transported by sea waves regarding the other seasons. The values of energy extraction are considerably lower during summer, while in spring and fall, they are intermediate and comparable among

themselves. The reason for these differences is the frequency of occurrence of highly energetic waves with great amplitude and period.

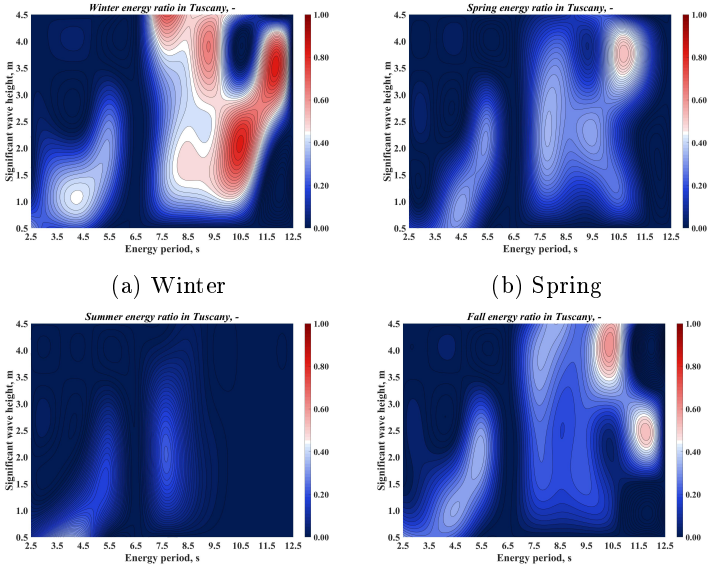


(a) Winter (b) Spring

(c) Summer (d) Fall

Figure 7.40: Seasonal maps of energy ratio distribution for the system operating with the Wells turbine in Tuscany, during **(a)** winter, **(b)** spring, **(c)** summer, and **(d)** fall.

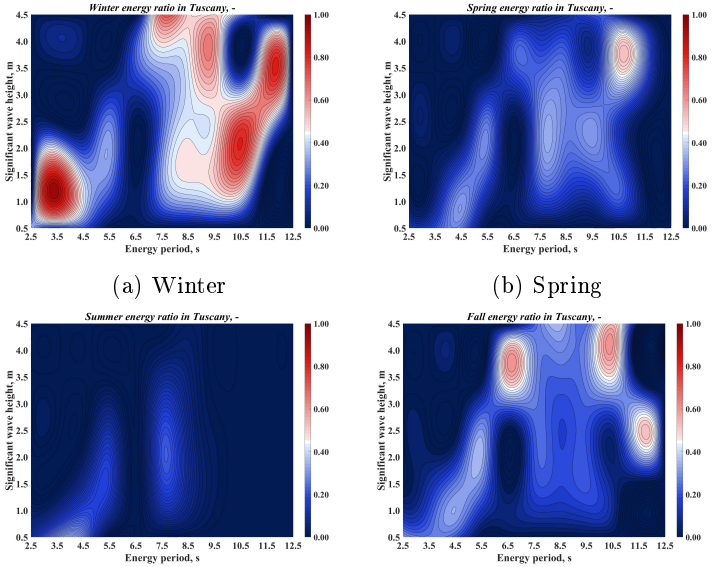


(a) Winter (b) Spring

(c) Summer (d) Fall

Figure 7.41: Seasonal maps of energy ratio distribution for the system operating with the impulse turbine in Tuscany, during **(a)** winter, **(b)** spring, **(c)** summer, and **(d)** fall.

The comparison of the seasonal energy distribution of the two wave energy converters shows that, during all seasons, the system with the Wells turbine extracts greater energy from the highly energetic wave conditions and lower energy from the other wave conditions regarding the impulse turbine. The difference in energy harvesting is maximum during winter, when the former configuration has higher performance, and during summer when the latter configuration reaches greater values. The Wells turbine prevails on the impulse turbine in energy conversion in spring, while the opposite occurs in fall.

Figures 7.42 and 7.43, illustrate the seasonal efficiency ratio.

For both systems, the greatest values of efficiency are achieved during winter for almost all the conditions of the scatter matrices. Conversely, during summer, the efficiency markedly reduces, especially for the highly energetic wave classes. Intermediate values of efficiency characterise the operation of the wave energy converters in spring and fall.

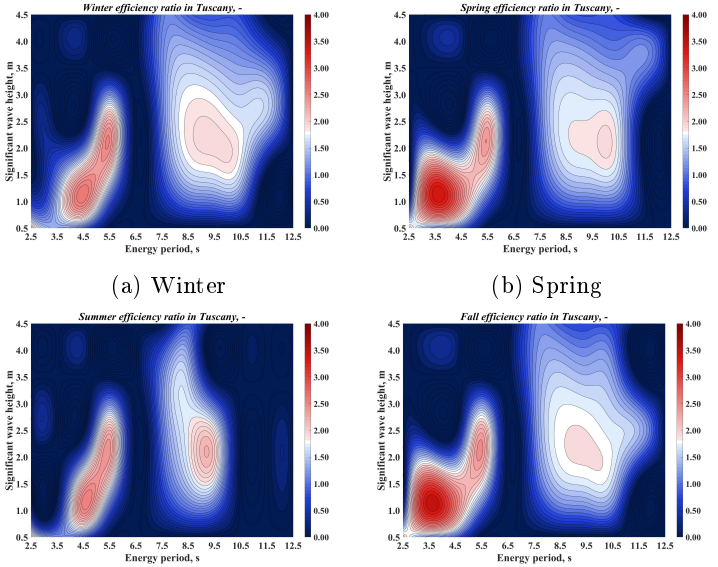


(a) Winter (b) Spring

(c) Summer (d) Fall

Figure 7.42: Seasonal maps of efficiency ratio distribution for the system operating with the Wells turbine in Tuscany, during **(a)** winter, **(b)** spring, **(c)** summer, and **(d)** fall.

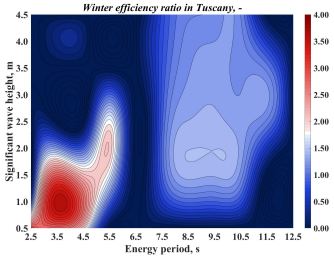


(a) Winter

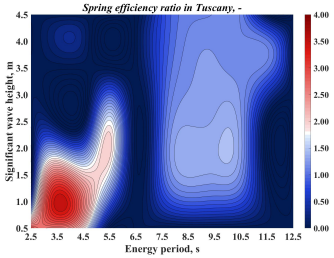


(b) Spring

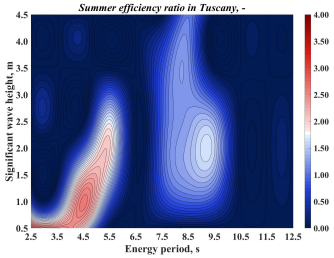


(c) Summer

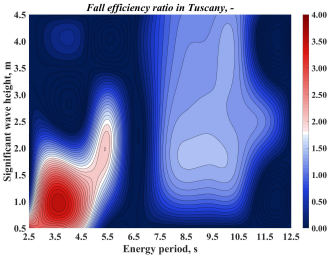


(d) Fall

Figure 7.43: Seasonal maps of efficiency ratio distribution for the system operating with the impulse turbine in Tuscany, during **(a)** winter, **(b)** spring, **(c)** summer, and **(d)** fall.

By comparing the two configurations, the system with the Wells turbine generally operates with significantly higher efficiency regarding the impulse turbine for wave conditions with $H_{m0}$ ranging from 1.5 m and 3.5 and $T_{m-1,0}$ between 4.5 s and 11.5 s. During spring, the higher efficiency of this configuration extends to waves with an energy period of 3.5 s. Considering the overall efficiency, the values reached by the Wells turbine are higher for all seasons except for summer. This different behaviour is mainly to the contribution of the wave classes with a significant height of 0.5 m and an energy period between 2.5 and 4.5 s.

The global energy harnessed by the two selected wave energy converters was increased through the determination of the best-suited design rotational velocity for each season of the year. In Table 7.30, the values of rotor speed maximising the overall energy extraction are resumed for both system configurations.

| Season | Wells turbine | Impulse turbine |
|---|---|---|
| Winter, rpm | 900 | 300 |
| Spring, rpm | 825 | 275 |
| Summer, rpm | 725 | 200 |
| Fall, rpm | 900 | 300 |

Table 7.30: Design values of rotor angular speed selected for the Wells and impulse turbines during each season of the year in Tuscany.

The definition of the specific values of design rotational speed for each season determines the increase of the global energy harvesting from 14.47 to 14.67 MWh/year for the wave energy converter with the Wells turbine and from 13.94 to 14.00 MWh/year for the system with the impulse turbine. The related efficiency calculated based on the scatter matrices is 5.89% and 5.63%, respectively, and decreases to 5.32% and 5.08%, respectively, considering the overall energy transported by sea waves.

### 7.6.4 Seasonal system operation in Sardinia

The seasonal functioning of the two wave energy converters operating in Sardinia was analysed by considering the maps of energy and efficiency ratio and the effects of different values of design rotational speed for the seasons.

The distributions of seasonal energy ratio depend on the spe-

cific season, as visible in Figures 7.44 and 7.45. Even for Sardinia, the frequency of occurrence of highly energetic wave conditions during a specific season determines the energy converted by the two systems during this time. The maximum energy extraction is achieved during winter for the high energy conveyed by sea waves, mainly owing to the relevant frequency of conditions with great values of height and period. The values of energy extraction are considerably lower during summer, while in spring and fall, they are intermediate and comparable among themselves.

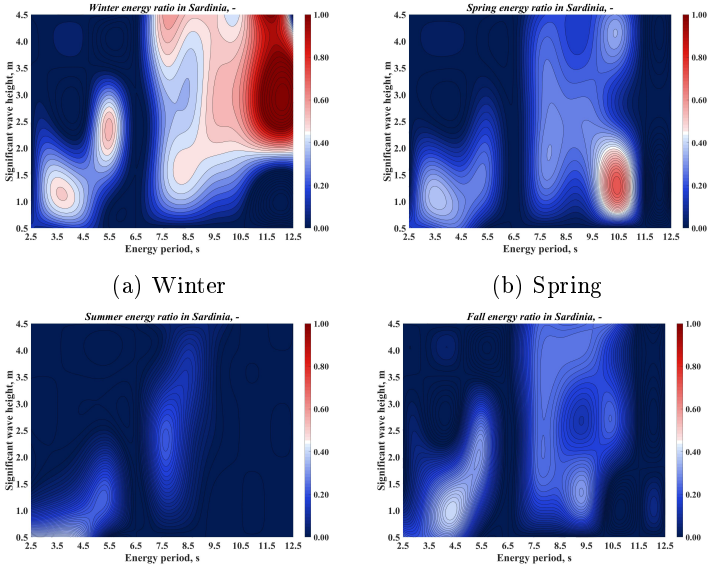


(a) Winter (b) Spring

(c) Summer (d) Fall

Figure 7.44: Seasonal maps of energy ratio distribution for the system operating with the Wells turbine in Sardinia, during **(a)** winter, **(b)** spring, **(c)** summer, and **(d)** fall.

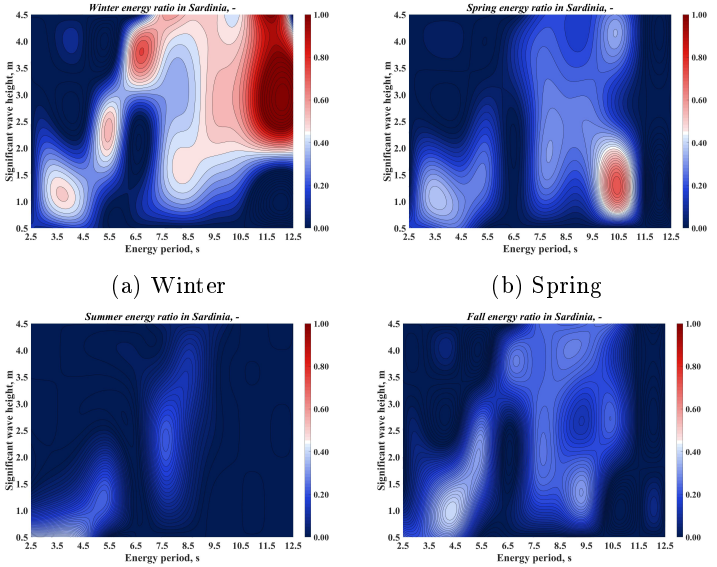


(a) Winter (b) Spring

(c) Summer (d) Fall

Figure 7.45: Seasonal maps of energy ratio distribution for the system operating with the impulse turbine in Sardinia, during **(a)** winter, **(b)** spring, **(c)** summer, and **(d)** fall.

Comparing the two systems, the effects of the different wave conditions of the four seasons on the operation are similar. Even on a seasonal basis, the highest peaks and the overall values of energy extraction are reached by the system functioning with the Wells turbine. In contrast, the maps of the system working with the impulse turbine have a smoother trend [24]. The highest difference is reached during winter due to the better operation of the former configuration under highly energetic wave conditions. The discrepancy is slight during summer, as the contribution of these wave conditions is significantly reduced. The differences assume intermediate and similar values during spring and fall.

The seasonal efficiency ratio is presented in Figures 7.46 and 7.47 for both systems. Even for the operation in Sardinia, the systems function with the highest efficiency in winter and with the lowest efficiency in summer for almost all the wave classes of the scatter matrices. During spring and fall, the values are intermediate.

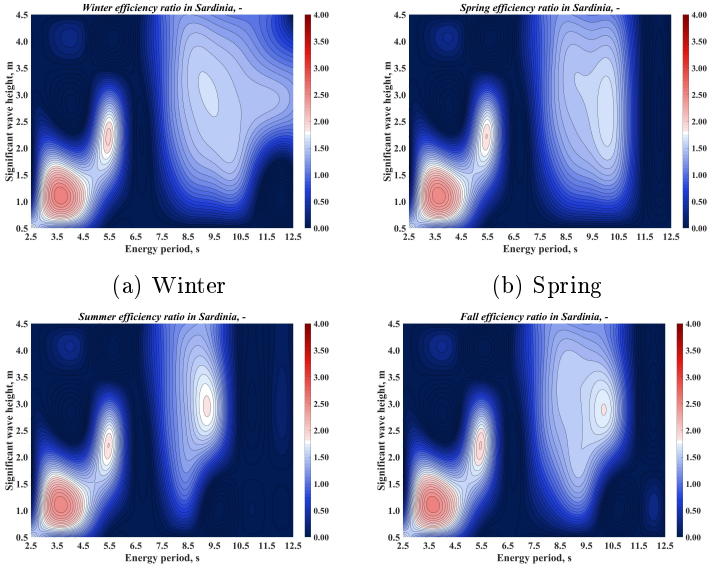


(a) Winter (b) Spring

(c) Summer (d) Fall

Figure 7.46: Seasonal maps of efficiency ratio distribution for the system operating with the Wells turbine in Sardinia, during **(a)** winter, **(b)** spring, **(c)** summer, and **(d)** fall.

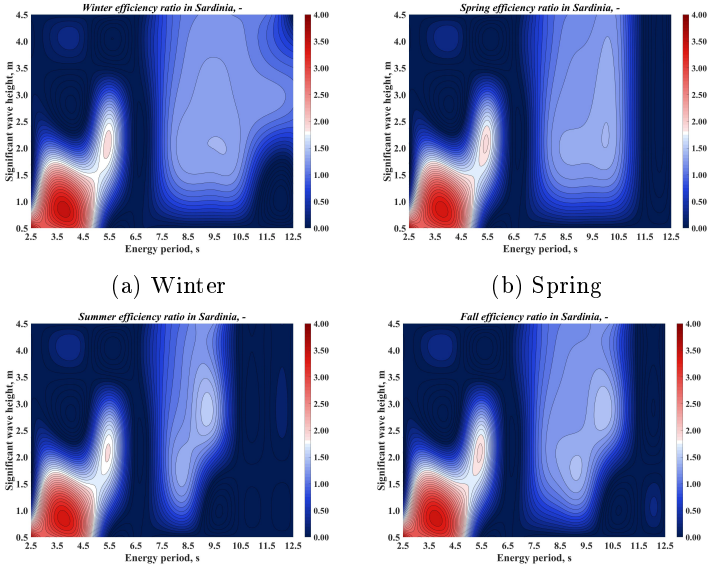


(a) Winter (b) Spring

(c) Summer (d) Fall

Figure 7.47: Seasonal maps of efficiency ratio distribution for the system operating with the impulse turbine in Sardinia, during **(a)** winter, **(b)** spring, **(c)** summer, and **(d)** fall.

The configuration with the Wells turbine operates with higher efficiency regarding the impulse turbine for almost all the wave classes with significant wave height equal or superior to 1.5 m during the four seasons. The greatest and smallest differences in seasonal efficiency ratio are obtained in winter and summer, respectively. The Wells turbine reaches higher values for all seasons, taking into account the overall efficiency ratio.

With the aim of enhancing the global energy harvested by the two wave energy converters, the analysis was further detailed by determining the most suited design rotational speed for each season. The values of rotor speed that maximise the overall energy

extraction are resumed in Table 7.31 for both configurations [24].

| Season | Wells turbine | Impulse turbine |
|---|---|---|
| Winter, rpm | 1000 | 300 |
| Spring, rpm | 950 | 300 |
| Summer, rpm | 875 | 275 |
| Fall, rpm | 950 | 300 |

Table 7.31: Design values of rotor angular speed selected for the Wells and impulse turbines during each season of the year in Sardinia.

The global energy conversion is increased from 47.20 to 47.67 MWh/year for the system operating with the Wells turbine and from 40.97 to 41.14 MWh/year for the device working with the impulse turbine. The corresponding efficiency is 6.95% and 6.00%, respectively, if only the calculated wave conditions are considered, and reduces to 5.77% and 4.98%, respectively, taking into account the overall energy conveyed by sea waves.

## 7.7 Predictions of the wave-to-wire model

Literature data allowing for a direct comparison with the performance calculated through the proposed wave-to-wire model are not available for OWC wave energy converters operating in the selected reference sites. With the aim of providing an example for a partial comparison, the power production and efficiency of an existing European wave farm located in the Atlantic Ocean and based on the OWC concept can be considered, even if the wave spectrum of this location is significantly different with respect to those of the selected application sites located in the Mediterranean Sea. The OWC plant of Mutriku, in Spain, oper-

ates with 14 Wells turbines rated 18.5 kW each, delivering total annual energy of 246,468 MWh with a plant efficiency index of 26%. Therefore, each turbine converts 17.605 MWh/year [258].

The values of energy conversion and system efficiency achieved with the developed model appear to be low but they are unfortunately not too far from the present state of the art. In particular, the values of efficiency of the secondary conversion stage are in line with the literature. On the other hand, the current system configuration is penalised by the low efficiency of the primary converter. This proves that an integrated simulation method accounting for the mutual interactions, like the one presented in this study, can clearly indicate the components that need to be optimised. To increase the overall efficiency of the wave energy converters, the optimisation of the primary converter will be performed in future for the specific wave conditions of the selected site, jointly with the definition of the best-suited Wells and impulse turbines [24].

Considerations regarding the methodology applied in the wave-to-wire model developed are important as it is based on analytical models of the individual converters of an OWC system.

Concerning the analytical model of the primary converter, the rigid piston approach is a consolidated solution for solving the hydrodynamics, thermodynamics, and aerodynamics of the chamber. The accuracy of its predictions mainly depends upon the equations utilised to model the forces and losses, the techniques applied for determining its properties and hydrodynamic coefficients, and the method used for coupling the chamber with the turbine. The approach described in this Chapter aims at maximising the accuracy of the modelling.

The analytical models of the Wells and impulse turbines generally provide results that slightly overestimate power and efficiency. The differences determined in Chapter 6 through the comparison of the results of the analytical model developed with the numerical and experimental data are around 10% and 15%, respectively. These discrepancies are in line with the values indicated in the literature. An important aspect is that the trend of all the performance parameters is similar for all these models. Furthermore, these discrepancies are not significantly sensitive to the variations of the geometric parameters and operating conditions of the turbomachines considered.

Therefore, their application for selecting the optimal turbine design through a wave-to-wire model is particularly indicated during the first phase of the project to analyse a wide set of configurations with high velocity and satisfactory accuracy. In the following design phases, the application to the best configurations identified of approaches with higher accuracy as numerical and experimental ones is recommended.

# Chapter 8

# Conclusions

*The present work collects a relevant part of the activities performed during the Ph.D. course on structures and devices for energy conversion from sea waves. Conclusions regarding the methodology applied, the models developed, and the main achievements are discussed to provide a brief outline of the study. Moreover, future research recommendations on the topic are specified to indicate the aspects to consider in further investigations.*

## 8.1 Results achieved

One of the global challenges of the millennium is bringing renewable energy conversion systems to industrial maturity. Sea is a significant resource in terms of extension and energy potentially exploitable by waves, currents, tides, and thermal gradients. Amongst these physical phenomena, sea waves are the source with the highest energy density. Oscillating water column systems, operating with self-rectifying Wells or impulse turbines, are among the most credited solutions for effectively converting

the considerable energy conveyed by sea waves. Despite a renewed interest, however, they are often still at a demonstration phase, and additional research is required to develop this technology for providing a significant contribution to the satisfaction of energy demand.

The literature review showed that OWC systems gained a renewed interest in the last few years. The usual approach carried out relies on the separate design of each of the three converters, represented by the chamber structure (primary converter), the air turbomachine (secondary converter), and the electrical generator (tertiary converter). Several wave-to-wire models have been realised so far; however, they apply very simplified methods for modelling turbine aerodynamics. The approach is typically based on general correlations expressing the flow rate, pressure, and power coefficients and the total-to-static efficiency of the turbine. The coupling of the primary and secondary converters is achieved with ideal relations connecting the pressure coefficient to the flow coefficient of the system through the damping coefficient. This limits the possibility of an inner coupling of the turbine with the flow conditions delivered by the chamber. Furthermore, the present models often do not provide a specific design of the caisson and the turbomachine for the distinctive wave conditions of the application site. For these reasons, a complete wave-to-wire model of a wave energy converter based on the OWC technology was developed. The proposed model applies an analytical approach to pursue a good compromise between accuracy and computational cost. These features make it particularly recommended in the early design stages to evaluate the energy extractable from sea waves and correctly select the location and the main geometric and operating parameters of the device.

The tool is of engineering type, thus running smoothly on an ordinary computer with an interesting compromise between accuracy and computational cost. Simultaneously, it is sufficiently accurate to provide a first energy assessment, which is pivotal to evaluating the correct location and expected performance. With this aim, the single analytical models were created coupling *MATLAB* and *Simulink*. The approach combines the solution of the hydrodynamics, thermodynamics, and hydrodynamics of the chamber (primary converter) with the aerodynamics and dynamics of the turbine (secondary converter) and the dynamics of the electric generator (tertiary converter). A rigid piston approach is utilised to analyse the caisson, constituted by a fixed and detached structure regarding the sea bottom. A Wells and an axial impulse turbine were investigated by applying low-order aerodynamic models based on the design practice of axial turbomachines. In both cases, the rows were modelled as groups of blades, composed of a finite set of airfoils. A regulation algorithm was implemented to enhance the electric energy delivered to the grid by controlling the rotor torque and angular velocity.

The joint analysis of the complete OWC system allows determining the dynamics of all the converters taking into account their interaction during the whole functioning time. This aspect is paramount as the damping of the OWC chamber depends on its geometry and incident wave conditions, and, in turn, the performance of the air turbine regulated by the control strategy relies on the pressure difference made available by the chamber. Conversely, the separate analysis of the converters may determine the incorrect evaluation of their operating conditions. Therefore, the optimisation of the design of a single converter or

all the converters requires the analysis of the entire system.

The developed model was applied in two selected sites located in Italy. The sites were determined as highly energetic spots for the Italian wave climate with characteristics proper of a moderate Mediterranean sea state. One location is positioned in the central area of Tuscany (latitude: 4826150 m N, longitude: 587255 m E, WGS84-UTM32 coordinates) and the other one in front of the north-west coast of Sardinia (latitude: 4509971 m N, longitude: 424733 m E, WGS84-UTM32 coordinates). The sea wave conditions were determined in terms of energy transport and frequency for each combination of significant wave height and energy period in a sea depth of 50 m. A wave hindcasting dataset for a period of 20 years from 2000 to 2019 was utilised.

The geometry and properties of the OWC chamber were determined by scaling up of factor 50 the data obtained from an experimental campaign previously performed under wave conditions typical of a moderate Mediterranean climate. The parameters were determined as optimal for the maximisation of the primary energy conversion of the system. Based on this chamber, a turbine selection procedure was applied to optimise the geometric and operating parameters of both a Wells and an impulse turbine to maximise the annual energy conversion from waves to wire. The performance parameters, the operating curves and maps, and the energy conversion of the entire system were determined. For the two optimal configurations, the functioning was investigated, also considering the seasonal wave conditions to increase the overall energy harvesting.

In addition to the analytical wave-to-wire model of the entire system, computational fluid dynamics models of the secondary

converter were developed for both the Wells and the impulse turbine with *ANSYS ICEM*, *ANSYS Fluent*, and *ANSYS CFD-Post*. A three-dimensional multi-block technique was applied to create the computational domain of the air with a fully mapped mesh composed of hexahedral elements. The employment of circumferential periodic boundary conditions allowed for the reduction of computational power and time. Both steady and unsteady Reynolds-averaged Navier-Stokes schemes were used, and the turbulence closure was performed with either the realisable $k\kappa - \epsilon$ model with enhanced wall functions and the $\kappa - \omega$ stress transport model with low Reynolds number correction to the turbulent viscosity. Three different approaches were utilised for modelling rotation: the multiple reference frame model with a moving reference frame, the mixing plane, and the sliding mesh model.

The validation of the analytical and CFD models of the secondary converters was achieved by comparing their results among themselves and with literature analytical and experimental data. The results of the different models showed good agreement.

The main tools developed are resumed below.

- An analytical model of the primary converter was created based on the rigid piston approach applying the linear wave theory. The chamber was assumed to be detached and fixed regarding the seabed.
- An analytical model applying the actuator disc theory and the blade element momentum theory was developed for evaluating the aerodynamics of Wells turbines. The model is suited for evaluating several configurations of the tur-

bine: monoplane isolated, monoplane with inlet and outlet guide vanes, co-rotating, and contra-rotating.

- ◇ A novel analytical model of an axial impulse turbine was developed based on experimental correlations widely used to design axial turbomachines, following the similarities between these applications.
- ◇ A control strategy for regulating the rotor angular speed and the mechanical transmission of the torque from the turbine to the electric generator was realised.
- ◇ The CFD models of a monoplane isolated Wells turbine and an axial impulse turbine were created, defining completely automated procedures.

The key achieved results of the research are summarised in the following.

- ◇ Two sites were selected as highly energetic locations of the Mediterranean Sea surrounding Italy. The site positioned in the central sea of Tuscany has a mean annual wave power of 3.3 kW/m, while the site located in front of the north-west coast of Sardinia has a mean annual wave power of 10.5 kW/m. The annual and seasonal scatter matrices of specific wave energy distribution and frequency of occurrence were determined for both systems.
- ◇ The geometry and properties of an OWC chamber optimised for operating in a moderate wave climate typical of the Mediterranean Sea were determined. The chamber has an inner area of 82.5 $m^2$, a height of 14.5 m, a front wall draught of 4.5m, a front wall freeboard of 8 m, an added mass of 535000 kg, and an undamped natural frequency of 0.85 rad/s.

- An optimisation procedure was performed to determine the best geometry and operating conditions of wave energy converters operating with a monoplane isolated Wells turbine or an axial impulse turbine. The Wells turbine has a casing radius of 1 m, a hub-to-tip ratio of 0.5, an aspect ratio of 1.4, 6 blades, and a design rotational speed of 875 rpm for the application site located in Tuscany; for the case of Sardinia, the casing radius is 1 m, the hub-to-tip ratio 0.5, the aspect ratio 1.1, the blades are 5, and the angular velocity is 950 rpm. The optimal impulse turbine for the wave conditions of Tuscany has the casing radius of 0.80 m, the hub-to-tip ratio of 0.65, 26 blades for the stators and 30 blades for the rotor, and rotates at 275 rpm; for the application in Sardinia, the turbine casing is 0.85 m, the hub-to-tip ratio 0.7, the blades are 26 and 30 for the stator and the rotor, respectively, and the angular velocity 300 rpm.

- The angular velocity of the rotor of the selected Wells turbine is 3.18 times bigger, and the radius of the turbine casing is 25.00% greater regarding the impulse turbine, determining a blade speed ratio of 3.98 for the case of Tuscany. The rotational speed ratio of the selected Wells turbine to that of the impulse turbine is 3.17 and the turbine casing radius is approximately 17.65% bigger for the former turbine regarding the latter, leading to a ratio of around 3.73 between the blade speeds for the case of Sardinia. In either case, the acoustic emissions due to aerodynamics are significantly higher for the Wells turbine, while the inertia is markedly greater for the impulse turbine.

- The operating maps of the two machines show that the

optimisation of Wells turbines leads to higher turbine dimensions and rotational speeds when compared to impulse turbines. These turbines have a wider operating range, function with lower pressure drops to parity of volume flow rate, and have a smoother efficiency curve. However, the impulse turbines analysed reach lower efficiency values and have a lower capacity of maximising the energy conversion from specific highly energetic wave conditions, determining a lower energy conversion for both the cases of Tuscany and Sardinia.

- ◇ The optimal Wells and impulse turbines for the operation in Tuscany are capable of harvesting 14.47 MWh and 13.94 MWh during one year, respectively. The control strategy enhances the yearly energy harvesting of 30.27% and 3.78%, respectively. For the case of Sardinia, the annual energy harnessing is 47.20 MWh and 40.97 MWh, respectively. The control algorithm increases these values of 11.30% and 3.46%, respectively.

- ◇ The calculated efficiency of power transformation from resource to the grid is 5.81% for the system operating in Tuscany with the Wells turbine and 5.60% for the device working with the impulse turbine. The values of efficiency reduce to 5.25% and 5.05%, respectively, regarding the overall energy transported by the sea. The calculated efficiency for the case of Sardinia is 6.88% for the configuration with the Wells turbine and 5.98% for the impulse turbine. For this application site, the values of efficiency decrease to 5.71% and 4.96%, respectively, considering the global energy conveyed by sea waves.

- ◇ The efficiency of the single converters is 17.33% for the

chamber and 35.67% for the turbine operation in Tuscany with the Wells turbine, while the efficiencies are 21.36% and 27.87%, respectively, for the impulse turbine. In Sardinia, the primary efficiency is 20.79% for the chamber and 37.83% for the Wells turbine; for the case of the impulse turbine, the efficiencies are 25.39% and 25.05%, respectively. In all the cases, the efficiency of the tertiary converter was assumed to be 90.25%.

◇ The analysis of the annual and seasonal performance of the system states that the energy harvesting is maximum in winter owing to the considerably higher energetic level regarding the other seasons. In spring and fall, the energy extraction has similar values that are intermediate between winter and summer. The regulation of the design rotor speed during the year is beneficial for increasing global energy extraction.

◇ The optimal design values of the rotational speed for the seasonal operation with the Wells turbine in Tuscany are 900 rpm in winter, 825 rpm in spring, 725 rpm in summer, and 900 rpm in fall. For the impulse turbine, the best-suited values are 300 rpm during winter and fall and 275 rpm during spring and summer. For the site located in Sardinia, the optimal velocities are 1000 rpm in winter, 950 rpm in spring, 875 rpm in summer, and 950 rpm in fall for the Wells turbine. The optimal value is 300 rpm for the impulse turbine, apart from fall, which has 275 rpm.

◇ The global energy conversion in Tuscany is increased from 14.47 to 14.67 MWh/year for the wave energy converter with the Wells turbine and from 13.94 to 14.00 MWh/year for the system with the impulse turbine. For the case of

Sardinia, the energy harnessing is enhanced from 47.20 to 47.67 MWh/year with the Wells turbine and from 40.97 to 41.14 MWh/year for the device working with the impulse turbine.

◇ The efficiency of energy conversion calculated based on the scatter matrices is 5.89% and 5.63% for the systems operating in Tuscany with the Wells and impulse turbines, respectively, and decreases to 5.32% and 5.08%, by considering the overall energy transported by sea waves. For the functioning in Sardinia, the calculated efficiency is 6.95% and 6.00%, respectively, and corresponds to 5.77% and 4.98%, respectively, based on the overall energy conveyed by sea waves.

As a final remark, it can be affirmed that the results of the research conducted showed that oscillating water column systems operating with Wells and impulse turbines might be a competitive solution for energy conversion from sea waves. The research on this technology is worthy of further investigation.

The Mediterranean is characterised by low values of energy conveyed by waves. However, using a comprehensive design tool may lead to the extraction of favourable energy values. Therefore, a holistic approach is necessary for a combined optimisation of the converters for specific wave conditions. For these reasons, the analytical wave-to-wire model developed is the most suited solution for the initial design of OWC wave energy converters, allowing for the investigation of a wide variety of design solutions with the need for reduced computational power and time.

## 8.2 Future work

The further work recommended and planned to be performed in the future regards the aspects resumed in the following.

- ◇ Application of the wave-to-wire model to investigate the system operation under irregular waves to obtain a more accurate modelling of the energy conveyed by the resource.
- ◇ Analysis of the system operation on a monthly or daily basis.
- ◇ Forecasting the wave conditions to regulate in real-time the operating conditions of the turbine and electric generator.
- ◇ Selection of the optimal primary converter, specifically designed for the wave conditions of the application sites considered.
- ◇ Use of boundary element codes for determining the hydrodynamic parameters and properties of the OWC chamber when experimental data are not available.
- ◇ Integration of the models of the other configurations of Wells turbine developed into the wave-to-wire model.
- ◇ Definition of advanced control strategies for the wave energy converter.
- ◇ Creation of an experimental test rig at a laboratory scale based on the geometric and operating parameters determined with the analytical wave-to-wire model, and comparison of their results.
- ◇ Joint engineering and economic optimisation of the entire system considering the reciprocal effects of the possible solutions.

- ◇ Techno-economic risk assessment of the realisation of OWC systems with the analysis of the specific component life and determination of the costs related to production and maintenance for a more detailed evaluation of the turbine selection.
- ◇ Life cycle assessment of an OWC wave energy converter for quantifying the potential environmental impacts of all its components during their entire existence.

# Appendix A

# Turbulence models

The fundamental equations of the turbulence models utilised for the development of the CFD models of the Wells and impulse turbines.

## A.1 Two equations realisable $\kappa$-$\epsilon$ model

The $\kappa - \epsilon$ model is one of the most commonly used turbulence models. It is a two equation model, that means, it includes two extra transport equations to represent the turbulent properties of the flow. This allows a two equation model to account for history effects like convection and diffusion of turbulent energy.

The $\kappa - \epsilon$ model uses the turbulent energy and turbulent energy dissipation rate for computing the spatial and temporal scales and thus the turbulent viscosity. For this purpose, two separate transport equations are applied.

The realizable version of the turbulence model introduces an improved formulation of the dissipation rate transport equation, relying upon the transport equation for the mean-square vortic-

ity fluctuation [247] and a new eddy-viscosity formula involving a variable $\mathcal{C}_\mu$ originally proposed by Reynolds [259].

The realizable $\kappa - \epsilon$ model was tested and validated for a wild variety of flows and provides upgraded modelling of the fluid dynamics of flows involving rotation, boundary layers subject to significant adverse pressure gradients and separation, and recirculation [260, 261].

This turbulence model assumes that the flow is fully turbulent.

The formulation implemented by the software *ANSYS Fluent* is based on the modelling proposed in 1995 by Shih [260]. The distributions of kinetic turbulent energy and specific turbulence dissipation are provided by the solution of the transport equations expressed by Eq. (A.1) and (A.2).

$$\frac{\partial(\rho\kappa)}{\partial t} + \frac{\partial(\rho\kappa u_i)}{\partial x_i} = \frac{\partial}{\partial x_i}\left[\frac{\partial\kappa}{\partial x_i}\left(\mu + \frac{\mu_t}{\sigma_\kappa}\right)\right] + \\ + \mathfrak{P}_\kappa + \mathfrak{P}_\mathfrak{b} - \rho\epsilon \tag{A.1}$$

$$\frac{\partial(\rho\epsilon)}{\partial t} + \frac{\partial(\rho\epsilon u_i)}{\partial x_i} = \frac{\partial}{\partial x_i}\left[\frac{\partial\epsilon}{\partial x_i}\left(\mu + \frac{\mu_t}{\sigma_\kappa}\right)\right] + \\ + \rho\mathcal{C}_1\mathcal{S}\epsilon - \rho\mathcal{C}_2\frac{\epsilon^2}{\kappa + \sqrt{\nu\epsilon}} + \mathcal{C}_{1\epsilon}\frac{\epsilon}{\kappa}\mathcal{C}_{3\epsilon}P_b \tag{A.2}$$

where $\mathfrak{P}_\kappa$ and $\mathfrak{P}_\mathfrak{b}$ represent the production of turbulence kinetic energy owing to velocity gradients and buoyancy, respectively, and $\sigma_\kappa$ and $\sigma_\omega$ are the Prandtl turbulent numbers for the turbulence kinetic energy and the specific turbulence dissipation, respectively.

The production of turbulence kinetic can be determined with Eqs. (A.3) and (A.4).

$$\mathcal{S} = \sqrt{2\mathcal{S}_{ij}\mathcal{S}_{ji}} \tag{A.3}$$

$$\mathcal{P}_\kappa = \mu_t \mathcal{S}^2 \tag{A.4}$$

where $\mathcal{S}$ is the magnitude of the mean rate-of-strain tensor $\mathcal{S}$.

The variable $\mathcal{C}_1$ is defined by Eq. (A.5) and is a function of the variable $\eta$ given by Eq. (A.6).

$$\mathcal{C}_1 = max\left[0.43, \frac{\eta}{\eta + 5}\right] \tag{A.5}$$

$$\eta = \mathcal{S}\frac{\kappa}{\epsilon} \tag{A.6}$$

The constants utilised in the $\kappa - \epsilon$ turbulence model are resumed in Table A.1.

| $\mathcal{C}_{1\epsilon}$ | $\mathcal{C}_2$ | $\sigma_\kappa$ | $\sigma_\epsilon$ |
|---|---|---|---|
| 1.44 | 1.90 | 1.00 | 1.20 |

Table A.1: Constants applied in the $\kappa - \epsilon$ turbulence model.

The main discrepancies introduced by the realizable $\kappa-\epsilon$ turbulence model regarding its standard version is the formulation of the turbulent viscosity and the amendment of the transport equation of the specific turbulence dissipation.

The turbulent viscosity $\mu_t$ is computed with Eq. (A.7) as in the standard formulation. However, in the realizable version $\mathcal{C}_\mu$ is not a constant and varies based on the turbulence kinetic energy, the average strain value and the turbulence dissipation,

as expressed by Eq. (A.8).

$$\mu_t = \rho \mathcal{C}_\mu \frac{\kappa^2}{\epsilon} \tag{A.7}$$

$$\mathcal{C}_\mu = \frac{1}{\mathcal{A}_0 + \mathcal{A}_S \frac{\kappa \mathcal{U}^*}{\epsilon}} \tag{A.8}$$

The constant $A_0$ assumes value 4.04, while the variable and $\mathcal{A}_S$ is provided by equations from Eq. (A.9) to Eq. (A.13).

$$\mathcal{A}_S = \sqrt{6} \cos \phi \tag{A.9}$$

$$\phi = \frac{1}{3} \cos\left(\sqrt{6\mathcal{W}}\right) \tag{A.10}$$

$$\mathcal{W} = \frac{\mathcal{S}_{ij}\mathcal{S}_{jk}\mathcal{S}_{ki}}{\breve{\mathcal{S}}^3} \tag{A.11}$$

$$\mathcal{S}_{ij} = \frac{1}{2}\left(\frac{\partial u_j}{\partial x_i} + \frac{\partial u_j}{\partial x_i}\right) \tag{A.12}$$

$$\breve{\mathcal{S}} = \sqrt{\mathcal{S}_{ij}} \tag{A.13}$$

The variable $\mathcal{U}^*$ included in the formula of the coefficient $\mathcal{C}_\mu$ is defined by Eq. (A.14) and is based on Eqs. (A.15) and (A.16).

$$\mathcal{U}^* = \sqrt{\mathcal{S}_{ij}\mathcal{S}_{ij} + \breve{\Omega}_{ij}\breve{\Omega}_{ij}} \tag{A.14}$$

$$\breve{\Omega}_{ij} = \Omega_{ij} - 2\epsilon_{ijk}\omega_\kappa \tag{A.15}$$

$$\Omega_{ij} = \overline{\Omega}_{ij} - \epsilon_{ijk}\omega_\kappa \tag{A.16}$$

where $\overline{\Omega}_{ij}$ is the average rate-of-rotation tensor observed in a

rotating reference frame with the angular velocity $\omega_\kappa$.

It is very important to highlight that in the applications of the turbulence model performed in this thesis, the term $-2\epsilon_{ijk}\omega_\kappa$ was set to zero in the calculation of $\breve{\Omega}_{ij}$ as multiple reference frames and sliding meshes were utilised. This is needed not to includes the effects of mean rotation in the definition of the turbulent viscosity, that are not compatible with the aforementioned schemes for modelling rotation.

## A.2 Two equations standard $\kappa$-$\omega$ model

The $\kappa-\omega$ model is one of the most widespread turbulence models. It is an empirical model based on the introduction of two additional transport equations to represent the turbulent properties of the flow.

The standard version of the $\kappa-\omega$ relies on the formulation of Wilcox, that includes amendments of the low-Reynolds-number effects, the compressibility, and the shear flow spreading [240]. The transport equations are utilised to determine the turbulence kinetic energy $\kappa$ and the specific turbulence dissipation $\omega$, that is obtained as the ratio of $\epsilon$ to $\kappa$. This model is particularly suited for the computation of wall-bounded flows and free shear flows, as provides good predictions of the free shear flow spreading rates, which are in close agreement with measurements for far wakes, mixing layers, and plane, round, and radial jets [34]. However, this model may lack of accuracy for the computation of free shear flows.

The model implemented in *ANSYS Fluent* is a modification of the Wilcox $\kappa-\omega$ as additional production terms are included

in the transport equations of $\kappa$ and $\omega$ to improve the accuracy of the approach for the prediction of free stream flows [34].

The first transported variable of the of the standard $\kappa - \omega$ model is the turbulent kinetic energy $\kappa$, as expressed by Eq. (A.17). The second transported variable through Eq. (A.18) is the specific turbulence dissipation $\omega$. The former variable determines the energy in the turbulence, while the latter evaluates the scale of the turbulence.

$$\frac{\partial(\rho\kappa)}{\partial t} + \frac{\partial(\rho\kappa u_i)}{\partial x_i} = \frac{\partial}{\partial x_j}\left[\frac{\partial\kappa}{\partial x_j}\left(\mu + \frac{\mu_t}{\sigma_\kappa}\right)\right] + \mathcal{P}_\kappa - \mathcal{Y}_\kappa \quad \text{(A.17)}$$

$$\frac{\partial(\rho\omega)}{\partial t} + \frac{\partial(\rho\omega u_i)}{\partial x_i} = \frac{\partial}{\partial x_j}\left[\frac{\partial\omega}{\partial x_j}\left(\mu + \frac{\mu_t}{\sigma_\omega}\right)\right] + \mathcal{P}_\omega - \mathcal{Y}_\omega \quad \text{(A.18)}$$

where $\mathcal{P}_\kappa$ and $\mathcal{P}_\omega$ are the production terms of kinetic turbulent energy and specific turbulence dissipation, respectively, and $\mathcal{Y}_\kappa$ and $\mathcal{Y}_\omega$ indicate the dissipation of $\kappa$ and $\omega$ caused by turbulence, respectively.

The production of kinetic turbulent energy is a function of the production of specific turbulence dissipation, as expressed by Eq. (A.19).

$$\mathcal{P}_\omega = \alpha\frac{\omega}{\kappa}\mathcal{P}_\kappa \quad \text{(A.19)}$$

The coefficient $\alpha$ is given by Eq. (A.20) as a function of the turbulent Reynolds number.

$$\alpha = \frac{\alpha_\infty}{\alpha^*}\left(\frac{\alpha_0 + {Re_t}/{\mathcal{R}_\omega}}{1 + {Re_t}/{\mathcal{R}_\omega}}\right) \quad \text{(A.20)}$$

where $\alpha_\infty$ and $\alpha^*$ are constants that assume values 1 and 2.95, respectively.

The turbulent viscosity $\mu_t$ is calculated by combining kinetic turbulent energy and specific dissipation rate through Eq. (A.21).

$$\mu_t = \alpha^* \frac{\rho \kappa}{\omega} \tag{A.21}$$

where the constant $\mathcal{R}_\kappa$ is equal to 6.

The coefficient $\alpha^*$ of Eq. (A.22) damps the turbulent viscosity for flows with low Reynold number introducing a correction based on the local Reynolds number [34]. Conversely, for flows with high Reynolds number, the variables $\alpha^*$ and $\alpha^*_\infty$ are unitary.

$$\alpha^* = \alpha^*_\infty \left( \frac{\alpha^*_0 + {Re_t}/{\mathcal{R}_\kappa}}{1 + {Re_t}/{\mathcal{R}_\kappa}} \right) \tag{A.22}$$

For the calculation of Eq. (A.22), Eqs. (A.23), (A.24), and (A.25) are needed.

$$Re_t = \frac{\rho \kappa}{\mu \omega} \tag{A.23}$$

$$\alpha^*_0 = \frac{\beta_i}{3} \tag{A.24}$$

$$\beta_i = 0.072 \tag{A.25}$$

The dissipation of kinetic turbulent energy is expressed by Eq. (A.26) by applying the summation notation.

$$\mathcal{Y}_\kappa = \rho \beta^* f_{\beta^*} \kappa \omega \tag{A.26}$$

The variable $f_{\beta^*}$ assumes the values of Eq. (A.36) depending on $\chi_\kappa$.

$$f_{\beta^*} = \begin{cases} 1 & for \quad \chi_\kappa \leq 0 \\ \dfrac{1+680\chi_\kappa^2}{1+400\chi_\kappa^2} & for \quad \chi_\kappa > 0 \end{cases} \tag{A.27}$$

The variable $\chi_\kappa$ is computed through Eq. (A.28).

$$\chi_\kappa = \frac{1}{\omega^3}\frac{\partial \kappa}{\partial x_j}\frac{\partial \omega}{\partial x_j} \tag{A.28}$$

The function $\beta^*$ is computed by applying Eqs. (A.29) and (A.30).

$$\beta^* = \beta_i^* \left[1 + \zeta^* \mathcal{F}(\mathcal{F}_t)\right] \tag{A.29}$$

$$\beta_i^* = \beta_\infty^* \left[\frac{4/15 + \left(Re_t/Re_\beta\right)}{1 + \left(Re_t/Re_\beta\right)} + \right] \tag{A.30}$$

The dissipation of specific turbulence dissipation is provided by Eq. (A.31).

$$\mathcal{Y}_\omega = \rho \beta f_\beta \omega^2 \tag{A.31}$$

The variables necessary for the calculation of $\mathcal{Y}_\omega$ are given by equations from Eq. (A.32) to Eq. (A.35).

$$f_\beta = \frac{1+70\chi_\omega}{1+80\chi_\omega} \tag{A.32}$$

$$\chi_\omega = \left|\frac{\Omega_{ij}\Omega_{jk}\mathcal{S}_{\kappa i}}{(\beta_\infty^*\Omega)^3}\right| \tag{A.33}$$

$$\Omega_{ij} = \frac{1}{2}\left(\frac{\partial u_i}{\partial x_j} - \frac{\partial u_j}{\partial x_i}\right) \tag{A.34}$$

$$\beta = \beta_i^* \left[ 1 - \frac{\beta_i^*}{\beta_i} \zeta^* \mathcal{F}(\mathcal{M}_t) \right] \tag{A.35}$$

The function $\mathcal{F}(\mathcal{M}_t)$ accounts for the compressibility effects [34].

$$\mathcal{F}(\mathcal{M}_t) = \begin{cases} 0 & for \mathcal{F}(\mathcal{M}_t \leq \mathcal{M}_{t0} \\ \mathcal{M}_t^2 - \mathcal{M}_{t0}^2 & for \mathcal{F}(\mathcal{M}_t > \mathcal{M}_{t0} \end{cases} \tag{A.36}$$

The influence of compressibility depends upon the constant $\mathcal{M}_{t0}$ equal to 0.25 and the variable $\mathcal{M}_t^2$ expressed by Eq. (A.37).

$$\mathcal{M}_t^2 = \frac{2\kappa}{\gamma \mathcal{R} \mathcal{T}} \tag{A.37}$$

Therefore, for incompressible fluids $\beta^*$ is equivalent to $\beta_i^*$. For flows with high Reynols number, $\beta_i^* = \beta_{infty}^*$.

The constants utilised in the two equations standard $\kappa - \omega$ model are resumed in Table .

| $\alpha_\infty^*$ | $\alpha_\infty$ | $\alpha_0$ | $\beta_\infty^*$ | $\beta_1$ | $\zeta^*$ |
|---|---|---|---|---|---|
| 1 | 0.52 | 1/9 | 0.09 | 0.072 | 1.5 |
| $\mathcal{R}_\beta$ | $\mathcal{R}_\kappa$ | $\mathcal{R}_\omega$ | $\sigma_\kappa$ | $\sigma_\omega$ | $\mathcal{M}_{t0}$ |
| 8 | 6 | 2.95 | 2 | 2 | 0.25 |

Table A.2: Constants applied in the standard $\kappa - \omega$ turbulence model.

## A.3 Two equations κ-ω SST model

The shear-stress transport (SST) κ-ω model is an improvement of the standard formulation of the turbulence model based on the turbulence kinetic energy and the specific dissipation rate. The SST version was firstly introduced by Menter in 1994 blending

the $\kappa$-$\epsilon$ and the standard $\kappa$-$\omega$ models with the aim of selecting their best features. The free-stream independence of the former model in the far field is coupled with the robustness and accuracy of the latter model in the near-wall region. To achieve this target, a blending function was introduced to combine the equations of the standard $\kappa$-$\omega$ model with the converted equations of the $\kappa$-$\epsilon$ model. This function assumes unitary value in the near-wall region to activate the standard $\kappa$-$\omega$ model, while it is null away from the wall to activate the transformed $\kappa$-$\epsilon$ model [34]. Moreover, a damped cross-diffusion derivative term is included in the transport equation of the specific dissipation rate. The definition of the turbulent viscosity is modified for considering the transport of the turbulent shear stress. The constants applied in the SST version are differ from those of the standard version.

The two transport equations for the turbulent kinetic energy $\kappa$ and the specific dissipation $\omega$ are provided by Eqs. (A.38) and (A.39), respectively. The former variable determines the energy in the turbulence, while the latter evaluates the scale of the turbulence.

$$\frac{\partial(\rho\kappa)}{\partial t} + \frac{\partial(\rho\kappa u_i}{\partial x_i)} = \frac{\partial}{\partial x_j}\left[\frac{\partial\kappa}{\partial x_j}\left(\mu + \frac{\mu_t}{\sigma_\kappa}\right)\right] + \mathcal{P}_\kappa - \mathcal{Y}_\kappa \quad \text{(A.38)}$$

$$\frac{\partial(\rho\omega}{\partial t)} + \frac{\partial(\rho\omega u_i}{\partial x_i)} = \frac{\partial}{\partial x_j}\left[\frac{\partial\omega}{\partial x_j}\left(\mu + \frac{\mu_t}{\sigma_\omega}\right)\right] + \mathcal{P}_\omega - \mathcal{Y}_\omega + \mathcal{D}_\omega \quad \text{(A.39)}$$

The term $\mathcal{D}_\omega$ is the additional cross-diffusion, which is expressed by Eq. (A.40).

$$\mathcal{D}_\omega = 2(1-\mathcal{F}_1)\frac{\rho}{\omega\sigma_{\omega 2}}\frac{\partial\kappa}{\partial x_j}\frac{\partial\omega}{\partial x_j} \tag{A.40}$$

where $\sigma_{\omega 2}$ is a constant value equal to 1.168 and $\mathcal{F}_1$ is the blending function, which depends upon the distance from the closest surface $y$.

The turbulent viscosity, $\mu_t$, is computed though Eq. (A.41).

$$\mu_t = \frac{\rho\kappa}{\omega}\frac{1}{\max\left[\frac{1}{\alpha^*}, \frac{\mathcal{SF}_2}{a_1\omega}\right]} \tag{A.41}$$

where the variable $\mathcal{S}$ is the strain rate magnitude and $\alpha^*$ is a damping coefficient computed in analogy to the standard $\kappa$-$\omega$ model.

The function $\mathcal{F}_2$ is defined by Eq. (A.42) and is calculated based on the result of Eq. (A.43).

$$\mathcal{F}_2 = \tanh\left(arg_2^2\right) \tag{A.42}$$

$$arg_2 = \max\left[2\frac{\sqrt{\kappa}}{0.09\omega y}, \frac{500\mu}{\rho y^2\omega}\right] \tag{A.43}$$

The turbulent Prandtl numbers related to the turbulence kinetic energy and the specific dissipation rate are expressed by Eqs. (A.44) and (A.45), respectively.

$$\sigma_\kappa = \frac{1}{\frac{\mathcal{F}_1}{\sigma_{\kappa,1}} + \frac{1-\mathcal{F}_1}{\sigma_{\kappa,2}}} \tag{A.44}$$

$$\sigma_\omega = \frac{1}{\frac{\mathcal{F}_1}{\sigma_{\omega,1}} + \frac{1-\mathcal{F}_1}{\sigma_{\omega,2}}} \tag{A.45}$$

The blending function $\mathcal{F}_1$ for combining the transport equa-

tions is defined by Eq. (A.46), based on Eq. (A.47).

$$\mathcal{F}_1 = \tanh\left(arg_1^4\right) \tag{A.46}$$

$$arg_1 = \min\left[\max\left[\frac{\sqrt{\kappa}}{0.09\omega y}, \frac{500\mu}{\rho y^2 \omega}\right], \frac{4\rho\kappa}{\sigma_{\omega,2}\mathcal{D}_\omega^+ y^2}\right] \tag{A.47}$$

The variable $\mathcal{D}_\omega^+$ is defined with Eq. (A.48) as the positive part of the additional cross-diffusion term $\mathcal{D}_\omega$ for the transport equation of the specific turbulence dissipation.

$$\mathcal{D}_\omega^+ = \max\left[2\frac{\rho}{\omega\sigma_{\omega,2}}\frac{\partial\kappa}{\partial x_j}\frac{\partial\omega}{\partial x_j}, 10^{-10}\right] \tag{A.48}$$

The calculation of the turbulence kinetic energy $\kappa$ is performed as in the standard version of the $\kappa$-$\omega$ model. Instead, in the SST formulation, the production of turbulence kinetic energy is obtained with Eq. (A.49).

$$\mathcal{P}_\omega = \frac{\alpha\alpha^*}{\nu_t}\mathcal{P}_\kappa \tag{A.49}$$

Moreover, in the SST version, $\alpha_\infty$ is variable, as expressed by Eq. (A.50).

$$\alpha_\infty = \mathcal{F}_1\alpha_{\infty,1} + (1 + \mathcal{F}_1)\,\alpha_{\infty,2} \tag{A.50}$$

The variables $\alpha_{\infty,1}$ and $\alpha_{\infty,2}$ are given by Eqs. (A.51) and (A.52), respectively.

$$\alpha_{\infty,1} = \frac{\beta_{i,1}}{\beta_\infty^*} - \frac{\hat{k}^2}{\sigma_{w,1}\sqrt{\beta_\infty^*}} \tag{A.51}$$

$$\alpha_{\infty,2} = \frac{\beta_{i,2}}{\beta_\infty^*} - \frac{\hat{k}^2}{\sigma_{w,2}\sqrt{\beta_\infty^*}} \tag{A.52}$$

where $\hat{k}$ is a constant equal to 0.41.

The dissipation of the turbulent kinetic energy $\mathcal{Y}_\kappa$ is defined by Eq. (A.53) similarly to the standard version of the $\kappa$-$\omega$ turbulence model. The difference is in the term $f_{\beta^*}$, which in this case is not a piecewise function and assumes a constant unitary value.

$$\mathcal{Y}_\kappa = \rho\beta^*\kappa\omega \tag{A.53}$$

The definition of the dissipation of specific turbulence dissipation $\mathcal{Y}_\omega$ is given by Eq. (A.55) and is similar to the standard $\kappa$-$\omega$ model. The difference is in the computation of the terms $\beta_i$ and $f_\beta$. In the standard formulation, $\beta_i$ is a constant of value 0.072 and $f_\beta$ is a function of $\chi_\omega$. For the SST version, $\beta_i$ is provided by Eq. (A.55) and $f_\beta$ is an unitary constant.

$$\mathcal{Y}_\omega = \rho\beta\omega^2 \tag{A.54}$$

$$\beta_i = \mathcal{F}_1\beta_{i,1} + (1 - \mathcal{F}_1)\beta_{i,2} \tag{A.55}$$

The constants used in the two equations SST $\kappa - \omega$ model which differ from the standard formulation are resumed in Table A.3.

| $\sigma_{\kappa,1}$ | $\sigma_{\kappa,2}$ | $\sigma_{\omega,1}$ | $\sigma_{\kappa,2}$ | $a_1$ | $\hat{k}$ | $\beta_{i,1}$ | $\beta_{i,2}$ |
|---|---|---|---|---|---|---|---|
| 1.176 | 1 | 2 | 1.168 | 0.31 | 0.41 | 0.075 | 0.0828 |

Table A.3: Constants applied in the SST $\kappa-\omega$ turbulence model.

# Appendix B

# List of publications

The articles published during the Ph.D. course are listed in the following.

- L. Ciappi, M. Stebel, J. Smołka, L. Cappietti, G. Manfrida, "Analytical and computational fluid dynamics models of Wells turbines for oscillating water column systems", Journal of Energy Resources Technology, 144(5), 050903, 2021.

  Doi:10.1115/1.4052216.

- L. Ciappi, L. Cheli, I. Simonetti, A. Bianchini, L. Talluri, L. Cappietti, G. Manfrida, "Wave-to-wire models of Wells and impulse turbines for oscillating water column wave energy converters operating in the Mediterranean Sea", Energy, 238, part A, 121585, 2021.

  Doi:10.1016/j.energy.2021.121585.

- P. H. Niknam, L. Talluri, L. Ciappi, D. Fiaschi, "Numerical assessment of a two-phase Tesla turbine: Parametric analysis", Applied Thermal Engineering, 197, 117364, 2021.

Doi:10.1016/j.applthermaleng.2021.117364.

◇ L. Talluri, G. Manfrida, L. Ciappi, "Exergo-economic assessment of OTEC power generation", Proceedings of the ICAE Conference, Italy, October 2020.

Doi:10.1051/e3sconf/202123801015.

◇ L. Ciappi, L. Cheli, I. Simonetti, A. Bianchini, G. Manfrida, L. Cappietti, "Wave-to-wire Model of an Oscillating-Water-Column Wave Energy Converter and Its Application to Mediterranean Energy Hot-Spots", Energies, 13(21), 5582, 2020.

Doi:10.3390/en13215582.

◇ L. Ciappi, M. Stebel, J. Smołka, L. Cappietti, G. Manfrida, "Computational fluid dynamics models of Wells turbines for oscillating water column systems", Proceedings of the 6th CPOTE Conference, Cracow, Poland, September 2020.

◇ L. Ciappi, L. Cheli, I. Simonetti, A. Bianchini, L. Talluri, L. Cappietti, G. Manfrida, "Analytical Models of Oscillating Water Column Systems Operating with Air Turbines in the Mediterranean Sea", Proceedings of the 15th SDEWES Conference, Cologne, Germany, September 2020.

ISSN 1847-7178.

◇ L. Pacini, L. Ciappi, L. Talluri, D. Fiaschi, G. Manfida, J. Smołka, "Computational Investigation of Partial Admission Effects on the Flow Field of a Tesla Turbine for ORC Applications", Energy, 212, 118687, 2020.

Doi:10.1016/j.energy.2020.118687.

◇ L. Cappietti, L. Ciappi, A. Esposito, D. Fiaschi, G. Manfrida, B. Melka, M. Nowak, I. Simonetti, M. Stebel, J.

Smołka, L. Talluri, "Experimental investigation of velocity-augmented barriers for tidal stream turbines", Proceedings of the 14th SDEWES Conference, Dubrovnik, Croatia, 2019.

◇ L. Pacini, L. Ciappi, L. Talluri, D. Fiaschi, G. Manfida, J. Smołka, "Partial admission effects on the flow field of an ORC Tesla turbine", Proceedings of the 5th International Seminar on ORC Power Systems, Athens, Greece, 2019.

◇ L. Ciappi, D. Fiaschi, G. Manfrida, S. Salvadori, J. Smołka, L. Talluri, "Heat Recovery for a Textile Stenter: CFD Analysis of Air Curtain Benefits", Energies, 12(3):482, 2019.

Doi:10.3390/en12030482.

◇ L. Ciappi, D. Fiaschi, P. H. Niknam, L. Talluri, "Computational investigation of the flow inside a Tesla turbine rotor", Energy, 173, 207-217, 2019.

Doi:10.1016/j.energy.2019.01.158.

◇ L. Talluri, D. Fiaschi, G. Neri, L. Ciappi, "Design and optimization of a Tesla turbine for ORC", Applied Energy, 226, 300-319, 2018.

Doi:10.1016/j.apenergy.2018.05.057.

# Bibliography


[1] A. F. O. Falcão and Henriques J. C. C. Oscillating-water-column wave energy converters and air turbines: A review. *Renewable Energy*, 85:1391–1424, 2016, doi:10.1016/j.renene.2015.07.086.

[2] Y. Masuda and T. Miyazaki. Development of wave power generator. *Ocean Management*, (4):259–271, 1978.

[3] A. Hiramoto, I. Tamaki, and Y. Masuda. Shore based wave energy conversion system development. pages 595–596, 1985.

[4] O. Malmo and A. Reitan. Development of the Kvaerner Multiresonant OWC. *Hydrodynamics of wave utilization*, 1985, 10.1007/978-3-642-82666-5_4.

[5] J. Brooke. *Wave energy conversion*. Elsevier, 2003, ISBN 0-08-044212-9.

[6] M. McCormick. A Theoretical Analysis of a Self-Propelled Backward Bent Duct Buoy Wave Energy Conversion System. *Transactions of the ASME*, 1991.

[7] S. Takahashi, H. Nakada, H. Ohneda, and M. Shikamori. Wave Power Conversion by a Prototype Wave Power Ex-

tracting Caisson in Sakata Port. *23rd International Conference on Coastal Engineering*, 2012.

[8] V. S. Raju, Jayakumar, and S. Neelamani. Concrete caisson for a 150 kW wave energy pilot plant: design, construction and installation aspects. San Francisco, Ca, USA, 1992, ISBN 1-880653-00-1.

[9] T. J. T. Whittaker, W. Beattie, S. Raghunathan, and T. Thompson. The Islay wave power project: an engineering perspective. *Proceedings of the Institution of Civil Engineers - Water, Maritime and Energy*, 124(3):189–201, 1997, doi:10.1680/iwtme.1997.29783.

[10] T. W. Thorpe. A Brief Review of Wave Energy, 1999.

[11] Y. Washio, H. Osawa, Y. Nagata, F. Fujiii, H. Furuyama, and T. Fujita. The offshore floating type wave power device Mighty Whale: open sea tests. Seattle, Washington, USA, 2000, ISBN 1.880653.46.X.

[12] C. Boake. Overview and Initial Operational Experience of the LIMPET Wave Energy Plant. *Proceedings of The Twelfth International Offshore and Polar Engineering Conference*, Kitakyushu, Japan, 2002.

[13] S. Doyle and G. A. Aggidis. Investigation into multi-oscillating water column wave energy converters and a novel concept. Lisbon, Portugal, 2018.

[14] L. Martinelli. Experimentally based model to size the geometry of a new OWC device, with reference to the Mediterranean Sea wave environment. *Energies*, 2013.

[15] S. Ribeiro e Silva, R. P: F. Gomes, and A. F. O. Falcão. Hydrodynamic optimization of the UGEN: Wave energy

converter with U-shaped interior oscillating water column. *International Journal of Marine Energy*, 15:112–126, 2016, doi:10.1016/j.ijome.2016.04.013.

[16] I. Heras-Saizarbitoria. Social acceptance of ocean wave energy: a case study of an OWC shoreline plant. *Renewable and sustainable energy reviews*, 27, 2013.

[17] L. M. C. Gato, A. F. O. Falcão, J. C. C. Henriques, R. Gomes, P. Vicente, P. Ruiz-Minguela, P. Ricci, J. Varandas, and L. Trigo. Experimental Validation of a Spar Buoy Design for Wave Energy Conversion, 2012.

[18] T. Kelly, T. Dooley, J. Campbell, and J. V. Ringwood. Comparison of the Experimental and Numerical Results of Modelling a 32-Oscillating Water Column, V-Shaped Floating Wave Energy Converter. *Energies*, 6:4045–4077, 2013, doi:10.3390/en6084045.

[19] A. Kurniawan, D. Greaves, and J. Chaplin. Wave energy devices with compressible volumes. volume 135, 2014, doi:10.1098/rspa.2014.0559.

[20] F. Arena, A. Romolo, G. Malara, and A. Ascanelli. On Design and Building of a U-OWC Wave Energy Converter in the Mediterranean Sea: A Case Study. 2013, doi:10.1115/OMAE2013-11593.

[21] S. L. Dixon. *Fluid Mechanics and Thermodynamics of Turbomachinery*. 6th Edition, Elsevier, United Kingdom, 2010, ISBN 978-1856177931.

[22] S. Raghunathan. The Wells air turbine for wave energy conversion. *Progress in Aerospace Sciences*, 31:335–386, 1995, doi:10.1016/0376-0421(95)00001-F.

[23] W. Sheng, R. Alcorn, and Lewis A. On thermodynamics in the primary power conversion of oscillating water column wave energy converters. *Journal of Renewable and Sustainable Energy*, 5(2):023105, 2013, doi:10.1063/1.4794750.

[24] L. Ciappi, L. Cheli, I. Simonetti, A. Bianchini, L. Talluri, L. Cappietti, and G. Manfrida. Wave-to-wire models of Wells and impulse turbines for oscillating water column wave energy converters operating in the Mediterranean Sea. *Energy*, 238(part A):121585, 2021, doi:10.1016/j.energy.2021.121585.

[25] A. R. Howell. Design of Axial Compressors. *Proceeding of the Institution of Mechanical Engineers*, 153(1), 1945.

[26] S. A Sjolander. Overview of Tip-Clearance Effects in Axial Turbines. Von Karman Institute for Fluid Dynamics, Sint-Genesius-Rode, Belgium, 1997.

[27] P. Lampart. Tip Leakage Flows in Turbines, 2006.

[28] D. G. Ainley and G. C. R. Mathieson. An Examination of the Flow and Pressure Losses in Blade Rows of Axial-Flow Turbines. *Aeronautical Research Council Reports and Memoranda*, 1955.

[29] S. H. Moustapha, S. C. Kacker, and B. Tremblay. An Improved Incidence Losses Prediction Method for Turbine Airfoils. *Journal of Turbomachinery*, 112(2):267–276, 1990.

[30] L. Ciappi, M. Stebel, J. Smoł ka, L. Cappietti, and G. Manfrida. Computational fluid dynamics models of Wells turbines for oscillating water column systems. Cracow, Poland, 2020.

[31] L. Ciappi, M. Stebel, J. Smoł ka, L. Cappietti, and G. Manfrida. Analytical and computational fluid dynamics models of Wells turbines for oscillating water column systems. *Journal of Energy Resources Technology*, 144(5):050903, 2021, doi:10.1115/1.4052216.

[32] T. Setoguchi, M. Takao, S. Santhakumar, and K. Kaneko. Study of an impulse turbine for wave power conversion: Effects of Reynolds number and hub-to-tip ratio on performance. *Journal of Offshore Mechanics and Arctic Enginnering, Transactions of the ASME*, 126:137–140, 2004, doi:10.1115/1.1710868.

[33] L. Ciappi, L. Cheli, I. Simonetti, A. Bianchini, G. Manfrida, and L. Cappietti. Wave-to-Wire Model of an Oscillating-Water-Column Wave Energy Converter and Its Application to Mediterranean Energy Hot-Spots. *Energies*, 13(21):5582, 2020, doi:10.3390/en13215582.

[34] ANSYS Incorporated. ANSYS Fluent Theory Guide, July 2019.

[35] I. Simonetti. *Optimization of Oscillating Water Column Wave Energy Converters in Moderate Wave Climate*. PhD thesis, Ph.D. Thesis, University of Florence, University of Braunschweig, 2016.

[36] I. Crema, I. Simonetti, L. Cappietti, and H. Oumeraci. Laboratory Experiments on Oscillating Water Column Wave Energy Converters Integrated in a Very Large Floating Structure. Nantes, France, 2015.

[37] G. Mork, S. Barstow, A. Kabuth, and T. M. Pontes. Assessing the global wave energy potential. Shanghai, China, 2010, doi:10.1115/OMAE2010-20473.

[38] K. Gunn and C. Stock-Williams. Quantifying the global wave power resource. *Renewable Energy*, 44:296–304, 2012, doi:10.1016/j.renene.2012.01.101.

[39] BP. Statistical Review of World Energy, 2019.

[40] R. Curran, T. J. T. Whittaker, and T. P. Stewart. Aerodynamic conversion of ocean power from wave to wire. *Energy Conversion and Management*, 39:1919–1929, 1998, doi:10.1016/S0196-8904(98)00064-8.

[41] A. F. O. Falcão and Henriques J. C. C. Wave energy utilization: a review of the technologies. *Renewable and Sustainable Energy Reviews*, 14:899–918, 2010, doi:10.1016/j.rser.2009.11.003.

[42] M. Melikoglu. Current status and future of ocean energy sources: A global review. *Ocean Engineering*, 148:563–573, 2018, doi:10.1016/j.oceaneng.2017.11.045.

[43] A. F. O. Falcão, Henriques J. C. C., and L. M. C. Gato. Self-rectifying air turbines for wave energy conversion: A comparative analysis. *Renewable and Sustainable Energy Reviews*, 91:1231–1241, 2018, doi:10.1016/j.rser.2018.04.019.

[44] A. F. O. Falcão and L. M. C. Gato. Air turbines, in: Sayigh, A. Comprehensive Renewable Energy. *Elsevier*, 8:111–149, Oxford, England, 2012, doi:10.1016/B978-0-08-087872-0.00805-2.

[45] S. Astariz and G. Iglesias. The economics of wave energy: A review. *Renewable and Sustainable Energy Reviews*, 45:397–408, 2015, ISSN 1364-0321, doi:10.1016/j.rser.2015.01.061.

[46] IRENA. Renewable power generation costs in 2019, 2019.

[47] Iglesias G. Lopez I, Carballo R. Site-specific wave energy conversion performance of an oscillating water column device. *Energy Conversion and Management*, 195:457–465, 2019, doi:10.1016/j.enconman.2019.05.030.

[48] Iglesias G. Lopez I, Carballo R. Intra-annual variability in the performance of an oscillating water column wave energy converter. *Energy Conversion and Management*, 207:12536, 2020, doi:10.1016/j.enconman.2020.112536.

[49] V. Vannucchi and L. Cappietti. Wave Energy Assessment and Performance Estimation of State of the Art Wave Energy Converters in Italian Hotspots. *Sustainability*, 8:1300, 2016, doi:10.3390/su8121300.

[50] L. M. C. Gato and A. F. O. Falcão. On the theory of Wells turbine. *Journal of Engineering for Gas Turbines and Power*, 106(3), 1984.

[51] S. Raghunathan, C. P. Tan, and O. O. Ombaka. Performance of the Wells self-rectifying air turbine. *The Aeronautical Journal*, 89(890):369–379, 1985, doi:10.1017/S0001924000096743.

[52] L. M. C. Gato and A. F. O. Falcão. Performance of the Wells turbine with a Double Row of Guide Vanes. *International Journal of the Japan Society of Mechanical Engineers*, 33(2):265–271, 1990.

[53] S. Raghunathan, T. Setoguchi, and K. Kaneko. Aerodynamics of monoplane Wells turbine – A review. In *Proceedings of the First International Offshore and Polar Engi-*

*neering Conference*, volume 1, pages 370–379, Edinburgh, Scotland, 1991, ISBN 0-9626104-6-1.

[54] K. Kaneko, T. Setoguchi, H. Hamakawa, , and Inoue M. Biplane axial turbine for wave power generator. *International Journal of Offshore and Polar Engineering*, 1:122–128, 1991, doi:10.1299/kikaib.55.1159.

[55] S. Raghunathan. A methodology for Wells turbine design for wave energy conversion. *Proceedings of the Institution of Mechanical Engineers*, 209:221–232, 1995, doi:10.1243/PIME_PROC_1995_209_040_02.

[56] R. Curran and L. M. C. Gato. The energy conversion performance of several types of Wells turbine designs. In *Proceedings of the Institution of Mechanical Engineers: Journal of Power and Energy*, volume 211, pages 133–145, 1997, doi:10.1243/0957650971537051.

[57] M. Govardhan and T. S. Dhanasekaran. Effect of guide vanes on the performance of a variable chord self-rectifying air turbine. *Journal of Thermal Science*, 7:209–217, 1998, doi:10.1016/S0960-1481(01)00124-0.

[58] L. M. C. Gato and M. Webster. An experimental investigation into the effect of rotor blade sweep on the performance of the variable-pitch Wells turbine. volume 215, pages 611–622, 2001, doi:10.1243/0957650011538848.

[59] A. Brito-Melo, L. M. C. Gato, and A. J. N. A. Sarmento. Analysis of Wells turbine design parameters by numerical simulation of the OWC performance. *Ocean Engineering*, 29:1463–1477, 2002, doi:10.1016/S0029-8018(01)00099-3.

[60] T. Kim, Y. W. Lee, I. K. Park, T. Setoguchi, and C. S. Kang. Numerical analysis for unsteady flow characteristics of the Wells turbine. volume 1, pages 694–699, Kitakyushu, Japan, 2002.

[61] T. H. Kim, T. Setoguchi, M. Takao, K. Kaneko, and S. Santhakumar. Study of turbine with self-pitch-controlled blades for wave energy conversion. *International Journal of Thermal Sciences*, 41(1):101–107, 2002, doi:10.1016/S1290-0729(01)01308-4.

[62] T. Setoguchi, S. Santhakumar, M. Takao, T. H. Kim, and K. Kaneko. A modified Wells turbine for wave energy conversion. *Renewable Energy*, 28(1):79–91, 2003, doi:10.1016/S0960-1481(02)00006-X.

[63] H. A. Heikal, A. A. Hafiz, N. N. Bayomi, and M. H. Ahmed. Theoretical and Experimental Investigation on the Wells Turbine Performance. Cairo, Egypt, 2003.

[64] Y. Kinoue, M. Mamun, T. Setoguchi, , and K. Kaneko. Hysteretic characteristics of monoplane and biplane Wells turbine for wave power conversion. *International Journal of Sustainable Energy*, 26:51–60, 2004, doi:10.1016/j.enconman.2003.08.021.

[65] T. Setoguchi, Y. Kinoue, M. Mohammad, K. Kaneko, and M. Takao. Unsteady Flow Phenomena of Wells Turbine in Deep Stall Condition. *Proceedings of the 14th International Offshore and Polar Engineering Conference*, pages 266–271, Toulon, France, 2004.

[66] M. Torresi, S. M. Camporeale, G. Pascazio, and B. Fortunato. Fluid dynamic analysis of the solidity of a Wells turbine. 2004.

[67] A. Thakker and R. Abdulhadi. Effect of Blade Profile on the Performance of Wells Turbine under Unidirectional Sinusoidal and Real Sea Flow Conditions. *International Journal of Rotating Machinery*, pages 1–9, 2007, doi:10.1155/2007/51598.

[68] Z. Taha, Sugiyono, and T. Sawada. A comparison of computational and experimental results of Wells turbine performance for wave energy conversion. *Applied Ocean Research*, 32:83–90, 2010, doi:10.1016/j.apor.2010.04.002.

[69] Z. Taha, Sugiyono, T. M. Y. S. Tuan Ya, and T. Sawada. Numerical investigation on the performance of Wells turbine with non-uniform tip clearance for wave energy conversion. *Applied Ocean Research*, 33:321–331, 2011, doi:10.1016/j.apor.2010.04.002.

[70] M. Torresi, D. Pranzo, S. M. Camporeale, and G. Pascazio. Improved Design of High Solidity Wells Turbine. *Proceedings of the 9th European Wave and Tidal Energy Conference*, Southampton, United Kingdom, 2011.

[71] R. Starzmann and T. H. Carolus. Effect of Design Parameters on Aeroacoustic and Aerodynamic Performance of Wells Turbines. Rotterdam, The Netherlands, 2011.

[72] S. Shaaban and A. Abdel Hafiz. Effect of duct geometry on Wells turbine performance. *Energy Conversion and Management*, 61:51–58, 2012, doi:10.1016/j.enconman.2012.03.023.

[73] M. Paderi, , and Puddu P. Experimental investigation in a Wells turbine under bidirectional flow. *Renewable Energy*, 57:570–576, 2013, doi:10.1016/j.renene.2013.02.016.

[74] M. H. Mohamed and S. Shaaban. Optimization of blade pitch angle of an axial turbine used for wave energy conversion. *Energy*, 56:229–239, 2013, doi:10.1016/j.energy.2013.04.035.

[75] R. Starzmann and T. H. Carolus. Effect of Blade Skew Strategies on the Operating Range and Aeroacoustic Performance of the Wells Turbine. *Journal of Turbomachinery*, 136(1):011003, 2013, doi:10.1115/1.4025156.

[76] P. Halder and A. Samad. Effect of guide vane angle on Wells turbine performance. New Delhi, India, 2014, doi:10.1115/GTINDIA2014-8183.

[77] T. Ghisu, P. Puddu, and F. Cambuli. A Comparison Between Experimental and Numerical Analysis of a Wells Turbine. Madrid, Spain, 2015.

[78] S. Shaaban. Aero-economical optimization of Wells turbine rotor geometry. *Energy Conversion and Management*, 126:20–31, 2016, doi:10.1016/j.enconman.2016.07.068.

[79] P. Halder, S. H. Rhee, and A. Samad. Numerical optimization of Wells turbine for wave energy extraction. *International Journal of Naval Architecture and Ocean Engineering*, 9:11–24, 2016, doi:10.1016/j.ijnaoe.2016.06.008.

[80] P. Halder and A. Samad. Torque and efficiency maximization for a wave energy harvesting turbine: an approach to modify multiple design variables. *International Journal of Energy Research*, 41(7), 2016, doi:10.1002/er.3694.

[81] T. Ghisu, P. Puddu, and F. Cambuli. A detailed analysis of the unsteady flow within a Wells turbine. volume 231, pages 197–214, 2017, doi: 10.1177/0957650917691640.

[82] T. Ghisu, P. Puddu, F. Cambuli, and I. Virdis. On the Hysteretic Behavior of Wells Turbines. *Energy Procedia*, 126, 2017, doi:10.1016/j.egypro.2017.08.303.

[83] S. Shaaban. Wells turbine blade profile optimization for better wave energy capture. *International Journal of Energy Research*, 41(4), 2017, doi:10.1002/er.3745.

[84] P. Halder, M. H. Mohamed, and S. Samad. Wave energy conversion: Design and shape optimization. *Ocean Engineering*, 150:337–351, 2018, doi:10.1016/j.oceaneng.2017.12.072.

[85] P. M. Kumar, P. Halder, A. Husain, and A. Samad. Performance enhancement of Wells turbine: Combined radiused edge blade tip, static extended trailing edge, and variable thickness modifications. *Ocean Engineering*, 185:47–58, 2018, doi:10.1016/j.oceaneng.2019.05.041.

[86] T. Ghisu, F. Cambuli, P. Puddu, I. Virdis, M. Carta, and F. Licheri. A lumped parameter model to explain the cause of the hysteresis in OWC-Wells turbine systems for wave energy conversion. *Applied Ocean Research*, 94, 2020, doi:10.1016/j.apor.2019.101994.

[87] T. K. Das, K. Kumar, and A. Samad. Experimental analysis of a biplane Wells turbine under different load conditions. *Energy*, 206:118205, 2020, doi:10.1016/j.energy.2020.118205.

[88] F. Licheri, F. Cambuli, P. Puddu, and T. Ghisu. A comparison of different approaches to estimate the efficiency of Wells turbines. *Journal of Fluids Engineering*, 36(5):386–402, 2021, doi:10.1115/1.4049686.

[89] Y. Masuda and M. E. McCormick. Experiences in pneumatic wave energy conversion in Japan, in: McCormick, M. E., Kim, Y. C., Utilization of Ocean Waves: Wave to Energy Conversion. In *American Society of Civil Engineering*, pages 1–33, New York City, New York State, USA, 1986.

[90] T. W. Kim, K. Kaneko, T. Setoguchi, and M. Inoue. Aerodynamic performance of an impulse turbine with self-pitch-controlled guide vanes for wave power generator. Seoul, South Korea, 1988.

[91] H. Maeda, S. Santhakumar, T. Setoguchi, M. Takao, Y. Kinoue, and K. Kaneko. Performance of an impulse turbine with fixed guide vanes for wave power conversion. *Renewable Energy*, 17:535–547, 1999, doi:10.1016/s0960-1481(98)00771-x.

[92] T. Setoguchi, S. Santhakumar, H. Maeda, M. Takao, and K. Kaneko. A review of impulse turbines for wave energy conversion. *Renewable Energy*, 23:261–292, 2001, doi:10.1016/s0960-1481(00)00175-0.

[93] A. Thakker and F. Hourigan. Modeling and scaling of the impulse turbine for wave power applications. *Renewable Energy*, 29:305–317, 2004, doi:10.1016/S0960-1481(03)00253-2.

[94] T. Setoguchi and M. Takao. Current status of self rectifying air turbines for wave energy conversion. *Energy Conversion and Management*, 47:2382–2396, 2006, doi:10.1016/j.enconman.2005.11.013.

[95] A. Thakker, J. Jarvis, and A. Sahed. Design charts for impulse turbine wave energy extraction using exper-

imental data. *Renewable Energy*, 34:2264–2270, 2009, doi:10.1016/j.renene.2009.04.002.

[96] R. P. F. Gomes, J. C. C. Henriques, L. M. C. Gato, and A. F. O. Falcão. Multi-point aerodynamic optimization of the rotor blade sections of an axial-flow impulse air turbine for wave energy conversion. *Energy*, 45:570–580, 2012, doi:10.1016/j.energy.2012.07.042.

[97] R. Badhurshah, A. Samad, and J. Sangwai. Analysis of Flow Through Ocean Energy Harvesting Bidirectional Impulse Turbine. *The International Journal of Ocean and Climate Systems*, 5(2), 2014, doi:10.1260/1759-3131.5.2.51.

[98] Y. Cui and Z. Liu. Effects of Solidity Ratio on Performance of OWC Impulse Turbine. *Advances in Mechanical Engineering*, page 121373, 2014, doi:10.1155/2014/121373.

[99] R. Badhurshah and A. Samad. Multi-objective optimization of a bidirectional impulse turbine. volume 229, pages 584–596, 2015, doi:10.1177/0957650915589271.

[100] R. Badhurshah and A. Samad. Multiple surrogate based optimization of a bidirectional impulse turbine for wave energy conversion. *Renewable Energy*, 74:749–760, 2015, doi:10.1016/j.renene.2014.09.001.

[101] Z. Liu, Y. Cui, K. W. Kim, and H. D. Shi. Numerical study on a modified impulse turbine for OWC wave energy conversion. *Ocean Engineering*, 111:533–542, 2016, doi:10.1016/j.oceaneng.2015.11.005.

[102] A. George, R. Balakrishnan, A. Samad, and P. V. Dudhgaonkar. Evaluation of impulse turbines for a wave

energy converter. volume 38, Bangalore, India, 2017, doi:10.1115/GTINDIA2017-4567.

[103] K. Ezhilsabareesh, S. H. Rhee, and A. Samad. Shape optimization of a bidirectional impulse turbine via surrogate models. *Engineering Applications of Computational Fluid Mechanics*, 12(1), 2017, doi:10.1080/19942060.2017.1330709.

[104] R. Badhurshah, P. Dudhgaonkar, P. Jalihal, and A. Samad. High efficiency design of an impulse turbine used in oscillating water column to harvest wave energy. *Renewable Energy*, 121:344–354, 2018, doi:10.1016/j.renene.2018.01.028.

[105] K. Nielsen, M. M. Kramer, F. Ferri, A. S. Zurkinden, and M. Alves. Overview of Wave to Wire Models, Aalborg University, Denmark, 2014, ISSN 1901-726X.

[106] F. X. Fay, J. C. C. Henriques, M. Marcos, and E. Robles. Review of control strategies for oscillating water column wave energy converters. Nantes, France, 2015.

[107] M. Penalba and J. V. Ringwood. A Review of Wave-to-Wire Models for Wave Energy Converters. *Energies*, 9(7):506–550, 2016, doi:10.3390/en9070506.

[108] L. Wang, J. Isberg, and E. Tedeschi. Review of control strategies for wave energy conversion systems and their validation: the wave-to-wire approach. *Renewable and Sustainable Energy Reviews*, 1:366–379, 2018, doi:10.1016/j.rser.2017.06.074.

[109] A. Maria-Arenas, A. J. Garrido, E. Rusu, and I. Garrido. Control Strategies Applied to Wave Energy Convert-

ers: State of the Art. *Energies*, 12(16):3115–3133, 2019, doi:10.3390/en12163115.

[110] A. F. O. Falcão and P. Justino. OWC wave energy devices with air flow control. *Ocean Engineering*, 26:1275–1295, 1999, doi:10.1016/s0029-8018(98)00075-4.

[111] M. Amundarain, M. Alberdi, A. J. Garrido, and I. Garrido. Modeling and Simulation of Wave Energy Generation Plants: Output Power Control. *IEEE Transactions on Industrial Electronics*, 58(1), 2011, doi:10.1109/TIE.2010.2047827.

[112] M. Alberdi, M. Amundarain, A. J. Garrido, I. Garrido, O. Casquero, and M. De la Sen. Complementary Control of Oscillating Water Column-Based Wave Energy Conversion Plants to Improve the Instantaneous Power Output. *IEEE Transactions on Energy Conversion*, 26(4):1021–1032, 2011, doi:10.1109/TEC.2011.2167332.

[113] Henriques J. C. C., A. F. O. Falcão, R. P. F. Gomes, and L. M. C. Gato. Latching Control of an Oscillating Water Column Spar-Buoy Wave Energy Converter in Regular Waves. *Journal of Offshore Mechanics and Arctic Engineering*, 135(2):618–626, 2013, doi:10.1115/1.4007595.

[114] J. C. C. Henriques, J. C. Chong, A. F. O. Falcão, and R. P. F. Gomes. Latching Control of a Floating Oscillating Water Column Wave Energy Converter in Irregular Waves. San Francisco, California, USA, 2014.

[115] J. C. C. Portillo, J. C. C. Henriques, A. F. O. Falcão, R. P. F. Gomes, and L. M. C. Gato. Theoretical and experimental investigation on causal latching and rotational

speed control of an OWC spar-buoy wave energy converter. *Renew, 1st International Conference on Renewable Energies Offshore*, Lisbon, Portugal, 2014.

[116] J. F. Kelly, W. M. D. Wright, W. Sheng, and K. O'Sullivan. Implementation and Verification of a Wave-to-Wire Model of an Oscillating Water Column With Impulse Turbine. *IEEE Transactions on sustainable energy*, 7(2), 2015, doi:10.1109/TSTE.2015.2504463.

[117] S. K. Song and J. B. Park. Modeling and Control Strategy of an Oscillating Water Column-Wave Energy Converter with an Impulse Turbine Module. Busan, South Korea, 2015, doi:10.1109/ICCAS.2015.7364693.

[118] S. K. Song and J. B. Park. Control Strategy of an Impulse Turbine for an Oscillating Water Column-Wave Energy Converter in Time-Domain Using Lyapunov Stability Method. volume 6, 2016, doi:10.3390/app6100281.

[119] J. C. C. Henriques, R. P. F. Gomes, L. M. C. Gato, A. F. O. Falcão, E. Robles, and S. Ceballos. Testing and control of a power take-off system for an oscillating-water-column wave energy converter. *Renewable Energy*, 85(2):714–724, 2016, doi:10.1016/j.renene.2015.07.015.

[120] J. C. C. Henriques, L. M. C. Gato, J. M. Lemos, R. P. F. Gomes, and A. F. O. Falcão. Peak-power control of a grid-integrated oscillating water column wave energy converter. *Energy*, 109:378–390, 2016.

[121] H. Bailey, B.R. Robertson, and B.J Buckham. Wave-to-wire simulation of a floating oscillating water column wave energy converter. *Ocean Engineering*, 125:248–260, 2016, doi:10.1016/j.oceaneng.2016.08.017.

[122] R. Suchithra, K. Ezhilsabareesh, and A. Samad. Development of a reduced order wave to wire model of an OWC wave energy converter for control system analysis. *Ocean Engineering*, 172:614–628, 2019, doi:10.1016/j.oceaneng.2018.12.013.

[123] J. Henriques, J. Portillo, W. Sheng, L. Gato, and A. F. O. Falcão. Dynamics and control of air turbines in oscillating-water-column wave energy converters: Analyses and case study. *Renewable and Sustainable Energy Reviews*, 112(2):571–589, 2019, doi:10.1016/j.rser.2019.05.010.

[124] F.-X. Fay, J. Henriques, J. Kelly, M. Mueller, M. Abusara, W. Sheng, and M. Marcos. Comparative assessment of control strategies for the biradial turbine in the Mutriku OWC plant. *Renewable Energy*, 146:2766–2784, 2020, doi:10.1016/j.renene.2019.08.074.

[125] P. Benreguig, J. Kelly, V. Pakrashi, and J. Murphy. Wave-to-Wire Model Development and Validation for Two OWC Type Wave Energy Converters. *Energies*, 12:3977, 2019, doi:10.3390/en12203977.

[126] L. Ciappi, L. Cheli, I. Simonetti, A. Bianchini, L. Talluri, L. Cappietti, and G. Manfrida. Analytical Models of Oscillating Water Column Systems Operating with Air Turbines in the Mediterranean Sea. Cologne, Germany, 2020, ISSN 1847-7178.

[127] A. Scialò, J. C. C. Henriques, G. Malara, A. F. O. Falcão, L. M. C. Gato, and F. Arena. Power take-off selection for a fixed U-OWC wave power plant in the Mediterranean Sea: The case of Roccella Jonica. *Energy*, 215(Part A):119085, 2021, doi:10.1016/j.energy.2020.119085.

[128] J. Courtney. Automatic Signal Buoy, 1876.

[129] J. M. Courtney. Whistling Buoys, 1885.

[130] T. Heath. A review of oscillating water columns. *Philosophical transaction of the Royal Society, A*, pages 235–245, 2012.

[131] Y. Masuda. The progress of wave power generator in Japan. In *Proceedings of the First Pacific/Asia Offshore Mechanics Symposium*, Seoul, South Korea, 1990.

[132] Y. Masuda. Wave-activated power generator, 1989.

[133] Y. Masuda. Improvement of wave power generator system for navigational buoy and other use. In *Proceeding of the First Pacific/Asia Offshore Mechanics Symposium*, Seoul, South Korea, 1990.

[134] Y. Masuda. Study of Backward Bent Duct Buoy. In *Institute of Electrical and Electronics Engineers*, 1987.

[135] Y. Masuda. The Backward Bent Duct Buoy - an improved floating type wave power device. In *Institute of Electrical and Electronics Engineers*, 1988.

[136] Y. Masuda. An experience of wave power generator through test and improvement. *Hydrodynamics of wave energy utilization*, pages 445–452, 1985.

[137] T. Miyazaki and Y. e Masuda. Test on the wave power generator Kaimei. In *Offshore Technology Conference*, pages 101–110, 1980.

[138] K. Kudo and S. Yoshida. Study on the Hull Form of the Kaimiei-type Wave Power Absorber. In *1st Symposium on wave energy utilization*, pages 570–571, 1985.

[139] S. Ischii, Y. Masuda, T. Miyazaki, K. Kudo, H. Hotta, and Y. Washio. Results on 1st sea trial and plan on 2nd sea trial of wave power generator Kaimei. pages 597–598, 1985.

[140] M. Takao and T. Setoguchi. Air turbines for wave energy conversion. *International Journal of Rotating Machinery*, pages 1–10, 2012, doi:10.1155/2012/717398.

[141] N. Delmonte, D. Barater, F. Giuliani, P. Cova, and G. Buticchi. Review of Oscillating Water Column Converters. In *Institute of Electrical and Electronics Engineers, Transactions on Industry Applications*, 2015, doi:10.1109/TIA.2015.2490629.

[142] Y. Masuda. Design study of wave power generators for power supply to islands in far east. In *Proceedings of the Fourth International Offshore and Polar Engineering Conference*, Osaka, Japan, 1994, ISBN 1-880653-10-9.

[143] Y. Masuda, T. Kuboki, M. Ravindrum, and X. Linag. Development of Backward Bent Duct Buoy. In *Proceedings of the Ninth International Offshore and Polar Engineering Conference*, Brest, France, 1999, ISBN 1-880653-39-7.

[144] M. Suzuki, C. Arakawa, and S. Takahashi. Performance of Wave Power Generating System Installed in Breakwater at Sakata Port in Japan. pages 202–209, 2004, ISBN 1-880653-62-1.

[145] A. F. O. Falcão. Modelling of wave energy conversion. pages 1275–1295, 2014.

[146] S. Neelamani. A decade of wave power development in India - The challenges. *Marine Technology Society Journal*, 36(4):59–73, 2002.

[147] A. S. Sehata, Q. Xiao, K. M. Saqr, and S. Day. Wells turbine for wave energy conversion: A review. *International Journal of Energy Research*, 41(1):6–38, 2017, doi: 10.1002/er.3583.

[148] Y. Washio, H. Osawa, and T. Ogata. The open sea tests of the offshore floating type wave power device "Mighty Whale" -characteristics of wave energy absorption and power generation. 2001.

[149] H. Hotta, Y. Washio, H. Yokozawa, and T. Miyazaki. Research and Development on wave power device "Mighty Whale". *Renewable Energy*, 9(1-4), 1996.

[150] H. Osawa and T. Miyazaki. Wave-PV hybrid generation system carried in the offshore floating type wave power device "Mighty Whale". volume 4, pages 1860–1866, 2004, doi:10.1109/OCEANS.2004.1406427.

[151] T. Ogata. The open sea tests of the offshore floating type wave power device Mighty Whale - Performance of the prototype. 2002.

[152] A. Brito-Melo. Full-scale data assessment in OWC Pico Plant. Lisbon, Portugal, 2007.

[153] A. F. O. Falcão, A. J. N. A. Sarmento, L. M. C. Gato, and A. Brito-Melo. The Pico OWC wave power plant: its life from conception to closure 1986-2018. *Advances in renewable energies offshore*, 98:102104, 2020.

[154] European wave energy plant on the island of Pico, Azores, Portugal. Phase two: equipment, 1998.

[155] A. Sarmento and F. Neumann. A Oscillating water column - Pico plant. *Ocean wave energy - Current status and future perspectives*, 2008.

[156] T. J. T. Whittaker. Islay LIMPET Wave Power Plant, 2002.

[157] M. Folley. Comparison of LIMPET contra-rotating Wells. *Ocean Engineering*, 33, 2006.

[158] D. Zhang. Wave energy in China: Current status and perspectives. *Renewable Energy*, 34:2089–2092, 2009.

[159] A. Gareev. *Analysis of variable pitch air turbines for oscillating water column wave energy converters.* PhD thesis, Ph.D. Thesis, University of Wollongong, 2011.

[160] J. Kofoed. *The wave energy sector.* Handbook of ocean wave energy, 2017.

[161] L. Martinelli. Selection of design power of wave energy converters based on wave basin experiments. *Renewable Energies*, 36, 2001.

[162] L. Martinelli, P. Roul, and G. Cortellazzo. On mooring design of wave energies converters: the Seabreath application. *Coastal Structures*, 2013, doi:10.9753/icce.v33.structures.3.

[163] L. Martinelli. On mooring design of wave energies converters: the Seabreath application. *Institute of Electrical and Electronics Engineers*, 2011.

[164] E. G. Moliner. *Cost Analysis of the UGEN.* PhD thesis, Master Thesis, Instituto Superior Técnico, 2016.

[165] Y. Torre-Enciso. Mutriku Wave Power Plant: from the thinking out to the reality. 2009.

[166] Henriques J. C. C., W. Sheng, A. F. O. Falcão, and L. M. C. Gato. A Comparison of Biradial and Wells Air Turbines on the Mutriku Breakwater OWC Wave Power Plant. *ASME 2017 36th International Conference on Ocean, Offshore and Arctic Engineering (OMAE2017)*, 2017, doi:10.1115/OMAE2017-62651.

[167] I. Garrido. Oscillating Water Column control and monitoring. 2016.

[168] I. Garrido, A. J. Garrido, E. Lekube, J. Otaola, E. Carrascal, and M. de la Sen. Advantages of rotational speed control in oscillating water column devices. pages 1–5, 2016, doi:10.1109/OCEANSE.2017.8084687.

[169] F. Mzoughi. Intelligent airflow controls for a stalling-free operation of an Oscillating Water Column-based wave power generation plant. *Electronics*, 2019.

[170] A. Carrelhas, L. M. C. Gato, J. C. C. Henriques, and A. F. O. Falcão. Test results of a 30 kW self-rectifying biradial air turbine-generator prototype. *Renewable and Sustainable Energy Reviews*, 109:187–198, 2019, doi:10.1016/j.rser.2019.04.008.

[171] A. F. O. Falcão, Henriques J. C. C., and J. J. Candido. Dynamics and optimization of the OWC spar buoy wave energy converter. *Renewable Energy*, 48:369–381, 2016, doi:10.1016/j.renene.2012.05.009.

[172] F. Arena, A. Romolo, G. Malara, V. Fiamma, and V. Laface. The First Full Operative U-OWC Plants in

the Port of Civitavecchia. 2017, doi:10.1115/OMAE2017-62036.

[173] F. Arena, A. Romolo, G. Malara, A. Ascanelli, S. Ghiretti, W. Allsop, and K. Burgess. A New U-OWC Device to Produce Electrical Power from Ocean Waves: Some Applications to Italian Coasts. *ICE Virtual Library*, 2014, doi:10.1680/fsts.59757.0346.

[174] R. Cascajo, E. García, E. Quiles, A. Correcher, and F. Morant. Integration of Marine Wave Energy Converters into Seaports: A Case Study in the Port of Valencia. *Energies*, 12(5):787, 2019, doi:10.3390/en12050787.

[175] A. Carrelhas, L. M. C. Gato, J. C. C. Henriques, and A. F. O. Falcão. Experimental study of a self-rectifying biradial air turbine with fixed guide-vanes arranged into two concentric annular rows. *Energy*, 198:117211, 2019, doi:10.1016/j.energy.2020.117211.

[176] A. A. Wells. Fluid Driven Rotary Transducer, 1976.

[177] S. Raghunathan, R. Curran, and T. J. T. Whittaker. Performance of the Islay Wells air turbine. *Proceedings of the Institution of Mechanical Engineers*, 209:55–62, 1995, doi:10.1243/PIME_PROC_1995_209_009_02.

[178] F. Weining. *Die stromung um die schaufeln von turbomaschinen*. Barth, Germany, 1935.

[179] N. Scholtz. Aerodynamics of Cascades, Amsterdam, The Netherlands, 1977.

[180] M. Suzuki, T. Arakawa, and T. Tagori. Comparison of performance of Wells turbine with different blade shapes.

*Preprint of Turbomachinery Society of Japan*, 13:62–67, 1984, doi:10.1243/PIME_PROC_1995_209_009_02.

[181] M. Inoue, K. Kaneko, T. Setoguchi, and S. Raghunathan. Simulation of starting characteristics of Wells turbine. Atlanta, Georgia, USA, 1986a.

[182] M. Inoue, K. Kaneko, and T. Setoguchi. Determination of optimum geometry of Wells turbine rotor for wave energy generator. New Orleans, Louisiana, USA, 1986.

[183] S. Raghunathan, T. Setoguchi, and K. Kaneko. The effect of inlet conditions on the performance of Wells turbine. Cincinnati, Ohio, USA, 1987.

[184] S. Raghunathan, T. Setoguchi, and K. Kaneko. Hysteresis on Wells turbine blades. Cincinnati, Ohio, USA, 1987.

[185] R. Tagori, C. Arakawa, and M. Suzuki. Estimation of prototype performance and optimum design of Wells turbine. *Research in Natural Energy*, SPEY 20:127–132, 1987.

[186] S. Raghunathan, T. Setoguchi, and K. Kaneko. Correlation of test rig and wind tunnel tests for performance prediction of Wells turbine. In *Proceedings of the Offshore Mechanics and Arctic Engineering Conference*, The Hague, The Netherlands, 1989.

[187] E. N. Jakob and A. Sherman. Airfoil Section Characteristics as Affected by Variations of the Reynolds Number, NACA Technical Report no. 586, 1937.

[188] S. Raghunathan. Aerodynamic forces on aerofoils at high angles attack. In *American Institute of Aeronautics and Astronautics National Fluid Dynamics Congress*, page Paper 883697, Cincinnati, Ohio, USA, 1988.

[189] S. Raghunathan, A. Eves, T. J. J. Whittaker, and A. E. Long. The bi-plane Wells turbine. In *Proceedings of the Conference on Ocean, Offshore and Arctic Engineering*, Houston, Texas, USA, 1987a.

[190] K. Kaneko, S. Raghunathan, and T. Setoguchi. Performance of multiplane Wells turbine for an OWC type wave energy conversion. Hoikodo, Japan, 1993.

[191] J. V. Wehausen. The Motion of Floating Bodies. *Annual Review of Fluid Mechanics*, 3(1):237–268, Available at: http://www.annualreviews.org/doi/abs/10.1146/annurev.fl.03.010171.001321, Accessed on July the 1st 2019.

[192] D. V. Evans. The Oscillating Water Column Wave-energy Device. *IMA Journal of Applied Mathematics*, 22(4):423–433, 1978, doi:10.1093/imamat/22.4.423.

[193] D. V. Evans. Power From Water Waves. *Annual Review of Fluid Mechanics*, 13(1):157–187, 1981, doi:10.1146/annurev.fl.13.010181.001105.

[194] R. W. Robinson. The effects of geometry-wave field interactions o the performance of oscillating water column wave energy converters. *Queens University, Belfast, Northern Ireland*, 1982.

[195] K. C. Watts, K. M. Hassan, S. N. Sarwal, H. C. Alexander, and J. W. Graham. Non-linear analysis of a non-vertical walled OWC ocean wave energy converter. Dallas, Texas, USA, 1985.

[196] H. Maeda, T. Kinoshita, K. Masuda, and W. Kato. Fundamental Research on Oscillating Water Column Wave

Power Absorbers. *Journal of Energy Resources Technology*, 1070(1):81, 1985.

[197] Q. W. Ma. Nonlinear analysis on hydrodynamic performance of oscillating water column wave energy device with a lateral opening. Copenhagen, Denmark, 1985.

[198] A. Brendmo, J. Falnes, and P. M. Lillebekken. Linear modelling of OWC including viscous loss. *Applied Ocean Research*, 18:65–75, 1996.

[199] M. F. P. Lopes, J. Hals, R. P. F. Gomes, T. Moan, L. M. C. Gato, and A. F. O. Falcão. Experimental and numerical investigation of non-predictive phase-control strategies for a point-absorbing wave energy converter. *Ocean Engineering*, 143(5):051205, 2021, doi:10.1115/1.4049686.

[200] F. Gouaud, V. Rey, J. Piazzola, and R. Van Hooff. Experimental study of the hydrodynamic performance of an onshore wave power device in the presence of an underwater mound. *Coastal Engineering*, 57(11–12):996–1005, 2010, doi:10.1016/j.coastaleng.2010.06.003.

[201] G. Nunes, D. Valério, P. Beirão, and J. Sá da Costa. Modelling and control of a wave energy converter. *Renewable Energy*, 36(7):1913–1921, 2011, 10.1016/j.renene.2010.12.018.

[202] R. Gervelas, F. Trarieux, and M. H. Patel. A time-domain simulator for an oscillating water column in irregular waves at model scale. *Ocean Engineering*, 38:1007–1013, 2011, doi:10.1016/j.oceaneng.2011.04.006.

[203] R. K. Sykes, A. W. Lewis, and G. P. Thomas. Predicting

Hydrodynamic Pressure in Fixed and Floating OWC Using a Piston Model. Southampton, England, 2011.

[204] A. F. O. Falcão, J. C. C. Henriques, and J. J. Cândido. Dynamics and optimization of the OWC spar buoy wave energy converter. *Renewable Energy*, 48:369–381, 2012, doi:10.1016/j.renene.2012.05.009.

[205] R. P. F. Gomes, J. C. C. Henriques, L. M. C. Gato, and A. F. O. Falcão. Hydrodynamic optimization of an axisymmetric floating oscillating water column for wave energy conversion. *Renewable Energy*, 44:328–339, 2012, doi:10.1016/j.renene.2012.01.105.

[206] P. Ricci, J.-B. Saulnier, A. F. O. Falcão, and M. T. Pontes. Time-Domain Models and Wave Energy Converters Performance Assessment. pages 699–708, Estoril, Portugal, 2008.

[207] J. Cruz. *Ocean Wave Energy - Current Status and Future Prospectives*. Springer Series in Geeen Energy and Technology, 2009.

[208] T. Setoguchi, S. Santhakumar, M. Takao, T. H. Kim, and K. Kaneko. Effect of guide vane shape on the performance of a Wells turbine. *Renewable Energy*, 23:1–15, 2001, doi:10.1016/S0960-1481(00)00175-0.

[209] L. Ciappi, L. Cheli, I. Simonetti, A. Bianchini, G. Manfrida, and L. Cappietti. A rigid piston model of a fixed and detached oscillating water column chamber for wave energy converters, September 2019.

[210] L. Cheli. *Modellazione numerica di un sistema OWC con*

*turbina ad impulso*. PhD thesis, Master Thesis, University of Florence, 2019 (in Italian).

[211] W. Duane and F. L. Hunt. On X-Ray Wave-Lengths. *Physical Review*, 6(2):166–172, 1915.

[212] J. D. Eckart. The propagation of gravity waves from deep to shallow water, Washington, DC, USA, 1952.

[213] M. Patel and J. Harrison. The mechanics of a compliant motion suppression system for semisubmersibles. *Journal of Sound and Vibration*, 106:491–507, 1986, doi:10.1016/0022-460x(86)90194-x.

[214] A. H. Techet. Design Principles for Ocean Vehicles, 2005.

[215] I. Simonetti, L. Cappietti, H. El Safti, and H. Oumeraci. Numerical Modelling of Fixed Oscillating Water Column Wave Energy Conversion Devices: Toward Geometry Hydraulic Optimization. 2015.

[216] W. Wang and R. X. Huang. Wind Energy Input to the Surface Waves. *Journal of Physical Oceanography*, 34(5):1276–1280, 2004.

[217] A. Uihlein and D. Magagna. Wave and tidal current energy – A review of the current state of research beyond technology. *Renewable and Sustainable Energy Reviews*, 58:1070–1081, 2016, doi:10.1016/j.rser.2015.12.284.

[218] Y. Wang, C. Fan, J. Zhang, J. Meng, Y. Dai, L. Li, P. Sun, W. Zhou, J. Wang, and X. Zhang. Wave Energy Resource Assessment off the Coast of China around the Zhoushan Islands. *Energies*, 10(9):1320, 2017, doi:10.3390/en10091320.

[219] F. He and Z. Huang. Hydrodynamic performance of pile-supported OWC-type structures as breakwaters: An experimental study. *Ocean Engineering*, 88:618–626, 2014, doi:10.1016/j.oceaneng.2014.04.02.

[220] S. Whitaker. Flow in porous media I: A theoretical derivation of Darcys law. *Transport in Porous Media*, 1:3–25, 1986, doi:10.1007/BF01036523.

[221] J. H. Horlock. *Axial flow compressors.* Fluid Mechanics and Thermodynamics, 1973.

[222] L. Ciappi, L. Cappietti, and G. Manfrida. A blade element momentum model for the analysis of Wells turbines for oscillating water column systems, October 2018.

[223] W. M. Kutta. *Lifting Forces in Flowing Fluids.* G. Braunbeck and Gutenberg, Berlin, Germany, 1902.

[224] C. Xu. Kutta Condition for sharp edge flows. *Mechanics Research Communications*, 25:415–420, 1998.

[225] R. E. Sheldahl and P. C. Klimas. Aerodynamic Characteristics of Seven Symmetrical Airfoil Sections Through 180-Degree Angle of Attack for Use in Aerodynamic Analysis of Vertical Axis Wind Turbines, 1981.

[226] D. D. Jr. Anderson. *Fundamentals of Aerodynamics.* Southpointe 2600 ANSYS Drive Canonsburg, Pennsylvania 15317, 2019.

[227] L. Ciappi, L. Cheli, A. Bianchini, L. Cappietti, and G. Manfrida. A blade element momentum model for the analysis of impulse turbines for oscillating water column systems, July 2019.

[228] G. Cafaggi. *Sviluppo di strumenti per l'analisi di turbine a impulso bidirezionali per sistemi OWC*. PhD thesis, Master Thesis, University of Florence, 2015 (in Italian).

[229] A. Thakker, H. B. Khaleeq, M. Takao, and T. Setoguchi. Effects of hub-to-tip ratio and Reynolds number on the performance of impulse turbine for wave energy power plant. *KSME Interantional Journal*, 17(11):1767–1774, 2003, doi:10.1007/BF02983607.

[230] Z. Liu, Y. Cui, M. Li, and H. D. Shi. Steady state performance of an axial impulse turbine for oscillating water column wave energy converters. *Energy*, 141:1–10, 2017, doi:10.1016/j.energy.2017.09.068.

[231] L. M. C. Gato, A. A. D. Carrelhas, and A. F. A. Cunha. Performance improvement of the axial self-rectifying impulse air-turbine for wave energy conversion by multi-row guide vanes: Design and experimental results. *Energy Conversion and Management*, 243:114305, 2021, doi:10.1016/j.enconman.2021.114305.

[232] H. Maeda, T. Setoguchi, K. Kaneko, T. W. Kim, and M. Inoue. Effect of turbine geometry on the performance of impulse turbine with self-pitch-controlled guide vanes for wave power conversion. *International Journal of Offshore and Polar Engineering*, 5(1):72–74, 1995.

[233] J. D. Denton. Loss Mechanisms in Turbomachines. *Journal of Turbomachinery*, 115:621–656, 1993, doi:10.1115/1.2929299.

[234] B. Lakshminarayana and J. H. Horlock. Review: Secondary Flows and Losses in Cascades and Axial-Flow Tur-

bomachines. *Interantional Journal of Mechanical Sciences*, 5:287–307, 1963, doi:10.1016/0020-7403(63)90055-9.

[235] S. C. Kacker and U. Okapuu. A Mean Line Prediction Method for Axial Flow Turbine Efficiency. *Journal of Engineering for Power*, 104(1):111–119, 1982.

[236] J. Dunham and P. Came. Improvements to Ainley-Mathieson method of turbine performance prediction. *Transactions of the American Society of Mechanical Engineers*, Series A(92), 1970.

[237] F. M. White. *Fluid mechanics*. McGraw-Hill, New York, NY, 5th Edition, 2003.

[238] S. B. Pope. *Turbulent flows*. Cambridge University Press, Cambridge, England, 2000.

[239] J. O. Hinze. *Turbulence*. McGraw-Hill, New York, NY, USA, 1975.

[240] D. C. Wilcox. *Turbulence modelling for CFD*. DCW Industries Incorporation, La Cañada Flintridge, CA, USA, 1998.

[241] M. Bassetti, A. Corsini, G. Delibra, G. Faggiolati, S. Piccinini, F. Rispoli, G. Romani, M. Ruggeri, and E. Tuccimei. An integrated procedure for the design of a Wells turbine developed for Mediterranean operation. Rome, Italy, 2012, ISBN 978-88-8286-283-1.

[242] M. Bassetti, A. Corsini, G. Delibra, and F. Rispoli. Progetto e prima verifica operativa di una micro-turbina Wells per il Mar Mediterraneo, 2014 (in English).

[243] M. Torresi, S. M. Camporeale, P. D. Strippoli, and G. Pascazio. Accurate numerical simulation of a high solidity Wells turbine. *Renewable Energy*, 33:735–747, 2008, 10.1016/j.renene.2007.04.006.

[244] T. Setoguchi, Y. Kinoue, T. H. Kim, K. Kaneko, and Inoue M. Hysteretic Characteristics of Wells Turbine for Wave Power Conversion. *Renewable Energy*, 28(13):2113–2127, 2003, doi:10.1016/S0960-1481(03)00079-X.

[245] P. Halder, A. Samad, and D. Thevenin. Improved design of a Wells turbine for higher operating range. *Renewable Energy*, 106:122–134, 2017, doi:10.1016/j.renene.2017.01.012.

[246] I. Hashem, H. S. Abdel Hameed, and M. H. Mohamed. An axial turbine in an innovative oscillating water column (OWC) device for sea-wave energy conversion. *Ocean Engineering*, 164:536–562, 2018, doi:10.1016/j.oceaneng.2018.06.067.

[247] B. E. Launder and D. B. Spalding. *Lectures in Mathematical Models of Turbulence*. Academic Press, London, England, 1972, ISBN 0124380506.

[248] F. R. Menter. Two-Equation Eddy-Viscosity Turbulence Models for Engineering Applications. *American Institute of Aeronautics and Astronautics Journal*, 32:1598–1605, 1994, doi:10.2514/3.12149.

[249] H. L. Tolman. User Manual and System Documentation of Wavewatch iii Version 4.18, NOAA, NSW, NCEP, USA, 2014.

[250] D. Pelli, L. Cappietti, H. Oumeraci, and C. Soares. Assessing the wave energy potential in the Mediterranean

Sea using Wavewatch iii. *Journal of Sound and Vibration*, 106:491–507, 2016, doi:10.1201/9781315229256-4.

[251] A. Elhanafi. Prediction of regular wave loads on a fixed offshore oscillating water column-wave energy converter using CFD. *Journal of Ocean Engineering and Science*, 1(4):268–283, 2016, doi:10.1016/j.joes.2016.08.001.

[252] I. Simonetti, L. Cappietti, H. Elsafti, and H. Oumeraci. Optimization of the geometry and the turbine induced damping for fixed detached and asymmetric OWC devices: A numerical study. *Energy*, 139:1197–1209, 2017, doi:10.1016/j.energy.2017.08.033.

[253] M. Zabihi, S. Mazaheri, and M. M. Namin. Experimental hydrodynamic investigation of a fixed offshore Oscillating Water Column device. *Applied Ocean Research*, 85:20–33, 2019, doi:10.1016/j.apor.2019.01.036.

[254] J. Chen, H. Wen, Y. Wang, and G. Wang. Correlation study of optimal chamber width with the relative front wall draught of onshore OWC device. *Energy*, 225:120307, 2021, doi:10.1016/j.energy.2021.120307.

[255] A. Çelik and A. Altunkaynak. Experimental investigations on the performance of a fixed-oscillating water column type wave energy converter. *Energy*, 188:116071, 2019, doi:10.1016/j.energy.2019.116071.

[256] A. Elhanafi, G. Macfarlane, A. Fleming, and Z. Leong. Scaling and air compressibility effects on a three-dimensional offshore stationary OWC wave energy converter. *Applied Energy*, 189:1–20, 2016, doi:10.1016/j.apenergy.2016.11.095.

[257] I. Simonetti, L. Cappietti, H. Elsafti, and H. Oumeraci. Evaluation of air compressibility effects on the performance of fixed OWC wave energy converters using CFD modelling. *Renewable Energy*, 119:741–753, 2018, doi:10.1016/j.renene.2017.12.027.

[258] G. Ibarra-Berastegi, J. Sáenz, A. Ulazia, P. Serras, G. Esnaola, and C. Garcia-Soto. Electricity production, capacity factor and plant efficiency index at the Mutriku wave farm (2014–2016). *Ocean Engineering*, 174:20–29, 2018,doi:10.1016/j.oceaneng.2017.10.018.

[259] W. C. Reynolds. Fundamentals of turbulence for turbulence modeling and simulation, 1987.

[260] T.-H. Shih, W. W. Liou, A. Shabbir, Z. Yang, and J. Zhu. A New $k$-$\epsilon$ Eddy-Viscosity Model for High Reynolds Number Turbulent Flows - Model Development and Validation. *Computers Fluids*, 24(3):227–238, 1995.

[261] S. E. Kim, D. Choudhury, and B. Patel. Computations of Complex Turbulent Flows Using the Commercial Code ANSYS Fluent. Hampton, VA, USA, 1997.

[262] S. Astariz and G. Iglesias. The economics of wave energy: A review. *Renewable and Sustainable Energy Reviews*, 45:397–408, 2015, ISSN 1364-0321, doi:10.1016/j.rser.2015.01.061.

[263] N. F. Brooklyn, R. P. F. Gomes, and L. M. C. Gato. Analysis of oscillating-water-column wave energy converter configurations for integration into caisson breakwaters. *Applied Energy*, 295:117023, 2021, doi:10.1016/j.apenergy.2021.117023.

[264] A. Çelik and A. Altunkaynak. Estimation of Water Column Surface Displacement of a Fixed Oscillating Water Column by Simple Mechanical Model with Determination of Hydrodynamic Parameters via Physical Experimental Model. *Journal of Waterway, Port, Coastal, and Ocean Engineering*, 146:04020030, 2020, doi:10.1061/(asce)ww.1943-5460.0000593.

[265] L. Ciappi, L. Cappietti, and G. Manfrida. Revision of the state of the art for turbines for oscillating water column wave energy converters, September 2018.

[266] L. Ciappi, M. Stebel, J. Smoł ka, L. Cappietti, and G. Manfrida. Computational fluid dynamics models of a monplane isolated Wells turbine for OWC systems, May 2019.

[267] A. Iturrioz, R. Guanche, J. A. Armesto, M. Alves, C. Vidal, and I. Losada. Time-domain modeling of a fixed detached oscillating water column towards a floating multichamber device. *Ocean Engineering*, 76:65–74, 2014, doi:10.1016/j.oceaneng.2013.11.023.

[268] K. Kihara. A practical estimation method of PTO and sea test of a PW-OWC type WEC using a wave dissipating double caisson. *Advances in renewable energies offshore - Proceedings of the 3rd international conference on renewable energies offshore*, 2018.

[269] Y. Masuda. Wave-activated generator. In *Proceedings of the International Colloquium on the Exposition of Oceans*, Bordeaux, France, 1971.

[270] Y. Masuda. Wave power use for island supply by a Backward Bent Duct Buoy. In *Offshore Technology Conference*, 1997.

[271] R. W. Miller. *Flow Measurement Engineering Handbook*. McGraw-Hill, New York, NY, USA, ISBN 978-0-07-042366-4.

[272] S. Raghunathan and C. P. Tan. The performance of biplane Wells turbine. *Journal of the American Institute of Aeronautics and Astronautics*, 7:741–742, 1983.

[273] F. M. Strati, G. Malara, and F. Arena. Performance optimization of a U-Oscillating-Water-Column wave energy harvester. *Renewable Energy*, 2016, doi:10.1016/j.renene.2016.07.080.

[274] V. Vannucchi and L. Cappietti. Wave energy estimation in four Italian nearshore areas. Nantes, France, 2013.